Measurements of $\mu\mu$ pairs from $c\bar{c}$, $b\bar{b}$ and Drell-Yan in p+p and p+Au collisions at $\sqrt{s_{NN}} = 200$ GeV with PHENIX at RHIC

A Dissertation presented

by

Yue Hang Leung

to

The Graduate School

in Partial Fulfillment of the

Requirements

for the Degree of

Doctor of Philosophy

in

Physics

Stony Brook University

May 2019

(include this copyright page only if you are selecting copyright through ProQuest, which is optional)

Stony Brook University

The Graduate School

Yue Hang Leung

We, the dissertation committee for the above candidate for the

Doctor of Philosophy degree, hereby recommend

acceptance of this dissertation

Axel Drees - Dissertation Advisor
Professor, Department of Physics and Astronomy

Dmitri Kharzeev - Chairperson of Defense
Professor, Department of Physics and Astronomy

Dominik Schneble
Professor, Department of Physics and Astronomy

Jin Huang
Physicist, Brookhaven National Laboratory

This dissertation is accepted by the Graduate School

Charles Taber
Dean of the Graduate School

Abstract of the Dissertation

Measurements of $\mu\mu$ pairs from charm, bottom and Drell-Yan in p+p and p+Au collisions at $\sqrt{s_{NN}} = 200$ GeV with the PHENIX detector at RHIC

by

Yue Hang Leung

Doctor of Philosophy

in

Physics

Stony Brook University

2019

Dilepton spectra are a classic probe to study ultra-relativistic heavy ion collisions. At $\sqrt{s_{NN}} = 200$ GeV, the dimuon continuum is dominated by correlated pairs from semi-leptonic decays of charm and bottom hadrons and the Drell-Yan process. Measuring the azimuthal correlations of heavy flavor decay lepton pairs can help constrain the relative contributions from different heavy flavor production mechanisms in p+p collisions, and may provide further insight on cold nuclear matter effects in p+A collisions. Measuring the Drell-Yan cross-section in p+A collisions can provide constraints to nuclear parton distribution functions, and further our understanding in initial state effects.

In this dissertation, measurements of muon pairs from charm, bottom, and Drell-Yan, using data collected by the Relativistic Heavy Ion Collider (RHIC) and the Pioneering High Energy Nuclear Interaction eXperiment (PHENIX), in p+p and p+Au collisions at $\sqrt{s_{NN}} = 200$ GeV are presented.

To my family.

Table of Contents

Contents

List of Figures/Tables/Illustrations

List of Figures

List of Tables

Acknowledgements

First and foremost, I would like to thank my thesis advisor Prof. Axel Drees. Axel's strong intuition and unwavering optimism has not only made this thesis possible but also profoundly formed me.

I also would like to express my gratitude to multiple people that have offered me help in completing this work. Dr. Deepali Sharma, a good friend and mentor, laid the foundations to my PhD career. Getting past the first few PhD years would not have been possible if not for her. I would like to also thank Dr. Sanghoon Lim. Our e-mail thread has recently exceeded 1000 messages and is a testimony of his endless patience. He has always offered good advice, both in data analysis and future career, and has made my brief stay in Los Alamos an unforgettable experience.

I would like to extend my thanks to Dr. Cesar da Silva. With his help, I had the opportunity to visit the Los Alamos National Laboratory and which proved to be a fruitful experience. I am also thankful to Dr. Jin Huang, who introduced me to muon analysis in PHENIX. I am grateful to Prof. Xiaochun He, he and the Georgia State group made the first endeavors into the like-sign muon pair spectra and laid the groundwork to this dissertation.

I also want to thank all my colleagues in the Physics Department in Stony Brook. I am blessed to have you as my friends.

Last but not least, I want to thank my family for their unconditional understanding and support.

1 Introduction

1.1 The Big Bang and the Quark Gluon Plasma

1.1.1 The Big Bang and the Strong Force

The *Big Bang Theory* proposes that the universe began as an extremely hot and dense dot. Since then, it grew over 14 billion years into the vast and cooler expanding cosmos that we currently live in.

The physics in the current world can be largely described by the *Standard Model*. The Standard Model, developed in the early 1970s, is a theory describing three of the four known fundamental forces, the electromagnetic interaction, the weak interaction and the strong interaction; it also classifies all known elementary particles [1]. Figure 1 is a summary of all known elementary particles. The existence of the Higgs boson, the last particle in the standard model to be discovered, was finally confirmed in 2013 at the Large Hadron Collider (LHC).

It is conjectured that in the early universe, the aforementioned three fundamental forces, together with gravity, were unified as a single force, known as the *Grand Unified force*. As the universe expands and cools, it crosses transition temperatures at which forces separate from each other. These phase transitions can be intuitively visualized as similar to the condensation phase transition of ordinary matter. When steam condenses into water, the water molecules change their structure and behave in a completely different manner [51].

Approximately 10^{-43} seconds after the big bang, the *Grand Unified Force* separates into gravity and the conjectured electrostrong interaction [52]. Around 10^{-36} seconds later, the electrostrong interaction further separated into the strong and the electroweak interactions. As the universe further cools down, two important phase transitions are expected to occur, one governed by the weak interaction, the other governed by the strong interaction. The former phase transition is known as the *electroweak phase transition*, in which the electromagnetic force is separated from the weak force. This phase transition causes all fundamental particles that interact with the Higgs field, e.g. quarks, to become *massive*. The second phase transition, the nuclear matter phase transition, from the *Quark-Gluon Plasma* phase to the *hadron* phase, occurs about 10 μs after the electroweak phase transition.

It is hypothesized that until the nuclear matter phase transition, the

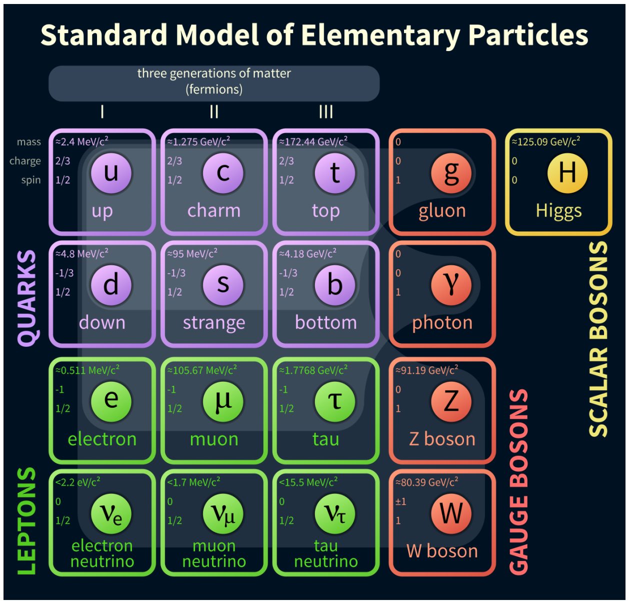

Figure 1: Elementary particles of the standard model. [1]

early universe consists of a mixture of asymptotically free quarks and gluons, known as the *Quark-Gluon Plasma* [53] (QGP), a state of matter that exist at extremely high temperature and density. This contrasts to the current world that we live in, where the strong force binds quarks and gluons are tightly inside composite particles known as *hadrons*, as dictated by the theory of Quantum Chromodynamics (QCD) [54]. This is known as *confinement*; the attraction between quarks and gluons grows stronger as the distance between them increases.

It has been predicted by H. D. Politzer [55] and F. Wilczek and D. Gross [56] in 1973, that the strong coupling coupling constant α_S, which determines the strength of the strong interaction, becomes asymptotically weaker as the length scale decreases, or equivalently, as the energy scale increases. This phenomenon is known as *asymptotic freedom*. In the weak coupling regime, the coupling constant can be evaluated using perturbative Quantum Chromodynamics (pQCD). The pQCD computed α_S as a function of the momentum transfer Q is shown in Fig. 2 and compared to experimentally measured values. The calculations are consistent with experimental data at small α_S. However, as the energy scale approaches a certain value

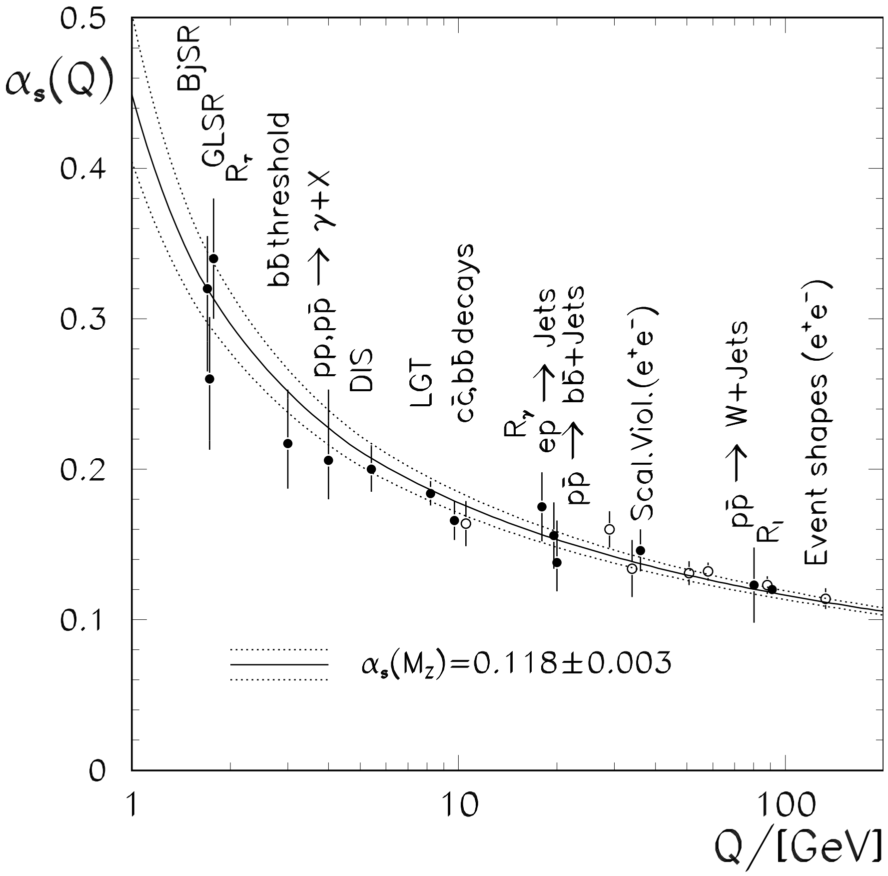

Figure 2: Running of the strong coupling constant established by various types of measurements at different scales, compared to the pQCD prediction for $\alpha_s = 0.118 \pm 0.003$ [2]

known as the QCD scale $\Lambda_{\mathrm{QCD}} \approx 220$ MeV, perturbative theory is no longer applicable. To overcome this problem, lattice QCD, which in the simplistic sense, is QCD evaluated on a grid or lattice of points in space and time, has been applied to the non-perturbative regime. Lattice QCD calculations predict a phase transition of nuclear matter at higher temperature and energy density, from bound colorless hadrons to deconfined quarks and gluons. The phase transition is expected to occur around a critical temperature of $T_C \sim 173 \pm 8$ MeV ($(2.01 \pm 0.09) \times 10^{12}$ Kelvins) [57, 4], as illustrated in Fig. 3. A lattice QCD calculation which showcases this phase transition is

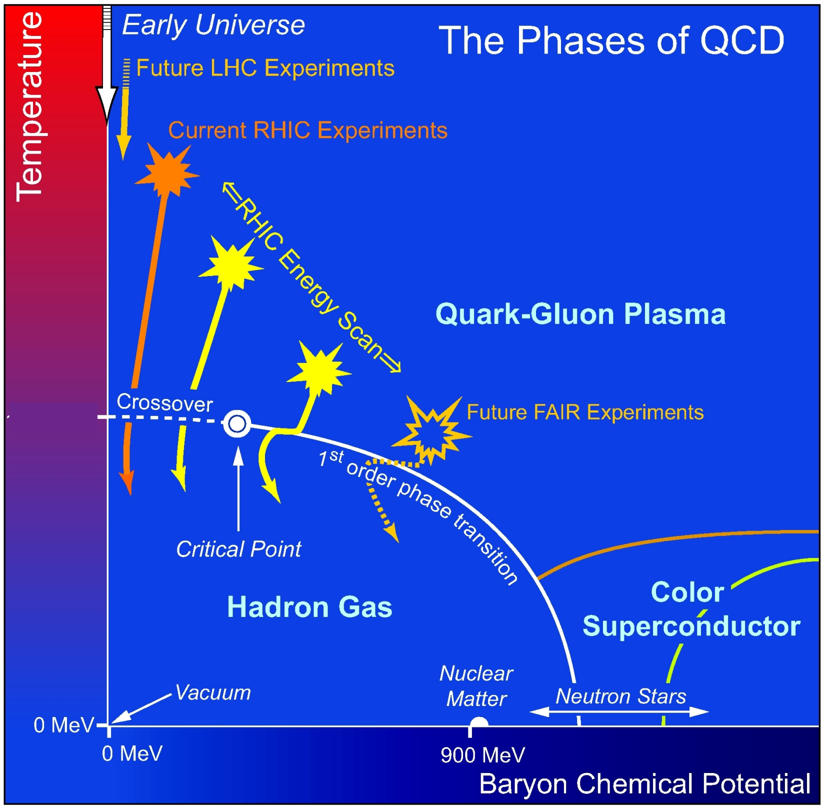

Figure 3: The QCD phase diagram [3].

shown in Fig. 4, which is a plot of the energy density ϵ divided by the fourth power of the temperature T^4 as a function of T/T_C. The quantity ϵ/T^4 is representative of the relavant degrees of freedom. One can see that from lattice QCD calculations, around the critical temperature, there is a steep increase in ϵ/T^4, which corresponds to a drastic increase in the degrees of freedom of nuclear matter. This is explained by the fact that below T_C, quarks and gluons are confined inside bound states, having fewer degrees of freedom, while above T_C, the quarks and gluons are liberated and the system has much more degrees of freedom.

This phase transition of nuclear matter gives rise to most of the visible mass in the universe today. The basic building blocks of matter, protons and neutrons, consist of three valence quarks, two up quarks and one down quark for the proton, and one up quark and two down quarks for the neutron. The mass of the up and down quarks due to the coupling to the Higgs boson are 2.2 MeV/c^2 and 4.8 MeV/c^2 respectively, while the mass of the proton and the neutron are 938 MeV/c^2 and 940 MeV/c^2 respectively, vastly larger than the sum of masses of the quarks. The source of the bulk of the proton's and neutron's mass arises from the strong interaction between quarks and gluons. In the following, we will discuss theoretical and experimental efforts to characterize the quark gluon plasma and the QCD phase transition.

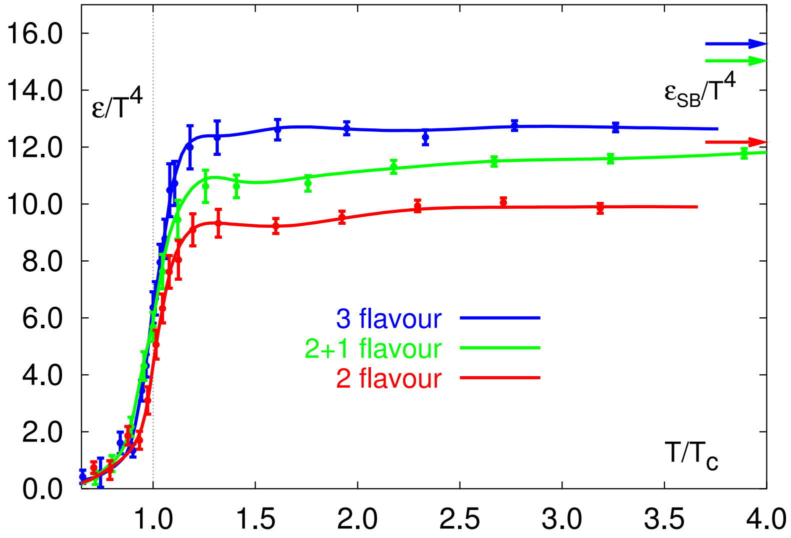

Figure 4: The energy density $/T^4$ as a function of the temperature scaled by the critical temperature T_C from lattice QCD calculations for two and three flavor. Arrows in the figure indicate the Stefan-Boltzmann limits of ideal gas. [4]

1.1.2 Little Bangs: Heavy ion collisions in the laboratory

In order to recreate the quark gluon plasma and study its properties, one needs to reproduce conditions similar to those of the very early universe.

These conditions can be achieved by accelerating heavy ions to velocities close to the speed of light and subsequently colliding them. The Relativistic Heavy Ion Collider (RHIC), located at Brookhaven National Laboratory (BNL), was specifically built to produce such collisions to discover and then study of the quark gluon plasma. Since 2000, the four experiments at RHIC, BRAHMS [58], PHOBOS [59], STAR [60] and PHENIX [61] collected compelling evidence that a quark gluon plasma can be created in the laboratory [53]. The Large Hadron Collider (LHC), located at the European Organization for Nuclear Research (CERN), is another major facility that has the capability to accelerate heavy ions to ultrarelativistic velocities. The four LHC experiments, ALICE [62], ATLAS [63], CMS [64] and LHCb [65] recorded the first collisions of lead nuclei in 2015. At both facilities, droplets of QGP and the QCD phase transition are recreated in collisions of heavy nuclei tens of thousands of times per second.

In a heavy ion collision, thousands of particles are produced, and these particles' momentum or energy can then be measured as they traverse the detectors. In order to study the properties of the quark gluon plasma created in ultrarelativistic heavy ion collisions, we focus on particles, or *probes* that are sensitive to the medium properties. *Penetrating probes*, in the simplest sense, are particles that can penetrate through the QGP, and are typically divided into two main classes:

- **Electromagnetic probes**

  Electromagnetic probes are particles that interact electromagnetically and are non-strongly interacting, hence they leave the QGP unscathed. As such, they carry direct information about the properties of the medium that led to their creation. Examples include photons and lepton pairs.

- **Hard probes**

  Hard probes refer to particles with large momenta or masses created during the very early stage of the collision before the formation of QGP. As hard probes are produced from the initial interaction, they propagate through and may be modified by the medium formed. Examples include high p_T particles from jets, and hadrons that contain a heavy flavor quark (charm or bottom).

Hadrons that consist of two heavy flavor quarks ($c\bar{c}$ or $b\bar{b}$) are commonly known as *quarkonia* or *hidden heavy flavor*, whereas hadrons that are made up of one heavy flavor quark and one or two light quarks are referred to as *open heavy flavor*. In the following, we focus on the latter.

1.1.3 Open Heavy Flavor Production

Heavy flavor production is often used as a probe to study the quark gluon plasma, which is created in heavy ion collisions. Due to the large masses of the heavy quarks, the majority of the heavy quarks are produced in the early stages of the collision. As the heavy quarks traverse the the QGP, they interact with the matter and experience collisional or radiation energy loss; these effects are commonly referred to as *hot nuclear matter effects*. To measure these effects one can compare the heavy flavor yield in heavy ion collisions to that in proton-proton (p+p) collisions, in which QGP is not expected to form. The deviations of the yield in heavy ion collisions to the p+p baseline is commonly interpreted as modifications arising from the formed medium, and allow us to infer information on the characteristics, such as transport coefficients, of the formed medium.

However, besides the nuclear modification due to the QGP, other nuclear effects may exist. These nuclear modifications are referred to as *cold nuclear matter effects*. Examples include the modification of the nuclear parton distribution functions in nuclei, and the energy loss of partons when they traverse nuclei. Therefore, in order to quantify effects arising directly from the QGP, one needs a good understanding of the cold nuclear matter effects. To isolate and study cold nuclear matter effects, we turn to collisions involving one light and one heavy ion, such as proton-gold or deuteron-gold collisions. In such small systems, the formation of QGP is not expected, and thus by comparing the heavy flavor yield in small systems with the p+p baseline, one can isolate and quantify cold nuclear matter effects.

It is often assumed that heavy flavor quarks are produced in the very early stages of the collision. However, there are higher order processes (such as gluon splitting), in which the heavy quark pair is created from a splitting of a gluon. In such cases, the gluon itself may be modified by the medium, in heavy ion collisions, before splitting into a heavy quark pair. Thus, understanding the relative contributions of heavy flavor production processes, which we can study in p+p collisions, is critical in order to quantitatively study the QGP created in larger systems.

Currently, despite considerable experimental and theoretical effort, our understanding of the open heavy flavor production process, even in p+p collisions, remains incomplete. Significant differences persist between data and perturbative-quantum-chromodynamics (pQCD) based model calculations [66, 67, 12, 68, 69, 70]. In light-heavy ion collisions, significant differences with respect to the p+p baseline have been observed [19, 20], with the mechanism behind such modifications still poorly understood. Further measurements of open heavy flavor in both p+p and small systems are of utmost importance if heavy flavor is to be used as a probe to quantitatively study the QGP.

1.2 Discovery of QGP at RHIC

Experiments at RHIC have produced strong evidence that droplets of quark gluon plasma are produced in Au+Au collisions at $\sqrt{s_{NN}} = 200$ GeV [58, 59, 60, 61]. These produced droplets of quark gluon plasma have the following important features:

- can be described by hydrodynamical models
- causes energy loss of colored objects traversing the medium
- has minimal viscosity to entropy ratio similar to that of a perfect fluid

The experimental evidence leading to this characterization is discussed in the following, while simultaneously introducing important concepts that will be used in this thesis.

1.2.1 Droplet described by hydrodynamics

At RHIC, gold ions with a per nucleon energy of 200 GeV are collided with each other. The particles arising from these collisions traverse the detectors, and their transverse momentum p_T can be measured. Fig. 5 shows the transverse momentum spectra for pions, kaons, protons and anti-protons in Au+Au collisions at $\sqrt{s_{NN}} = 200$ GeV [5] in two *centrality* selections, namely the most *central* $0-5\%$ and the most *peripheral* $60-92\%$. Here, *centrality* is a quantity related to the impact parameter of the two heavy ions, with smaller centrality values (referred to as *central*) corresponding to

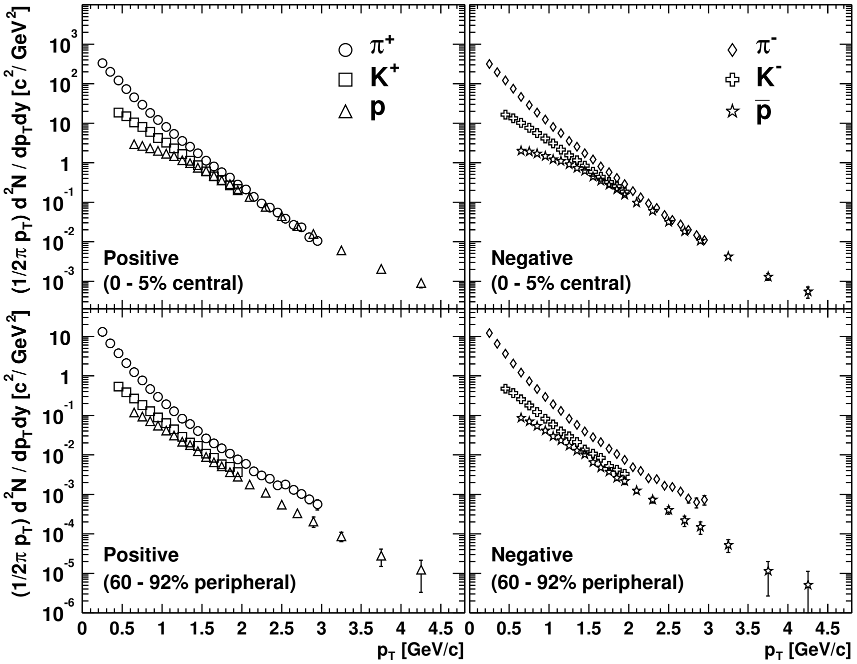

Figure 5: Transverse momentum p_T distributions for pions, kaons, protons and anti-protons in Au+Au collisions at $\sqrt{s_{NN}} = 200$ GeV [5]. The upper panels show p_T spectra for the most central $0-5\%$ collisions. The bottom panels show the most peripheral $60-92\%$ collisions.

smaller impact parameters, and larger centrality values (referred to as *peripheral*) corresponding to larger impact parameters. The measured spectra are approximately exponential over the measured p_T range, with the exception being the spectra for protons and anti-protons which flatten at p_T lower than 1.5 GeV/c. In particular, these pion, kaon and proton spectra are found to be consistent with models that assume the creation of a thermal, expanding source, based on relativistic hydrodynamics [71].

In order to characterize the change in spectra as a function of the impact parameter, the average p_T, $\langle p_T \rangle$, for each spectrum are calculated for different centrality classes and the results are shown in Fig. 6. Instead of presenting $\langle p_T \rangle$ as a function of centrality, the number of participating nucleons N_{part} is used in this particular instance. The average number of participating

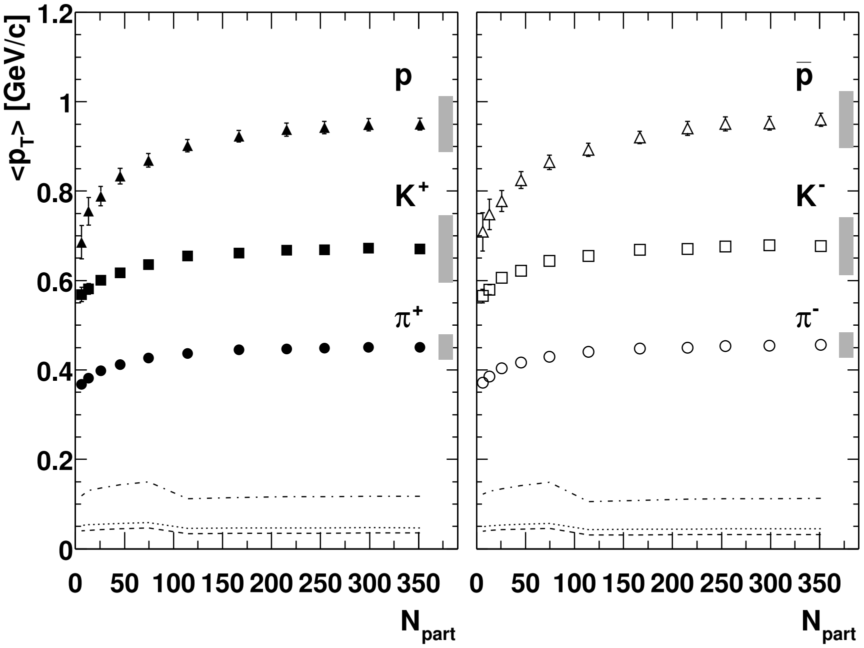

Figure 6: Mean transverse momentum $\langle p_T \rangle$ as a function of N_{part} for pions, kaons, protons and anti-protons in Au+Au collisions at $\sqrt{s_{NN}} = 200$ GeV [5]. The systematic uncertainty from extrapolation in unmeasured kinematic range, scaled by a factor of two for clarity, are shown in the bottom for pions (dashed lines), kaons (dotted lines), and protons and anti-protons (dashed-dotted lines). The shaded bars on the right represent the systematic uncertainty.

nucleons N_{part} for a certain centrality class is determined using the Glauber model, which models the nucleus as uncorrelated nucleons sampled from measured density distributions. An in-depth discussion of the Glauber model can be found in Ref. [72]. Larger N_{part} values correspond to larger centralities and smaller impact parameters. The $\langle p_T \rangle$ increases for all particle species as a function of N_{part}. This is consistent with the notion of the creation of a thermal, expanding source [71], in which the expansion is most violent for more central collisions.

The mean transverse momentum as a function of mass for different centrality selections is shown in Fig. 7. $\langle p_T \rangle$ increases approximately linearly

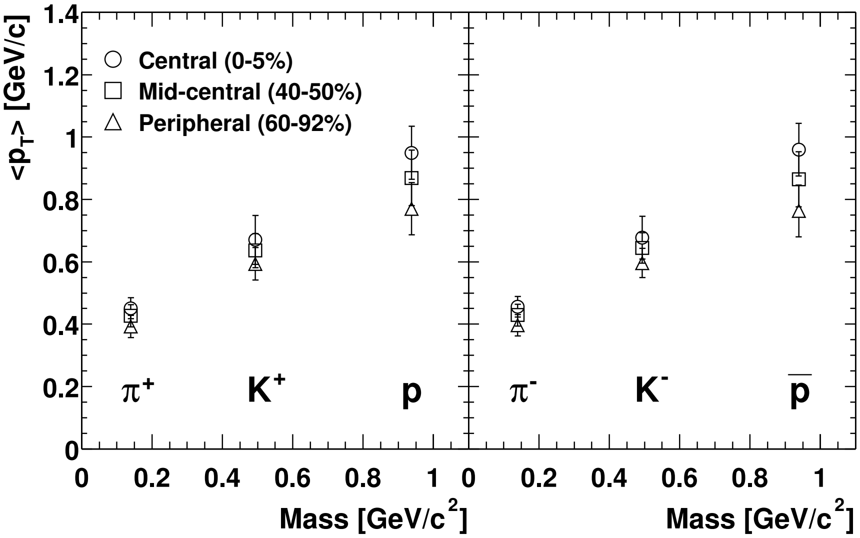

Figure 7: Mean transverse momentum $\langle p_T \rangle$ as a function of particle mass for most central $0-5\%$, mid-central $40-50\%$ and most peripheral $60-92\%$ in Au+Au collisions at $\sqrt{s_{NN}} = 200$ GeV [5]. The left (right) panel shows the case for positive (negative) particles.

with the mass of the particle. In the hydrodynamical picture of an expanding medium, pressure gradients push the particles outwards, which leads to *radial flow*. The very low momentum particles inside the medium will gain momentum from the expanding volume, thus increasing the average momentum of the particles. The transverse velocity of the expanding medium increases as the radial distance; this is analagous to the Hubble expansion of the universe. In particular, assuming a collective expansion velocity of the medium created, higher mass particles will gain more momentum compared to lower mass particles, leading to a larger $\langle p_T \rangle$ for higher mass particles, which is consistent with what is observed from the data. This is the first piece of evidence that, not only is a strongly coupled medium formed in Au+Au collisions, but the medium behaves hydrodynamically.

An additional piece of evidence that the created medium behaves hydrodynamically is the manifestation of *elliptic flow*. Since the gold nucleus is fairly spherical, in a Au+Au collision where the impact parameter close to zero (central collisions), the shape of the overlap region is circular. However, as the impact parameter increases (non-central collisions), the overlap region becomes more and more elliptical. Here, we define the reaction plane as the plane formed by the beam axis and the impact parameter. In non-central collisions, due to the spatial anisotropy of the overlap region, models that assume the medium to behave hydrodynamically predict that the pressure gradients in the reaction plane are larger than those out of plane, as illustrated in Fig. 8. In these hydrodynamical models, the initial spatial anisotropy of the overlap region leads to an anisotropy in momentum space through these pressure gradients. Elliptic flow can be understood as a modulation of radial flow; both are driven by pressure gradients of the medium formed. While radial flow characterizes the isotropic expansion of the medium, elliptic flow characterizes the azimuthal anisotropy of the medium. Compared to radial flow which increases for more central collisions, elliptic flow is absent in the most central collisions where the overlap region is circular and there is no spatial anisotropy, and becomes stronger in non-central collisions.

Elliptic flow is typically characterized by the second Fourier coefficient v_2 of the Fourier expansion on the angular distribution of the produced particles, i.e.

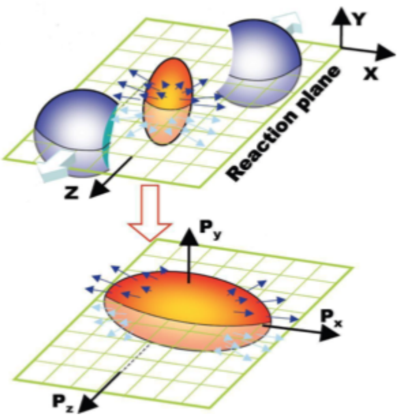

Figure 8: Spatial anisotropy (top panel) developing into momentum anisotropy (bottom panel).

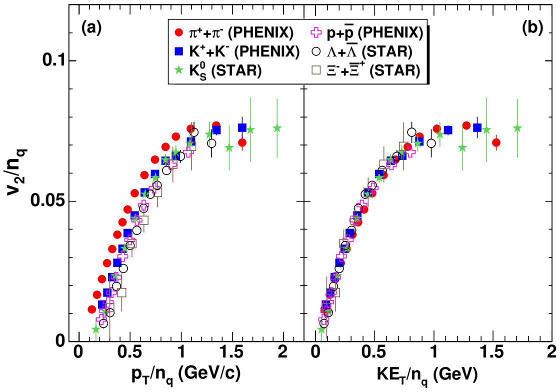

Figure 9: Scaled v_2 by quark numbers n_q as a function of p_T and transverse kinetic energy KE_T in Au+Au collisions at $\sqrt{s_{NN}} = 200$ GeV measured by PHENIX [6] and STAR [7, 8].

$$E\frac{d^3N}{dp^3} = \frac{1}{2\pi p_T}\frac{d^2N}{dp_T dy}(1 + \sum_{n=1}^{\infty} 2v_n cos(n(\phi - \Psi_{RP}))) \tag{1}$$

In particular, the scaling of elliptic flow for different hadron species with the number of constituent quarks n_q ($n_q = 2(3)$ for mesons (baryons)) from PHENIX [6] and STAR measurements [7, 8] (see Fig. 9) suggests that collectivity is developed in the partonic state rather than the hadronic state, and provides further evidence for the formation of QGP in heavy ion collisions. Through rigorous phenomenological analysis in conjunction with the experimental data, the initial temperature T_{init} and formation time τ_{init} of the Quark-Gluon Plasma created at RHIC have been determined to lie within the following ranges: 300 MeV $< T_{init} <$ 600 MeV, 0.2 fm/c $< \tau_{init} <$ 1.2 fm/c [73].

1.2.2 Energy loss of colored objects

When energetic partons traverse through the hot and dense medium that is expected to be formed in heavy ion collisions, they suffer energy loss due to medium-induced gluon radiation as well as soft collisions with partons in the medium. This leads to jet quenching: the modification of jet fragmentation functions as compared to the unquenched case. The first evidence of such parton energy loss is the suppression of high p_T hadrons [9] in Au+Au collisions at $\sqrt{s_{NN}} = 130$ GeV measured by the PHENIX collaboration. In order to quantify the effects that arise due to the quark gluon plasma that is expected to form in Au+Au collisions, we typically use the *nuclear modification factor*, R_{AA}, defined as the ratio:

$$R_{AA}(p_T) = \frac{d^2N^{A+A}/dp_T d\eta}{\langle N_{coll}\rangle \times d^2N^{p+p}/dp_T d\eta}, \tag{2}$$

where $d^2N^{p+p}/dp_T d\eta$ is the yield per event in p+p collisions, $d^2N^{A+A}/dp_T d\eta$ is the yield per event in A+A collisions in a certain centrality class, and N_{coll} is the average number of binary collisions for a certain centrality class. Similar to the average number of participating nucleons N_{part}, the average number of binary collisions for a certain centrality class is determined using the Glauber model [72]. As shown in Fig. 10, the R_{AA} for hadrons is much less than one, which indicates a significant suppression of hadrons in the most central Au+Au collisions. Through a quantitative study of high p_T π^0 suppression at RHIC, with assistance from hydrodynamical modelling, the energy-loss transport coefficient $\hat{q}$ at the very early stage in the evolution of Au+Au collisions has been determined to be $\hat{q} = 2$–10 GeV^2/fm [74].

Investigating the angular correlation between hadrons is an alternate method to probe jet modification in QGP. This is because jets are primarily produced during the hard scattering process, and at leading order, the two jets (dijet) produced are back-to-back in azimuthal angle. The angular correlations between two hadrons have been measured by the STAR collaboration in Au+Au, d+Au and p+p collisions at $\sqrt{s_{NN}} = 200$ GeV [10] and are shown in Fig. 11. The back-to-back peak originating from dijets is clear seen in p+p and d+Au collisions, but is strongly suppressed in Au+Au collisions. These correlation measurements indicate that the suppression phenomena seen in central Au+Au collisions are due to final state interactions, and is consistent with the formation of QGP in heavy ion collisions.

1.2.3 A Perfect Liquid

The experimental evidence presented above establishes that dense partonic matter is formed in Au+Au collisions at RHIC, and that the matter formed can be described by hydrodynamical models. As heavy quarks are primarily produced in the early stages of the collision, further insight into the properties of the medium may be gained from the production and propagation of particles carrying heavy quarks.

The measured R_{AA} of heavy flavor electrons in $0-10\%$ central collisions are shown in the upper panel of Fig. 12, and the measured v_2 of heavy flavor electrons in minimum bias electrons are shown in the lower panel of Fig. 12 [11]. A large energy loss and flow of heavy quarks in Au+Au collisions is observed, which provides strong evidence for the coupling of heavy quarks to the produced medium. The data are also compared to various theoretical models. It is found that Langevin-based heavy quark transport calculations, corresponding to curves (II) [75] and (III) [76] on Fig. 12, can reasonably describe the R_{AA} and v_2 of heavy flavor electrons simultaneously. The model calculations are sensitive to the diffusion coefficient D_{HQ}, and is found that a diffusion coefficient of $D_{HQ} \times (2\pi T) = 4-6$ can reasonably reproduce the data. D_{HQ} in turn provides an upper bound for the bulk matter's diffusion coefficient D. The observation [76] that $D \approx 6 \times \eta/(\epsilon + p)$ gives an estimate

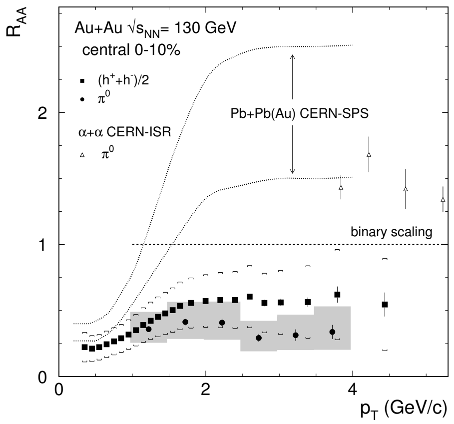

Figure 10: The nuclear modification factor R_{AA} for charged hadrons and neutral pions in central Au+Au collisions [9]. Also shown are the ratio of inclusive cross sections in α+α compared to p+p collisions at $\sqrt{s_{NN}} = 31$ GeV, and spectra from central Pb+Pb, Pb+Au compared to p+p collisions at $\sqrt{s_{NN}} = 17$ GeV shown as a band indicating the range of uncertainty.

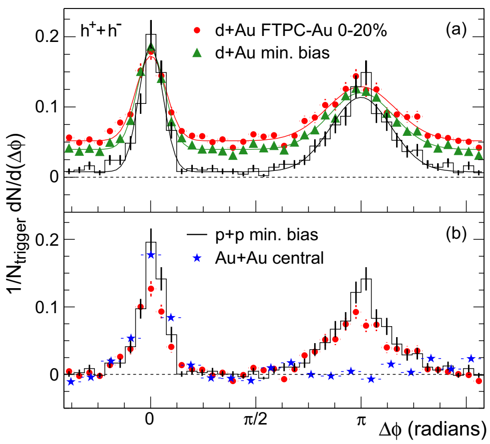

Figure 11: (a) Efficiency corrected two-particle azimuthal distributions for minimum bias and central d+Au collisions, and p+p collisions. (b) Comparison of two-particle azimuthal distributions for central d+Au collisions to those seen in p+p and central Au+Au collisions [10].

for the viscosity to entropy ratio $\eta/s \approx (\frac{4}{3} - 2)/4\pi$, remarkably close to the conjectured quantum lower bound $1/4\pi$ [77], which provides evidence that the produced medium not only obeys hydrodynamical laws, but intriguingly, behaves like a near perfect fluid.

1.3 Production of heavy flavor via the strong force and cold nuclear matter effects

1.3.1 Heavy flavor production in p+p collisions

Measurements of $c\bar{c}$ and $b\bar{b}$ in p+p collisions are important to further our understanding of the $c\bar{c}$ and $b\bar{b}$ production process, which despite consid-

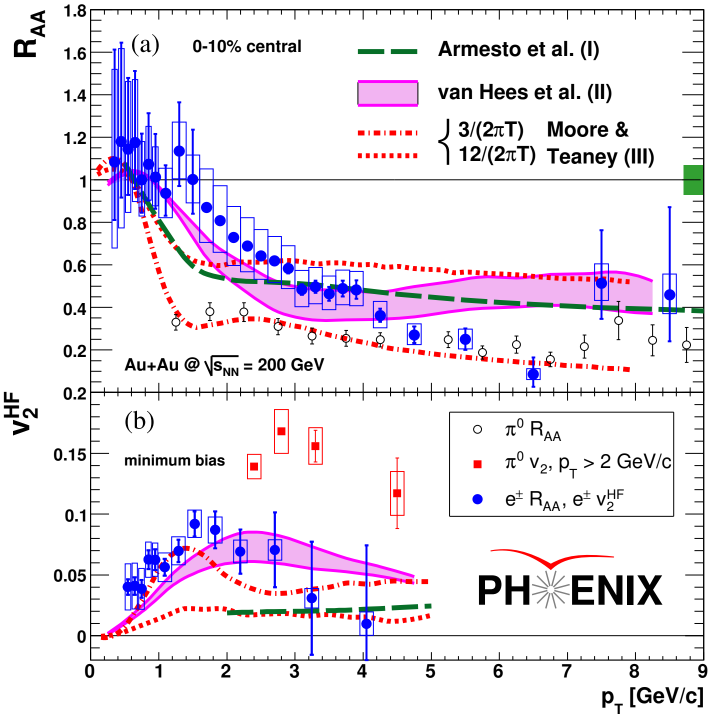

Figure 12: (a) R_{AA} of heavy flavor electrons in $0 = 10\%$ central collisions compared with π^0 data and model calculations. (b) v_2 of heavy flavor electrons in minimum bias collisions compared with π^0 data and the same models [11].

erable experimental and theoretical effort remains incomplete. Significant differences persist between data and perturbative-quantum-chromodynamics (pQCD) based model calculations [66, 67, 12, 68, 69, 70].

Numerous theoretical calculations are available which can be used to predict heavy flavor cross sections. To calculate the total heavy flavor cross section in proton-proton collisions, which depends on $\sqrt{s}$, the center of mass energy of the two protons, and m the mass of the heavy quark, one can invoke the QCD factorization theorem [78]. Calculations of heavy flavor cross sections in hadron-hadron collisions involve a combination of both short- and long-distance behavior. Since perturbative QCD is valid only at short distances where the strong coupling constant α_s is small, heavy flavor production cross sections in hadron-hadron collisions cannot be directly computed from pQCD. The QCD factorization theorem, which is expected to hold for heavy flavor [70], states that such cross sections can be factorized into a long distance part, commonly referred to as *parton distribution functions*, and a short distance part that arises from parton-parton hard scattering, and is calculable from pQCD. By invoking the factorization theorem, the total proton-proton heavy flavor cross section, for heavy quarks with mass m and a collision energy $\sqrt{s}$ is given by:

$$\sigma_{pp}(\sqrt{s}, m^2) = \sum_{i,j=q,\bar{q},g} \int d_{x_1} d_{x_2} f_i^p(x_1, \mu_F^2) f_j^p(x_2, \mu_F^2) \hat{\sigma}_{i,j}(\hat{s}, m^2, \mu_F^2, \mu_R^2). \quad (3)$$

Here, μ_R and μ_F are the renormalization and factorization scales, which are scale factors to cure infrared and ultraviolet divergences. $\hat{s}$ is the partonic center-of-mass energy, x_1 and x_2 are the fraction of momenta carried by the colliding partons, and f_i^p are the parton distribution functions, which represent the probability densities to find a parton of species i (either quark, antiquark or gluon) carrying a momentum fraction x. More details on the parton distribution functions and the factorization theorem can be found in the following sections.

The partonic cross section, $\hat{\sigma}_{ij}$ can be evaluated using perturbative QCD. Currently, many heavy flavor calculations evaluate the partonic cross section at next-to-leading order (NLO) accuracy, while next-to-next-to-leading order (NNLO) calculations are less accessible. However, in an actual experiment, the total heavy flavor cross section cannot be measured directly, as the experiments have limited coverage, and the heavy flavor hadrons, or leptons coming from semi-leptonic decays of the heavy flavor hadrons, can only be measured up to some lower threshold in momentum. Thus, measured differential cross sections of the heavy flavor hadrons, or their decay leptons are often used to test the theoretical calculations. The theoretical calculations that enable such comparisons can be typically divided into two categories [79].

The first category is the Fixed-Order plus Next-to-Leading Log (FONLL) framework [66], in which one matches fixed next-to-leading QCD with all-order resummation to next-to-leading log (NLL) accuracy in the limit where the transverse momentum of the heavy quark is much larger than its mass. The cross section of leptons l arising from heavy flavor quarks Q, calculated using the FONLL approach can be schematically written as:

$$E\frac{d^3\sigma_l}{dp^3} = E_Q\frac{d^3\sigma_Q}{dp_Q^3} \otimes D(Q \to H_Q) \otimes f(H_Q \to l), \tag{4}$$

where $\otimes$ denotes a generic convolution. Here, $E_Q\frac{d^3\sigma_Q}{dp_Q^3}$ and $E\frac{d^3\sigma_l}{dp^3}$ are the invariant differential cross sections of the heavy quark and their decay leptons respectively. $D(Q \to H_Q)$ is the non-perturbative *fragmentation functions*, which can be interpreted as the probability of a heavy quark Q to hadronize into a hadron H_Q. Fragmentation is a non-perturbative process and the fragmentation functions are described by phenomenological input extracted from e^+e^- data. Finally, $f(H_Q \to l)$ describes the weak decay of H_Q into leptons, and the branching ratios corresponding to the decays are extracted from experimental data. Under this approach, one can calculate predictions for single particle inclusive distributions of a heavy quark, hadron or their decay leptons, while the degrees of freedom of all other particles in the event are integrated over. This approach, however, does not allow the study of the correlations of the heavy quark and anti-quark.

The second category is the (N)LO+PS approach, in which a leading order (e.g. PYTHIA, HERWIG) or next-to-leading order (e.g.POWHEG, MC@NLO) matrix element is used for the hard scattering process and is subsequently matched to existing parton showering (PS) programs, to handle the fragmentation, hadronization and decays. Such calculations, unlike FONLL, provide a complete and fully exclusive description of the final state, which enables the study of the correlations between different particles, and are commonly referred to as *event generators*. In leading order calculations, various parameters that may be tuned, such as the intrinsic transverse momentum (k_T) of the incoming partons, to emulate higher order effects. In such LO event generators, heavy flavor production may be divided into three different categories: pair creation, flavor excitation and gluon splitting [12, 80]. The classification depends on the number of heavy quarks in the final state of the hard scattering process, defined as the process in the event with the highest virtuality. The Feynman diagrams corresponding to these processes are shown in Fig. 51. This approach, though allowing a phenomelogical categoriazation of different production processes, has the inherent disadvantage of neglecting interference terms between different diagrams. In contrast, for the NLO event generators, the hard scattering process is calculated using NLO matrix elements. Different approximations, however, are necessary in

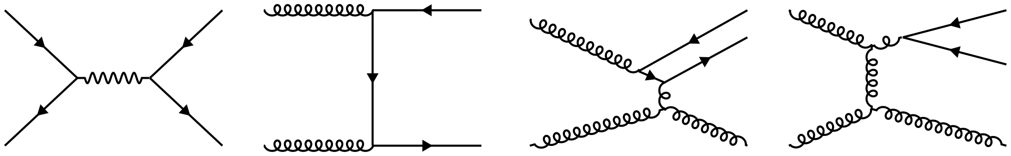

(a) s-channel Flavor Creation

(b) t-channel Flavor Creation

(c) Flavor Excitation

(d) Gluon Splitting

Figure 13: Feynman diagrams corresponding to flavor creation (a,b), flavor excitation (c) and gluon splitting (d) [12, 13].

the parton shower matching step in order to avoid double counting of phases space, which may lead to inaccuracies in the predictions for final state observables.

Single p_T spectra of charm and bottom mesons, as well as their decay leptons have been measured over a wide range of beam energies and rapidity. For charm production, precise measurements at RHIC [14, 81, 82], Tevatron [83] and the LHC [15, 84, 85, 86] indicate that pQCD calculations underestimate the charm cross section, even when contributions beyond leading order are taken into account [67, 69, 68, 66] (See Fig. 14 and 15). For bottom production, the case is less clear. At RHIC, the bottom cross section has been measured via various channels by PHENIX [87, 88, 21] and STAR [89]. The measured bottom cross sections also tend to be above pQCD predictions, albeit with relatively large uncertainties. At higher energies, the bottom cross sections measured by D0 at $\sqrt{s} = 1.8$ TeV [90], ALICE at $\sqrt{s} = 2.76$ and 7 TeV [91], and ATLAS at $\sqrt{s} = 7$ TeV [92] again tend to be above pQCD predictions, while similar measurements from CDF at $\sqrt{s} = 1.8$ TeV [93], CMS at $\sqrt{s} = 7$ TeV [94] and LHCb at $\sqrt{s} = 7$ and 13 TeV [95] do not demonstrate significant deviations from pQCD.

1.3.2 Nuclear modification: “Cold nuclear matter effects”

We have discussed various pieces of evidence pointing towards the formation of QGP in heavy ion collisions. In order to quantify the characteristics of the QGP, one needs needs to isolate nuclear effects related to the QGP, commonly referred to as *hot nuclear matter effects*, from the nuclear effects that are unrelated to QGP, or *cold nuclear matter effects*. One well known source of such cold nuclear effects is the modification of parton distribution functions in nuclear matter. We can study such cold nuclear matter effects in smaller

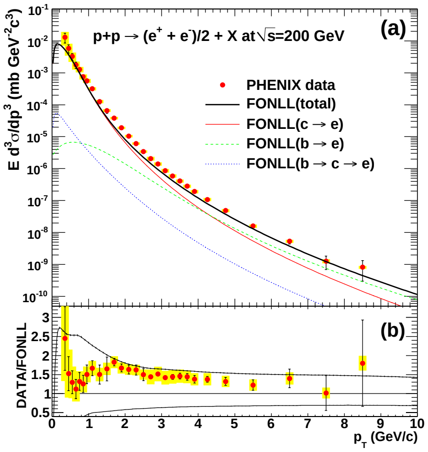

Figure 14: Invariant differential cross section of single electrons as a function of p_T in p+p collisions at $\sqrt{s}$ = 200 GeV, measured by PHENIX [14]. The error bars (bands) represent the statistical (systematic) errors. The curves are the FONLL calculations, and the ratio of data to FONLL are shown in the bottom panel.

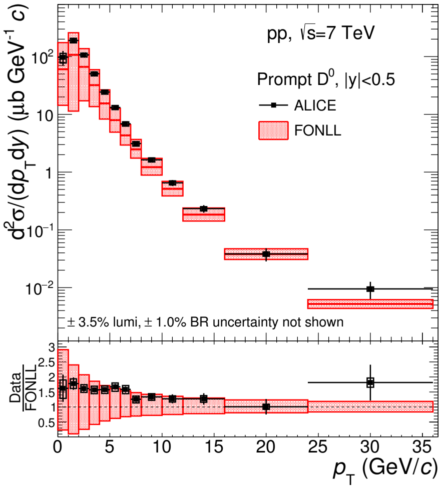

Figure 15: p_T-differential production cross section of prompt D^0 mesons with $|y| < 0.5$ in the interval $0 < p_T < 36$ GeV/c in p+p collisions at $\sqrt{s}$ = 7 TeV, measured by ALICE [15]. The cross section is compared to FONLL, and the ratio of data to FONLL are shown in the bottom panel.

collision systems, including proton-proton (p+p) and proton/deuteron-ion (p/d+A) collisions. In p/d+A collisions, it has long been believed that no hot and dense medium is formed, thus enabling us to isolate and quantify cold nuclear matter effects.

The search for cold nuclear matter effects goes as far back as the early 1970s. An enhancement (suppression) in particle production in the intermediate (low) p_T region was observed in p+A collisions compared to p+p collisions [96]. This broadening of the p_T spectrum is commonly known as the *Cronin effect*, and is usually attributed to multiple scattering of partons inside a nucleus before the hard scattering process. However, no definitive conclusion regarding the underlying mechanism leading to the Cronin effect has been reached.

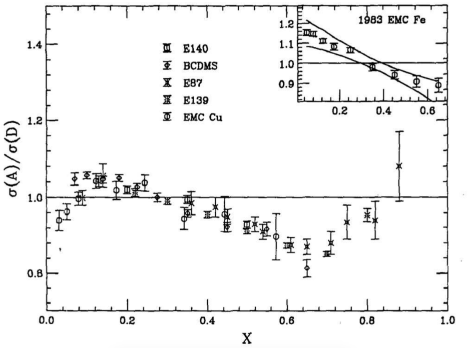

Figure 16: Ratios of the DIS cross sections of iron and copper targets to deuterium. The inset shows the original EMC result from 1983. [16]

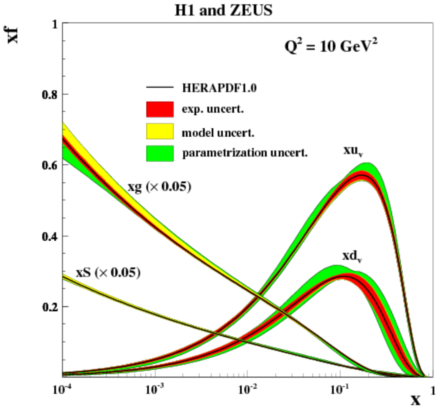

Figure 17: The parton distribution functions from HERAPDF1.0 at $Q^2 = 10$ GeV^2. The gluon and sea distributions are scaled down by a factor of 20. The experimental, model and parametrization uncertainties are shown separately [17].

Another piece of the puzzle was discovered in the early 1980s. Results from deep inelastic scattering experiments have shown that the parton distributions functions in heavy nuclei are modified compared to the proton. In 1983, the European Muon Collaboration (EMC) published the ratio of iron to deuteron cross sections as a function of Bjorken x, measured through muon deep inelastic scattering [97]. The results are shown in the inset of Fig. 16. These measurements stirred interest in the nuclear physics community and since then, other experiments have extended the Bjorken x reach. The results are summarized in the main panel of Fig. 16 [16, 98]. The Bjorken x range in the above plot is customarily divided in to four regions:

- **Shadowing**

  The cross section ratio for heavy nuclei (iron and copper) to deuteron, σ_A/σ_D is less than unity below $x \approx 0.1$. This is typically attributed to multiple soft scattering or effects due to overlapping nuclear wave functions. As shown in Fig. 17, low x partons are dominated by gluons. In a dense nucleus, the nucleon separation may be smaller than the spatial extent of the gluon wave function, and thus may deplete the number of low x partons in a heavy nuclei through the fusion of two low x gluons.

- **Anti-shadowing**

  The ratio σ_A/σ_D is above unity between $x \approx 0.1$ and $x \approx 0.3$. This is often believed to be the reverse effect of gluon shadowing, namely, the enhancement of the ratio in this region is due to the fusion of two low x gluons into a single higher x gluon.

- **EMC effect**

  The ratio σ_A/σ_D shows a steady decline between $x \approx 0.3$ and $x \approx 0.7$. There is no concensus on the source of this decline.

- **Fermi motion**

  The ratio σ_A/σ_D rises above unity above $x \approx 0.7$. This is attributed to the quantum motion of nucleons inside a nucleus [99].

The search for cold nuclear matter effects is far from over. At RHIC, using d+Au data taken in 2008, the *nuclear modification factor* for d+Au collisions, defined as:

$$R_{dA}(p_T) = \frac{1}{N_{coll}} \cdot \frac{d^2N^{dA}/dp_T dy}{d^2N^{pp}/dp_T dy}, \tag{5}$$

where N_{coll} is the number of binary collisions, N_{dA} and N_{pp} are the relavant yields in d+A and p+p collisions respectively, has been measured for pions, kaons, protons and phi mesons [18]. As shown in Fig. 18, while p_T broadening has been observed for pions, kaons and protons alike, there appears to be a mass dependence on the broadening. Further studies show broadening in the p_T spectra for J/ψ mesons [100] as well as open heavy flavor decay leptons [19, 20].

The heavy flavor decay lepton spectra have been measured at forward ($1.4 < y < 2.0$), backward ($1.4 < y < 2.0$) [20] and mid ($y = 0$) [19] rapidity for d+Au collisions at $\sqrt{s_{NN}} = 200$ GeV by the PHENIX collaboration. The spectra are compared to the binary scaled p+p spectra and the nuclear

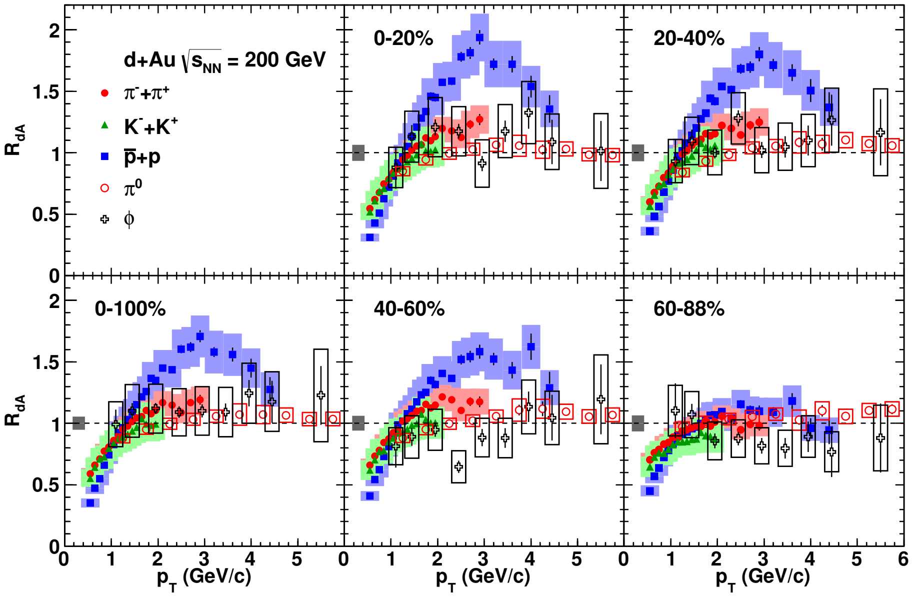

Figure 18: The nuclear modification factor of various hadrons in d+Au collisions as a function of p_T [18].

modification factor R_{dA} are shown in Fig. 19. In the most peripheral collisions, the measured R_{dA} is consistent with unity, indicating that no nuclear modifications are observed in such collisions. However, for the most central collisions, the yield is significantly enhanced at moderate p_T at backward and mid-rapidities, and suppressed at forward rapidity. This trend is consistent with the expectations from anti-shadowing and shadowing. However, when we compare the measured R_{dA} to the estimated modifications from EPS09 [101], which are nuclear parton distribution functions (nPDFs) obtained from a global analysis of experimental input from deep inelastic scattering, Drell-Yan dilepton production, and inclusive pion production, the enhancement at backward rapidity in the data cannot be quantitatively described by EPS09. This suggests that additional cold nuclear matter effects may need to be accounted for in order to quantitatively describe the data. There are hints of p_T broadening, especially at forward rapidity, which can stem from the same origin as the Cronin effect observed for other hadrons. More systematic studies, such as widening the rapidity window to extend the x range, or charm and bottom separation to probe the mass dependence, may be necessary to shed light on this issue.

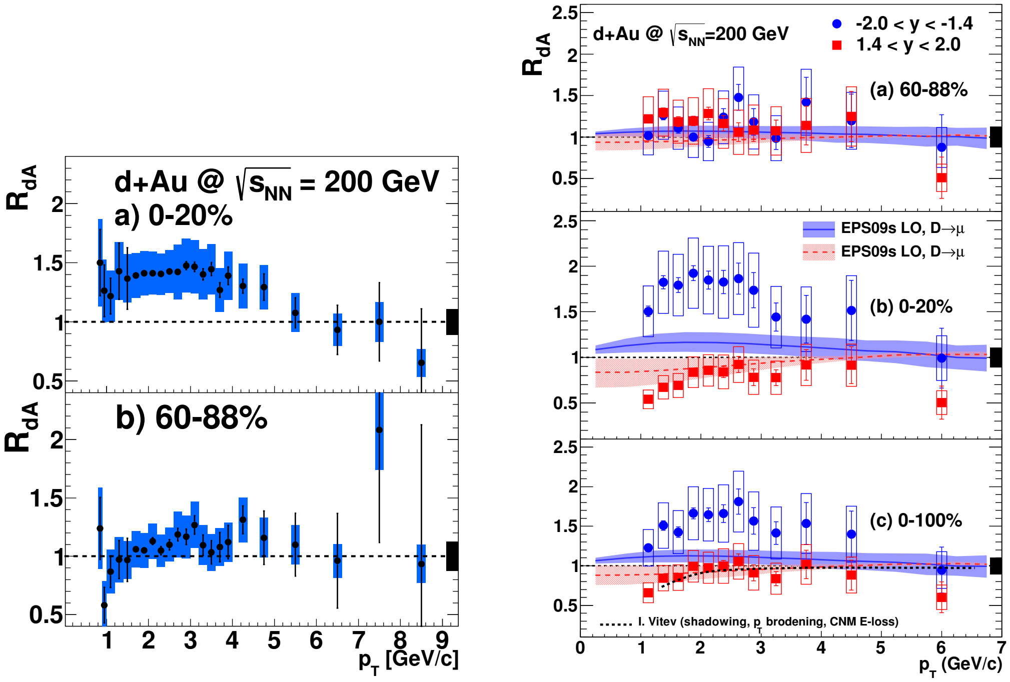

Figure 19: The R_{dA} of heavy flavor decay leptons at mid-rapidity [19] (left panel), forward [20] (red squares, right panel) and backward [20] rapidity (blue circles, right panel).

Despite significant efforts in the study of cold nuclear matter effects for more than thirty years, the modifications of the nuclear PDFs, nor the Cronin effect are well understood; yet new mysteries have unravelled themselves. Recently, a comprehensive analysis of elliptic and triangular flow has been performed, using data collected by PHENIX in 2015 and 2016 of p+Au, d+Au and He^3+Au collisions at $\sqrt{s_{NN}}$ = 200 GeV [102]. The study indicates that the data are well described by models assuming that a hydrodynamically expanding medium is created, and is inconsistent with, particularly for two of the six flow patterns, the predictions based on the quantum-mechanical gluon interactions. This is by far the strongest evidence of quark gluon plasma droplets being formed in small systems. At the LHC, measurements of two-and multi-particle angular correlations as a function of charged-particle multiplicity in p+p collisions at $\sqrt{s} = 5$, 7, and 13 TeV have been performed [103]. In high multiplicity p+p collisions, a mass ordering of v_2 signals is found, with lighter particle species exhibiting a stronger azimuthal anisotropy signal below $p_T \approx 2$ GeV/c. This provides strong evidence for a collective origin of the observed long-range correlations in high-multiplicity p+p collisions. These recent measurements seem to blur the line between hot and cold nuclear matter effects, and indicate that there are important mysteries still unresolved, not only in heavy ion collisions, but also in smaller systems.

Although often perceived as a control measurement for heavy ion collisions, small systems and cold nuclear matter effects are interesting and worth studying in their own right, and in light of the recent discoveries, will certainly continue to be an object for intense investigation for years to come.

1.4 The Drell-Yan process

In a nucleon-nucleon collision, the Drell-Yan process is the annihilation of a quark in one nucleus with an anti-quark from another nucleus, creating a virtual photon or a Z boson, which then decays into a pair of oppositely charged leptons. The Feynman diagram for the Drell-Yan process is shown in Fig. 20. The Drell-Yan process was first proposed by Sidney Drell and Tung-Mow Yan in 1970 [104] and was first observed by J.H. Christenson et al. [105] in proton-uranium collisions at the Alternating Gradient Synchrotron.

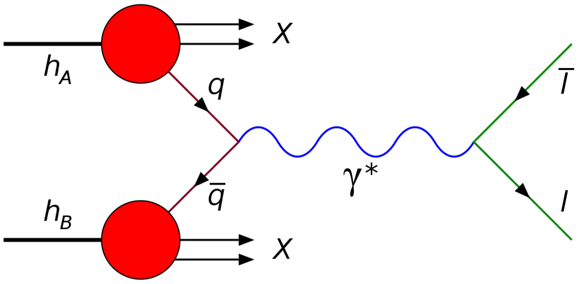

Figure 20: Feynman diagram for the production of a lepton pair via the Drell-Yan process.

The Drell-Yan process plays a special role in our understanding of the proton, and is among one of the few hadron-hadron processes in which the factorization theorem has been rigorously proven [78].

The basic problem addressed by QCD factorization theorems is how to calculate high energy cross sections. In general, any cross section is a combination of short- and long-distance behavior, and is hence not computable directly in pQCD, which is only applicable at short distances, or correspondingly large energy scales, where the coupling constant is small. QCD factorization theorems are applicable to a certain subset of processes, in which the cross section is factorized into long distance effects, which are not perturbatively calculable, and short distance effects, which are perturbatively calculable. The long distance effects are described by functions that describe the distribution of partons in a hadron. These can be measured experimentally, and should universally apply to all such processes. The short distance cross section describes the hard scattering of partons, and can be computed from pQCD.

At leading order, the Drell-Yan process can be denoted by the following relationship:

$$A + B \to l^+ + l^- + X, \tag{6}$$

where A and B are hadrons and X can be anything. Denoting q as the momentum of the lepton pair and Q^2 the square of the lepton pair mass, i.e. $Q^2 = q^\mu q_\mu$, the factorization theorem can be written as [78]:

$$\begin{aligned}\frac{d\sigma}{dQ^2dy} \sim \sum_{a,b} \int_{x_A}^{1} d\xi_A \int_{x_B}^{1} d\xi_B \times \\ \times f_{a/A}(\xi_A, \mu) H_{ab}\big(\frac{x_A}{\xi_A}, \frac{x_B}{\xi_B}, Q; \frac{\mu}{Q}, \alpha_s(\mu)\big) f_{b/B}(\xi_B, \mu).\end{aligned} \tag{7}$$

Here, a and b label the parton types, and $x_A = e^y\sqrt{Q^2/s}$ and $x_B = e^{-y}\sqrt{Q^2/s}$, with y being the rapidity of the lepton pair. μ is the renormalization scale, and $\alpha_s(\mu)$ is the strong coupling constant at the renormalization scale. H_{ab} denotes the hard scattering cross section that is calculable in perturbation theory. The functions $f_{a,A}(\xi, \mu)$ and $f_{b,B}(\xi, \mu)$ are the *parton distribution functions*, which is interpreted as the probability to find a parton of type a (or b), which can be a gluon, a quark or an anti-quark, in a hadron of type A (or B) carrying a fraction ξ to $\xi + d\xi$ of the hadron's momentum.

Thus, by measuring the Drell-Yan cross sections in hadron-hadron collisions experimentally, and determining the hard scattering cross sections from pQCD, one can constrain the quark and anti-quark components of the parton distribution functions. An example of the parton distribution functions of the proton is shown in Fig. 17.

In proton-nucleon collisions, the lepton pair produced from the Drell-Yan process escapes the nuclei unscathed as they do not interact strongly. Thus, there are no final state interactions, and any modification observed should be attributed to initial state effects. This advantage, coupled with the fact that its proton-proton production cross sections are well understood theoretically, establishes the Drell-Yan process as one of the golden probes experimentally to study nucleon structure.

1.5 $\mu\mu$ pairs as a probe

This thesis focuses on the study of lepton pair spectra in p+p and p+Au collisions at $\sqrt{s_{NN}} = 200$ GeV. More specifically, we focus on the contribution of $c\bar{c}$, $b\bar{b}$ decays and the Drell-Yan process to the lepton pair continuum at forward and backward rapidities above a mass of 1 GeV/c^2.

In this study, we make use of the fact that muon pairs from $c\bar{c}$ and $b\bar{b}$ decays and from Drell-Yan production contribute with different strength to the muon pair continuum in different phase-space regions for $\mu^+\mu^-$ and $\mu^\pm\mu^\pm$ charge combinations. Neither $c\bar{c}$ decays nor Drell-Yan production contribute to $\mu^\pm\mu^\pm$ pairs. In contrast, $b\bar{b}$ decays do. As illustrated in Fig. 21, $\mu^\pm\mu^\pm$ muon pairs from bottom arises from two separate mechanisms, (i) from a combination of $B \to \mu$ and $B \to D \to \mu$ decay chains [1] or (ii) from decays following $B^0\bar{B}^0$ oscillations [106]. These two contributions dominate the high mass $\mu^\pm\mu^\pm$ spectrum, which allows for a precise measurement of the bottom cross section.

At midrapidity the e^+e^- pair continuum is dominated by pairs from heavy flavor decays in the measurable range from 1 to 15 GeV/c^2 [21], and thus having established the $b\bar{b}$ contribution would be sufficient to extract the $c\bar{c}$ cross section. However, at forward rapidity, $\mu^+\mu^-$ pairs from Drell-Yan cannot be neglected. The Drell-Yan process involves quark-antiquark annihilation [104], whereas heavy flavor production is dominated by gluon fusion [12]. Due to the relatively large Bjorken-x of valence quarks compared to gluons, at forward rapidity the $\mu\mu$ pair yield above a mass of 6 GeV/c^2 is dominated by pairs from the Drell-Yan process. Thus, the Drell-Yan contribution can be

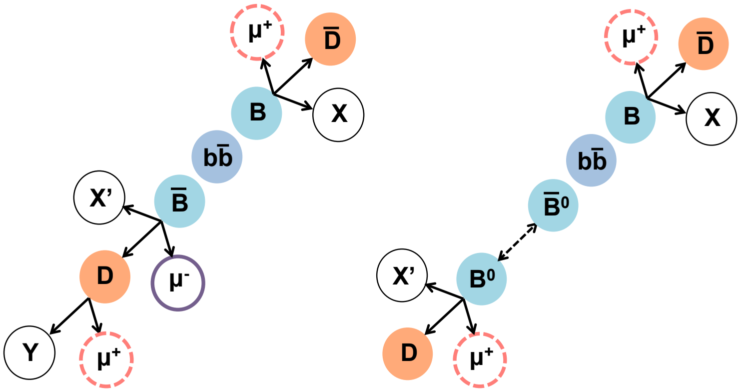

Figure 21: Like-sign muon pairs from bottom may arise from a combination of $B \to \mu$ and $B \to D \to \mu$ decay chains or from decays following $B^0\bar{B}^0$ oscillations.

determined from $\mu^+\mu^-$ pairs at high masses. Once the contributions from $b\bar{b}$ decays and Drell-Yan production are constrained, the yield from $c\bar{c}$ can be measured in the mass range from 1 to 3 GeV/c^2, where it is significant, but only one of multiple contributions to the total yield in the mass range.

Thus, a simultaneous analysis of the unlike- and like-sign pairs gives us separate cross section measurements on $c\bar{c}$, $b\bar{b}$ and the Drell-Yan process. The motivation for these measurements are outlined below.

1.5.1 Open Heavy Flavor

Lepton pair spectra provide access to the correlations of the heavy flavor decay leptons, which in turn is related to the correlation of the heavy quark pair.

Angular correlations of quarks and anti-quarks are a unique probe for studying heavy flavor production in p+p collisions. As shown in Fig. 23, leading-order (LO) pair-creation processes feature a strong back-to-back azimuthal angular correlation, while the distributions from NLO processes are broader [12, 13]. Thus, relative contributions from different production mechanisms can be disentangled by studying the azimuthal angular correlations of heavy mesons or their decay products. As the fraction of NLO processes is expected to increase with beam energy [12] (see Fig. 22), angular correlations provide an important handle for investigating the energy dependence of heavy flavor production.

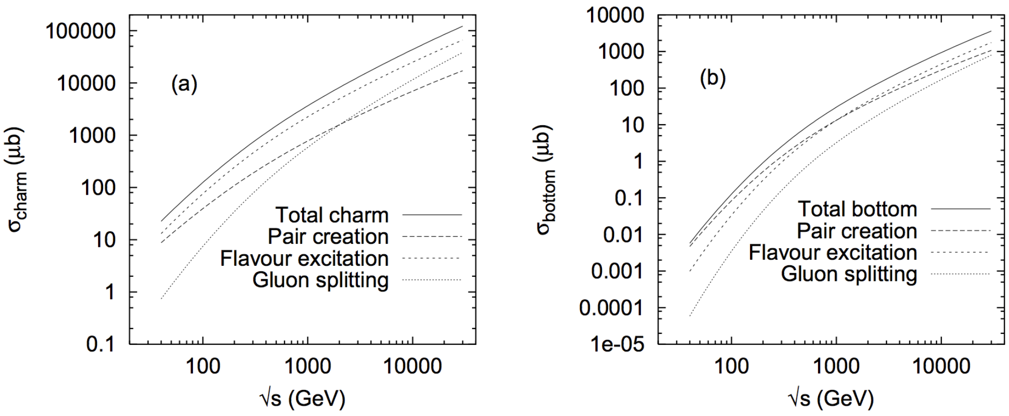

Figure 22: The predicted total (a) charm and (b) bottom cross sections for pp collisions as a function of the beam energy from [12]. The contributions from pair creation, flavor excitation and gluon splitting are shown separately.

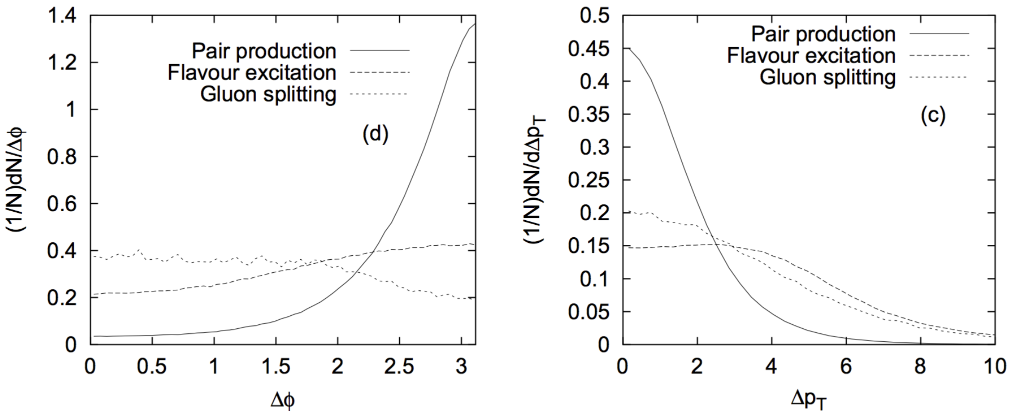

Figure 23: Correlations between b and $\bar{b}$ generated using PYTHIA at a 2 TeV $p\bar{p}$ collider. Panel (c) shows the difference in transverse momentum $\Delta p_\perp = |p_{\perp,b} - p_{\perp,\bar{b}}|$ and panel (d) shows the azimuthal opening angle $\Delta\phi = |\phi_b - \phi_{\bar{b}}|$ [12]. The contributions from pair creation, flavor excitation and gluon splitting, are normalized to unity for a shape comparison.

Only a few heavy-flavor correlation measurements have been performed at high energies. At the Tevatron [107] and the LHC [108, 109, 110] data are reasonably well described by NLO perturbative quantum chromodynamics (pQCD) calculations, but only a few quantitative constraints have been extracted on the relative contributions of different heavy-flavor production mechanisms. At RHIC, as shown in in Figs. 24 and 25, inclusive measurements of *ee* [21] and $e\mu$ [22] pairs from predominantly $c\bar{c}$ at mid-midrapidity and mid-forward rapidity in p+p collisions at $\sqrt{s} = 200$ GeV are consistent with pQCD models within experimental uncertainties. However, the limited statistical accuracy of these measurements prohibits us from providing strong constraints on heavy flavor production mechanisms.

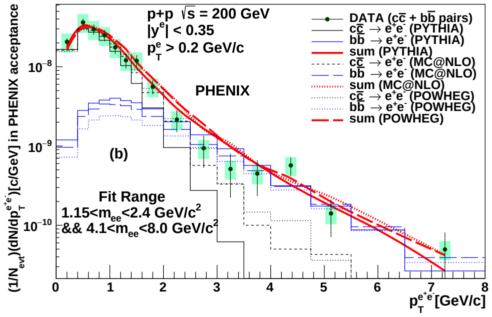

Figure 24: The e^+e^- pair yield as a function of pair p_T, compared to calculations from PYTHIA, MC@NLO and POWHEG [21]. Contributions from $c\bar{c}$ are shown as black lines, contributions from $b\bar{b}$ are shown as blue lines, and the sum is shown as red line.

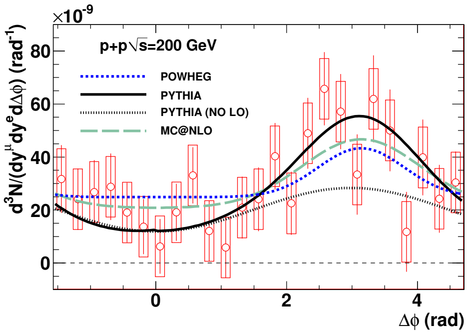

Figure 25: Comparison of the measured p+p pair yield (red points) with distributions generated using POWHEG (blue), PYTHIA (solid black) and MC@NLO (green) [22]. The $e\mu$ pair yield from the subset of PYTHIA events, where the $c\bar{c}$ is not produced at the event vertex (i.e. flavor excitation and gluon splitting events by definition) is plotted as the dotted black line.

In asymmetric collision systems like p/d+Au, deviations from the p+p baseline are often interpreted as cold nuclear matter effects. As shown previously in Figs. 19, significant modifications of single heavy flavor lepton spectra have been observed at backward, forward and mid-rapidities. Pair correlations may provide additional insight on the origin of such modifications. Previous dilepton correlation studies indicated a significant modification of the heavy flavor yields at forward-midrapidity in d+Au collisions, as displayed in Fig. 27 [22]. However, as shown in Fig. 26, at mid-midrapidity

[21], no nuclear modification has been observed within the experimental uncertainties. Thus, correlation studies at forward-forward rapidity can give further input on the possible rapidity dependence of modifications to the pair spectra.

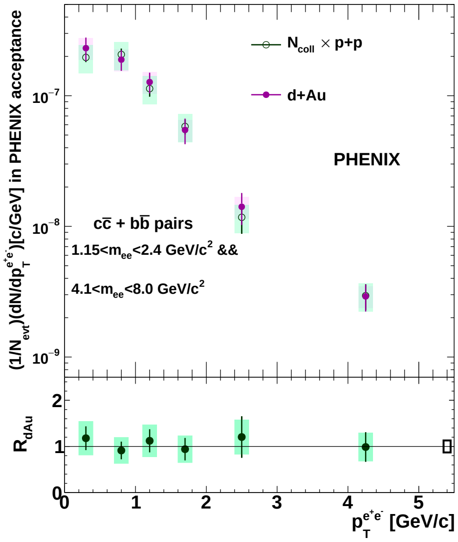

Figure 26: The e^+e^- pair yield as a function of pair p_T in d+Au collisions (violet) at $\sqrt{s_{NN}} = 200$ GeV, compared to the yield in p+p collisions (green) scaled by the number of binary collisions in d+Au. The nuclear modification factor is shown in the lower panel [21].

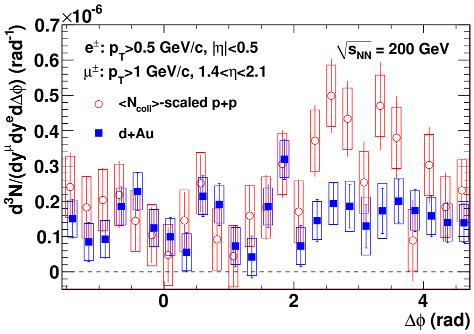

Figure 27: The $e^{\pm}\mu^{\mp}$ pair yield as a function of the azimuthal opening angle in d+Au collisions (blue) at $\sqrt{s_{NN}} = 200$ GeV, compared to the yield in p+p collisions (red) scaled by the number of binary collisions in d+Au [22].

In addition, in heavy-ion collisions the charm contribution is an important background to possible thermal dilepton radiation from the Quark Gluon Plasma [111, 23, 112]. Current uncertainties in our understanding of $c\bar{c}$ and $b\bar{b}$ production and other possible cold nuclear matter effects on heavy flavor prohibit this measurement at RHIC energies (see Fig. 28 [23]) and LHC energies (see Fig. 29 [24]) alike.

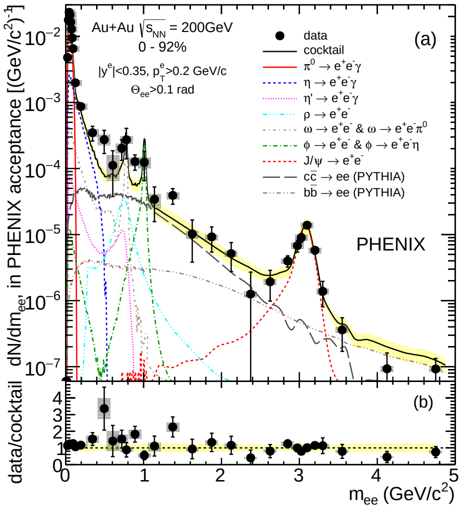

Figure 28: Invariant mass spectrum of e^+e^- pairs in minimum bias Au+Au collisions at $\sqrt{s_{NN}}$ = 200 GeV within the PHENIX acceptance compared to the cocktail of expected decays [23]. The lower panel shows the data to cocktail ratio.

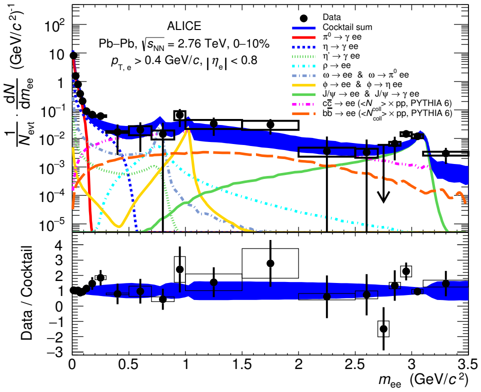

Figure 29: Invariant mass spectrum of e^+e^- pairs in central 0−10% Pb+Pb collisions at $\sqrt{s_{NN}}$ = 2.76 TeV compared to the cocktail of expected decays [24]. Arrows represent the upper limit at 90% C.L.. The lower panel shows the data to cocktail ratio.

1.5.2 Drell-Yan

In p+p collisions, measurements of the Drell-Yan process are invaluable to probe the quark and anti-quark structure of the proton. Precise cross section measurements differentially in mass and p_T can constrain transverse momentum dependent parton distribution functions, which is central to understanding the nuclear structure of the proton and a main physics goal of the future Electron Ion Collider (EIC) in the US.

To date, a Drell-Yan cross section measurement at 200 GeV is still missing. This is mainly due to two reasons. First, the background coming from contributions due to $b\bar{b}$ decays is not well constrained; the uncertainty in the $b\bar{b}$ cross section at 200 GeV is large. Second, the signal to background is low at mid-rapidity; the $b\bar{b}$ contribution is overwhelming because its main production process is gluon fusion and gluons dominate the contribution at low x. The analysis presented in this dissertation simultaneously solves these two problems. The $b\bar{b}$ contribution is well constrained using the like-sign pairs, and since the analysis measures lepton pairs at forward rapidity, the signal to background is around 1:1, well suited for a measurement of the Drell-Yan cross section.

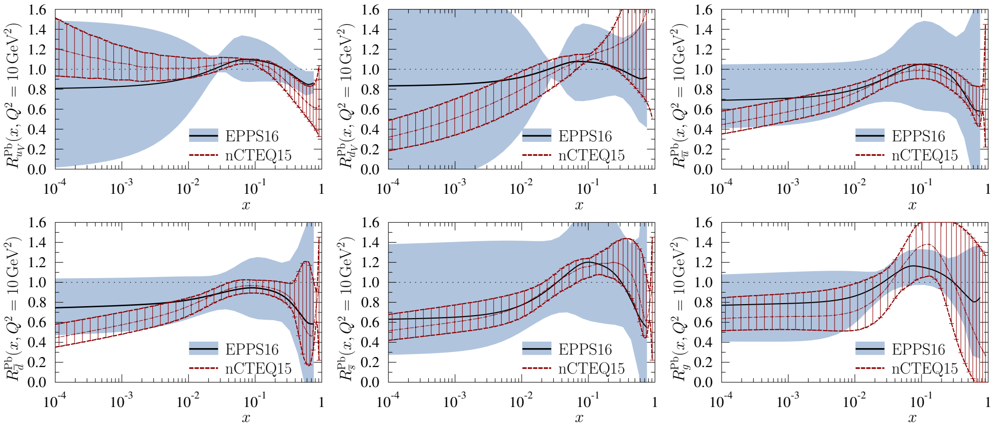

Figure 30: Comparison of the EPPS16 nuclear modifications [25] (black central curve with shaded uncertainty bands) with those from the nCTEQ15 analysis [26] (red curves with hatching) at $Q^2 = 10$ GeV^2.

Drell-Yan measurements in p+A collisions are arguably even more interesting, since lepton pairs are produced directly from hard scattering through the Drell-Yan process and do not interact strongly, the leptons leave the nuclear medium unscathed. Thus, Drell-Yan measurements are an ideal probe to study initial state effects, such as energy loss of partons traversing through nuclei, modification of PDFs, etc.

In particular, the nuclear PDFs at low x are poorly constrained, even after utilizing all the current global data sets available. EPPS16 [25] is the most up to date global analysis of nuclear parton distribution functions, utilizing recent data from p+Pb collisions from LHC. One can see from Fig. 30 that the nuclear PDFs below $x \approx 0.02$ have significant uncertainties. The kinematic regions spanned by the data used in the EPPS16 analysis, together with the kinematic region probed by the data presented in this anlysis, are shown in Fig. 31. The kinematic region spanned by the data at forward rapidity, corresponding to the p-going side in p+Au collisions is approximately $0.004 <$

$x < 0.018$ and $25 < Q^2$ [GeV/c^2]< 65; i.e. an unexplored regime. Thus, the measurements of Drell-Yan cross sections in p+Au collisions can potentially help constrain the nuclear modification of the parton distribution functions.

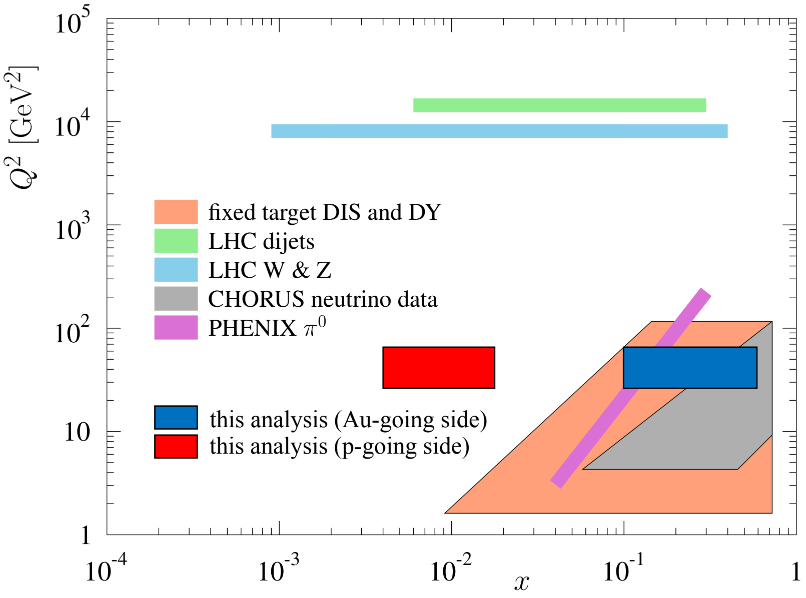

Figure 31: The approximate regions in the (x, Q^2) plane at which different data in the EPPS16 fit probe the nuclear PDFs [25]. The (x, Q^2) regions probed in this analysis is also shown.

2 Experimental Setup

This chapter outlines the experimental setup involved in the measurements presented in this dissertation.

2.1 RHIC (Relativistic Heavy Ion Collider)

RHIC, the first machine in the world capable of colliding ions as heavy as gold, is located at the Brookhaven National Laboratory (BNL) on Long Island, New York. The main goals of the RHIC is (i) to study the characteristics of the Quark Gluon Plasma [53], and (ii) to explore the spin structure of the proton.

An aerial view of RHIC is shown in Fig. 32. The colored lines represent the path traversed by the heavy ions or protons. Heavy ions are generated at the Tandem Van de Graaf, while protons are generated at the linear accelerator (LINAC). These heavy ions or protons are then injected to the Booster Synchrotron. There, the protons or ions are grouped into bunches and accelerated. They are then injected to the Alternating Gradient Synchroton (AGS), which then further accelerates the protons or ions to $\sim$ 10 GeV/c per nucleon. Finally, these bunches of protons or ions are injected into the two 3.834 km long RHIC rings, more commonly known as the blue ring and the yellow ring. The protons or ions circulate opposite directions inside these two rings, and are accelerated up to 255 GeV/c and 100 GeV/c per nucleon for protons and heavy ions respectively.

Fig. 33 shows all collision species and center-of-mass energies RHIC has delivered from 2001 up to 2018. PHENIX has managed to collect a wealth of valuable data in its 16 years of operation from 2001 to 2016, which span a wide range, not only in beam energy, but also in system size, thanks to the versatility of RHIC. The PHENIX experiment will be discussed in detail in the following section.

2.2 The PHENIX (Pioneering High Energy Nuclear Interaction eXperiment) experiment

2.2.1 Overview

PHENIX is one of the largest four experiments that have taken data at RHIC, and is located at the 8 o'clock direction of the RHIC ring. It is specifically

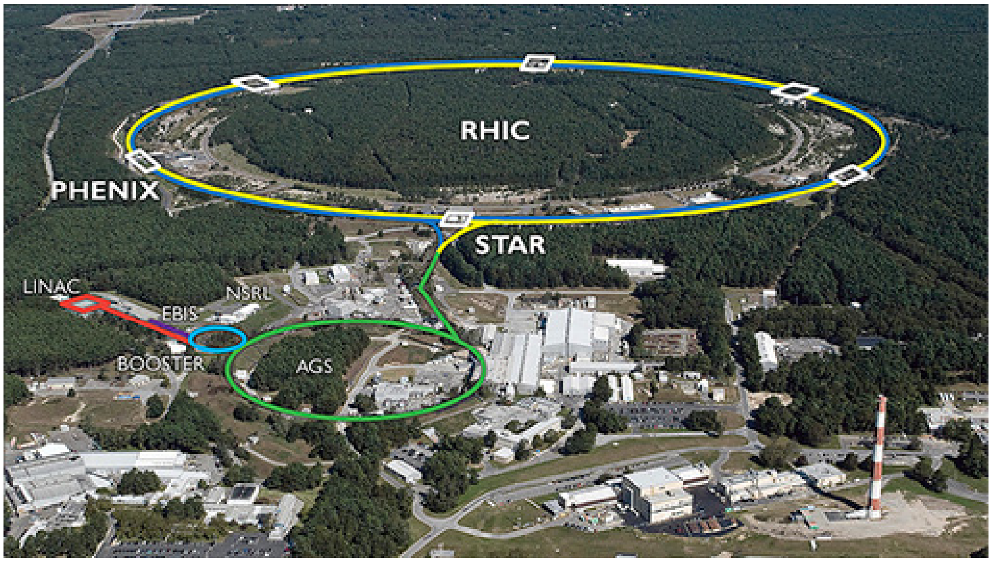

Figure 32: Aerial view of the RHIC complex [27].

designed to measure direct probes of the collision such as electrons, muons and photons [113]. Figure 34 shows the the PHENIX detector subsystems in the 2015 run. The beams inside the beam pipe collide at the interaction point (IP), which is at the center of the PHENIX detector. The produced particles in a collision then enter the PHENIX detector, which consists of two main spectrometers, known as the Central Arms and the Muon Arms, as well as other complementary detectors, which we will discuss in the following section.

The Central Arms

The Central Arms [114, 115, 116] cover $|\eta| < 0.35$ in rapidity and π in azimuth, and is designed to detect electrons, photons and hadrons with a set of particle identification and tracking detectors. The Central Arms consist of Silicon Vertex Detectors (VTX), Drift Chambers (DC), Pad Chambers (PC), Ring-Imaging Cherenkov detectors (RICH), Time-Of-Flight detectors (TOF) and Electromagnetic Calorimeters (EMCal). The VTX, newly installed in 2011, can give precise measurements of the collision point and the distance of closest approach of charged tracks, which enables charm bottom separation in

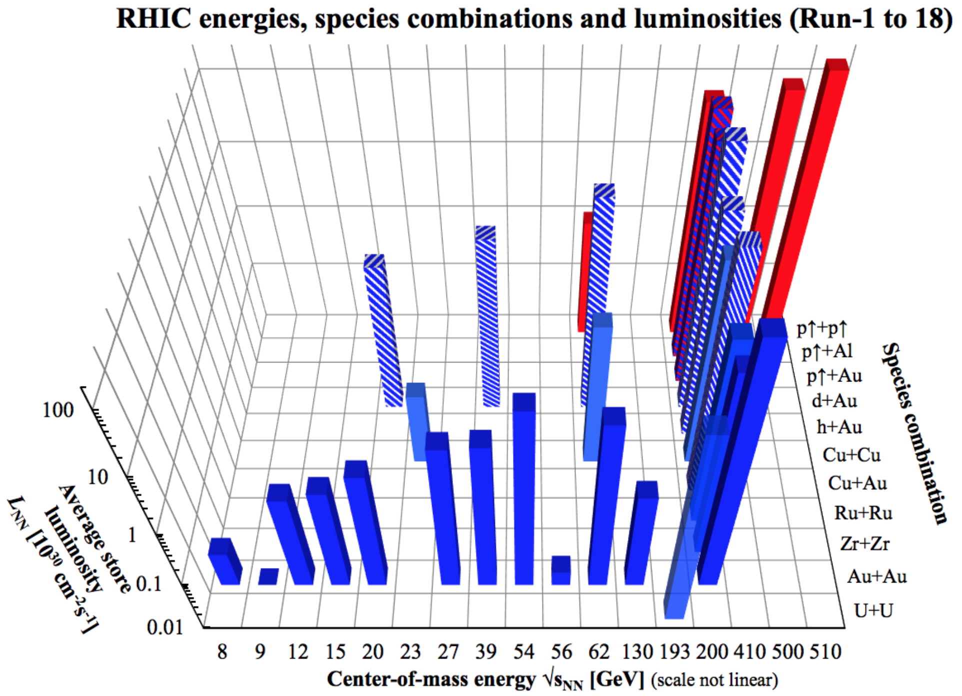

Figure 33: RHIC energies, species combinations and luminosities [28].

heavy flavor measurements. The DC, PC together with the Central Magnet form a set of tracking detectors, which determine the momentum of charged particles by measuring the bending angle of a particle trajectory in a magnetic field. The RICH and TOF are mainly used for particle identification. The EMCal, which consist of Lead Scintillator (PbSc) and Lead Glass (PbGl), measure particle energy though electromagnetic showers.

The Muon Arms

The Muon Arms [31], consisting of the South Muon arm and the North Muon arm, cover $-2.2 < |\eta| < -1.2$ and $1.2 < |\eta| < 2.4$ in rapidity respectively and 2π in azimuth. The Muon Arms is designed primarily to measure muons, although charged hadrons may be also be measured. Both Muon Arms consist of the forward Silicon Vertex Detector (FVTX), Muon Trackers (MuTr) and Muon Identifier (MuID). Charged particles traversing through the FVTX leaves hits in the FVTX, allowing a measurement of the distance of closest approach, which, similar to the VTX, enables charm bottom separation in heavy flavor measurements. Before particles enter the MuTr, they must pass through the Central Magnet, which acts as a hadron absorber. Muons together with a small fraction of hadrons then enter the MuTr where the momentum is measured. The MuID consists of five layers of alternate Iarocci tube detectors and steel walls, and provides identification of muons. Details of the sub-detectors of the Muon Arms will be described in Sec. 2.2.3.

Muon Piston Calorimeters (MPC)

The Muon Piston Calorimeter [117] cover $3.1 < |\eta| < 3.7$ in rapidity and 2π in azimuth, and is made of lead-tungsten glass. The primary purpose of the MPC is to measure π^0 and η mesons. In 2015, the Muon Piston Calorimeter Extension (MPC-EX) [118] which is made of silicon-tungsten, was installed in front of the MPC. The primary goal of this upgrade it to provide sufficient prompt photon and π^0 separation to allow a prompt photon measurement in the low-x region, to search for evidence of *gluon saturation* [119].

Global Detectors

The Beam Beam Counters (BBC) and the Zero Degree Calorimeters (ZDC) are categorized as the global detectors in the sense that their primary purpose is event characterization. The BBC are located at the very forward region ($3.0 < |\eta| < 3.9$). The BBC provide local level-1 triggers by requiring hits in both the south and north detectors, and also gives a measurement of the collision vertex and collision centrality. We defer an in-depth discussion of the BBC to Sec. 2.2.2. The ZDC is a hadron calorimeter, located downstream of the DX dipole magnets. Charged particles typically do not hit the ZDC due to the DX magnet. Thus, the ZDC can measure energy of neutral particles within a 2 mrad cone about the beam direction, and serves as a counter for spectator neutrons. The ZDC can also provide local level-1 triggers by requiring hits in both the south and north detectors.

2.2.2 Beam Beam Counters

The Beam Beam Counters [29] consist of two modules, south and north, situated at backward and forward rapidity respectively. As shown in Fig. 35, each arm comprises 64 quartz Cherenkov counters, separated radially into

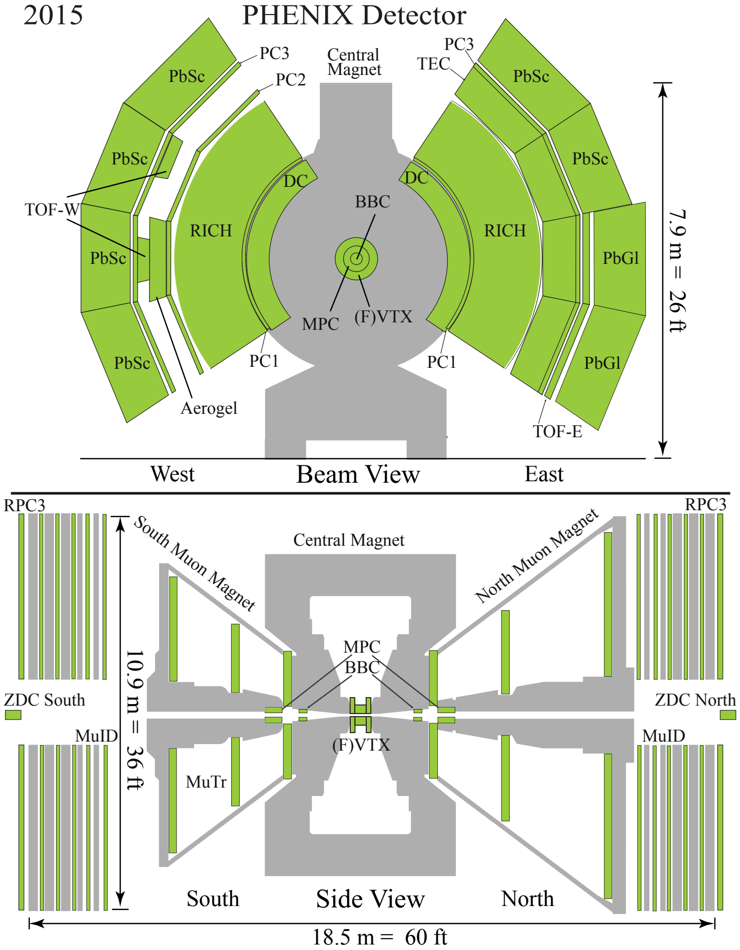

Figure 34: Beam view (top) and side view (bottom) of the PHENIX detector in the 2015 run.

three layers. The inner and out diameters are 10 cm and 30 cm respectively. The BBC can detect charged particles with velocities $v > 0.7c$. By measuring the time difference between charged particles arriving at each BBC, the time of collision T_0 and z-vertex position along the direction of the beam pipe z_{vtx} of the collision can be determined, according to the following relations:

$$z_{vtx} = \frac{(T_S - T_N) \cdot c}{2}, \tag{8}$$

$$T_0 = \frac{(T_S + T_N)}{2} - \frac{L}{c}, \tag{9}$$

where $L = 144.35$ cm is the distance between the center of PHENIX interaction point and each BBC, t_S and t_N are the average time of charged particles hitting the south and north BBC respectively, and c is the speed of light. An illustration can be found in Fig. 36.

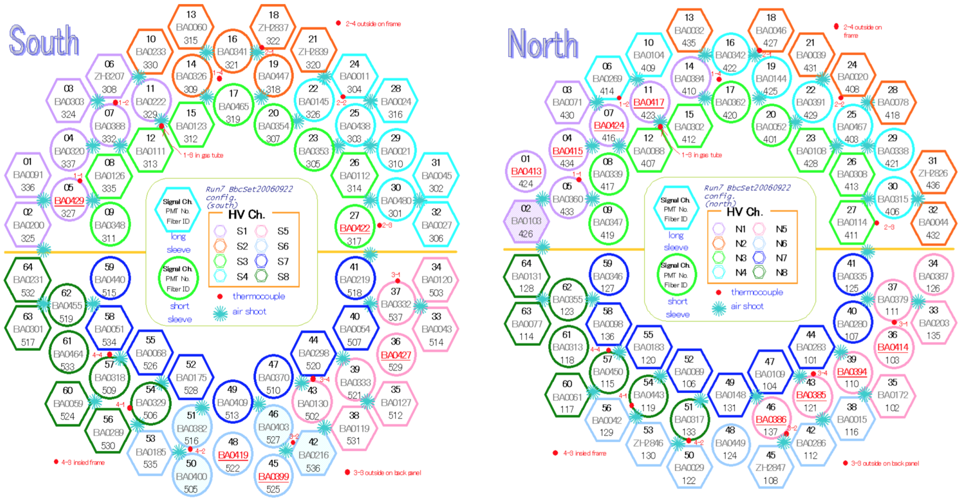

Figure 35: Configuration of Cherenkov counters in the south (left) and north (right) BBC [29].

The resolution of the event vertex is directly related to the charged particle multiplicity in the BBC acceptance, and varies between 0.5 cm for heavy ion collisions and 2.0 cm for p+p collisions. The online vertex calculation are often used for the minimum bias triggers, i.e. requiring a limited z-vertex range in addition to the requirement that there be at least one hit in both BBCs. A more precise vertex position is calculated offline after recalibration of the BBC.

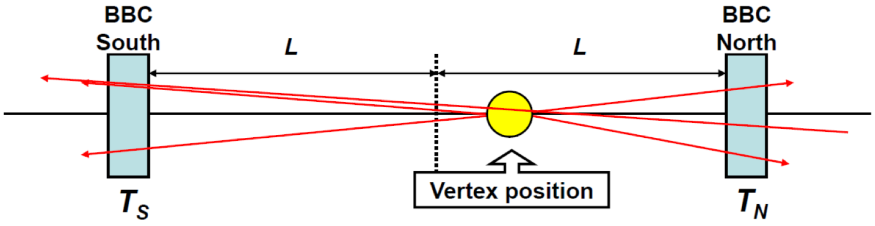

Figure 36: Illustration of the measurement of the z vertex position [30].

2.2.3 Muon Arm Detectors

Hadron Absorbers

The primary function of the muon arm detectors is the detection of muons. Particle identification is primarily achieved by placing an absorber upstream of the MuTr, such that particles other than muons (mainly hadrons and electrons) are absorbed by the absorber due to strong and electromagnetic interactions. As shown in Fig. 34, the Central Magnet, which is 60 cm thick, serves as an absorber for the muon arms. 20 cm-thick copper nose cones were installed at the inner surface of the Central Magnet. In addition, 35 cm-thick stainless steel absorbers are installed at the outer surface of the Central Magnet in 2012 to further reject hadrons. The pre-MuTr absorbers totals an interaction length of $7.1\lambda_I/cos\theta$, where θ is the polar angle, and roughly corresponds to a 1/1000 hadron rejection rate.

Behind the MuTr, a part of the Muon Magnet yoke, composed of steel and 20 (30) cm thick for the south (north) muon arm, acts as absorbers to further suppress the hadron background. Finally, the MuID has five layers of steel walls totalling a thickness of 80 cm. The total interaction length from the interaction point to the last gap of the MuIDs is $13.0\lambda_I/cos\theta$ ($13.4\lambda_I/cos\theta$) for the south (north) arm.

A summary of all hadron absorbers and their thickness and corresponding interaction lengths in the Muon Arms are shown in Table. 1.

Muon Tracker (MuTr)

The South and North Muon Trackers, covering backward ($-2.4 < \eta < -1.2$) and forward ($1.2 < \eta < 2.2$) rapidities respectively, are placed inside the

Table 1: List of hadron absorbers and their thickness in the Muon Arms.

Absorber	Material	South (North) Thickness (cm)	$\lambda_I/cos\theta$
Nose cone	Copper	20(20)	1.8(1.8)
Central Magnet	Steel	60(60)	3.1(3.1)
Stainless steel absorbers	Stainless Steel	35(35)	2.2(2.2)
Sum of pre-MuTr	-	115(115)	7.1(7.1)
Muon Magnet yoke	Steel	20(30)	1.1(1.5)
MuID 1st Layer	Steel	10(10)	0.6(0.6)
MuID 2nd Layer	Steel	10(10)	0.6(0.6)
MuID 3rd Layer	Steel	20(20)	1.2(1.2)
MuID 4th Layer	Steel	20(20)	1.2(1.2)
MuID 5th Layer	Steel	20(20)	1.2(1.2)
Sum of post-MuTr	-	100(110)	5.9(6.3)
Total	-	215(225)	13.0(13.4)

magnetic field of the South and North Muon Magnets as shown in Fig. 34. Each muon tracker consists of three multi-layered cathode strip chambers, referred to as "stations". The three stations are numbered 1, 2 and 3, from inner to outer stations (see Fig. 37), and are positioned at $1.80, 3.00, 4.60$ m and $1.80, 3.47, 6.12$ m from the origin for south and north respectively. A drawing of the south muon magnet and muon tracker can be found in Fig. 38. Station 1 is divided in to 4 segments (quadrants) and stations 2 and 3 are divided into 8 segments (octants), azimuthally. A drawing of the MuTr Station 2 is shown in Fig 39. Along the z direction, stations 1 and 2 consist of three layers, while station 3 comprises 2 layers. Each layer is referred to as "gap", and each includes an anode wire layer sandwiched between two cathode strip layers, forming a cathode strip chamber. The chambers are filled with a gas mixture, composed of 50% Ar, 30% CO_2 and 20% CF_4. 20μm Au-plated W sense wires and 75μm Au-plated Cu-Be field wires run alternately in the azimuthal direction with a wire spacing of 5 mm. The direction of one of the cathode plane strips of each chamber is exactly radial and perpendicular to the anode wire (*non-stereo plane*), while the direction of the other cathode plane is tilted by a small angle in order to measure the

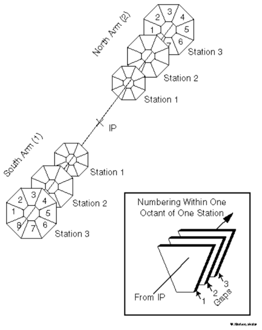

Figure 37: Muon Tracking nomenclature [31].

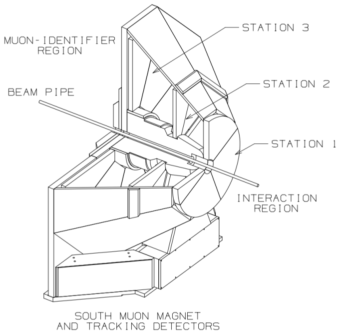

Figure 38: A drawing of the south muon magnet and muon tracker stations [31].

radial position of the particle (*stereo plane*). As shown in Fig. 40, the tilt angle of the stereo planes in each gap is different in order to eliminate ghost tracks. The nominal high voltage applied to the anode wires is 1900 V and the typical gain is 2×10^4.

The Muon Arm Magnets provide a radial magnetic field necessary for the MuTr to make a momentum measurement. The magnetic fields generated from the magnets are shown in Fig. 41. The magnets are around 10 meters tall. Two solenoidal coils produce the radial magnetic field. The $\oint \mathbf{B} \cdot \mathbf{dl}$ along a line at 15 degrees from the beam axis is 0.75 and 0.72 Tesla-meters for the south and north muon magnets respectively; the physics performance of both magnets are similar. More details on the PHENIX magnet system can be found at Ref. [120].

When a charged particle enters the MuTr, the component of its velocity perpendicular to the direction of magnetic field is affected by the Lorentz force. Thus, the momentum of the particle can be obtained by measuring the bending angle of the particle. The resolution of the momentum measured by the MuTr rises linearly with the momentum, and is directly related to the spatial resolution of the MuTr which is $\sim 100\mu$m.

Muon Identifier (MuID)

The Muon Identifier (MuID) is located behind the MuTr. It is composed of five alternating layers, referred to as gaps of steel walls and multi-wire chambers. The gaps are numbered 0 to 5 from the innermost to the outer-

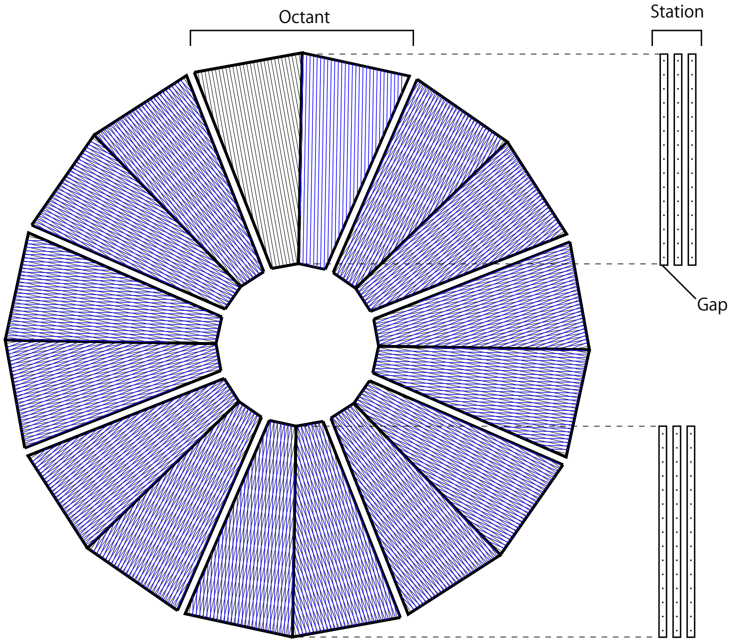

Figure 39: A drawing of the MuTr Station 2 [31]. The non-stereo planes are represented by black lines while the stereo planes are represented by blue lines.

most layers. The primary purpose of the MuID is to identify muons from the hadron background. This is achieved by requiring the muon candidates to pass through the 4th or the last layer of the MuID. Each gap consists of two planes, one horizontally oriented and one vertically oriented. Each plane is then divided into six overlapping panels, as shown in Fig. 42. Each plane consist of arrays of Iarocci tubes, which are planar drift tubes. Each tube consists of 100 μm Au-coated CuBe anode wires inside a resistive graphite-coated plastic cathode filled with a gas mixture of CO_2 and isobutane. Every two units of Iarocci tube arrays are bundled together, forming a *two-pack*; the two arrays are staggered by half of one channel (0.5 cm) as shown in Fig. 43 in order to increase detection efficiency. The horizontally or vertically aligned two-packs are grouped together as described above to form rectangular MuID panels. Since the MuID is located outside of the magnetic field of the Muon Magnets, particles travel along a straight line inside the MuID. A reconstructed track in MuID is referred to as a *road*. Details on

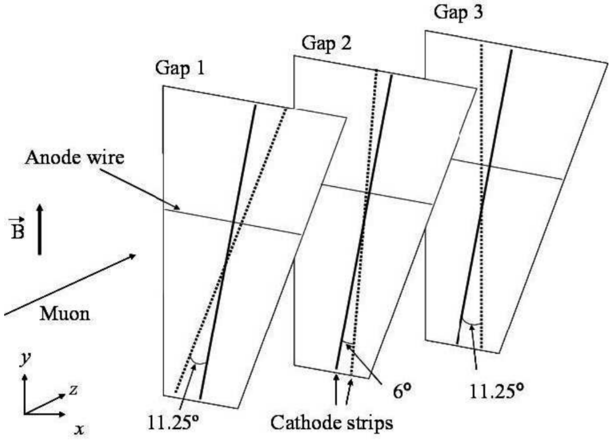

Figure 40: A drawing of different gaps in the MuTr [31]. The orientation of the stereo planes are different for each gap to eliminate ghost hits.

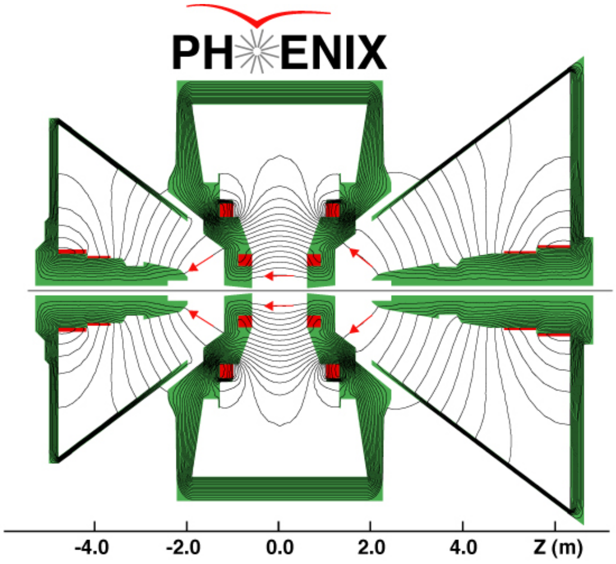

Magnetic field lines for the two Central Magnet coils in combined (++) mode

Figure 41: Magnetic field lines for the two Central Magnet coils in combined (++) mode [31].

track reconstruction will be described in Sec. 3.2.

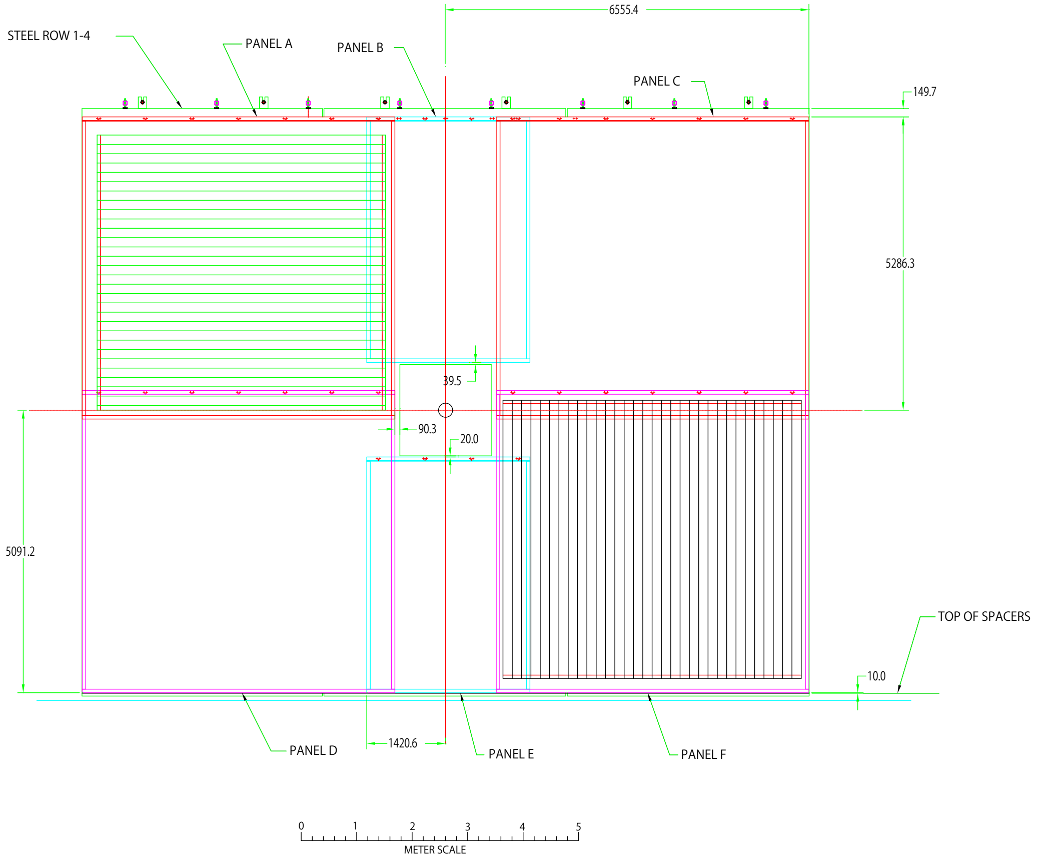

Figure 42: A drawing of a MuID gap [31].

2.3 Data Taking

2.3.1 Data Acquisition (DAQ)

The PHENIX data acquisition (DAQ) [32] is designed in a manner that allows taking data in collisions of both $p+p$ and heavy ions, which have significantly different requirements. For example, the collision rate of heavy ion collisions is typically a few kHz while the collision rate of $p+p$ collisions is a few MHz. The size of the data for a typical heavy ion collision event

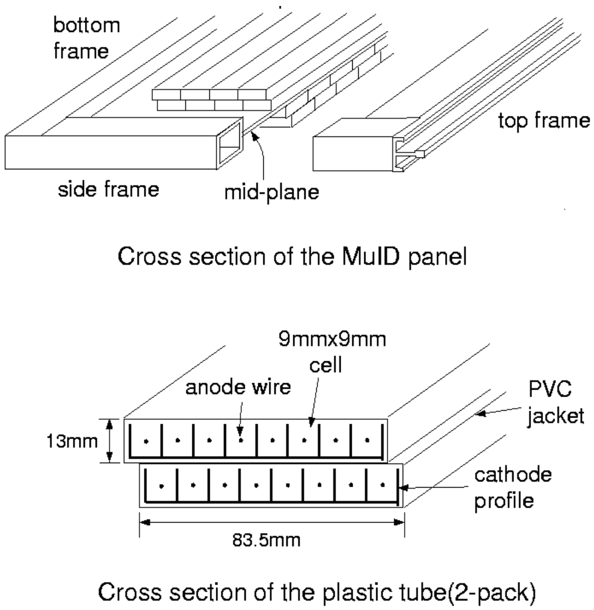

Figure 43: A drawing of the Iarocci tubes [31].

is also much larger than that of p+p collisions due to the higher multiplicity in heavy ion collisions. For heavy ion collisions, virtually every event contains some interesting feature, while for p+p collisions, the majority of collisions are somewhat uninteresting. The PHENIX DAQ employs a multi-event buffering system and a triggering system which can simultaneously handle high interaction rates and large event sizes. Fig. 44 is an illustration of the PHENIX DAQ system [121]. The implementation of the multi-event buffering system allows each component of the DAQ to have the ability to receive data, process data, and transmit data, in parallel. This feature allows the dead time to be minimized. The triggering system is described in detail in the following section.

2.3.2 Event Triggers

The PHENIX Level-1 Trigger system consists of the Local Level-1 (LL1) system and the Global Level-1 (GL1) system. The trigger systems are synchronized with the 9.4 MHz RHIC clock, which corresponds to the beam

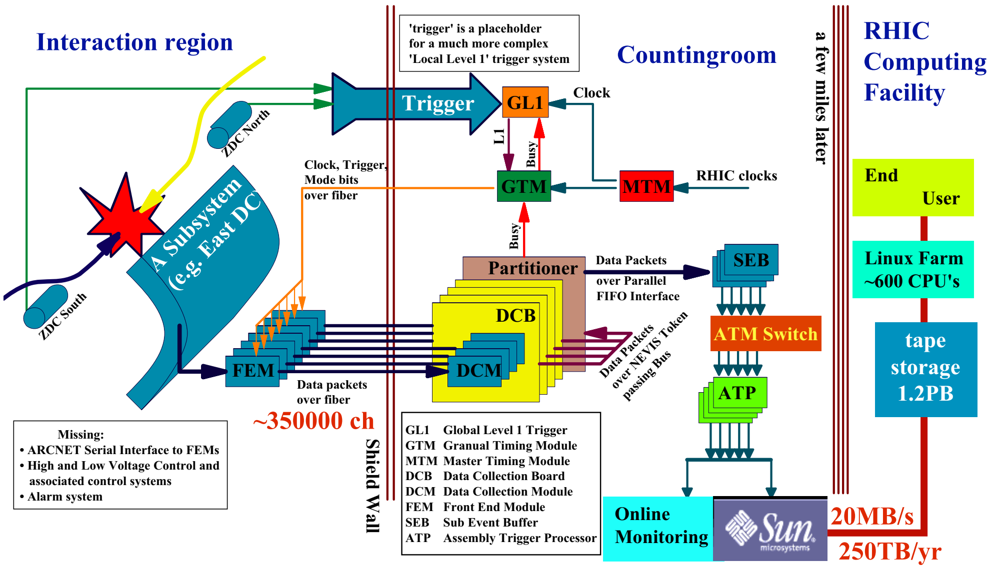

Figure 44: Illustration of the PHENIX DAQ system [32].

crossing frequency. The master timing module (MTM) distributes the RHIC timing information to the Global Level-1 (GL1) module and the Granule Timing Modules (GTMs), where the term “granule” refers to the minimal detector element in the DAQ. Data from front-end modules (FEMs) of various detector subsystems are transmitted to the LL1 system. The signals from LL1 are then transmitted to the GL1. The GL1 will issue a trigger signal to the GTMs, which signals the event is accepted and information of the event will be recorded, if the following two conditions are met: (i) any LL1 signal satisfies the corresponding LL1 trigger logic, and (ii) the GTMs are not all busy. The GTMs then transmits the trigger signal to the FEMs.

There are 32 bits assigned to Level-1 triggers, each with its own unique triggering conditions. Table. 2 shows a list of 32 triggers used in the data taking of run 15 p+p collisions.The *Scale Down*, shown in the second column of 2, is the number of skipped events corresponding to a certain trigger being fired after recording an event corresponding to the same trigger being fired. The *livetime*, shown in the third column of 2, is the the percentage of events in which the trigger condition is met and the DAQ is not busy, such that the event information is successfully recorded on tape. There are three type of counts, *raw counts*, *live counts*, and *scaled counts*. Raw counts is the number of events which satisfy a certain trigger condition, live counts is the number of events in which the trigger condition is satisfied and the DAQ is not busy, and scaled counts is the number of events in which the trigger condition is satisfied, the DAQ is not busy, and the event is recorded on tape. In the following, we describe in detail the the two triggers used in the analysis that is presented in this dissertation.

2.3.2.1 Minimum Bias Triggers (BBCLL1) The BBC Local Level-1 trigger (BBCLL1) is issued when there is at least one hit in each BBC. Since there is at least one hit in each BBC, the BBC can measure the collision time and vertex along the z-axis. The default BBCLL1 trigger requires a collision vertex to be within ±30 cm from the origin. There can be other vertex requirements, such as BBCLL1 narrowvtx, which requires the collision to be within ±15 cm from the origin, and BBCLL1 novtx, which does not have any vertex requirement. Many physics triggers are combined with BBCLL1, since the BBC trigger provides the collision timing.

The minimum bias (MB) trigger efficiency ϵ_{BBC}^{MB}, is defined as the probability for an inelastic collision to satisfy the minimum bias requirement in PHENIX, i.e. at least one hit on each BBC. This is 55±5% and 84±3% [122] in p+p and p+Au collisions at $\sqrt{s_{NN}} = 200$ GeV respectively.

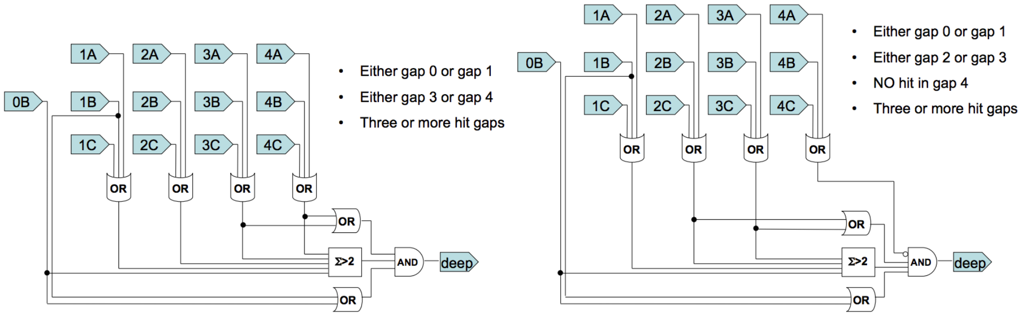

Figure 45: MuID symset logics. The MuID-1D (one Deep) logic is shown on the left panel while the MuID-1H (one Hadron) logic is shown on the right panel.

2.3.2.2 Muon Local Level-1 Trigger (MuIDLL1) The analysis presented in this dissertation use data sets taken with a combination of the minimum bias trigger (BBCLL1) and a muon local level-1 trigger (MuIDLL1). More specifically, we use MUIDLL1_2D triggers, where 2D is a shorthand for *2-Deep*.

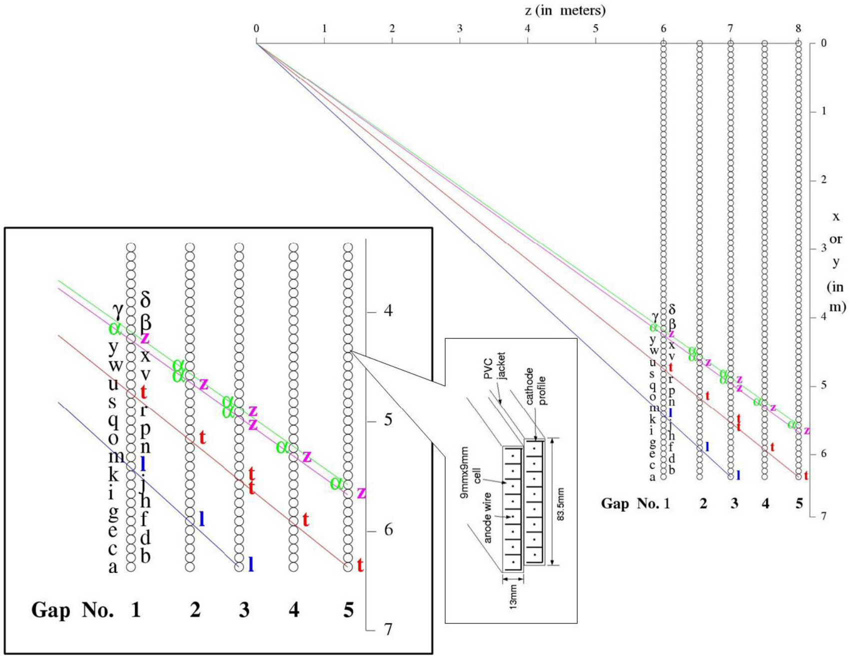

Figure 46: Symsets of the MuIDLL1 trigger

The MuIDLL1 trigger algorithm is completely dependent on the hit pattern in the MuID. The MuIDLL1_S and the MuIDLL1_N depends on the south and north MuID respectively, and the two triggers are independent of each other. Recall that each MuID gap has a horizontally oriented layer of two-packs and a vertically oriented layer of two-packs. Drawing straight lines from the origin to gap 4, these straight lines may intersect each gap at certain two-packs (with a certain orientation) as shown in Fig. 46. Two-packs that fall on one single straight line form a logical tube. All logical tubes sharing the same two-pack at gap 0 are then grouped together, and are referred to as a *symset*. The trigger condition is then checked for each symset. The symset logic for the MuID-1D (1-Deep) and 1H (1-Hadron) are shown schemetically in Fig. 45. The MuID-1D symset logic requires one hit in either gap 0 or gap

1, one hit in either gap 3 or gap 4, and a total of three or more gaps with a hit. The MuID-1D trigger is fired if there is (i) one vertical symset satisfying the symset logic and (ii) one horizontal symset satisfying the symset logic. The MuID-2D trigger is fired if there are (i) two vertical symsets satisfying the symset logic, and (ii) two horizontal symsets satisfying the symset logic, with the extra cavaet that one two-pack is skipped in the trigger algorithm if there is a hit in the “previous” two-pack, where the word “previous” refers to the numbering system in the triggering algorithm. In general, when two MuID roads are spatially close to each other, there is an extra inefficiency arising from this requirement. Thus, the MuID-2D trigger is not a simple product of two MuID-1D triggers. This feature will be explained in detail in Sec. A.

Table 2: List of triggers in Run15 p+p collisions.

Name	Scale Down	Livetime
BBCLL1(> 0 tubes)	2749	0.91
BBCLL1(> 0 tubes) novertex	4949	0.91
ZDCLL1wide	97	0.92
BBCLL1(noVtx)&(ZDCN||ZDCS)	225	0.92
BBCLL1(> 0 tubes) narrowvtx	12	0.91
ZDCNS	97	0.91
ERT_4x4b	0	0.83
ERT_4x4a&BBCLL1	0	0.93
ERT_4x4c&BBCLL1	0	0.93
ERTLL1_E&BBCLL1(narrow)	0	0.92
FVTX_HighMult_N	9999999	0.00
FVTX_HighMult_S	9999999	0.00
MPC_N_S_A	0	0.89
MPC_S_B	0	0.90
MPC_S_C&ERT_2x2	0	0.92
MPC_S_C&MPC_S_C	0	0.91
CLOCK	196077	0.91
MPC_N_B	0	0.87
MPC_N_C&ERT_2x2	0	0.92
MPC_N_C&MPC_N_C	0	0.16
MUIDLL1_N2D&BBCLL1novtx	0	0.77
MUIDLL1_S2D&BBCLL1novtx	0	0.81
MUIDLL1_N1D&BBCLL1novtx	1	0.91
MUIDLL1_S1D&BBCLL1novtx	0	0.90
MUON_N_SG3&MUIDLL1_(1D||1H) &BBCLL1novtx(nppg)	0	0.90
MUON_S_SG3&MUIDLL1_(1D||1H) &BBCLL1novtx(nppg)	0	0.91
MUON_N_SG3&BBCLL1novtx(nppg)	122	0.92
MUON_S_SG3&BBCLL1novtx(nppg)	15	0.92
PPG(Pedestal)	0	0.93
PPG(Test Pulse)	0	0.92
PPG(Laser)	0	0.93
Noise	0	0.00

3 p+p collisions: Data Analysis

3.1 Data Set and Event Selection

The data set analyzed for p+p collisions at $\sqrt{s} = 200$ GeV was taken in 2015. The data were selected with the $\mu\mu$ pair trigger (MuIDLL1-2D) in coincidence with the MB trigger. We require each event in the sample to have a reconstructed vertex within $z = \pm 30$ cm of the nominal collision point. The data sample corresponds to 1.2×10^{12} MB triggered events or to an integrated luminosity of $\int \mathcal{L} dt = 51$ pb^{-1}.

3.2 Track reconstruction

Each reconstructed muon track comprises a combination of a reconstructed tracklet in the MuTr and a reconstructed tracklet in the MuID. Quality cuts on the muon tracks are applied to reduce the number of background muons from light hadron decays. They are summarized in Tab. 3. The MuTr tracklet must have a minimum of 11 hits and a χ^2/NDF smaller than 15 (20) for the south (north) arm. The MuID tracklet has to penetrate to the last gap and must have at least 5 associated hits. MuID tracklets with χ^2/NDF larger than 5 are rejected. MuTr tracklets are projected to MuID gap 0. We apply cuts on the distance between the projection of the MuTr tracklet as well as the MuID tracklet (DG0) and the difference between the track angles (DDG0). Figure 47 displays DG0 and DDG0 distributions for muons with momenta of 4 to 5 GeV/c from $\mu\mu$ pairs in the mass region 2.8–3.4 GeV/c^2 where $\mu\mu$ pairs from J/ψ decays dominate the yield. Both distributions are compared to tracks from simulated J/ψ decays. These cut variables are well described by simulations. We apply a cut at 3σ (99.87% efficiency) of the momentum dependent matching resolution of signal tracks determined from Monte Carlo simulations with GEANT4 [123].

In addition to the basic track quality cuts, we enforce the condition that the momentum of all reconstructed muon tracks are within $3 < p$ [GeV/c] < 20 and that their rapidity to be $1.2 < |\eta| < 2.2$. These requirements limit effects from detector acceptance edges. The upper limit on p discards tracks from hadronic decays within the MuTr volume that lead to a mis-reconstructed momentum. In addition, we require that all tracks satisfy the MuIDLL1-1D trigger condition.

While traversing the absorber muons undergo multiple scattering and lose typically 2 GeV of their energy before they reach the MuTr, where the momentum of the track is measured. Thus, the momentum needs to be corrected to correspond to the momentum before entering the absorber. The relative resolution has two main components, the intrinsic resolution of the MuTr and the resolution of the energy loss correction. Below 10 GeV/c the resolution depends only moderately on rapidity or momentum and is approximately constant between 3.5% and 5%. Towards larger momenta, the resolution gradually increases but remains below 10% for all momenta considered in this analysis ($p < 20$ GeV/c). Multiple scattering in the absorber adds an uncertainty of $\sim$ 160 mrad on the angular measurement from the MuTr. This can be vastly improved with the FVTX, which measures the track in front of the absorber. However, we do not make use of this improvement in the current analysis due to reasons discussed in the following section.

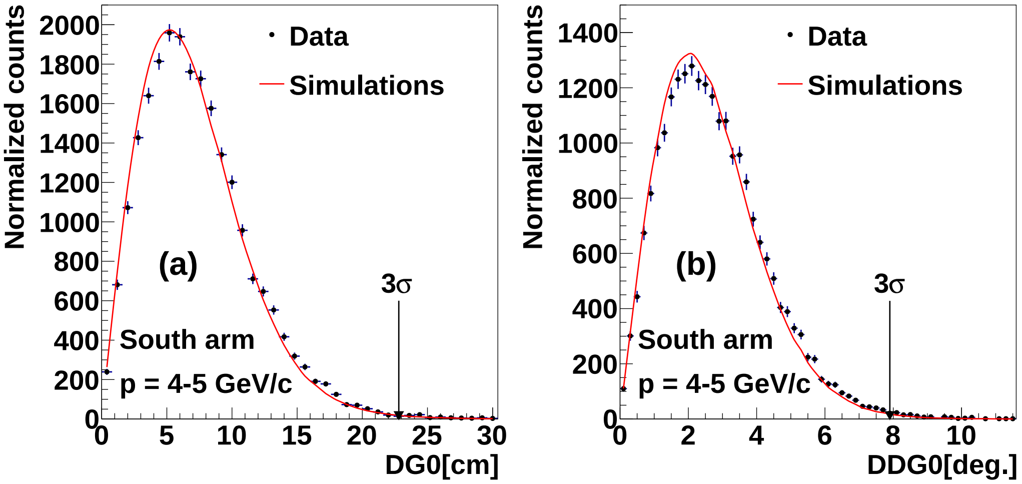

Figure 47: Matching of MuTr to MuID tracklets in distance (DG0) and angle (DDG0) for tracks from pairs in the J/ψ mass region. Data and simulations are compared. The 3σ cut applied in the data analysis is indicated.

3.3 Muon pair selection

All muon tracks in a given event are combined to pairs and their masses and momenta are calculated. The mass and momenta are computed from a fit to the two tracks with the constraint that both originate at a common vertex within the range ±40 cm around the nominal event vertex. This fitting procedure improves the resolution of the opening angle of the pair, which in turn significantly improves the mass resolution at $m < 3$ GeV/c^2 where the mass resolution is dominated by effects from multiple scattering. We achieve a mass resolution $\sigma_m/m \approx 12.6\%,\ 7.4\%,\ 5.7\%$ at $m = 1.02,\ 3.10,\ 9.46$ GeV/c^2, which correspond to the ϕ, J/ψ and $\Upsilon(1S)$ respectively. The achieved mass resolution is sufficient for the analysis of the $\mu\mu$ pair continuum.

In principle, the mass resolution could be further improved by constraining the fit to the measured vertex position. However, our data set contains on average 22% of pileup events with two collisions recorded simultaneously. For these events only an average vertex position can be measured by the BBC, which is often tens of centimeters away from one or both of the collision points. This leads to $\mu\mu$ pair masses reconstructed hundreds of MeV/c^2 different from the true mass and results in a mass resolution function with significant non-Gaussian tails.

Comparison of the mass distribution of the south muon arm and the north muon arm are shown in Fig. 48(a) and Fig. 48(b) respectively. The mass is calculated from the fits that constrain the tracks to originate from a vertex located at (i) ±40 cm of the nominal vertex (mass$_{\rm nominal}$), and (ii) ±2 cm of the measured vertex using the BBC (mass$_{\rm BBC}$). Although the width of the J/ψ is wider for mass$_{\rm nominal}$ as expected, the yield at the continuum on both sides of the J/ψ is significantly different for the two mass calculations. In order to further diagnose this issue, pairs with mass$_{\rm BBC}$ between 1.4 and 2.4 GeV/c^2 [panel (c)] and between 4.0 and 5.8 GeV/c^2 [panel (d)] are selected, and their mass$_{\rm BBC}$ and mass$_{\rm nominal}$ distributions are compared. In both mass$_{\rm BBC}$ selections, a clear J/ψ peak is observed for mass$_{\rm nominal}$, which indicates that the mass$_{\rm BBC}$ continuum contains a significant fraction of mis-reconstructed muon pairs from J/ψ mesons, where the mis-reconstructed mass is due to a mis-measured BBC vertex in pileup events. To avoid this undesirable complication of the analysis of the $\mu\mu$ pair continuum, we do not make use of the improvement of the mass resolution. The pileup events increase the yield of $\mu\mu$ pairs per event by about 10%, and is taken into account in the normalization procedure.

We apply additional quality cuts to the muon pairs, which are summarized in Table 4. The $\chi^2_{\rm vtx}$, calculated from the simultaneous fit of the two muon tracks, must be less than 5. This cut mainly removes tracks resulted from light hadron decays or that were scattered by large angles in the absorber. We also remove pairs with a momentum asymmetry ($|p_1-p_2|/|p_1+p_2|$) larger

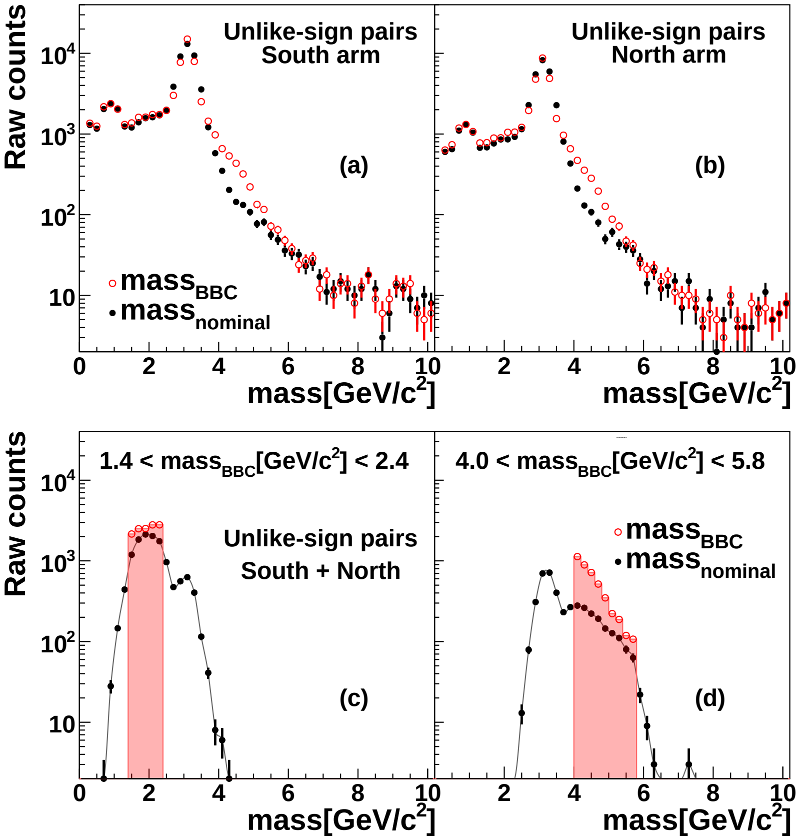

Figure 48: The mass spectra from the (a) south and (b) north arms, where the mass is calculated with different constraints to the vertex position: (i) a common vertex within ±40 cm around the nominal event vertex (mass$_{\text{nominal}}$, closed circles), and (ii) the vertex measured by the BBC (mass$_{\text{BBC}}$, open circles). mass$_{\text{BBC}}$ and mass$_{\text{nominal}}$ distributions are compared with pairs selected with mass$_{\text{BBC}}$ (c) between 1.4 and 2.4 GeV/c^2, and (d) between 4.0 and 5.8 GeV/c^2.

than 0.55 since these pairs are mostly from random pairs where one hadron has decayed into a muon inside the MuTr volume and is mis-reconstructed as a higher momentum track, thus yielding a fake high mass pair.

Finally, we impose cuts to ensure spatial separation between two tracks in the MuTr and MuID volumes. Specifically we require that the vertical and

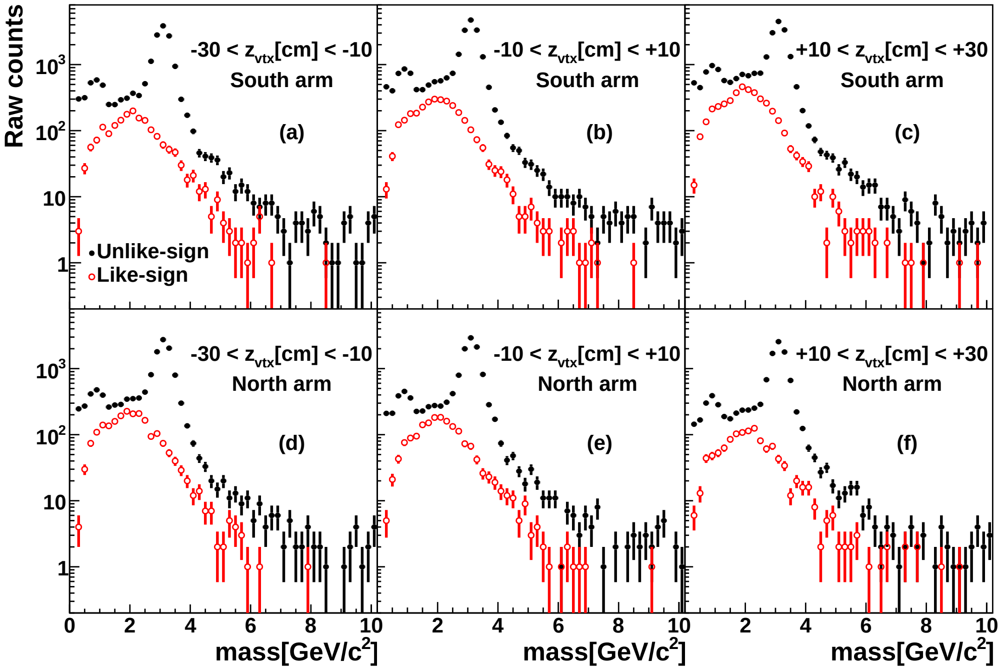

Figure 49: Raw mass spectra for the south (a,b,c) and north (d,e,f) muon arms in different z_{vtx} slices.

horizontal spatial separation of the two tracks at the MuID gap 0 exceeds 20 cm, and that the two tracks do not share the same MuTr octant. These cut removes all pairs with tracks that overlap so that for the remaining pairs the pair reconstruction and trigger efficiencies factorize into a product of single track efficiencies.

Figure 49 shows the raw mass spectra after imposing all single and pair cuts. Spectra are presented for $\mu^+\mu^-$ and $\mu^\pm\mu^\pm$ pairs measured for collisions in three vertex regions separately for the south and north arms.

The most prominent feature in the spectra is the J/ψ peak at ~ 3.1 GeV/c^2. For each arm the yield is independent of z within 10%–20%. Pairs in the north arm are reconstructed with about 2/3 of the efficiency compared to the south arm, which is mostly due to a larger dead area in the north MuTr, but otherwise the spectra are similar for mirrored z ranges. The like-sign spectra have the lowest yield for the z range closest to the absorber, negative and positive z for south and north arm, respectively. The $\mu^\pm\mu^\pm$ yield increases by roughly a factor of three as the collision point moves away

Table 3: Track quality cuts used in this analysis.

	south	north
Penetrate MuID last gap		
MuTr χ^2	< 15	< 20
Number of hits in MuTr	> 10	> 10
MuID χ^2	< 5	< 5
Number of hits in MuID	> 5	> 5
DG0(p)	$< 3\sigma$	$< 3\sigma$
DDG0(p)	$< 3\sigma$	$< 3\sigma$

Table 4: Pair cuts used in this analysis.

χ^2_{vtx}	< 5
$\lvert p_1 - p_2\rvert / \lvert p_1 + p_2\rvert$	< 0.55
Muon pair do not share the same MuTr octant	
Δx, Δy at MuID gap 0	> 20 cm

from the absorber and more pions and kaons decay in flight before reaching the absorber.

3.4 Modelling of Expected Pair Sources

3.4.1 Physical $\mu\mu$ pair sources

3.4.1.1 Hadron Decays to $\mu\mu$ pairs ($h \rightarrow \mu\mu(X)$) Decays from η, η', ω, ρ, and ϕ dominate the $\mu^+\mu^-$ pair yield below a mass of 1 GeV/c^2, while decays from J/ψ, ψ', and $\Upsilon(1S+2S+3S)$ dominate the $\mu^+\mu^-$ pair yield in narrow mass regions at higher masses. Existing data is used to constrain the input distributions for these mesons whenever possible.

The ρ, ω, ϕ, and J/ψ are generated based on the measured differential cross sections [41, 40] that are displayed in Fig. 50(c). The Gounaris/Sakurai parameterization is used to describe the line shape of the ρ meson mass distribution [124]. The ρ production cross section is fixed to the ω production cross section with $\sigma_\rho/\sigma_\omega = 1.21 \pm 0.13$, which is consistent with the value found in jet fragmentation [1]. For the η and η', there is no measurement at forward rapidity. We constrain the η and η' using measurements at midrapidity [37, 36, 38], which is shown in Fig. 50(a), and use PYTHIA v6.428 [67] to extrapolate to forward rapidity.

The p_T spectra of ψ' and Υ are generated using PYTHIA and normalized using the measurements of ψ' to J/ψ ratio [125] and $B_{\mu\mu}dN_{\Upsilon}/dy$ [126], respectively. All mesons are decayed using PYTHIA.

3.4.1.2 Open Heavy flavor The $\mu\mu$ pairs that originate from semileptonic decays of heavy flavor hadrons, referred to as *heavy flavor pairs* in this dissertation, are simulated using two event generators, PYTHIA and POWHEG.

We use PYTHIA version v6.428 [67]. The input parameters for PYTHIA are shown in Table 9 in Appendix B. In contrast to using the forced $c\bar{c}$ and $b\bar{b}$ production modes (MSEL4 or 5), which include only the lowest order process of flavor creation ($gg \rightarrow Q\bar{Q}$), we used the mode (MSEL1) which also simulates higher-order processes of flavor excitation ($gQ \rightarrow gQ$) and gluon splitting ($gg \rightarrow Q\bar{Q}g$). Figure 51 shows the Feynman diagrams for heavy flavor production. Leading order matrix elements are used for the initial hard scattering process, and next-to-leading order corrections are implemented with a parton-shower approach. A classification of the three classes of processes can be achieved by assessing the event record which contains the full ancestry of any given particle; a detailed account of the characterization of these three classes can be found in Ref. [12].

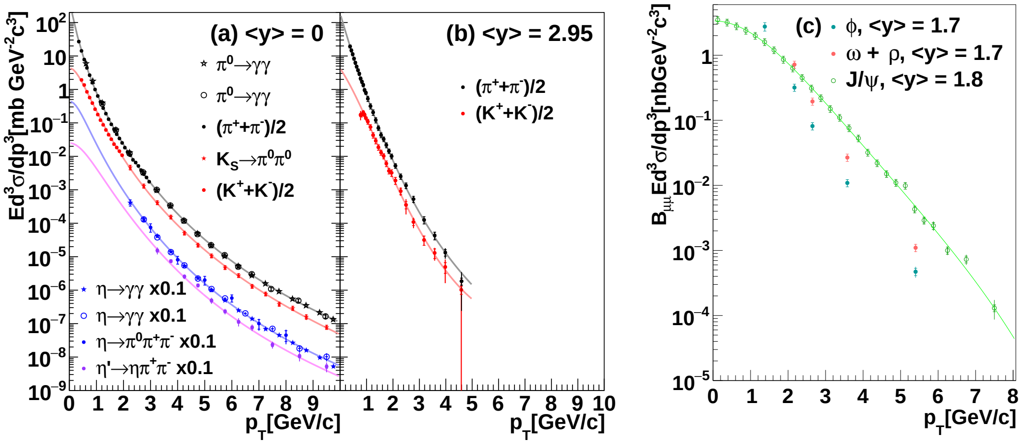

Figure 50: Compilation of meson production in p+p collisions at $\sqrt{s} = 200$ GeV at (a) $\langle y \rangle = 0$, (b) $\langle y \rangle = 2.95$ and (c) $\langle y \rangle = 1.6 - 1.7$. The data at $\langle y \rangle = 0$ is taken from PHENIX: $\pi^0 \to \gamma\gamma$ [33](black star),[34](black open circle), $(\pi^+{+}\pi^-)/2$ [35], $K_S \to \pi^0\pi^0$ [36], $(K^+{+}K^-)/2$ [35], $\eta \to \gamma\gamma$ [37](blue star),[38](blue open circle), $\eta \to \pi^0\pi^+\pi^-$ [37], $\eta' \to \eta\pi^+\pi^-$ [36]. The data at $\langle y \rangle = 2.95$ is taken from BRAHMS: $(\pi^+ + \pi^-)/2$ [39], $(K^+ + K^-)/2$ [39]. The data at $\langle y \rangle = 1.7 - 1.8$ is taken from PHENIX: $\phi \to \mu\mu$ [40], $\omega + \rho \to \mu\mu$ [40], $J/\psi \to \mu\mu$ [41]. The curves are fits to data.

We also use POWHEG version v1.0 [68] interfaced with PYTHIA v8.100 [127] to generate heavy flavor pairs. We use the default setting for both $c\bar{c}$ and $b\bar{b}$ production, including the choices for normalization and factorization scales and heavy quark masses. CTEQ6M is used for parton distribution functions of the proton. In contrast to PYTHIA, NLO corrections are implemented by using next-to-leading order matrix elements in the hard scattering calculation directly. The classification of processes in PYTHIA is therefore not applicable for POWHEG; there is no trivial connection between the classes of processes in the PYTHIA formalism and the POWHEG formalism.

A single muon is said to fall within the *ideal muon arm acceptance* if the following two requirements are met: (i) the muon has a momentum $p > 3$ GeV/c, and (ii) the muon falls into the pseudorapidity range $1.2 < |\eta| < 2.2$. The simulated mass spectra of pairs in the ideal muon arm acceptance for pairs from $c\bar{c}$ and $b\bar{b}$ are shown in Fig. 52. Like-sign pairs from $c\bar{c}$ are found to be negligible compared to like-sign pairs from $b\bar{b}$ in the entire kinematic region and are hence neglected for this analysis.

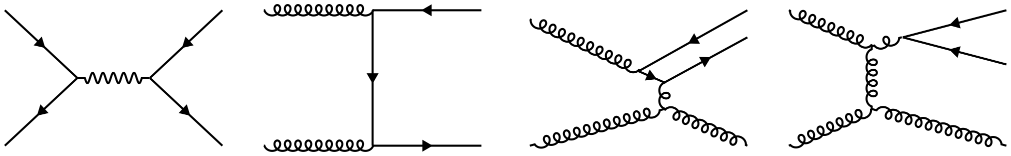

(a) s-channel Flavor Creation

(b) t-channel Flavor Creation

(c) Flavor Excitation

(d) Gluon Splitting

Figure 51: Feynman diagrams corresponding to flavor creation (a,b), flavor excitation (c) and gluon splitting (d) [12, 13].

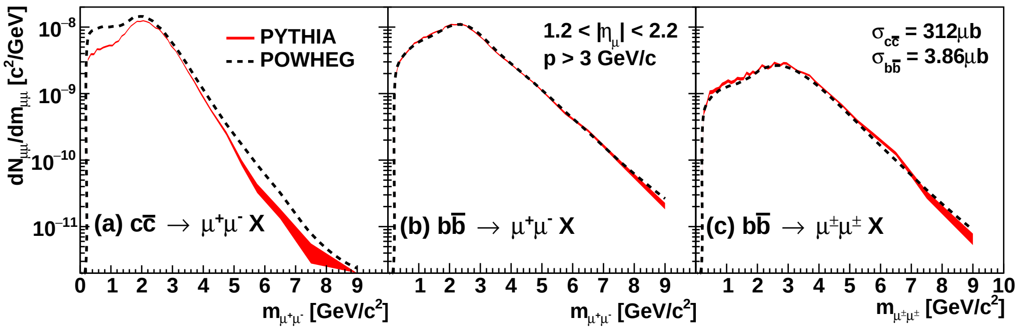

Figure 52: Comparison of $\mu\mu$ yield in the ideal muon arm acceptance determined using PYTHIA (red solid) and POWHEG (black dotted). Both are normalized using cross sections($\sigma_{cc} = 312\mu b$, $\sigma_{bb} = 3.86\mu b$), obtained from [21]. The width of the band for the PYTHIA calculation represents the statistical uncertainty in the calculation.

The generated $\mu^+\mu^-$ and $\mu^\pm\mu^\pm$ pair spectra from $b\bar{b}$ are very similar for PYTHIA and POWHEG; this is consistent with the findings in Refs. [128, 21]. Due to the large b-quark mass the muon pair spectra are dominated by decay kinematics rather than the correlation between the b and $\bar{b}$ quarks. In contrast, there is a significant model dependence for $\mu^+\mu^-$ pairs from $c\bar{c}$, indicating a much larger sensitivity of the muon pair spectra to the correlation between the c and $\bar{c}$ quarks. Similar to ee pairs [23], this model dependence is most pronounced at low masses. This is due to differences in the description of the correlations between the c and $\bar{c}$ quarks; the azimuthal opening angle distributions in POWHEG are flatter and lead to higher lepton pair yields at low masses. A smaller but non-negligible discrepancy at higher masses is also observed. Since high mass pairs are dominated by back-to-back pairs from leading order processes, this difference is likely due to a harder p_T spectrum predicted by POWHEG compared to PYTHIA.

3.4.1.3 Drell-Yan We use PYTHIA v6.428 to simulate $\mu\mu$ pairs from the Drell-Yan mechanism, referred to *Drell-Yan pairs* in this dissertation. The input parameters are shown in Table 10 in Appendix B. The primordial k_T is generated from a Gaussian distribution with a width of 1.1 GeV/c. The width is determined by investigating the p_T distribution of unlike-sign pairs in the mass region 4.8 – 8.6 GeV/c^2 where the yield is expected to be dominated by Drell-Yan [129]. The procedure and its associated uncertainties will be explained in detail in Sec. 3.10.1.4.

3.4.2 Unphysical $\mu\mu$ pair sources

Unphysical pair background is customarily divided into combinatorial and correlated pairs. Here the idea is that for combinatorial pairs, the two tracks have no common origin and thus are uncorrelated. In contrast, for correlated pairs, the tracks do have a common origin, for example they both stem from the decay chain of a heavy hadron or they were part of the fragmentation products of a jet.

However, in p+p collisions, or generally in low multiplicity events, the distinction between combinatorial and correlated pairs is not well defined. A p+p collision typically produces hard scattered partons accompanied by an underlying event, which consists of initial and final state radiation, beam-beam remnants and multiple parton interactions. The complex event structure in a single p+p event prohibits a clear identification of whether two particles stem from a common origin or not, even in principle. More generally, all particles are produced from the two colliding protons, and thus are correlated through momentum and charge conservation laws. Therefore, the separation between combinatorial and correlated pairs is more procedural and is defined by how the relative contributions of correlated and combinatorial pairs are determined. We use an approach that maximizes the number of pairs considered combinatorial, which will be discussed in detail in Sec. 3.6.1.2.

The individual contributions of the unphysical pair background are determined using Monte-Carlo event generators. We treat pairs that are made from two hadronic tracks (*hadron-hadron pairs*: N_{hh}) and those with one hadronic track and the other being a muon from the decay of a D, B, or J/ψ meson (*muon-hadron pairs*: N_{Dh}, N_{Bh} and N_{Jh}) separately.

3.4.2.1 Hadron-hadron pairs: N_{hh} The N_{hh} pairs are simulated with PYTHIA, using Tune A parameters listed in Table 9. This setup reproduces jet-like hadron-hadron correlations at midrapidity in p+p collisions at $\sqrt{s}$ = 200 GeV [130] reasonably well. To also reproduce the hadron p_T spectra we use momentum dependent weighting to match the PYTHIA hadron p_T distributions to data. Currently, there are no data for p_T spectra of charged pions and kaons from p+p collisions at $\sqrt{s}$ =200 GeV in the rapidity region covered by the muon arms. Thus, we interpolate between p_T spectra measured at midrapidity [34, 33, 35, 36] and very forward rapidity ($\langle y \rangle$ = 2.95) [39]. The data are shown in Fig. 50. Weighting factors are calulated for both rapidity ranges as a function of p_T, by simply taking the ratio between data and PYTHIA,

$$w_h(y=0,p_T) = \frac{E\frac{d^3\sigma}{dp^3}|_{y=0,DATA}}{E\frac{d^3\sigma}{dp^3}|_{y=0,PYTHIA}}, \tag{10}$$

$$w_h(y=2.95,p_T) = \frac{E\frac{d^3\sigma}{dp^3}|_{y=2.95,DATA}}{E\frac{d^3\sigma}{dp^3}|_{y=2.95,PYTHIA}}, \tag{11}$$

where h stands for pion or kaon. For a given p_T, we linearly interpolate the weighting factors as a function of y:

$$\begin{aligned} w_h(y,p_T) =& \frac{y}{2.95} \times [w_h(y=2.95,p_T) - w_h(y=0,p_T)] \\ &+ w_h(y=0,p_T). \end{aligned} \tag{12}$$

The weighting factors for different values of y are shown in Fig. 53. Above p_T = 5 GeV/c, where there are no data at forward rapidity, the weights are assumed to be constant. The systematic uncertainties arising in this weighting procedure are discussed in Sec. 3.10. These weighting factors are applied to each input particle generated with the PYTHIA simulation according to the particle's y and p_T.

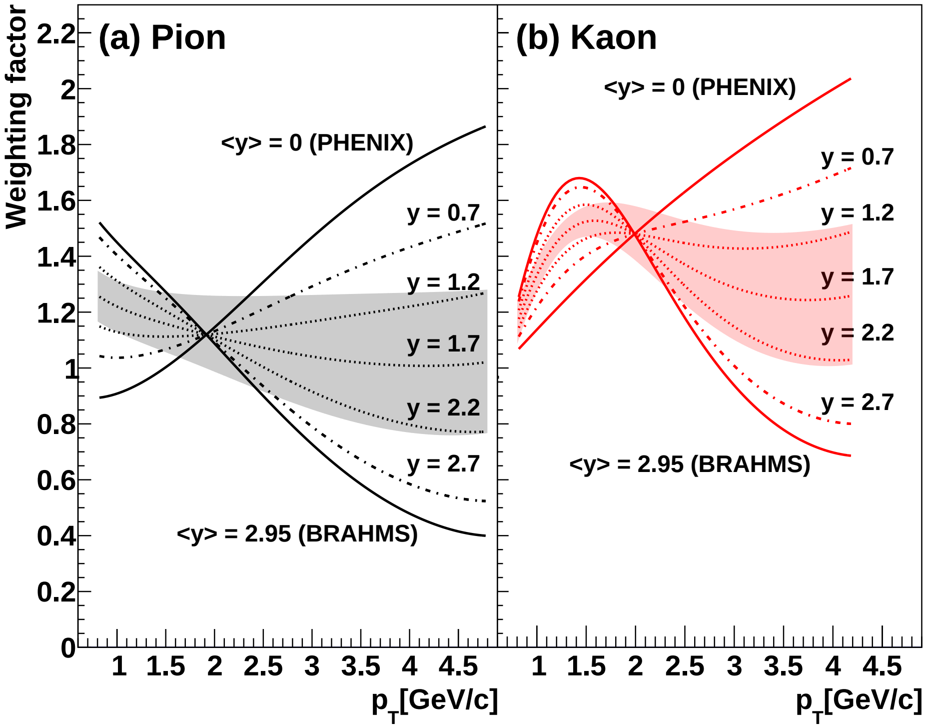

Figure 53: Weighting factors for (a) pions and (b) kaons in different rapidity slices. The shaded bands indicate uncertainty brackets used for the investigation of systematic uncertainties.

3.4.2.2 Muon-hadron pairs: N_{Dh}, N_{Bh}, and N_{Jh} Muon-hadron pairs N_{Dh} and N_{Bh} involving semi-leptonic decays of charm and bottom as defined above are constructed using the same PYTHIA and POWHEG simulations that determine the open heavy flavor pair input. The pion and kaon p_T spectra are tuned the same way as discussed in the above section. For the muon-hadron pairs involving decays of the J/ψ (N_{Jh}) we also match the PYTHIA J/ψ momentum spectrum at forward rapidity to reproduce the measured J/ψ-hadron yield per minimum bias event [41] (see Fig. 50).

3.4.2.3 Combinatorial pair background The combinatorial pair background is constructed via an event mixing technique, which combines tracks from different events of similar z vertex position. This is done separately for data and the events used to simulate hadron-hadron pairs, and muon-hadron pairs.

To optimize the description of the pair background, we maximize the contribution identified as combinatorial pair background, subtract the combinatorial component from the simulation of hadron-hadron pairs and muon-hadron pairs, and substitute the combinatorial pair background with the one determined from data. The details of the normalization of the individual components are discussed in Sec. 3.6.1.2.2.

3.5 Simulation Framework

In order to directly compare the expected sources to the data, the $\mu\mu$ pairs from the expected sources are propagated through a Monte-Carlo simulation of the PHENIX detector. This simulation is designed to emulate in detail the detector response, and the recording and analysis of data taken with the PHENIX experiment. Histograms of the expected number of $\mu\mu$ pairs are constructed in mass-p_T bins, which serve as templates for the subsequent fitting procedure.

The $\mu\mu$ pairs from all physical sources are propagated through the default PHENIX simulation framework. The same approach is impractical for unphysical pair background from π and K decays. Due to the large ($\sim$1/1000) rejection power for these backgrounds arising mainly from the hadron absorbers, an undesirably large amount of simulations would be necessary to reach sufficient statistical accuracy. Therefore, we use a fast Monte-Carlo (FastMC), developed specifically for this analysis. For a detailed descriptions of the two simulation chains, see Appendix A.

3.6 Charm, Bottom and Drell-Yan Cross-Sections Extraction

In the previous two sections we have discussed the different expected sources of $\mu\mu$ pairs and how template distribution of $\mu\mu$ pairs are generated for each. In this section we compare the templates for the expected sources to the experimental data and determine the absolute contribution of each source.

After an initial normalization is chosen for each template, the key sources, $c\bar{c}$, $b\bar{b}$, Drell-Yan, and the hadronic pair background, are normalized in an iterative template fitting procedure.

3.6.1 Initial normalization and data-driven tuning of cocktail

3.6.1.1 Physical $\mu\mu$ pair sources The normalization of muon pairs from hadron decays $h \rightarrow \mu\mu(X)$ is fixed because the cross sections of the parent hadrons are set by experimental data as discussed in Sec. 3.4.1.1. In contrast, the distributions for muon pairs from $c\bar{c}$, $b\bar{b}$, and Drell-Yan are not normalized using previous experimental data; not only because there is no existing data but because these are the measurements that we want to obtain from the data. We refer the normalization parameters for $c\bar{c}$, $b\bar{b}$ and Drell-Yan as $\kappa_{c\bar{c}}$, $\kappa_{b\bar{b}}$, and κ_{DY} respectively. These parameters will be determined via the iterative fitting procedure presented in this section. The initial values of $\kappa_{c\bar{c}}$, $\kappa_{b\bar{b}}$, and κ_{DY} are set based on measured data [21].

3.6.1.2 Correlated hadrons and combinatorial pair background The composition and normalization of the unphysical pair background sources is key to understanding the $\mu\mu$ continuum and requires a more detailed discussion. In p+p collisions at $\sqrt{s} = 200$ GeV, since the multiplicity of produced particles is low, there is no definite method to differentiate between a correlated pair and a combinatorial pair. That being said, the procedure used to define combinatorial pairs and how their contribution is normalized should not affect the extraction of physical quantities.

One straightforward method to circumvent the distinction of correlated and combinatorial pairs is to generate hadron-hadron and muon-hadron pairs using a Monte-Carlo event generator such as PYTHIA interfaced to the FastMC framework; and then fit the generated distributions to the data, or even more simply, directly subtract the generate distributions from the data. Templates from a full event normalization include all background pair sources, hence the distinction between them is not necessary. However, this method of extracting physical cross sections is sensitive to how accurate PYTHIA describes the underlying event and how well GEANT4 treats hadronic interactions in the absorber. This may increase the systematic uncertainties on the extraction of the $c\bar{c}$, $b\bar{b}$, and Drell-Yan components.

In this analysis, we use a data-driven hybrid approach, in which

- the maximum possible number of combinatorial pairs is determined from the generated PYTHIA and/or POWHEG events,
- the correlated hadronic pairs are calculated by subtracting the combinatorial pairs determined by mixing generated events,

- the combinatorial pairs are replaced by the combinatorial pairs determined from data.

Although the distinction between correlated hadronic pairs and combinatorial pairs depends on the choice of the normalization procedure, using different procedures has a small effect on the extraction of physical cross sections, and in any case, this small effect is being assigned as a systematic uncertainty. The separation of these two components is mostly important for the evaluation of systematic uncertainties, because the correlated hadronic pairs depend on simulations and the combinatorial pairs do not. Replacing the combinatorial pairs from the generator with mixed pairs from data should be regarded as a correction to the simulations to reduce systematic uncertainties.

3.6.1.2.1 Normalizing hadron-hadron and muon-hadron pairs

The templates for hadron-hadron pairs $N_{hh}(m, p_T, z)$ are generated using PYTHIA simulations interfaced to the FastMC, as discussed above. Templates are determined separately for the three different z regions (z'_i) available in the FastMC simulations, $z'_0 = (-22.5, -17.5\text{ cm})$, $z'_1 = (-2.5, +2.5\text{ cm})$ and $z'_2 = (+17.5, +22.5\text{ cm})$, respectively. Only pions (π^+, π^-), kaons (K^+, K^-, K^0), and their decay products are considered. The momentum spectra are tuned to accurately describe experimental data where available (see Sec. 3.4.2.1). Therefore, N_{hh} contains the correct mix of individual hadron-hadron pair sources per event. N_{hh} is initially normalized as a per event yield for generated minimum bias p+p collisions.

Similarly, muon-hadron pair templates from $c\bar{c}$ and $b\bar{b}$ are constructed using PYTHIA and POWHEG generators interfaced to the FastMC. The templates $N_{Dh}(m, p_T, z)$ and $N_{Bh}(m, p_T, z)$ correspond to muon-hadron pairs from $c\bar{c}$ and $b\bar{b}$, respectively. Each is normalized per $c\bar{c}$ or $b\bar{b}$ event. Thus, after scaling by the normalization factors $\kappa_{c\bar{c}}$ and $\kappa_{b\bar{b}}$, used for the $\mu\mu$ pairs, $\kappa_{c\bar{c}}N_{Dh}$ and $\kappa_{b\bar{b}}N_{Bh}$ are the expected muon-hadron pair yields per minimum bias p+p event, and can be directly added to N_{hh}.

For J/ψ, the differential cross section at forward rapidity has been measured [41]. Analogous to the pion and kaon simulations, we weight the simulated J/ψ momentum distribution to match the J/ψ yield at forward rapidity. Because the simulated J/ψ yield is normalized to the measured yield, the muon-hadron pair template $N_{Jh}(m, p_T, z)$ represents a yield per minimum bias p+p event.

Thus, the full per MB p+p event hadronic pair background can be written as:

$$N_{hbg} = \kappa_{c\bar{c}} N_{Dh} + \kappa_{b\bar{b}} N_{Bh} + N_{hh} + N_{Jh}, \tag{13}$$

where the templates are functions of m, p_T, and z. Figure 54(a) shows N_{hbg} and its individual contributions integrated over z and p_T as a function of mass.

3.6.1.2.2 Choice and normalization of the combinatorial pair background To minimize the model dependence in N_{hbg} used in the analysis, we determine the combinatorial contribution to N_{hbg} from mixed generated events and replace it with the combinatorial pairs determined from the data. For each simulation we determine the combinatorial pairs by mixing either hadron-hadron pairs or muon-hadron pairs from different events at the same z'_i. For a given z'_i bin the combinatorial pairs are then constructed as:

$$N_{\text{comb,sim}} = \kappa_{c\bar{c}} N^{\text{mix}}_{Dh} + \kappa_{b\bar{b}} N^{\text{mix}}_{Bh} + N^{\text{mix}}_{hh} + N^{\text{mix}}_{Jh}, \tag{14}$$

which observes the same relative normalization of the individual components as in Eq. 13. The contributions of each component to the hadronic and the combinatorial pair background, normalized following the above procedure are shown in Fig. 54(b).

The normalization of the combinatorial pairs is determined statistically using the ZYAM (Zero Yield At Minimum) technique [131] as described below. We use the difference in the azimuthal angle $\Delta\phi_{prim}$ of the like-sign hadronic pairs with masses less than 3 GeV/c^2, where $\Delta\phi_{prim}$ is the difference of the azimuthal angles of the input particles (π, K, D, or B). The $\Delta\phi_{prim}$ distribution is shown in Fig. 55.

First, we remove muon-hadron pairs in which both tracks originated from heavy flavor ($c\bar{c}$ or $b\bar{b}$) pairs, because these pairs can uniquely be identified as correlated. This can be achieved by tracing particle ancestry in the event record. For the remaining pairs we assume that correlations result mostly from jet fragmentation. Thus, they should have a minimal contribution for $\Delta\phi_{prim} \sim \pi/2$. Our ZYAM assumption is that the correlated yield vanishes at $\Delta\phi_{prim} = \pi/2$. The excess yield for $\Delta\phi_{prim} < \pi/2$ can be interpreted as pairs from the same jet, whereas the excess yield for $\Delta\phi_{prim} > \pi/2$ correspond to

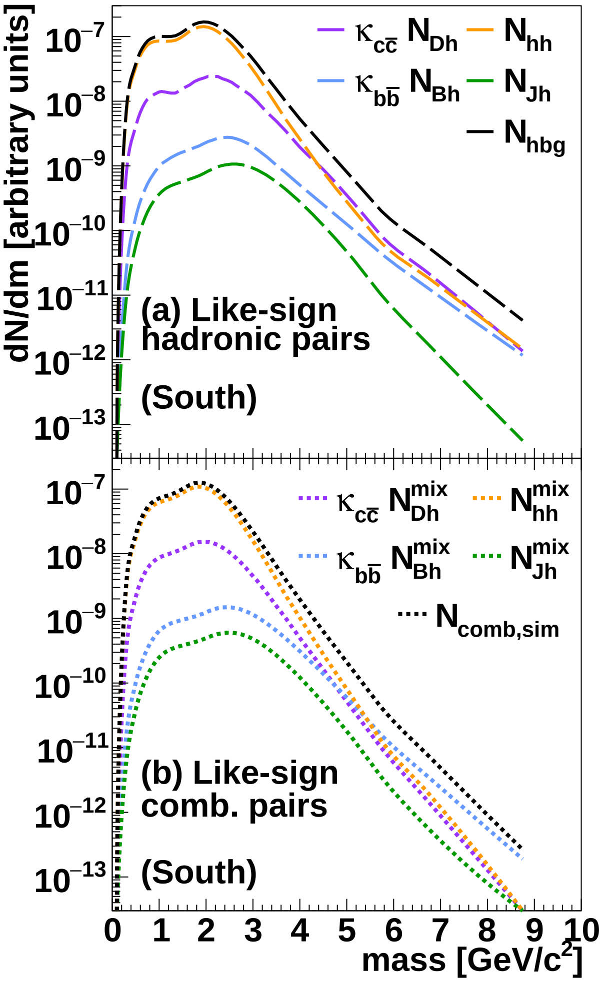

Figure 54: (a) full simulation for hadronic pairs and (b) combinatorial pairs for mass spectra of hadron-hadron and muon-hadron pairs from charm, bottom and J/ψ after initial normalization and tuning.

$\mu\mu$ pairs from back-to-back jets. The correlated $N_{\text{corr,sim}}$ and combinatorial $N_{\text{comb,sim}}$ contributions are now separated via the relations:

$$N_{\text{corr,sim}} = N_{hbg} - N_{\text{comb,sim}}. \tag{15}$$

The separation of N_{hbg} into correlated and uncorrelated components is

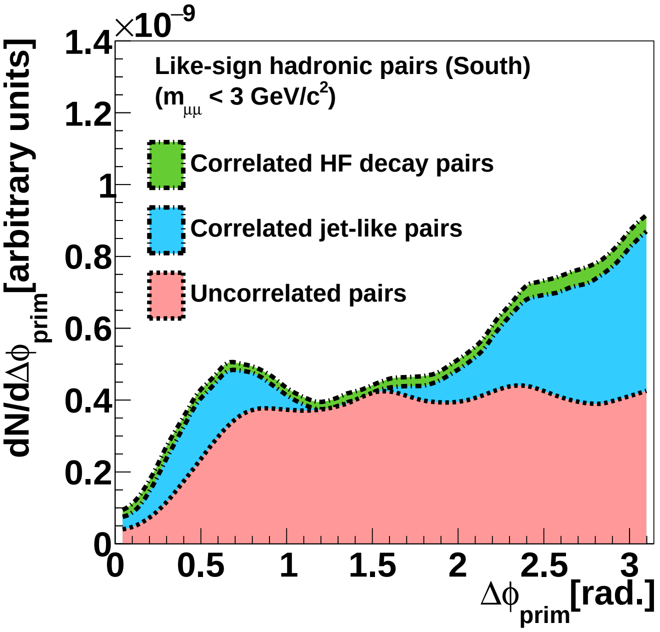

Figure 55: ZYAM normalization procedure for the south muon arm. The normalization of the uncorrelated pairs from event mixing (red) is determined by enforcing the requirement that the yield of the uncorrelated pairs to be identical to the yield of foreground pairs. The pairs from heavy flavor decay chains (green) are excluded at $\Delta\phi_{prim} \sim \pi/2$. The excess yield is from away-side and near-side jet-like correlations (blue). The periodicity of the distributions arises from the octant structure of the MuTr.

done separately for each of the three vertex region z'_i used in the FastMC simulations. In the data, mixed events are also constructed in 5 cm z-bins, but over the full range from -30 cm to 30 cm. The template distributions are aggregated for three broad vertex ranges, $z_0 = (-30, -10 \text{ cm})$, $z_1 = (-10, +10 \text{ cm})$ and $z_2 = (+10, +30 \text{ cm})$. The normalization of the mixed events from the data is matched to those from the simulation by scaling $N_{hbg}(z'_i)$ such that the number of combinatorial pairs of data and simulations are equal to each other in the normalization mass region $\mathcal{M}$ ($m < 3\text{GeV}/c^2$) for each z bin, i.e., we impose the following requirement:

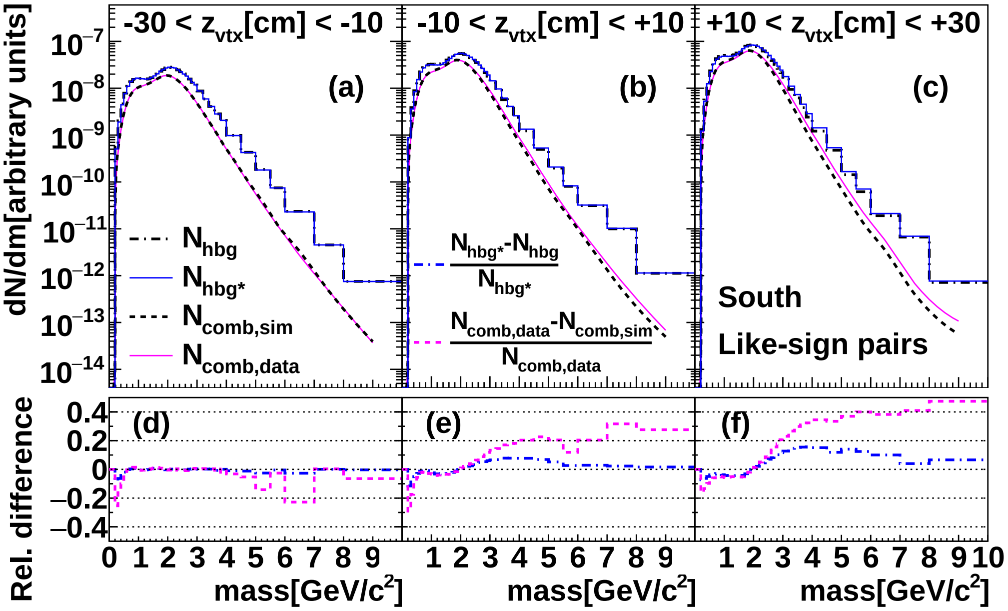

Figure 56: Like-sign mass spectra of the hadronic pair background, before and after correction by replacing with combinatorial pairs from data, and combinatorial background from simulations and data, in different z_{vtx} regions. Panels (d,e,f) show the relative difference between different mass spectra.

$$\int_{\mathcal{M}} N_{\text{comb,sim}}(z_i') = \int_{\mathcal{M}} N_{\text{comb,data}}(z_i) \tag{16}$$

This rescaling is necessary because we are approximating a Δz_i range of 20 cm from data with a $\Delta z_i'$ range of 5 cm from simulations. For the two z bins further away from the absorber, this approximation holds well even without rescaling. This is because the multiplicity falls approximately linearly with the distance from the absorber, and the center of the bin times the bin width is to first order a good approximation of the integral of the bin. However, for the z bin closest to the absorber, this linear relation no longer holds and a scaling factor of 1.2 is applied to $N_{\text{comb,sim}}$, according to Eq. 16.

We then replace the combinatorial background from simulations by data for each vertex region z_i:

$$N_{hbg*}(z_i) = N_{\text{corr,sim}}(z_i') + N_{\text{comb,data}}(z_i). \tag{17}$$

The hadronic pair background in each vertex slice for the south arm, both before and after the above replacement of the combinatorial pair background, is shown in Fig. 56. The relative mass-dependent difference between the two estimates of the hadronic pair background ranges from $\sim 0\%$ for the z_{vtx} region closest to the absorber to a maximum of $\sim 20\%$ at $m \sim 4$ GeV/c^2 for the z_{vtx} region furthest away from the absorber.

The same normalization is applied to unlike-sign hadronic pairs. Both the unlike- and like-sign hadronic pairs are scaled with a common normalization factor κ_h that will be determined in the fitting procedure. Finally, we define the correlated hadronic pairs, N_{cor} and combinatorial pairs, N_{comb} via the relations:

$$\begin{aligned} N_{\text{cor}} &= N_{\text{corr,sim}}, \\ N_{\text{comb}} &= N_{\text{comb,data}}. \end{aligned} \tag{18}$$

The distinction between correlated and combinatorial hadronic pairs depends on the details of the normalization procedure. Different normalization procedures can lead to differences in the relative contributions of correlated and combinatorial components. However, the effect on the extraction of physical cross sections is small, and the variations are included in the systematic uncertainties (see Sec. 3.10.1.5).

3.7 Iterative fit

3.7.0.3 Fit strategy The absolute contribution of $c\bar{c}$, $b\bar{b}$, Drell-Yan, and the hadronic pairs to the $\mu^+\mu^-$ and $\mu^\pm\mu^\pm$ spectra is determined by a fitting procedure using template distributions for each contribution. There are four fit parameters, $\kappa_{c\bar{c}}$, $\kappa_{b\bar{b}}$, κ_{DY}, and κ_h, which are normalization factors for the contributions from $c\bar{c}$, $b\bar{b}$, Drell-Yan, and the hadronic pairs.

We adopt the following iterative fitting strategy (tilded parameters correspond to fit values obtained in the previous step):

(i) With a fixed $\tilde{\kappa}_{c\bar{c}}$, fit the like-sign spectrum with $\kappa_{b\bar{b}}$ and κ_h as free parameters in mass-p_T-z_{vtx} slices in the mass range 1–10 GeV/c^2.

(ii) With the same $\tilde{\kappa}_{c\bar{c}}$ as in step (i) and $\tilde{\kappa}_{b\bar{b}}$ and $\tilde{\kappa}_h$ obtained in (i), fit mass and p_T slices in the unlike-sign mass region 4.4–8.5 GeV/c^2 with κ_{DY} as a free parameter.

(iii) With $\tilde{\kappa}_{b\bar{b}}$ and $\tilde{\kappa}_h$ obtained in (i) and $\tilde{\kappa}_{\mathrm{DY}}$ in (ii), fit mass and p_T slices in the unlike-sign mass region 1.4–2.5 GeV/c^2 with $p_T < 2$ GeV/c, with $\kappa_{c\bar{c}}$ as a free parameter.

(iv) Iterate with $\tilde{\kappa}_{c\bar{c}}$ from (iii).

This method of fitting exploits the fact that the like-sign pairs contain mainly contributions from hadrons and $b\bar{b}$; charm only contributes via muon-hadron pairs and is non-dominant while Drell-Yan does not contribute. Thus, the fit results in step (i) insensitive to the initial starting value of $\tilde{\kappa}_{c\bar{c}}$, provided that is value is sensible. We observe that the contribution of hadronic pairs to the $\mu^+\mu^-$ and $\mu^\pm\mu^\pm$ pairs increases as the distance between the event vertex z_{vtx} and the absorber becomes larger, due to the enhanced probability of pions and kaons to decay before they hit the absorber. In contrast, the yield of $\mu\mu$ pairs from $b\bar{b}$ is independent of z_{vtx}. To optimize the separating power between $\mu\mu$ pairs from $b\bar{b}$ and the hadronic pairs, in step (i) we fit like-sign pairs in mass-p_T-z_{vtx} slices. Step (i) gives strong constraints to $\kappa_{b\bar{b}}$ and κ_h which are to first order free from systematic uncertainties coming from $c\bar{c}$ and Drell-Yan components. With $\kappa_{b\bar{b}}$ and κ_h constrained, we move on to step (ii), where we fit using the unlike-sign pairs with mass 4.4–8.5 GeV/c^2. This mass region is chosen to avoid contributions from quarkonia decays. In this mass region, Drell-Yan and $b\bar{b}$ contributions are expected to dominate while contributions from $c\bar{c}$ and hadrons are subdominant. Although Drell-Yan also contributes to lower masses, the sensitivity of the low mass yields to the intrinsic k_T make it unfavorable to constrain κ_{DY} in the low mass region. With $\kappa_{b\bar{b}}$, κ_h and κ_{DY} constrained, we fit in the mass region 1.4–2.5 GeV/c^2 to constrain $\kappa_{c\bar{c}}$. This mass region is chosen to avoid contributions of decays from quarkonia and low mass mesons. In this step, we exclude the region with $p_T > 2$ GeV/c from the $\mu^+\mu^-$ spectra from the fit, to avoid the uncertainty of the shape of Drell-Yan contribution in this region due to its sensitivity to k_T. We then repeat this fitting procedure starting with the fitted $\kappa_{c\bar{c}}$ value obtained from step (iii), and iterate until stable fit results for all four parameters are obtained. Although the fit results in step (i) is not sensitive to the initial starting value of $\tilde{\kappa}_{c\bar{c}}$, this iterative procedure is still important to ensure consistency and robustness of the fit results.

3.7.0.4 Fit function We use the log-likelihood method which is applicable to bins having few or zero entries. For fitting the $\mu^{\pm}\mu^{\pm}$ spectra in step (i), we first divide the data and simulations into mass, p_T and $z_{\rm vtx}$ bins. The parameters $\kappa_{b\bar{b}}$ and κ_h are then varied to minimize the negative log-likelihood defined by:

$$\begin{aligned} ln\mathcal{L}(\kappa_{b\bar{b}}, \kappa_h) &= \sum_i y_i ln C(i; \kappa_{b\bar{b}}, \kappa_h) - \sum_i C(i; \kappa_{b\bar{b}}, \kappa_h), \\ C(i; \kappa_{b\bar{b}}, \kappa_h) &= \kappa_{b\bar{b}} N_{b\bar{b}}(i) + \kappa_h N_{hbg*}(i; \tilde{\kappa}_{c\bar{c}}, \kappa_{b\bar{b}}), \end{aligned} \tag{19}$$

where y_i is the number of counts in the $i^{\rm th}$ mass-p_T-$z_{\rm vtx}$ bin and $C(i; \kappa_{b\bar{b}}, \kappa_h)$ is the number of expected counts in the $i^{\rm th}$ mass-p_T-$z_{\rm vtx}$ bin from all cocktail components. $N_{b\bar{b}}(i)$ is the number of $\mu\mu$ pairs from $b\bar{b}$ in the i^{th} bin per generated $b\bar{b}$ event, $N_{hbg*}(i; \tilde{\kappa}_{c\bar{c}}, \kappa_{b\bar{b}})$ is the sum of the combinatorial and correlated hadronic pairs per minimum bias event, with fixed $\tilde{\kappa}_{c\bar{c}}$.

Similarly the log-likelihood function for step (ii) is defined as:

$$\begin{aligned} ln\mathcal{L}(\kappa_{\rm DY}) &= \sum_i y_i ln C(i; \kappa_{\rm DY}) - \sum_i C(i; \kappa_{\rm DY}), \\ C(i; \kappa_{\rm DY}) &= \kappa_{\rm DY} N_{\rm DY}(i) + \tilde{\kappa}_{b\bar{b}} N_{b\bar{b}}(i) + \tilde{\kappa}_{c\bar{c}} N_{c\bar{c}}(i) \\ &\quad + \tilde{\kappa}_h N_{hbg*}(i; \tilde{\kappa}_{c\bar{c}}, \tilde{\kappa}_{b\bar{b}})) + N_{h\to\mu\mu(X)}(i), \end{aligned} \tag{20}$$

where y_i is the number of counts in the $i^{\rm th}$ mass-p_T bin, $C(i; \kappa_{\rm DY})$ is the number of expected counts in the $i^{\rm th}$ mass-p_T bin from all cocktail components. The definitions for $N_{b\bar{b}}(i)$ is the same as in Eq. 19, while $N_{hbg*}(i; \tilde{\kappa}_{c\bar{c}}, \tilde{\kappa}_{b\bar{b}})$ is the sum of the combinatorial and correlated hadronic pairs per minimum bias event, with fixed $\tilde{\kappa}_{c\bar{c}}$ and fixed $\tilde{\kappa}_{b\bar{b}}$. $N_{c\bar{c}}(i)$ and $N_{\rm DY}(i)$ are the number of $\mu\mu$ pairs from $c\bar{c}$ and Drell-Yan pairs in the i^{th} bin per generated $c\bar{c}$ and Drell-Yan event respectively. $N_{h\to\mu\mu(X)}(i)$ is the number of $\mu\mu$ pairs from hadron decays which is constrained from previous measurements.

Finally, the log-likelihood function for step (iii) is defined as:

$$\begin{aligned} ln\mathcal{L}(\kappa_{c\bar{c}}) &= \sum_i y_i ln C(i; \kappa_{c\bar{c}}) - \sum_i C(i; \kappa_{c\bar{c}}), \\ C(i; \kappa_{c\bar{c}}) &= \kappa_{c\bar{c}} N_{c\bar{c}}(i) + \tilde{\kappa}_{\rm DY} N_{\rm DY}(i) + \tilde{\kappa}_{b\bar{b}} N_{b\bar{b}}(i) \\ &\quad + \tilde{\kappa}_h N_{hbg*}(i; \tilde{\kappa}_{c\bar{c}}, \tilde{\kappa}_{b\bar{b}})) + N_{h\to\mu\mu(X)}(i), \end{aligned} \tag{21}$$

where y_i is the number of counts in the i^{th} mass-p_T bin, $C(i;\kappa_{c\bar{c}})$ is the number of expected counts in the i^{th} mass-p_T bin from all cocktail components. The definitions for $N_{c\bar{c}}(i)$, $N_{b\bar{b}}(i)$, $N_{\text{DY}}(i)$, $N_{hbg*}(i;\tilde{\kappa}_{c\bar{c}},\tilde{\kappa}_{b\bar{b}})$, and $N_{h\to\mu\mu(X)}(i)$ are the same as in equations (19) and (20).

3.7.0.5 Fit results The three step fitting procedure is iterated until we obtain stable values of $\kappa_{c\bar{c}}$, $\kappa_{b\bar{b}}$, κ_{DY}, and κ_h. As explained previously, because the contribution of charm to the like-sign spectrum is very small, the fit converges after two to three iterations.

In this section, example fit results using the following simulation configurations are shown: $c\bar{c}$ and $b\bar{b}$ generated using POWHEG, Drell-Yan generated using PYTHIA with intrinsic $k_T = 1.1$ GeV/c. Variations of simulation settings are considered in the evaluation of systematic uncertainties, which will be discussed in Sec. 3.10. p_T integrated mass spectra of $\mu^+\mu^-$ and $\mu^\pm\mu^\pm$ pairs are shown in Figs. 57 and 58 respectively. Figs. 59 and 60, give a more detailed view of $\mu^+\mu^-$ and $\mu^\pm\mu^\pm$ mass spectra in p_T slices.

The data distributions are well described by the cocktail simulation in both mass and p_T except for a small kinematic region at $m < 1$ GeV/c^2 which is not important for this analysis.

3.8 Signal extraction

Different cocktail components contribute with different strength to the muon pair continuum in different mass regions for $\mu^+\mu^-$ and $\mu^\pm\mu^\pm$ charge combinations. To obtain differential measurements we identify mass regions for the $c\bar{c}$, $b\bar{b}$, and Drell-Yan signal, where the ratio of the signal to all other $\mu\mu$ pairs is the most favorable for that signal. These regions are referred to in this dissertation as the *charm mass region*, the *bottom mass region*, and the *Drell-Yan mass region*, respectively. The mass regions are:

- Charm: $1.5 < m_{\mu^+\mu^-} < 2.5$ GeV/c^2
- Bottom: $3.5 < m_{\mu^\pm\mu^\pm} < 10.0$ GeV/c^2
- Drell-Yan:

$$4.8 < m_{\mu^+\mu^-} < 8.2 \text{ GeV}/c^2$$
$$\text{and } 11.2 < m_{\mu^+\mu^-} < 15.0 \text{ GeV}/c^2$$

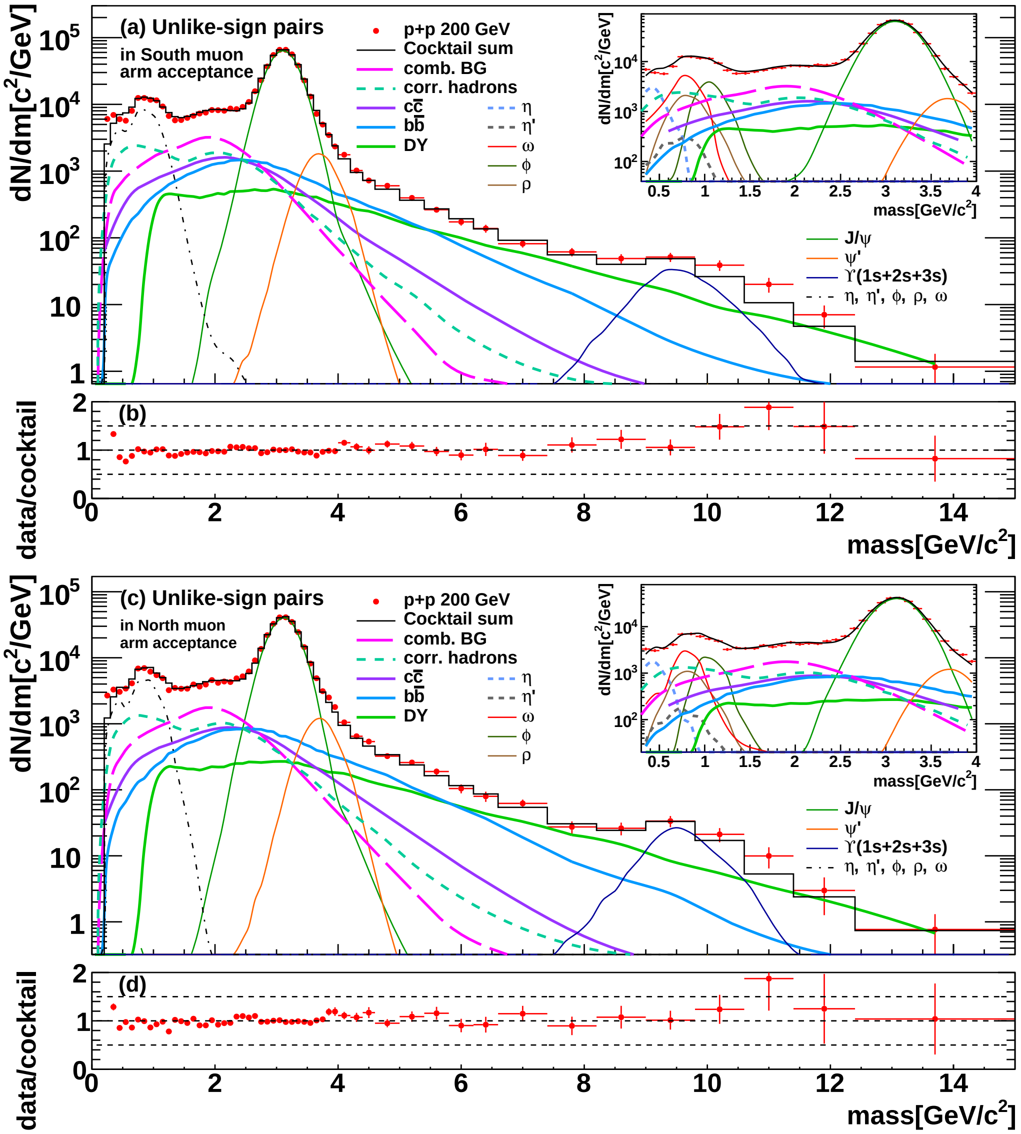

Figure 57: Inclusive $\mu^+\mu^-$ pair mass distributions from p+p collisions at $\sqrt{s} = 200$ GeV over the mass range from 0 to 15 GeV/c^2. The inset shows the mass region below 4 GeV/c^2 with more detail. Results are shown separately for the (a) south and (c) north muon arms. The data are compared to the cocktail of expected sources. Panels (b) and (d) show the ratio of the data divided by the known sources.

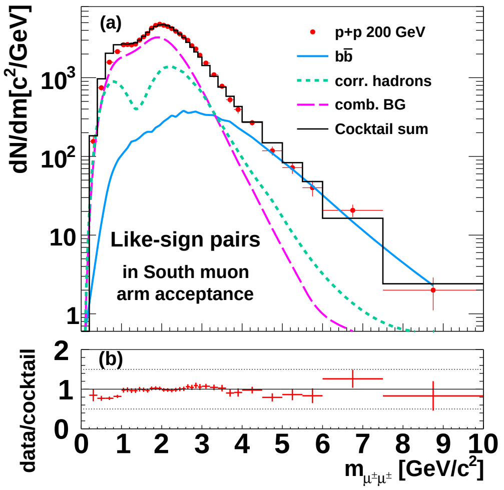

Figure 58: Inclusive like-sign $\mu\mu$ pair yield from p+p collisions as a function of mass for the (a) south and (b) north muon arms and (c) the ratio of data to expected sources.

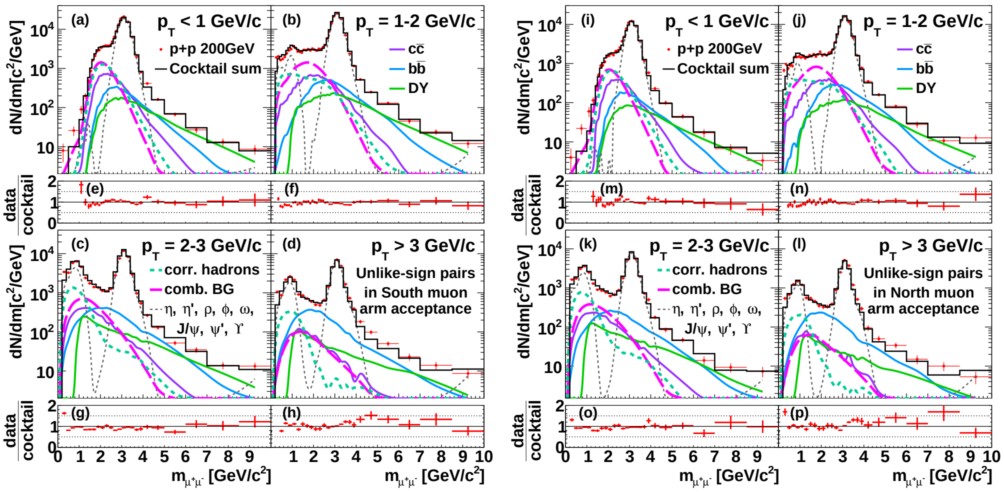

Figure 59: Inclusive unlike-sign $\mu\mu$ pair yield from p+p collisions at $\sqrt{s}$ = 200 GeV as a function of mass in different p_T slices for the (a,b,c,d) south and (i,j,k,l) north muon arms. The ratio of data to expected sources are shown in panels (e,f,g,h) for the south arm and (m,n,o,p) for the north arm.

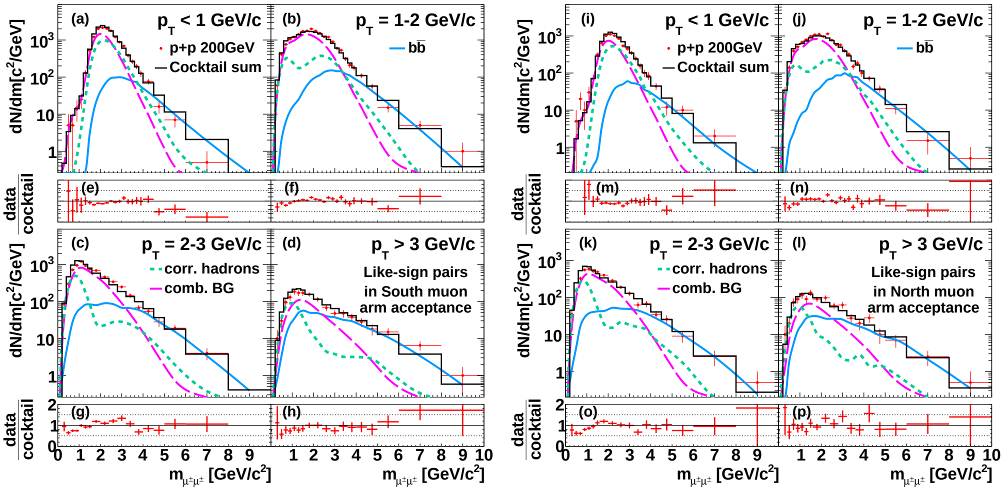

Figure 60: Inclusive like-sign $\mu\mu$ pair yield from p+p collisions at $\sqrt{s}$ = 200 GeV as a function of mass for the (a,b,c,d) south and north (i,j,k,l) muon arms. The ratio of data to expected sources are shown in panels (e,f,g,h) for the south arm and (m,n,o,p) for the north arm.

For each region we extract differential distributions by subtracting all other $\mu\mu$ pair sources.

3.8.1 Azimuthal correlations and pair p_T of $\mu^+\mu^-$ from $c\bar{c}$

Figure 61 shows the number of pairs per event as a function of their azimuthal opening angle, $\Delta\phi$, or their pair transverse momentum p_T in the charm mass region. The data are compared to all other sources that contribute in this region. For each $\Delta\phi$ or p_T bin, the number of unlike-sign pairs from charm decays ($N^{+-}_{c\bar{c}}$) is obtained as:

$$\begin{aligned} N^{+-}_{c\bar{c}} = N^{+-}_{\text{incl}} - N^{+-}_{b\bar{b}} - N^{+-}_{\text{DY}} - N^{+-}_{\rho,\phi,\omega} - N^{+-}_{J/\psi} \\ - N^{+-}_{\text{cor}} - N^{+-}_{\text{comb}}, \end{aligned} \tag{22}$$

where N^{+-}_{incl} is the number of pairs passing all single and pair cuts in Tables 3 and 4, $N^{+-}_{b\bar{b}}$ is the estimated number of pairs from bottom decays, N^{+-}_{DY} is the estimated number of pairs from Drell-Yan, $N^{+-}_{\rho,\phi,\omega}$ is the estimated number of pairs from low mass vector meson decays, $N^{+-}_{J/\psi}$ is the estimated number of

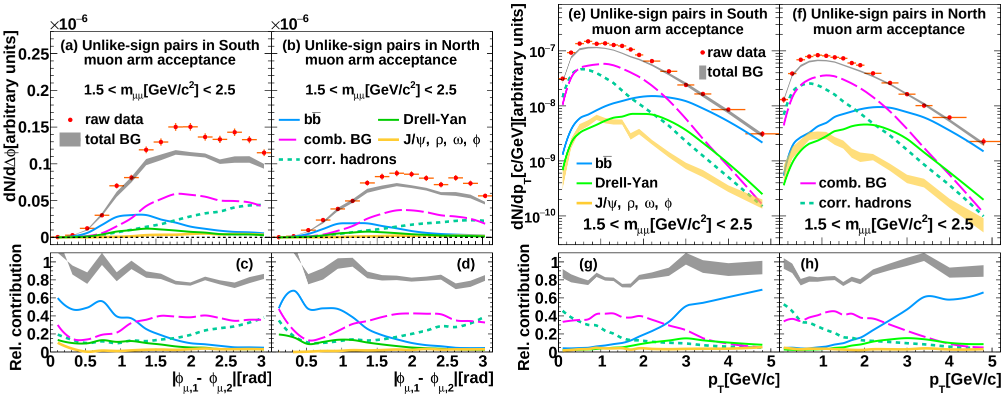

Figure 61: The $\mu\mu$ pair data in the charm mass region as a function of (a,b) $\Delta\phi$ or (c,d) pair p_T are shown. Contributions from all known sources other than charm decays are also shown. Panels (c,d,g,h) give the ratio of different components to the total yield. Gray bands indicate the systematic uncertainty on the sum of all contributions.

pairs from J/ψ decays, $N^{+-}_{\rm cor}$ is the estimated number of pairs from correlated hadrons, and $N^{+-}_{\rm comb}$ is the estimated number of combinatorial pairs.

3.8.2 Azimuthal correlations and pair p_T of $\mu^{\pm}\mu^{\pm}$ from $b\bar{b}$

The azimuthal opening angle distribution and pair p_T distribution for $\mu^{\pm}\mu^{\pm}$ pairs from the bottom mass region is shown in Fig. 62. Besides the $b\bar{b}$ contribution there are also contributions from correlated and combinatorial hadronic pairs. The number of like-sign pairs from bottom decays ($N^{\pm\pm}_{b\bar{b}}$) is obtained according to the following relation:

$$N^{\pm\pm}_{b\bar{b}} = N^{\pm\pm}_{\rm incl} - N^{\pm\pm}_{\rm cor} - N^{\pm\pm}_{\rm comb}, \qquad (23)$$

where $N^{\pm\pm}_{\rm incl}$ is the number of pairs passing all single and pair cuts in Tables 3 and 4, $N^{\pm\pm}_{\rm cor}$ is the estimated number of pairs from correlated hadrons, and $N^{\pm\pm}_{\rm comb}$ is the estimated number of combinatorial pairs. We subtract the background as a function of $\Delta\phi$ or pair p_T.

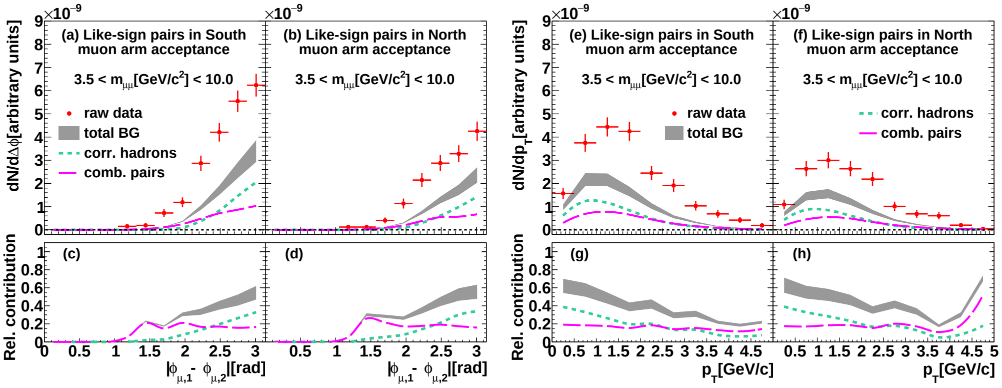

Figure 62: The like-sign $\mu\mu$ pair data in the bottom mass region as a function of (a,b) $\Delta\phi$ or (c,d) pair p_T are shown. Contributions from all known sources other than bottom decays are also shown. Panels (c,d,g,h) give the ratio of different components to the total yield. Gray bands indicate the systematic uncertainty on the sum of all contributions.

3.8.3 Pair mass and p_T distribution of $\mu^+\mu^-$ pairs from Drell-Yan

The Drell-Yan yield is extracted in a mass region that excludes the Υ mass region. The primary sources of background pairs are from bottom and charm decays. The number of pairs from Drell-Yan ($N^{+-}_{\rm DY}$) is obtained as:

$$\begin{aligned} N^{+-}_{\rm DY} = N^{+-}_{\rm incl} - N^{+-}_{b\bar{b}} - N^{+-}_{c\bar{c}} - N^{+-}_{J/\psi,\psi'} \\ -N^{+-}_{\Upsilon} - N^{+-}_{\rm cor} - N^{+-}_{\rm comb}, \end{aligned} \tag{24}$$

where $N^{+-}_{\rm incl}$ is the number of pairs passing all single and pair cuts in Tables 3 and 4, $N^{+-}_{J/\psi,\psi'}$ is the estimated number of pairs from J/ψ and ψ' decays, N^{+-}_{Υ} is the estimated number of pairs from the Υ family, $N^{+-}_{\rm cor}$ is the estimated number of pairs from correlated hadrons, and $N^{+-}_{\rm comb}$ is the estimated number of combinatorial pairs. The background contributions as a function of pair mass or p_T are shown in Fig. 63.

3.9 Acceptance and Efficiency Corrections

To obtain a physical yield or a cross section Γ, the raw yield Γ_{raw} determined in the previous section must be corrected for detector effects in multiple steps.

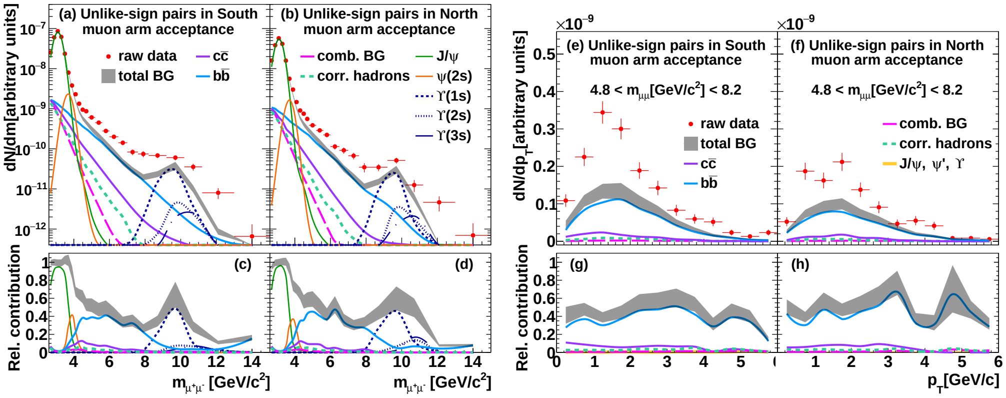

Figure 63: The unlike-sign $\mu\mu$ pair data used to determine the Drell-Yan contribution as a function of (a,b) mass or (c,d) pair p_T are shown. Contributions from all known sources other than the Drell-Yan process are also shown. Panels (c,d,g,h) give the ratio of different components to the total yield. Gray bands indicate the systematic uncertainty on the sum of all contributions.

$$\Gamma = \Gamma_{raw} \cdot \frac{\sigma_{\rm BBC}}{N_{\rm BBC} \cdot \epsilon_{\rm bias}} \cdot \frac{\alpha}{A \times \epsilon_{\rm rec}}, \tag{25}$$

where Γ and Γ_{raw} can represent differential or integrated quantities. The raw yield is converted to yield per event by dividing by $N_{\rm BBC}$, the number of sampled minimum bias events. The p+p cross section sampled by the BBC is $\sigma_{\rm BBC} = 23.0 \pm 2.2$ mb at $\sqrt{s} = 200$ GeV, it relates to the inelastic p+p cross section σ_{pp} by the following relation:

$$\sigma_{pp} = \frac{\sigma_{\rm BBC}}{\epsilon_{\rm BBC}}, \tag{26}$$

where $\epsilon_{\rm BBC} = 0.545 \pm 0.06$ is the fraction of inelastic p+p collisions recorded by the BBC. The BBC trigger bias for hard scattering events is $\epsilon_{\rm bias} = 0.79 \pm 0.02$ [132].

The other factors in Eq. 25 are $\epsilon_{\rm rec}$, the pair reconstruction efficiency that accounts for efficiency losses due to track reconstruction, single cuts and pair cuts, the software trigger efficiency, and detector inefficiency; A, the detector acceptance; and α, an additional normalization constant which will be discussed in detail in Sec. 3.10.4.

We note that the acceptance A has different meanings for the different measurements presented here. The azimuthal opening angle distributions for $\mu\mu$ pairs from $c\bar{c}$ and $b\bar{b}$ are corrected up to the ideal muon arm acceptance, which requires that each muon has a momentum $p > 3$ GeV/c and falls in the pseudorapidity range $1.2 < |\eta| < 2.2$. In contrast, for the $\mu\mu$ pairs from Drell-Yan production the correction is for the muon pair to be in the rapidity range $1.2 < |y^{\mu\mu}| < 2.2$. To determine the $b\bar{b}$ cross section we correct up to 4π, the full phase space. This correction is quantified in detail in Tab. 5. In general, $A \times \epsilon_{\text{rec}}$ is calculated using the default simulation framework. Input from the appropriate physics event generator is run through the simulation; the ratio of the reconstructed Γ_{raw}^{MC} yield over the input yield Γ^{MC} gives $A \times \epsilon_{\text{rec}}$.

Finally, the factor α accounts for the combined effect of double interactions, α_{double}; modifications of the reconstruction efficiency due to detector occupancy, α_{occ}; the change of the trigger livetime with luminosity, α_{live}; and additional variations with luminosity, α_{lum}; which are absent in the Monte-Carlo simulations. We determine α by comparing the measured J/ψ cross section [41] with the result using Eq. 25 with $\alpha = 1$. We obtain $\alpha = 1.30 \pm 0.16$ and $\alpha = 1.38 \pm 0.17$ for south and north muon arm, respectively. Our values are consistent with the product of the individual factors $\alpha_{double} \times \alpha_{\text{occ}} \times \alpha_{live} \times \alpha_{lum}$ within the systematic uncertainties, where the individual factors are determined with data driven methods. For an extended discussion, see Sec. 3.10.4.

3.9.1 Azimuthal correlations of $\mu\mu$ from $c\bar{c}$ and $b\bar{b}$

The fully corrected per event pair yield is given by Eq. 27.

$$\frac{dN}{dX} = \frac{N_{\text{HF}}}{\Delta X} \cdot \frac{\epsilon_{\text{BBC}}}{N_{\text{BBC}} \cdot \epsilon_{\text{bias}}} \cdot \frac{\alpha}{A \times \epsilon_{\text{rec}}(X)}, \tag{27}$$

where X is $\Delta\phi$ or pair p_T, ΔX is the corresponding bin width, and N_{HF} refers to $N_{c\bar{c}}^{+-}$ or $N_{b\bar{b}}^{\pm\pm}$ given by Eq. 22 and Eq. 23, respectively. All other factors are the same as in Eq. 25.

The pair reconstruction efficiency $\epsilon_{\text{rec}}(X)$ is determined using input distributions from PYTHIA and POWHEG and is computed by taking the ratio of reconstructed and generated yields with both generated tracks satisfying the condition of the ideal muon arm acceptance ($p > 3$ GeV/c and

$1.2 < |\eta| < 2.2$). Here we correct the data up to the ideal muon arm acceptance. We do not correct up to $\mu\mu$ pairs in $1.2 < |y_{\mu\mu}| < 2.2$ to reduce effects from model dependent extrapolations to a minimal. Systematic uncertainties for model dependent efficiency corrections are determined by comparing $\epsilon_{\mathrm{rec}}(X)$ using PYTHIA or POWHEG as input distributions. This will be discussed in detail in Section 3.10.

3.9.2 Drell-Yan

The differential cross section as a function of mass or p_T is given by Eq. 28 and Eq. 29:

$$\frac{d^2\sigma}{dmdy} = \frac{N_{\mathrm{DY}}}{\Delta m \Delta y} \cdot \frac{\sigma_{\mathrm{BBC}}}{N_{\mathrm{BBC}} \cdot \epsilon_{\mathrm{bias}}} \cdot \frac{\alpha \cdot \beta(m,y)}{A \times \epsilon_{\mathrm{rec}}(m,y)}, \tag{28}$$

$$\frac{1}{2\pi p_T}\frac{d^2\sigma}{dydp_T} = \frac{N_{\mathrm{DY}}}{2\pi p_T \Delta y \Delta p_T} \cdot \frac{\sigma_{\mathrm{BBC}}}{N_{\mathrm{BBC}} \cdot \epsilon_{\mathrm{bias}}} \cdot \frac{\alpha \cdot \beta(y,p_T)}{A \times \epsilon_{\mathrm{rec}}(y,p_T)}, \tag{29}$$

where N_{DY} is the raw yield of pairs from Drell-Yan given by Eq. 24. Δm, Δp_T, and Δy are the bin widths in pair mass, pair p_T and pair rapidity, respectively. $\beta(m,y)$ and $\beta(y,p_T)$ are correction factors which correct the cross section averaged over the bin to the cross section at the bin center. These correction factors are estimated using PYTHIA simulations and lie between 0.97 and 1.03. All other factors are the same as in Eq. 25.

The pair acceptance and efficiency $A \times \epsilon_{\mathrm{rec}}(m,y)$ and $A \times \epsilon_{\mathrm{rec}}(y,p_T)$ are determined using input distributions generated using PYTHIA. They correct the pair yield to one unit of rapidity at $1.2 < |y^{\mu\mu}| < 2.2$.

3.9.3 Bottom cross section

We determine the total $b\bar{b}$ cross section from the measured $\mu\mu$ pair yield from $b\bar{b}$. In the fitting procedure we determined the normalization $\kappa_{b\bar{b}}$, which was chosen such that it directly relates to the total $b\bar{b}$ cross section $\sigma_{b\bar{b}}$:

$$\sigma_{b\bar{b}} = \frac{\alpha \cdot \sigma_{\mathrm{BBC}}}{N_{\mathrm{BBC}} \cdot \epsilon_{\mathrm{bias}}} \cdot \kappa_{b\bar{b}}. \tag{30}$$

The acceptance and efficiency corrections, trigger efficiency, branching ratios, and oscillation parameters are all implicitly encapsulated in $\kappa_{b\bar{b}}$, because the templates for fitting already include all the considerations mentioned above.

We use two models PYTHIA and POWHEG, to estimate a possible model dependence in the total $b\bar{b}$ cross section. The extrapolation from the limited phase space of our $\mu\mu$ measurement to the entire kinematic region can be divided into four steps:

- Extrapolation from $\mu^{\pm}\mu^{\pm}$ muon pairs with $m_{\mu\mu} > 3$ GeV/c^2 in the *ideal* muon arm acceptance to all muon pairs ($\mu^{\pm}\mu^{\pm}$ and $\mu^{+}\mu^{-}$) with $m_{\mu\mu} > 3$ GeV/c^2 in the ideal muon arm acceptance.
- Extrapolation to all muon pairs in the entire mass region ($m_{\mu\mu} > 0$ GeV/c^2) in the ideal muon arm acceptance.
- Extrapolation to all muon pairs with the pseudorapidity of each muon satisfying $1.2 < |\eta_{\mu}| < 2.2$.
- Extrapolation to all muon pairs in 4π.

Table 5: Step by step reduction of phase space from 4π to the number of like-sign $\mu\mu$ pairs with $m_{\mu\mu} > 3$ GeV/c^2 in the ideal muon arm acceptance. Each step is cumulative to the previous, i.e. each row adds one more restriction to the phase space. Numbers are in units of pairs per generated $b\bar{b}$ event. The factors in brackets quantify the decrease of the number of pairs from the previous step.

	Event gen.	
condition	PYTHIA	POWHEG
4π	6.76×10^{-2} (15.4)	6.73×10^{-2} (15.6)
$1.2 < \|\eta_{\mu}\| < 2.2$	4.39×10^{-3} (10.7)	4.32×10^{-3} (10.7)
$p_{\mu} > 3$ GeV/c	4.11×10^{-4} (3.48)	4.04×10^{-4} (3.39)
$m_{\mu\mu} > 3$ GeV/c^2	1.18×10^{-4} (3.19)	1.19×10^{-4} (3.48)
$\mu^{\pm}\mu^{\pm}$ in PHENIX	3.71×10^{-5}	3.42×10^{-5}

Table 5 quantifies each step of the extrapolation procedure. For clarity they are shown in reversed order. The difference between PYTHIA and POWHEG is less than 8% in each step, which is consistent with the observation from Ref. [128], i.e. the model dependence of the extrapolation is small because the $\mu\mu$ (or ee) pair distributions from bottom are dominated by decay kinematics.

The differential cross section $d\sigma_{b\bar{b}}/dy_b|_{\langle y_b\rangle=\pm1.7}$ can be calculated as follows:

$$\frac{d\sigma_{b\bar{b}}}{dy_b}|_{\langle y_b\rangle=\pm1.7} = \frac{\alpha\cdot\sigma_{\mathrm{BBC}}}{N_{\mathrm{BBC}}\cdot\epsilon_{\mathrm{bias}}}\cdot\frac{dN_b}{dy_b}|_{\langle y_b\rangle=\pm1.7}\cdot\kappa_{b\bar{b},\frac{N}{S}}, \tag{31}$$

where $dN_b/dy_b|_{\langle y_b\rangle=\pm1.7}$ is the rapidity density of b quarks determined from the average of PYTHIA and POWHEG, $\kappa_{b\bar{b},\frac{N}{S}}$ is the fitted normalization for bottom from the north (south) muon arm.

3.10 Systematic uncertainties

We consider four types of sources of possible systematic uncertainties on the extraction of $\mu\mu$ pairs from $c\bar{c}$, $b\bar{b}$, and Drell-Yan. These are uncertainties:

- on the shape of the template distributions,
- on the normalization of template distributions,
- on the acceptance and efficiency corrections,
- and on the overall global normalization.

The first three sources of systematic uncertainties are point-to-point correlated, but allow for a gradual overall change in the shape of the distributions. We refer to these uncertainties as type B. Global normalization uncertainties that do not affect the shape of the distributions but only the absolute normalization are quoted separately as type C. This analysis does not contain type A uncertainties, which are point-to-point uncorrelated systematic uncertainties.

There are multiple contributors to each type of systematic error. For example, the $c\bar{c}$ and $b\bar{b}$ templates are model dependent and can be determined with PYTHIA or POWHEG. For each such case we repeat the full analysis with the different assumptions. The spread of the results around the default analysis is used to assign systematic uncertainties. If we considered two assumptions, such as in the example given, we quote the uncertainty relative to the average result. On the other hand, if there is a clearly preferred default case, we use the difference of results obtained with the extreme assumptions to assign systematic uncertainties.

We quantify all systematic uncertainties as standard deviations. The systematic uncertainties on the different measurements are summarized in Table. 6. For the differential distributions of $c\bar{c}$, $b\bar{b}$, and Drell-Yan, the systematic uncertainties vary with azimuthal opening angle, pair p_T or mass. A breakdown of all the systematic uncertainties are shown in Fig. 64.

3.10.1 Shape of simulated distributions

The $c\bar{c}$, $b\bar{b}$, Drell-Yan, and hadronic pair background components are correlated through the fitting procedure, thus an uncertainty on the shape for any one template distribution will simultaneously affect the fit results of all four components. For example, if one increases the hardness of the input pion p_T spectrum, the number of high mass like-sign hadron-hadron pairs will increase, which will lead to a smaller $\mu^{\pm}\mu^{\pm}$ pair yield from $b\bar{b}$. Because $b\bar{b}$ is the main competing source to the Drell-Yan process in the high $\mu^{+}\mu^{-}$ pair mass region, this will in turn lead to a larger Drell-Yan yield. Drell-Yan and bottom both contributes to the intermediate mass region where $c\bar{c}$ is extracted, and hence will the $c\bar{c}$ yield will also be modified.

In the following we will discuss the uncertainties on the shape of individual contributions and how these uncertainties propagate to the measurement of all components.

3.10.1.1 Input hadron spectra The input pion and kaon p_T spectra are tuned to match PHENIX and BRAHMS data at $\langle y \rangle = 0$ and $\langle y \rangle = 2.95$, respectively. This is achieved by applying weighting factors ($w_h(y)$) to the p_T spectra from PYTHIA, which are determined by a linear interpolation between the two ratios of PYTHIA to the data at $\langle y \rangle = 0$ and $\langle y \rangle = 2.95$ (see Fig. 53). In order to estimate the systematic uncertainties on the input hadron p_T spectra, we vary the weighting function: we use either $w_h(\langle y \rangle = 0)$ for all light hadrons, which gives a harder p_T spectra than the default case, or $w_h(\langle y \rangle = 2.95)$, which gives a softer p_T spectra. The shape of the hadron-hadron pair mass distribution changes significantly only for masses above 3 GeV/c^2.

Table 6: Summary of arm-averaged relative systematic uncertainties for the total bottom cross section $\sigma_{b\bar{b}}$, the differential Drell-Yan cross section $d^2\sigma_{DY\rightarrow\mu\mu}/dmdy$, and the $b\bar{b}$ ($c\bar{c}$) differential yields $dN_{b\bar{b}(c\bar{c})\rightarrow\mu\mu}/d\Delta\phi$. The systematic uncertainty type is indicated in the second column and is applicable only to the differential measurements. The uncertainties for the differential measurements vary with azimuthal opening angle, pair p_T, or mass. Asymmetric uncertainties are quoted in bracketed values. For the $c\bar{c}$ measurement, the regions $\Delta\phi < \pi/2$, $p_T < 0.5$ GeV/c and $p_T > 2.0$ GeV/c are excluded because the yield approaches zero and relative systematic uncertainties diverge. With these regions excluded, the difference between the systematic uncertainties of all measurements for the south and north muon arms differs by no greater than 2% for all systematic uncertainties sources.

	type	$\sigma_{b\bar{b}}$	$\frac{dN_{b\bar{b}\rightarrow\mu\mu}}{d\Delta\phi}$	$\frac{dN_{b\bar{b}\rightarrow\mu\mu}}{dp_T}$	$\frac{d^2\sigma_{DY\rightarrow\mu\mu}}{dmdy}$	$\frac{1}{2\pi p_T}\frac{d^2\sigma_{DY\rightarrow\mu\mu}}{dyp_T}$	$\frac{dN_{c\bar{c}\rightarrow\mu\mu}}{d\Delta\phi}$	$\frac{dN_{c\bar{c}\rightarrow\mu\mu}}{dp_T}$
Input hadron spectra	B	+4.7%	+(<6%)	+(<12%)	+(<14%)	+(<20%)	+(<9%)	+(<9%)
		−11.0%	−(<19%)	−(<25%)	−(<7%)	−(<9%)	−(<4%)	−(<4%)
Hadron simulation	B	2%	<1%	<1%	<1%	<1%	<1%	<1%
$c\bar{c}$ (shape)	B	2%	<4%	<5%	<4%	<6%	-	-
$b\bar{b}$ (shape)	B	-	-	-	<14%	<17%	<3%	<3%
Drell-Yan (shape)	B	<1%	< 1%	<1%	-	-	<6%	<5%
ZYAM normalization	B	<1%	<1%	<1%	<1%	<1%	<2%	<3%
PYTHIA h-h correlations	B	-	-	-	-	-	<14%	<13%
Simulations(ϕ,z)	B	<1%	< 4%	< 5%	<1%	<1%	< 8%	<8%
Fitting range	B	2%	<1%	<1%	< 1%	< 1%	<1%	<1%
$\phi, \omega, \rho, J/\psi, \psi', \Upsilon$ norm.	B	-	-	-	<2%	< 1%	<1%	<1%
Statistical uncertainty in fit	B	-	<4%	<4%	<6%	<8%	<10%	<10%
$b\bar{b}$ model dep. extrapolation	-	6.5%	-	-	-	-	-	-
Model dep. eff. corrections	B		<10%	<3%	-	-	<5%	<4%
Trigger efficiency	B	1.5%	1.5%	1.5%	1.5%	1.5%	1.5%	1.5%
MuTr efficiency	B	4%	4%	4%	4%	4%	4%	4%
MuID efficiency	B	2%	2%	2%	2%	2%	2%	2%
Sum of type B systematic uncertainties	-	+9.3%	+(4%–11%)	+(6%–14%)	+(4%–21%)	+(13%–28%)	+(10%–28%)	+(10%–20%)
		−13.2%	−(4%–22%)	−(6%–26%)	−(4%–17%)	−(11%–22%)	−(10%–20%)	−(8%–16%)
Global normalization	C	12%	12%	12%	12%	12%	12%	12%

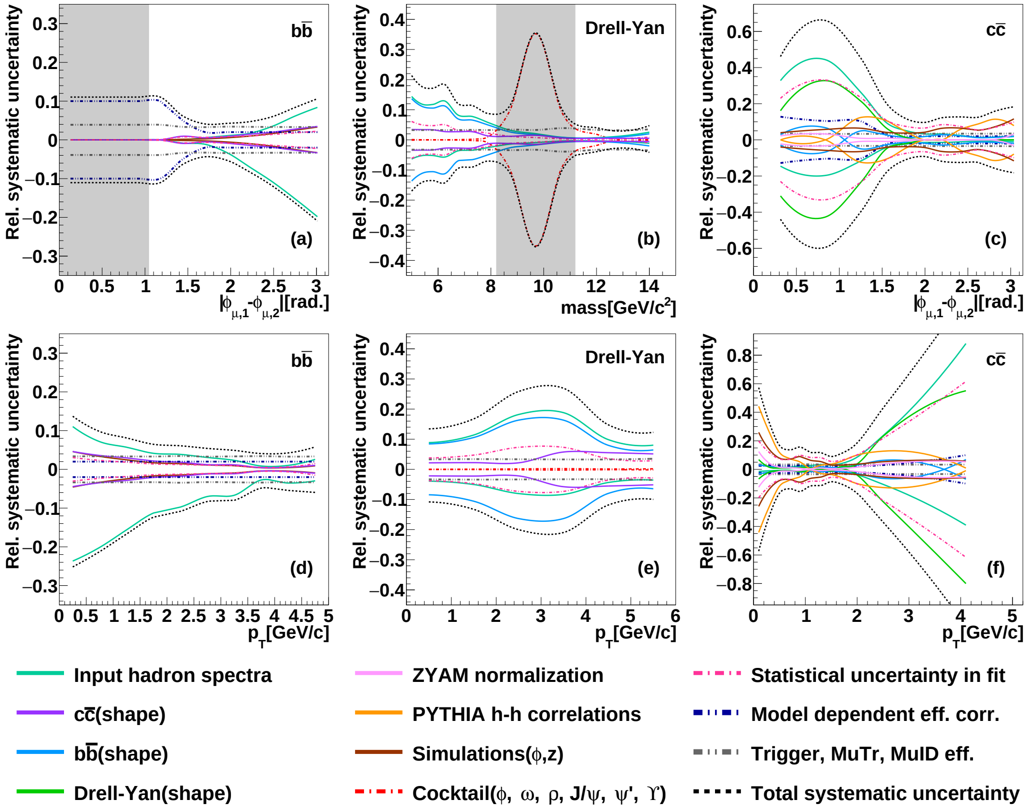

Figure 64: Relative two-arm averaged systematic uncertainties for $c\bar{c}$ and $b\bar{b}$ measurements as a function of $\Delta\phi$ or pair p_T and Drell-Yan measurement as a function of mass or p_T. The shaded regions are excluded from the respective measurements.

We take the difference of the cross sections obtained using these two sets of p_T spectra and the default p_T spectra as a systematic uncertainty on the input hadron spectra. For $\sigma_{b\bar{b}}$, this is determined to be +4.7% and −11.0%. The uncertainties are also propagated to the $b\bar{b}$ and $c\bar{c}$ azimuthal opening angle distributions, pair p_T spectra and the Drell-Yan yields. In all cases this is a dominant contributor to the systematic uncertainties (see Table 6).

We have also considered using the bands shown in Fig. 53 as limits for the weighting factors. However, this leads to smaller uncertainties and we choose to quote the more conservative estimate. Uncertainties related to the choice of parton distribution function (PDF) are estimated by evaluating the differences obtained with simulations using the CTEQ5, CTEQ6, MRST2001(NLO) [133] and GRV98(LO) [134] parton distribution functions. The differences are negligible compared to the uncertainty due to shapes of the light hadron p_T spectra.

3.10.1.2 Hadron simulation The default PHENIX GEANT4 simulation utilizes the standard HEP physics list QGSP-BERT. For hadronic interactions of pions, kaons and nuclei above 12 GeV, the quark gluon string model (QGS) is applied for the primary string formation and fragmentation. At lower energies, the Bertini cascade model (BERT) is used, which generates the final state from an intranuclear cascade.

To estimate possible uncertainties due to the description of the hadronic interactions in the absorbers, we use two other physics lists: (i) the FTFP-BERT list, which replaces QGS with the Fritiof model (FTF) for high energies. The FTF uses an alternative string formation model followed by the Lund fragmentation model. (ii) the QGSP-BIC list, where the low energy approach is replaced by the binary cascade model (BIC), which was optimized to describe proton and neutron interactions, but is less accurate for pions.

Using these different physics lists leads to a 2% difference of $\sigma_{b\bar{b}}$, and thus, a negligible difference to the charm and Drell-Yan normalizations.

3.10.1.3 Charm and bottom simulation There are potential model dependencies of the $\mu\mu$ and muon-hadron templates for $c\bar{c}$ and $b\bar{b}$. To estimate these, we compare the $\mu\mu$ and muon-hadron templates obtained using PYTHIA and POWHEG. Systematic uncertainties on charm and bottom are assumed to be uncorrelated and are added in quadrature.

Due to the large mass of the bottom quark, decay kinematics govern the shape of the distributions, hence the difference between PYTHIA and POWHEG is small (see Fig. 52). The largest effect of this uncertainty is exhibited at mass ~ 5 GeV/c^2 for the Drell-Yan measurement, where the contribution of $b\bar{b}$ is around 40% of the total yield.

The model dependence of charm is larger than that of bottom, particularly for $m < 1$ GeV/c^2. In the high mass region POWHEG tends to predict higher yields for both $\mu\mu$ and muon-hadron templates, which is likely due to a harder single muon p_T spectrum. However, the effect on the extraction of bottom and Drell-Yan yields in the high mass region is small where the contribution of charm is less than 10%.

3.10.1.4 Drell-Yan The intrinsic $k_T = 1.1$ GeV/c used in the PYTHIA simulations is determined by minimizing χ^2 of the p_T distribution of Drell-Yan pairs in the Drell-Yan mass region, between data and simulations. Background components are normalized using cross sections obtained from the fitting procedure and subtracted as a function of p_T. We find that an intrinsic k_T of 1.1 GeV/c best describes the p_T distribution of Drell-Yan pairs in the high mass region (see Fig. 65).

We vary the k_T by ± 0.1 GeV/c where the χ^2 changes by ~ 1 to estimate uncertainties in the Drell-Yan distributions. The uncertainty mainly affects the $c\bar{c}$ yield at $\Delta\phi < \pi/2$ and $p_T > 2$ GeV/c and is negligible elsewhere.

3.10.1.5 ZYAM normalization To estimate the effect of varying the relative contributions between correlated and uncorrelated pairs, we vary the mass region which we use for the $\Delta\phi_{prim}$ distribution. Besides the default normalization region $\mathcal{M}$ below 3 GeV/c^2, we select 3 separate regions: 0.7–1.3 GeV/c^2, 1.3–1.6 GeV/c^2, 1.6–2.2 GeV/c^2. This results in a variation of the ratio of correlated to uncorrelated pairs by ±10%. The relative effect on the sum of correlated and uncorrelated pairs is less than 2% over the entire mass region, and has a negligible effect on the determination of $b\bar{b}$, $c\bar{c}$, and Drell-Yan cross sections.

3.10.1.6 Hadron-hadron correlations from PYTHIA For the measurement of $c\bar{c}$ yields as a function of $\Delta\phi$ or pair p_T, correlated hadron pairs are a major background source. To estimate the uncertainty in the description of PYTHIA under Tune A settings, we compare distributions of like-sign pairs

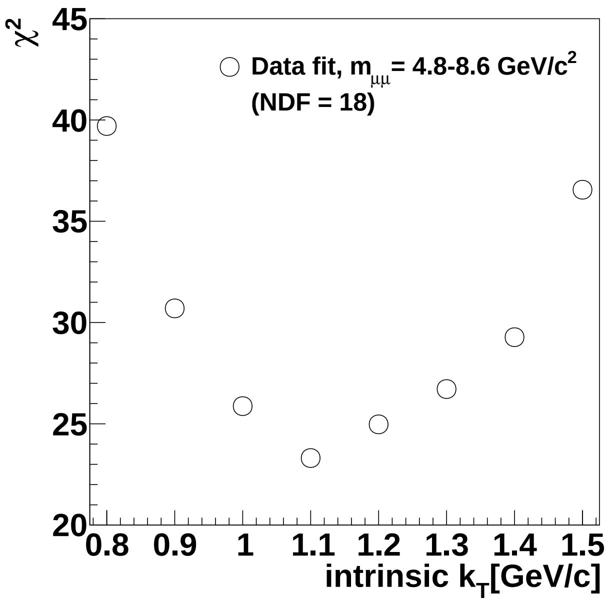

Figure 65: The χ^2 for the pair p_T spectrum of Drell-Yan pairs in the mass region 4.8–8.6 GeV/c^2 compared to PYTHIA simulations with different intrinsic k_T. The χ^2 is minimized at a k_T of 1.1 GeV/c.

between data and simulation in the same mass region (1.5–2.5 GeV/c^2) where other contributions, including $b\bar{b}$, are negligible. We observe that the width of the back-to-back peak at $\Delta\phi = \pi$ is slightly wider in data compared to PYTHIA simulation. This leads to a softer pair p_T spectrum in simulations compared to data, because the pair p_T is strongly correlated with $\Delta\phi$. The discrepancy is strictly less than 12% and varies with $\Delta\phi$ or p_T. One data driven approach would be to modify the unlike-sign hadronic pair background according to the $\Delta\phi$ or p_T dependent ratio between data and simulations obtained using the like-sign pairs. Here we take the average between the default Tune A setup and this data driven modification to be our central value, and assign a systematic uncertainty that is equal to the difference between these two approaches. The resultant systematic uncertainty on the $c\bar{c}$ yields is strongly $\Delta\phi$ and p_T dependent, ranging from 0% to 14%.

3.10.1.7 Azimuthal angle(ϕ) description in simulations We compare the ϕ distributions of single tracks in data, simulations with the default framework, and simulations with the FastMC. We find reasonable agreement between data and the default simulation and conclude that the uncertainty from the default simulation framework is negligible. However, for simulations using the FastMC, recall that we approximated the relative ϕ dependent efficiency by a weighting strategy in ϕ bins of finite width, which gives rise to a small smearing in the ϕ; and hence $\Delta\phi$ distributions. Since $\Delta\phi$ is strongly correlated with p_T, this also has a small effect on the p_T distributions. See Fig. 120 for a comparison of distributions generated using FastMC and default simulations. We assign 5% uncertainty to the $\Delta\phi$ distributions generated using the FastMC, which is estimated by comparing $\Delta\phi$ distributions of mixed pairs between FastMC and real data. This gives rise to an average of 5% and 3% to the $c\bar{c}$ and $b\bar{b}$ differential yields respectively.

3.10.1.8 z-vertex description of simulations We have generated hadronic pairs in discrete z_{vtx} regions that cover only a quarter of the full collision z_{vtx} region using the FastMC. Figure 66 shows a comparison of data and simulations in different z_{vtx} regions after the initial normalization (Sec. 3.6.1.2) and iterative fitting procedure (Sec. 3.7). Good agreement is seen between the simulations and data in all z_{vtx} regions; there is no indication that the approximations in the z_{vtx} description of correlated hadrons is biasing the fit of the like-sign pairs.

To estimate the systematic uncertainty on this approximation, recall that the yield of decay muons varies linearly with z_{vtx}, whereas the yield of prompt muons is constant with z_{vtx}[81]. Thus, the main effect of the z_{vtx} approximation is the uncertainty on the prompt muon to decay muon ratio. In the FastMC the ratio is determined in three vertex bins of 5 cm width at $z_{\text{vtx}} =$ -20, 0, and 20 cm, instead of the full 20 cm z_{vtx} slices. We assign a systematic uncertainty by manually varying the prompt muon to decay muon ratio separately for each z_{vtx} region. Because prompt muons are dominated by charm decays, we estimate this effect by manually varying the charm cross section by ±15% for one particular z slice separately. The effect on the fitted $b\bar{b}$ cross section is $\sim 1\%$ and is negligible compared to other sources of systematic uncertainties.

3.10.2 Normalization of simulated distributions

In addition to uncertainties due to the shape of distributions, uncertainties on the normalization of one component can affect the yield of other components.

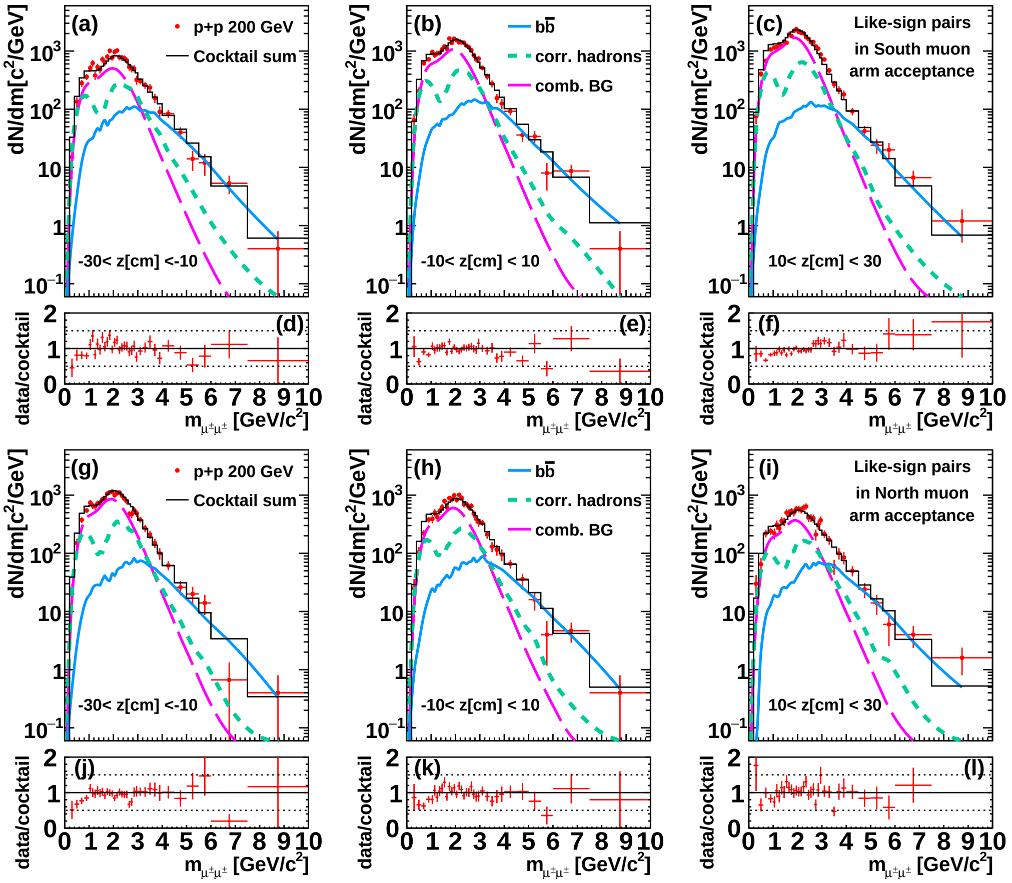

Figure 66: Inclusive like-sign $\mu\mu$ pair yield from p+p collisions at $\sqrt{s} = 200$ GeV as a function of mass in three z vertex bins for the south and north muon arms. The data are compared to the contributions from $b\bar{b}$ decays, and the correlated & combinatorial contribution from hadronic pairs.

The sources of such uncertainties are listed in this section.

3.10.2.1 Fitting

To estimate uncertainties in the fitting range, we vary the lower bound of the fit range of like-sign pairs from $m = 1.0$ GeV/c^2 to $m = 2.0$ GeV/c^2. The variation in $\sigma_{b\bar{b}}$ is around 2% and is assigned as the systematic uncertainty on the fit range. The unlike-sign fit range is also varied to diagnose possible effects due to non Gaussian tails of the mass distribution of $\mu^+\mu^-$ pairs from resonance decays. The variation of $\kappa_{c\bar{c}}$ is less than 5% with different fit ranges in the unlike-sign, and this $\kappa_{c\bar{c}}$ variation propagates into $< 1\%$ variation in $\sigma_{b\bar{b}}$.

We estimate uncertainties in fit stability by varying the binning of distributions. All variations are consistent within the statistical uncertainty. We therefore do not assign systematic uncertainties on fit stability.

3.10.2.2 Normalization of cocktail components

ϕ, ω, ρ, J/ψ, ψ', and Υ are background components to determine $N^{+-}_{c\bar{c}}$ and $N^{+-}_{\rm DY}$ in Eq. 22 and 24, respectively. The normalizations are fixed by previous measurements. The normalization of each component has associated statistical and systematic uncertainties from those measurements. We add these uncertainties in quadrature and vary normalizations of these background components to estimate propagated uncertainties in $N^{+-}_{c\bar{c}}$ and $N^{+-}_{\rm DY}$. Because we have explicitly avoided mass regions dominated by resonance decays in the analysis, these uncertainties give rise to a maximum of 2% uncertainty in all measurements.

3.10.2.3 Statistical uncertainty in fit result

Charm, bottom, and hadronic pairs are background components for $N^{+-}_{\rm DY}$. The statistical uncertainties on fitted values of $\kappa_{c\bar{c}}$, $\kappa_{b\bar{b}}$, and κ_h become a source of type B systematic uncertainty for $N^{+-}_{\rm DY}$. Similarly, systematic uncertainties for $N^{+-}_{c\bar{c}}$ arise from statistical uncertainties on κ_h, $\kappa_{\rm DY}$, and $\kappa_{b\bar{b}}$, and $N^{\pm\pm}_{b\bar{b}}$ from κ_h and $\kappa_{c\bar{c}}$. The statistical uncertainties for $\kappa_{b\bar{b}}$ and $\kappa_{\rm DY}$ is $\sim 8\%$, and for κ_h is $\sim 2\%$ for each arm. The associated systematic uncertainties depend on the signal to background ratio and varies from measurement to measurement.

3.10.3 Extrapolation, acceptance and efficiency

This section details systematic uncertainties related to acceptance and efficiency corrections.

3.10.3.1 Model dependence on $b\bar{b}$ We use the high mass like-sign pairs to constrain $\sigma_{b\bar{b}}$, hence a determination of $d\sigma_{b\bar{b}}/dy$ involves an extrapolation to zero mass at forward rapidity, whereas the determination of $\sigma_{b\bar{b}}$ involves a further extrapolation to the full rapidity region. This is dependent on correlations between $\mu\mu$ pairs from bottom as well as the branching ratios and oscillation parameters. To quantify the uncertainties in the extrapolation, we take the average of the fitted cross section $\sigma_{b\bar{b}}$ using PYTHIA and POWHEG and assign the difference (±6.5%) as the systematic uncertainty. We note that the difference between the default values of the time-integrated probability for a neutral B_d^0 (B_s^0) to oscillate χ_d (χ_s) of PYTHIA and the values from the PDG, $\chi_d = 0.1860 \pm 0.0011$ ($\chi_s = 499304 \pm 0.000005$) [1] is less than 2% and hence much less than the assigned uncertainty.

3.10.3.2 Model dependence on efficiency corrections For charm and bottom azimuthal corrections, we correct the data to the ideal muon arm acceptance. To assess the effect of different input distributions on the calculation of efficiency corrections, we compare the efficiency as a function of $\Delta\phi$ calculated from PYTHIA and POWHEG. No model dependence in the efficiency corrections is observed for $\mu\mu$ pairs with $\Delta\phi > 1.5$ from $c\bar{c}$ and $b\bar{b}$. For $\Delta\phi < 1.5$, we assign an additional uncertainty based on the difference of the efficiency corrections calculated by PYTHIA and POWHEG.

For charm and bottom pair p_T efficiency corrections, we again correct the data to the muon arm acceptance. No model dependence in the efficiency corrections is observed for $\mu\mu$ pairs in the measured p_T range. We assign an uncertainty based on the statistical uncertainty of the calculated efficiency corrections.

For Drell-Yan, we estimate the uncertainties in the model dependence of the acceptance and efficiency corrections by varying intrinsic k_T settings of PYTHIA within the systematic limits as described in Sec. 3.10.1.4. No model dependence in the acceptance and efficiency corrections is observed. We assign an uncertainty based on the statistical uncertainty of the calculated efficiency corrections.

3.10.3.3 Trigger efficiency The possible discrepancy between the software trigger emulator and the hardware trigger is quantified by a comparison of the real data trigger decision with the offline software trigger, as a function of mass. We find that they are consistent within 1.0% and 1.5% over the full mass region for the south and north arm, respectively. We use these values as estimates of the associated systematic uncertainty.

3.10.3.4 Reconstruction efficiency The muon track reconstruction and muon identification used in this analysis is the standard PHENIX muon reconstruction chain. The systematic uncertainties have been previously studied. We assign MuTr (4%) and MuID (2%) as systematic uncertainties on reconstruction efficiency based on the work published in [81].

3.10.4 Global normalization uncertainties

The absolute normalization of the $\mu\mu$ pair spectra is set by the measured J/ψ yield [41], which is measured with an accuracy of 12%. This is the systematic uncertainty on the scale for all results presented in this paper.

The normalization is expressed in Eq. 25 by the factor α, which accounts for the combined effect of the change of the trigger livetime with luminosity α_{live}, modifications of the reconstruction efficiency due to detector occupancy α_{occ}, additional variations of the efficiencies with luminosity α_{lum}, and the effect of double interactions α_{double}.

These individual factors were determined separately as a cross-check. The trigger livetime was monitored during data taking and the correction was found to be 1.35 (1.30) for the south (north) arm, respectively. The occupancy effect was studied by embedding simulated $\mu\mu$ pairs in p+p events and results in $\alpha_{\mathrm{occ}} = 1.06$ (1.04). In addition, there is a drop of the detector efficiency with increasing beam intensity that was found to give $\alpha_{lum} = 1.04$ (1.07). Finally, the approximately 20% double interactions in the sample increase the pair yield by about 11%, resulting in $\alpha_{double} = 0.90$. The yield increase is smaller than the number of double interactions mostly for two reasons: (i) Diffractive events contribute to events with double interactions but do not contribute significantly to the pair yield, and (ii) Events with double interactions contain collisions more than 40–50 cm away from the nominal collision point; pairs from these events have significantly reduced reconstruction efficiency. The combination of both effects approximately cancel the efficiency losses due to detector occupancy and high interaction rates.

The product of individual corrections to the normalization is $\alpha_{double} \times \alpha_{\mathrm{occ}} \times \alpha_{live} \times \alpha_{lum} = 1.33$ (1.34) for south (north). These values are consistent to within uncertainties with 1.30 ± 0.16 (1.38 ± 0.17), the values based on the J/ψ measurement.

4 p+Au collisions: Data analysis

4.1 Data Set and Event Selection

The data set analyzed for p+Au collisions at $\sqrt{s_{NN}} = 200$ GeV was taken in 2015. The data were selected with the $\mu\mu$ pair trigger (MuIDLL1-2D) in coincidence with the MB trigger. We require each event in the sample to have a reconstructed vertex within $z = \pm 30$ cm of the nominal collision point. The data sample corresponds to 2.1×10^{11} MB triggered events or to an integrated luminosity of $\int \mathcal{L}dt = 0.14$ pb^{-1}.

4.2 Track Reconstruction and Muon Pair Selection

The track reconstruction and muon pair selection criteria in p+Au are identical to those in p+p, and have been documented in detail in Sec. 3.2 and 3.3 respectively.

Figure 67 shows the raw mass spectra after imposing all single track and pair cuts. Spectra are presented for $\mu^+\mu^-$ and $\mu^\pm\mu^\pm$ pairs measured for collisions in three vertex regions separately. Comparing to the case in p+p collisions in Fig. 49, the ratio of like-sign pairs to unlike-sign pairs is higher in p+Au collisions, particularly for the Au-going side. This is indicative of an increase in the combinatorial background, and is expected since the number of collisions N_{coll} of minimum bias p+Au collisions is 4.7 ± 0.3, obtained from Glauber calculations [122]. The like-sign to unlike-sign ratio is higher for the Au-going side compared to the p-going side. Again, this is expected because there is an enhancement of hadron production at backward rapidity (corresponding to the anti-shadowing region), whereas there is a small suppression at forward rapidity (corresponding to the shadowing region) [135].

4.3 Modelling of Expected Pair Sources

4.3.1 Physical $\mu\mu$ pair sources

The differential yields of the various physical pair sources are modified in p+Au collisions. The following sections describe in detail the modelling of the physical pair sources in p+Au collisions.

4.3.1.1 Hadron Decays to $\mu\mu$ pairs ($h \rightarrow \mu\mu(X)$) η, η', ω, ρ and ϕ dominate the $\mu^+\mu^-$ pair yield for masses less than 1 GeV/c^2, while J/ψ, ψ'

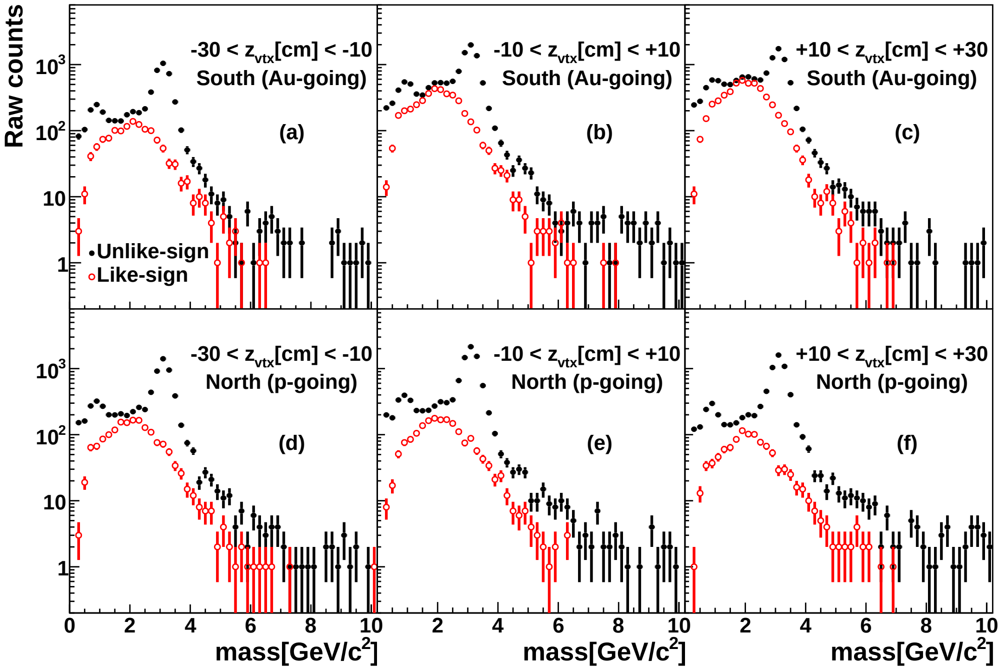

Figure 67: Raw mass spectra for the south (a,b,c) and north (d,e,f) muon arms in different z_{vtx} slices in p+Au collisions.

and $\Upsilon(1S{+}2S{+}3S)$ dominate narrow mass regions at higher masses. All such regions are excluded in the analysis, hence the modifications of these sources will not have an effect on the measurements. Nevertheless, we estimated modifications of the following sources as follows:

- ϕ

  The normalization of $\phi \to \mu\mu$ from p+p collisions is scaled by $R_{p+Au} \times N_{coll}$, where R_{p+Au} is measured on average over the rapidity range covered by the muon arms, using the preliminary results presented in [136]. These values are 0.8 ± 0.2 and 1.3 ± 0.3 for the p-going side and the Au-going side, respectively.

- J/ψ

  We adjusted the p_T spectra of J/ψ mesons by scaling the p+p spectra with $R_{p+Au}(p_T) \times N_{coll}$, where $R_{p+Au}(p_T)$ is taken from measurements presented in [137].

- ψ'

  The p_T spectra are adjusted in a two step process. We first applied a scaling factor based on the measured double ratio $[\frac{\sigma_\psi(2S)}{\sigma_\psi(1S)}]^{p+Au}/[\frac{\sigma_\psi(2S)}{\sigma_\psi(1S)}]^{p+p}$. These values are 0.48 ± 0.20 and 0.98 ± 0.24 for the Au-going and p-going sides, respectively [125]. A plausible explanation for the smaller value for the Au-going side is interactions of the fully formed color-neutral meson with comoving particles. We then applied $R_{p+Au}(p_T)$ taken from [137] to estimate modifications in the p_T spectra.

- $\Upsilon(1S), \Upsilon(2S), \Upsilon(3S)$

  We set the $\Upsilon(1S + 2S + 3S) \rightarrow \mu\mu$ yield by scaling the normalization for p+p collisions by $R_{p+Au} \times N_{coll}$, where R_{p+Au} is the measured R_{d+Au} [126] of the $\Upsilon(1S + 2S + 3S)$ cross section at forward and backward rapidities. These are 0.62 ± 0.29 and 0.91 ± 0.37 for the Au-going and p-going sides, respectively.

4.3.1.2 Open Charm In the p+p analysis, the charm contribution is generated with PYTHIA and POWHEG, and fitted to unlike-sign pairs in the mass region 1.4–2.5 GeV/c^2 in mass and p_T in order to obtain the normalization for the $c\bar{c}$ pairs. This method cannot be used for for p+Au collisions for three reasons.

- The combinatorial background in p+Au collisions is higher than that in p+p collisions. The statistical uncertainty of the $c\bar{c}$ normalization thus exceeds 30%.
- Besides statistical uncertainties, the systematic uncertainties on the contribution from correlated hadrons, which depend on knowledge of the hadron spectra with $p_T < 1$ GeV/c are large. This is due to the fact that there are no data to constrain the spectra in this momentum region (Sec. 4.3.2.1).
- Similarly, the low p_T component of muons from $c\bar{c}$ decays is also unconstrained by data (see below). This again leads to large systematic uncertainties.

The first two points mentioned above also prevents a measurement of $c\bar{c}$ in p+Au. However, measurements of $b\bar{b}$ and Drell-Yan are not particularly sensitive to $c\bar{c}$, as demonstrated in the p+p analysis. For these measurements, we estimate the contribution of $c\bar{c}$ in p+Au collisions as follows:

Mass and p_T distributions of $c\bar{c}$ are generated from PYTHIA and POWHEG, as in the p+p case. We absolutely normalize these, using the model dependent $c\bar{c}$ cross section obtained from fitting to data in p+p collisions (343μb for PYTHIA, 316μb for POWHEG). The uncertainty (statistical and systematic) on this normalization is $\sim$ 16%. To estimate possible modifications of the mass and pair p_T distributions of the pairs from $c\bar{c}$, we apply a weighting factor for each muon as a function of the muon p_T according to the measured R_{d+Au} [20] for inclusive heavy flavor muons. Thus, the weight of a pair is the product of the two weighting factors. The measured R_{d+Au} for inclusive heavy flavor muons is shown in Fig. 68.

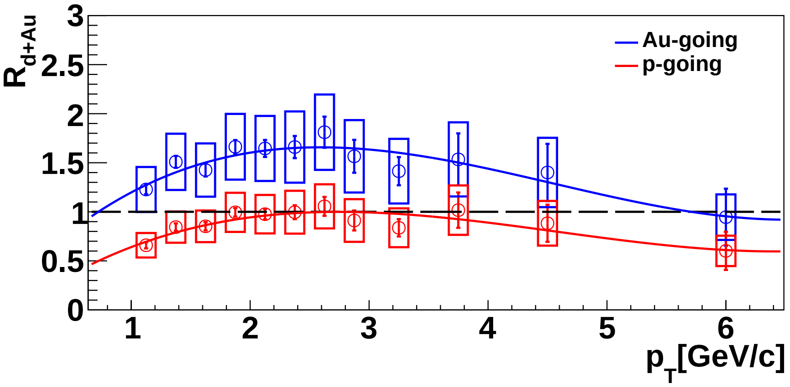

Figure 68: R_{d+Au} of single heavy flavor muons as a function of p_T [20]. The curves are fits to the data.

There are two cavaets in this procedure.

- Although $c\bar{c}$ is the main contributor to single heavy flavor muons, especially below 2 GeV/c, the measured R_{d+Au} contains contributions from $c\bar{c}$ and $b\bar{b}$.

- The nuclear modifications for d+Au and p+Au may be different.

  These two cavaets would be problematic only if the R_{p+Au} is not consistent with R_{d+Au} for inclusive muons within the assigned systematic uncertainties; or if the R_{p+Au} of single muons from $c\bar{c}$ at high p_T differs from those from $b\bar{b}$ at high p_T. Given that at high p_T the R_{d+Au}

becomes constant close to unity, the latter case is not very likely. Nevertheless, we assign systematic uncertainties conservatively, see details in Sec. 4.6.

4.3.1.3 Open bottom As described in the previous section, since the measured R_{d+Au} for single muons from inclusive heavy flavor is dominated by contributions from $c\bar{c}$ in the p_T region of interest, it serves as a good estimate for nuclear modifications in $p+Au$ for the $c\bar{c}$ contribution, but not necessarily for $b\bar{b}$. For $b\bar{b}$, due to the large mass of the b-quark compared to the muon, the initial angular and momentum distributions of the b and the $\bar{b}$-quarks do not have a large correlation with the resultant $\mu\mu$ pair mass and p_T distributions. This has been documented in detail in AN1156 [138]. Therefore, we do not expect the initial and final state nuclear modifications in p+Au to have a significant impact on the $\mu\mu$ pair distributions.

For the case of muons from $c\bar{c}$ and inclusive hadrons, a broadening of the p_T has been observed at forward and backward rapidities alike. However, there are no data to directly constrain the input p_T distributions for $b\bar{b}$. A p_T broadening has been observed at mid-rapidity for heavy flavor electrons [19] in $d + Au$ collisions, for π^0 in p+Au, d+Au and He$^3 + Au$ collisions, and for $\pi^{\pm}$, $K^{\pm}$ and $p(\bar{p})$ in d+Au collisions [18].

Due to the large mass of the b-quark, it is possible that nuclear effects on the B-hadrons are small over the entire p_T range of interest (i.e. $R_{p+Au}(p_T) \approx 1$). If that is the case, the expected modifications of the distributions of $\mu\mu$ pairs from $b\bar{b}$ are expected to be negligible. However, for the following we assume there is p_T broadening for B-hadrons. More specifically, we assume the B-hadron $R_{p+Au}(p_T)$ has a peak structure at moderate p_T and levels off at high p_T.

To assess the sensitivity of the $\mu\mu$ pair distributions to the B-hadron p_T spectrum, we explore different scenarios in which we vary the peak position, height and width of $R_{p+Au}(p_T)$ for B-hadrons. Starting with a moderate modification similar to the measured R_{d+Au} of inclusive muons (indicated by the blue dotted line in Fig. 69), the width and the height of the peak (see Fig. 69 panels (a),(b)), as well as the position of the peak (see Fig. 69 panels (c)) are varied.

Dimuon mass and p_T spectra from $b\bar{b}$ events are generated using POWHEG. Each muon pair is weighted according to the p_T of the parent B-hadrons of the muon pair. The weighting factor applied to the pair is the product of the

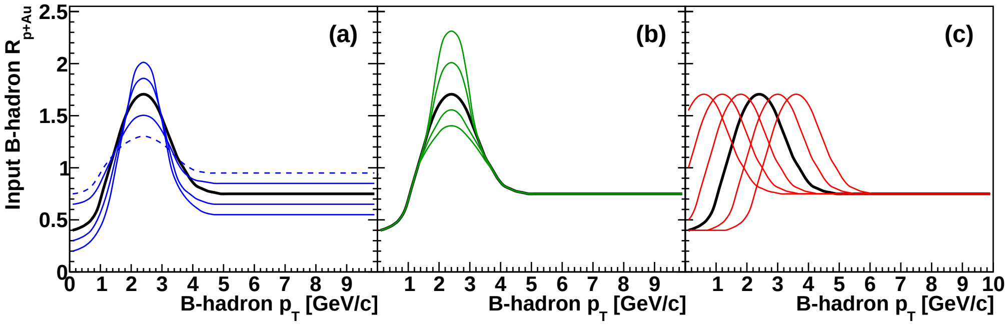

Figure 69: Different input R_{p+Au} of B-hadrons as a function of p_T used in this analysis to estimate the nuclear modifications of $b\bar{b}$. The R_{p+Au} used to generate the fitting results in Sec. 4.5.0.4 is shown in black.

weighting factor each muon, which is determined from that muon's parent B-hadron p_T, according to a chosen input B-hadron $R_{p+Au}(p_T)$ shown in Fig. 69. The weighted dimuon mass and p_T spectra are then fitted to the like-sign data and normalized, using the fitting procedure that will be discussed in Sec. 4.5.

4.3.1.4 Drell-Yan We use the same simulation set-up as for p+p collisions, as documented in Sec. 3.4.1.3. Drell-Yan does not suffer final state interactions, we therefore assume that any possible modification of the distributions comes from initial state effects, which are expected to be small. The initial k_T is varied from 0.9 to 1.3 GeV/c to estimate any nuclear modifications on the p_T spectrum.

As explained in Sec. 4.3.1.2, the $c\bar{c}$ normalization in p+Au is fixed, and we do not attempt to extract a $c\bar{c}$ measurement from the data. Hence the Drell-Yan shape does not affect the $c\bar{c}$ contribution, nor the $b\bar{b}$ contribution. The simulations for Drell-Yan only enter the analysis through the evaluation of the acceptance and efficiency corrections.

4.3.2 Unphysical $\mu\mu$ pair sources

4.3.2.1 Hadron-hadron pairs N_{hh} and Muon-hadron pairs $N_{\mu h}$ To estimate the modification of hadron-hadron pairs N_{hh} in p+Au collisions, compared to N_{hh} obtained in the p+p analysis, we apply an additional scaling factor. This scaling factor is obtained from fitting to the preliminary result of

R_{p+Au} of inclusive hadrons at $-2.2 < \eta < -1.2$ and $1.2 < \eta < 2.4$ presented in [135]. The preliminary data are shown in Fig. 70. Above the lower p_T threshold of 1.5 GeV/c, the curves are constrained by the data, while below 1.5 GeV/c the shape is not well defined. Systematic uncertainties will be discussed in detail in Sec. 4.6. For hadron-hadron pairs, the scaling factor for the pair is the product of the individual R_{p+Au} for the two muon candidates from their respective parent hadrons. For muon-hadron pairs, the scaling factor for the pair is the product of the individual R_{p+Au} for the two muon candidates, one from a hadron, and the other one from $c\bar{c}$, $b\bar{b}$ or J/ψ. If the muon arise from D or B mesons, the R_{p+Au} is estimated using measured R_{d+Au} of heavy flavor muons as discussed in Sec. 4.3.1.2; if the muon arise from a J/ψ meson, the R_{p+Au} is estimated using preliminary results for p+Au collisions as discussed in Sec. 4.3.1.1.

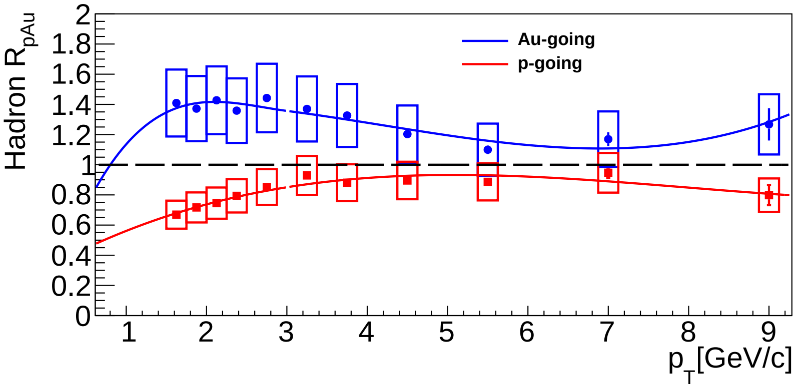

Figure 70: R_{p+Au} of inclusive hadrons as a function of p_T for the Au-going $(-2.2 < \eta < 1.2)$ and p-going. The curves are fits to the data.

4.3.2.2 Combinatorial Pair Background In p+p collisions, tracks from different events are grouped together pooled in 2 cm wide z vertex position bins. In p+Au collisions, in addition to pooling in z vertex position, we also group tracks together in 20% wide centrality bins. This is because the multiplicity and event structure varies significantly with the centrality.

4.4 Simulation Framework

We use the same simulation frameworks, namely the fastMC simulations for hadron simulations, and the default PHENIX simulation framework for all other simulations. However, the multiplicity is higher in p+Au collisions than in p+p collisions. We therefore carry out systematic studies due to the higher occupancy rate, by embedding hits in real data to our simulations. This is detailed in the following section.

4.4.1 Embedding studies

4.4.1.1 μ from $K^{\pm}$ Single kaons (K^{+}, K^{-}) are generated with flat p_T spectra. The simulations are then run through a full GEANT4 simulation and the reconstruction chain with the same single cuts as in the data (*non-embedded simulations*). In order to estimate the decrease in efficiency due to the higher occupancy rate in real data, hits in the MuTr and the MuID are sampled from minimum bias data, and merged with the hits from the GEANT4 simulations. After that, single tracks are reconstructed from the merged hits (*embedded simulations*). The ratio of the reconstructed muon yield for embedded simulations to non-embedded simulations as a function of p_T is shown in Fig. 71 separately for each arm and charge.

The efficiency loss is small (5.5% for Au-going side, 1.0% for p-going side). We expect this inefficiency to increase by approximately a factor of two for pairs. No charge or p_T dependency on efficiency loss is observed.

4.4.1.2 $\mu\mu$ from $b\bar{b}$ To assess the effect of occupancy on muon pair spectra, we also run $b\bar{b}$ simulations and embed the simulated hits with MuTr and MuID hits from real data. The ratio of the number of reconstructed pairs from embedded simulations to non-embedded simulations as a function of mass is shown in Fig. 72 for both arms. The ratio is constant with mass, 0.885 for the Au-going side and 0.975 for the p-going side, consistent to within 1% of the values (multiplied by a factor of two) obtained using single hadron simulations.

The $\mu\mu$ yield from $b\bar{b}$ is obtained in the mass region 3.5–10.0 GeV/c^2 as a function of $\Delta\phi$ and pair p_T. The ratio of the number of reconstructed pairs from embedded simulations to non-embedded simulations as a function of $\Delta\phi$ and p_T in this mass region is shown in Fig. 73 and 74 respectively. While the ratio is constant as a function of $\Delta\phi$, we see that the ratio increases by

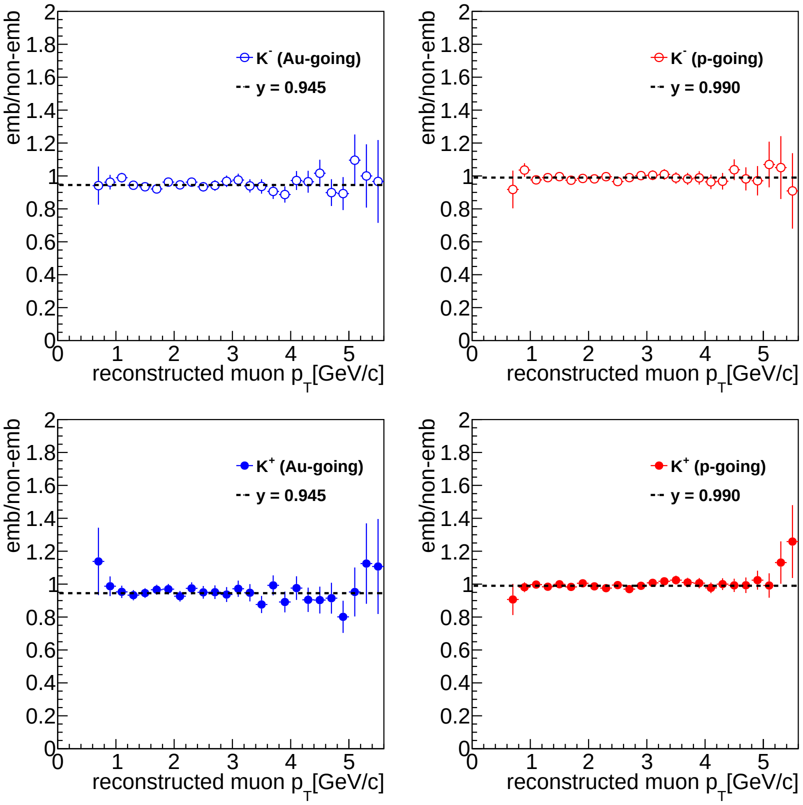

Figure 71: Ratio of number of reconstructed muons from embedded to non-embedded simulations as a function of reconstructed muon p_T for different charges and arms. A constant is fitted to guide the eye.

approximately 10% from 0 GeV/c to 5 GeV/c. Therefore, we apply a factor $\alpha = 0.885 \pm 0.05$ and $\alpha = 0.975 \pm 0.05$ to account for inefficiency due to occupancy effects to subsequent acceptance and efficiency corrections.

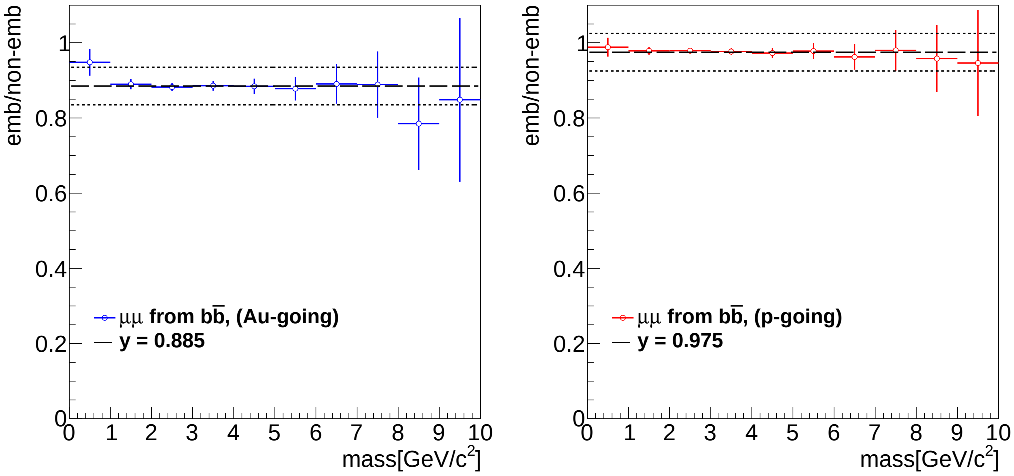

Figure 72: The ratio of number of reconstructed pairs from embedded to non-embedded simulations as a function of mass for different arms.

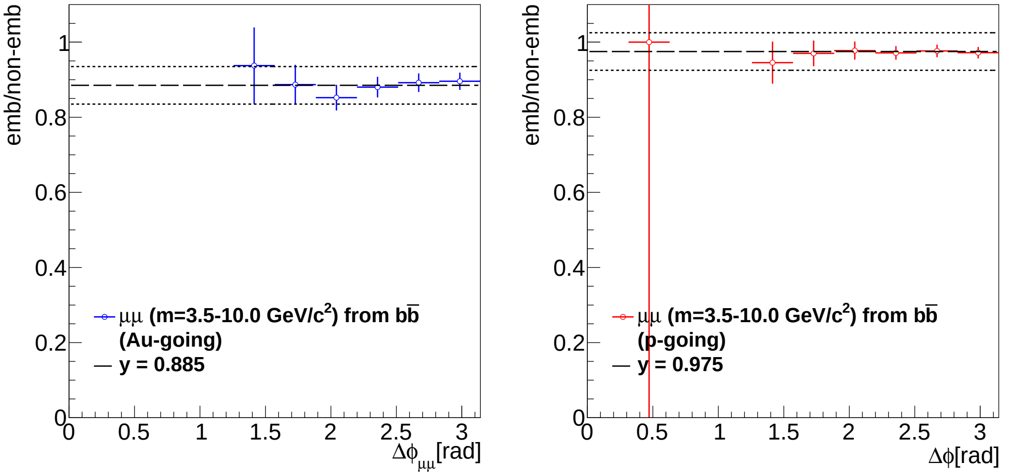

Figure 73: The ratio of number of reconstructed pairs from embedded to non-embedded simulations as a function of $\Delta\phi$ in the mass region 3.5-10.0 GeV/c^2 for different arms.

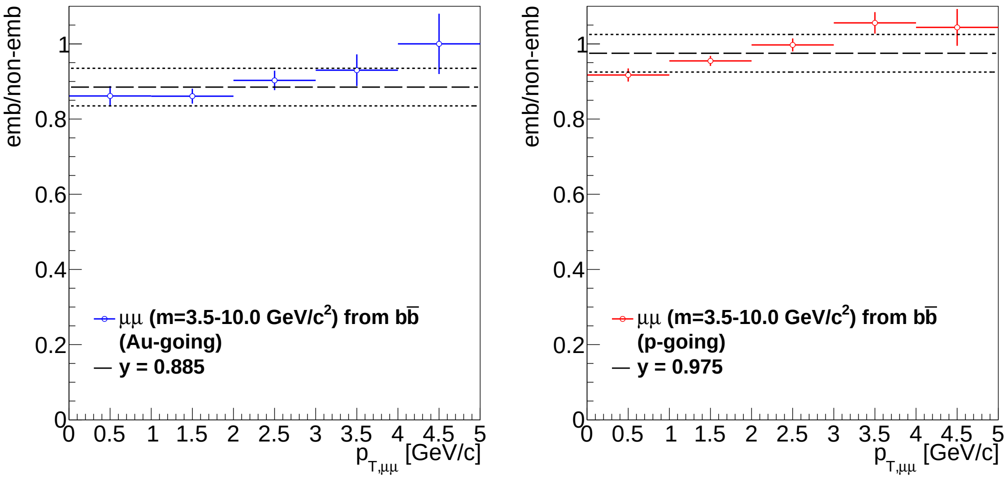

Figure 74: The ratio of number of reconstructed pairs from embedded to non-embedded simulations as a function of pair p_T in the mass region 3.5-10.0 GeV/c^2 for different arms.

4.5 Bottom and Drell-Yan Cross-Sections Extraction

4.5.0.3 Fit strategy In the p+p analysis, we have fitted contributions iteratively from hadrons, $c\bar{c}$, $b\bar{b}$ and Drell-Yan, with four free parameters κ_h, $\kappa_{c\bar{c}}$, $\kappa_{b\bar{b}}$ and κ_{DY}, utilizing both unlike- and like-sign muon pairs. In principle such a strategy is applicable for p+Au collisions as well.

However, due to the larger combinatorial background in p+Au collisions, the signal to background is significantly lower in p+Au collisions, especially for the charm mass region. The statistical accuracy for the charm normalization is poor ($\Delta\kappa_h \approx 50\%$). Hence, the benefit of constraining the charm contribution using the intermediate mass region that is present in p+p collisions, is not applicable to p+Au collisions. The large statistical and systematic uncertainties from the hadronic components also prohibits a measurement of $c\bar{c}$ using pairs in the intermediate mass region; for p+Au collisions we focus on measurements of $b\bar{b}$ and Drell-Yan only, where the hadronic background is non dominant.

In p+p, we have separated the hadronic pairs, generated from PYTHIA interfaced to the fastMC into a correlated, jet-like component, and an uncorrelated, combinatorial component via the ZYAM procedure. However, the event structure in p+Au collisions is different from that in p+p collisions; while the correlated jet-like component approximately scales as the number of binary collisions, the uncorrelated combinatorial component certainly does not.

To circumvent these issues, we modify the p+p analysis as follows. We absolutely normalize the contributions from $c\bar{c}$ and correlated hadrons, by first, scaling the normalizations obtained in the p+p analysis by the number of binary collisions and then, weighting by additional nuclear modification factors as detailed in Sec. 4.3.2.1 and 4.3.1.2 respectively. Since a $c\bar{c}$ measurement is not feasible for p+Au collisions, we only fit using the like-sign pairs, with two free parameters, κ_h and $\kappa_{b\bar{b}}$, the normalization factors for the combinatorial background and $b\bar{b}$ pairs respectively.

The like-sign data and simulations are divided into mass-p_T-z_{vtx} bins. The combinatorial background and $b\bar{b}$ pairs are fitted to the data in the mass region 1–10 GeV/c^2. We use the log-likelihood method that is applicable to data with bins having few or zero entries. The parameters κ_h and $\kappa_{b\bar{b}}$ are varied to minimize the negative log-likelihood defined by:

$$\begin{aligned} ln\mathcal{L}(\kappa_{b\bar{b}}, \kappa_h) &= \sum_i y_i lnC(i; \kappa_{b\bar{b}}, \kappa_h) - \sum_i C(i; \kappa_{b\bar{b}}, \kappa_h), \\ C(i; \kappa_{b\bar{b}}, \kappa_h) &= \kappa_{b\bar{b}} N_{b\bar{b}}(i) + \kappa_h N_{comb}(i) + N_{coll} \times \kappa_{h,pp} N_{cor}(i), \end{aligned} \tag{32}$$

where N_{coll} is the number of binary collisions and $\kappa_{h,pp}$ is the normalization for the correlated hadronic background obtained in p+p collisions.

4.5.0.4 Fit Results Example fit results using the following simulation configurations are shown: $c\bar{c}$ and $b\bar{b}$ generated using POWHEG and weighted with nuclear modifications of light hadrons, charm and bottom shown in Fig. 70, 68 and 69 respectively. Variations of simulation settings and nuclear modifications are considered in the evaluation of systematic uncertainties, which will be discussed in Sec. 4.6. p_T integrated mass spectra of $\mu^{\pm}\mu^{\pm}$ pairs are shown in Figs. 75 and the mass spectra of $\mu^{\pm}\mu^{\pm}$ pairs in different p_T slices are shown in Figs. 76. Other than a small kinematic region at $m < 1$ GeV/c^2 that is not important for this analysis, the like-sign data distributions are well described by the cocktail simulation in both mass and p_T.

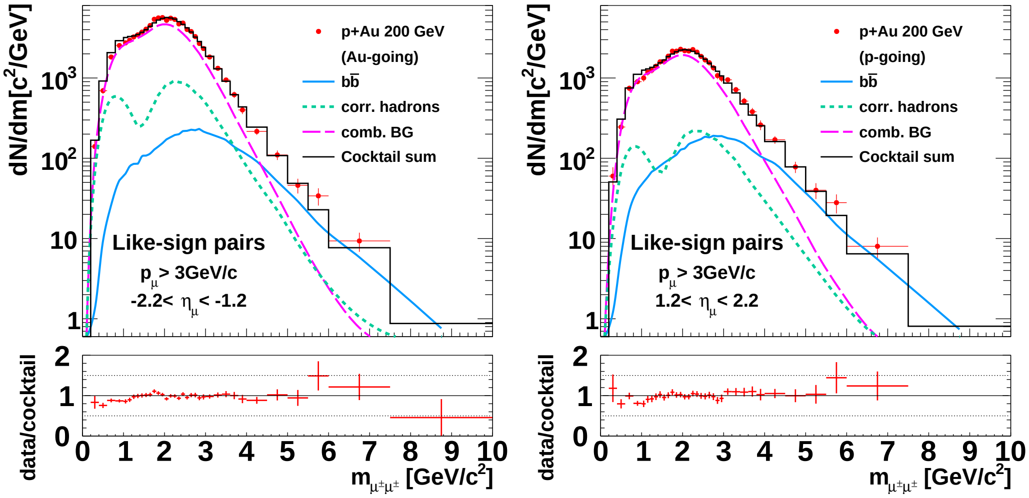

Figure 75: Inclusive like-sign $\mu\mu$ pair yield from p+Au collisions at $\sqrt{s_{NN}} =$ 200 GeV as a function of mass for the (a) south (Au-going) and (b) north (p-going) muon arms and (c) the ratio of data to expected sources.

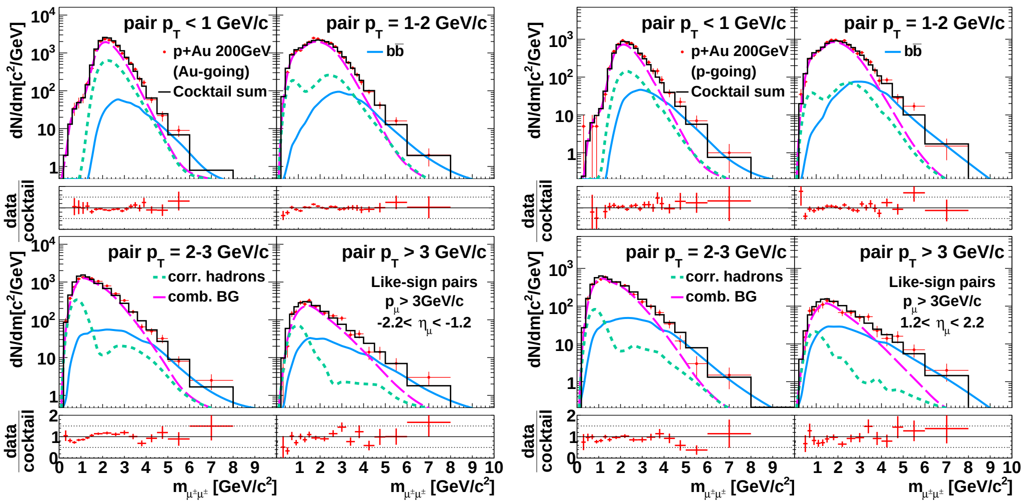

Figure 76: Inclusive like-sign $\mu\mu$ pair yield from p+Au collisions at $\sqrt{s_{NN}} =$ 200 GeV as a function of mass in different p_T slices for the (a,b,c,d) south (Au-going) and (b) (i,j,k,l) north (p-going) muon arms. Panels (e,f,g,h) and (m,n,o,p) shows the ratio of data to expected sources for the south and north arms respectively.

4.5.1 Signal extraction and acceptance and efficiency corrections

4.5.1.1 Azimuthal correlations and pair p_T of $\mu^\pm\mu^\pm$ from $b\bar{b}$ The azimuthal opening angle distribution and pair p_T distributions for $\mu^\pm\mu^\pm$ pairs from the bottom mass region is shown in Fig. 77. The number of like-sign pairs from bottom decays $N^{\pm\pm}_{b\bar{b}}$ is determined as in the p+p case using Eq. 23 and the yield is calculated according to the following:

$$\frac{d^3N}{dX_{\mu\mu}d\eta_{\mu,1}d\eta_{\mu,2}} = \frac{N^{\pm\pm}_{b\bar{b}}}{\Delta X_{\mu\mu}\Delta\eta_{\mu,1}\Delta\eta_{\mu,2}} \cdot \frac{C_{bias}}{N_{BBC}} \cdot \frac{1}{\epsilon_{rec}(X_{\mu\mu})}, \tag{33}$$

where $X_{\mu\mu}$ is $\Delta\phi_{\mu\mu}$ or $p_{T,\mu\mu}$, $\Delta X_{\mu\mu}$ is the corresponding bin width. $\Delta\eta_{\mu,1}$ and $\Delta\eta_{\mu,2}$ are the pseudorapidity window of the two muons and are 1. N_{BBC} is the number of minimum bias events sampled, $C_{bias} = 0.858 \pm 0.014$ is the bias factor which accounts for the correlation between hard scattering events and the increase in the charge the charge deposited in the BBC and any inefficiency in the BBC trigger. Finally, $\epsilon_{rec}(X)$ is the reconstruction efficiency, determined using input distributions as described above and is

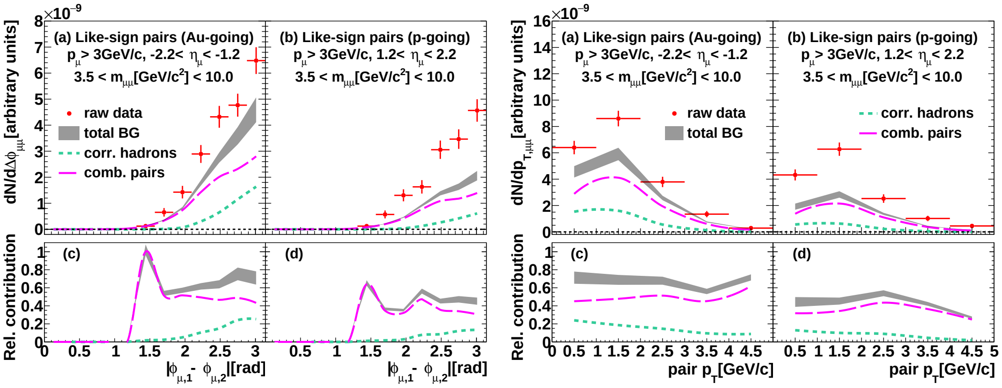

Figure 77: The like-sign $\mu\mu$ pair data in the bottom mass region as a function of (a,b) $\Delta\phi$ or (c,d) pair p_T are shown. Contributions from all known sources other than bottom decays are also shown. Panels (c,d,g,h) give the ratio of different components to the total yield. Gray bands indicate the systematic uncertainty on the sum of all contributions.

calculated by taking the ratio of reconstructed and generated yields with both the condition that both generated tracks are within the ideal muon arm acceptance ($p > 3$ GeV/c and $1.2 < |\eta| < 2.2$).

4.5.1.2 Pair mass and p_T distribution of $\mu^+\mu^-$ pairs from Drell-Yan

The number of pairs from Drell-Yan ($N_{\mathrm{DY}^{+-}}$) is obtained according to Eq. 24. The background contributions as a function of pair mass or p_T are shown in Fig. 78. The per nucleon cross sections $\frac{d^2\sigma}{dmdy}$ and $\frac{1}{2\pi p_T}\frac{d^2\sigma}{dmdp_T}$ are evaluated as follows:

$$\frac{d^2\sigma}{dmdy} = \frac{N_{\mathrm{DY}}^{+-}}{\Delta m \Delta y} \cdot \frac{C_{bias} \cdot \sigma_{inel}^{pAu}}{N_{\mathrm{BBC}} \cdot A} \cdot \frac{\beta(m,y)}{acc \times \epsilon_{\mathrm{rec}}(m,y)}, \tag{34}$$

$$\frac{1}{2\pi p_T}\frac{d^2\sigma}{dydp_T} = \frac{N_{\mathrm{DY}}^{+-}}{2\pi p_T \Delta y \Delta p_T} \cdot \frac{C_{bias} \cdot \sigma_{inel}^{pAu}}{N_{\mathrm{BBC}} \cdot A} \cdot \frac{\beta(y,p_T)}{acc \times \epsilon_{\mathrm{rec}}(y,p_T)}, \tag{35}$$

where Δm, Δp_T and Δy are the bin widths in mass, pair p_T and pair rapidity respectivey. $\beta(m,y)$ and $\beta(y,p_T)$ are small correction factors estimated using

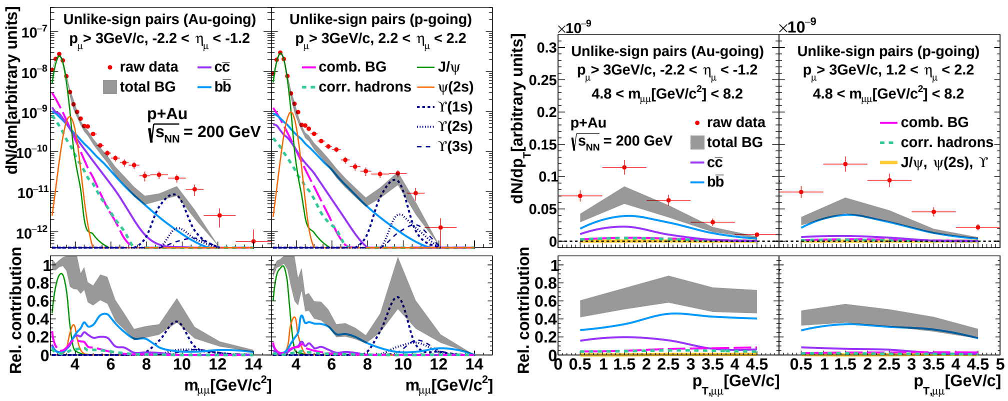

Figure 78: Unlike-sign $\mu\mu$ pair data used to determine the Drell-Yan contribution as a function of (a,b) mass or (c,d) pair p_T. Contributions from all known sources other than the Drell-Yan process are also shown. Panels (c,d,g,h) give the ratio of different components to the total yield. Gray bands indicate the systematic uncertainty on the sum of all contributions.

PYTHIA simulations that range from 0.97 to 1.03, which correct the cross section averaged over the bin to the cross section at the bin center. $acc \times \epsilon_{\rm rec}$ are pair acceptance and efficiency reconstruction factors that correct the pair yield to one unit of rapidity at $1.2 < |y_{\mu\mu}| < 2.2$. Finally, $\sigma^{pAu}_{inel} = 1.8 \pm 0.2$b is the inelastic p+Au cross selection, estimated using the relation: $\sigma^{pAu}_{inel} = A\sigma^{pp}_{inel}/N_{coll}$, where A=197 is the nucleon number, σ^{pp}_{inel} is the p+p inelastic cross section 42±3 mb and $N_{coll} = 4.7 \pm 0.3$ is the number of binary collisions estimated using Glauber calculations. All other factors are the same as in Eq. 33.

4.6 Systematic Uncertainties

As in the p+p analysis, we consider four types of sources of possible systematic uncertainties on the extraction of $\mu\mu$ pairs from $b\bar{b}$ and Drell-Yan, which are:

- on the shape of the template distributions,
- on the normalization of template distributions,
- on the acceptance and efficiency corrections,

- and on the overall global normalization.

The first three sources of systematic uncertainties are correlated on a point-to-point, but allow for a gradual change in the shape of the distributions. These uncertainties are referred to as type B. Global normalization uncertainties that affect the absolute normalization, but do not affect the shape of the distributions are quoted separately as type C.

All systematic uncertainties are quantified as standard deviations. In cases where multiple assumptions can be made (for example, the various input R_{p+Au} for B mesons shown in Fig. 69), the full analysis is repeated for the different assumptions and the spread of the results around the default analysis is used to assign the systematic uncertainties. The systematic uncertainties on the $b\bar{b}$ and Drell-Yan measurements are summarized in Fig. 79 and Fig. 80 respectively.

4.6.1 Shape of simulated distributions

4.6.1.1 Input Hadron Spectra The contributions from correlated hadrons are normalized using the normalization factor obtained in p+p collisions multiplied by N_{coll}, and subsequently scaled with the measured R_{p+Au} for inclusive hadrons as a function of the hadron p_T. The uncertainties on the normalization will be discussed in Sec. 4.6.2.5; here we focus on uncertainties on the shape of the generated spectra.

Since we apply scaling factors accounting for nuclear modifications in p+Au ($R_{p+Au,cor}$) on the generated p+p spectra ($N_{cor,p+p}$), the systematic uncertainties on the shape ΔN_{cor} can be separated into two components:

$$(\Delta N_{cor})^2 = (\Delta N_{cor,p+p})^2 + (\Delta R_{p+Au,cor})^2. \tag{36}$$

The uncertainties on the p+p spectra are estimated using mid-rapidity and very-forward pion and kaon measurements, here we refer to Sec. 3.10 for full details. For the estimated nuclear modifications, systematic uncertainties are assigned using the variations of the weighting factors within the systematic limits of the measured R_{p+Au}. These systematic uncertainties affect the $b\bar{b}$ yield as well as the Drell-Yan yield; even though hadrons are not a dominant background component in the Drell-Yan mass region, the $b\bar{b}$ background can affect the measured Drell-Yan yield. We estimate uncertainties in the input hadron spectra with three sets of variations, detailed as follows:

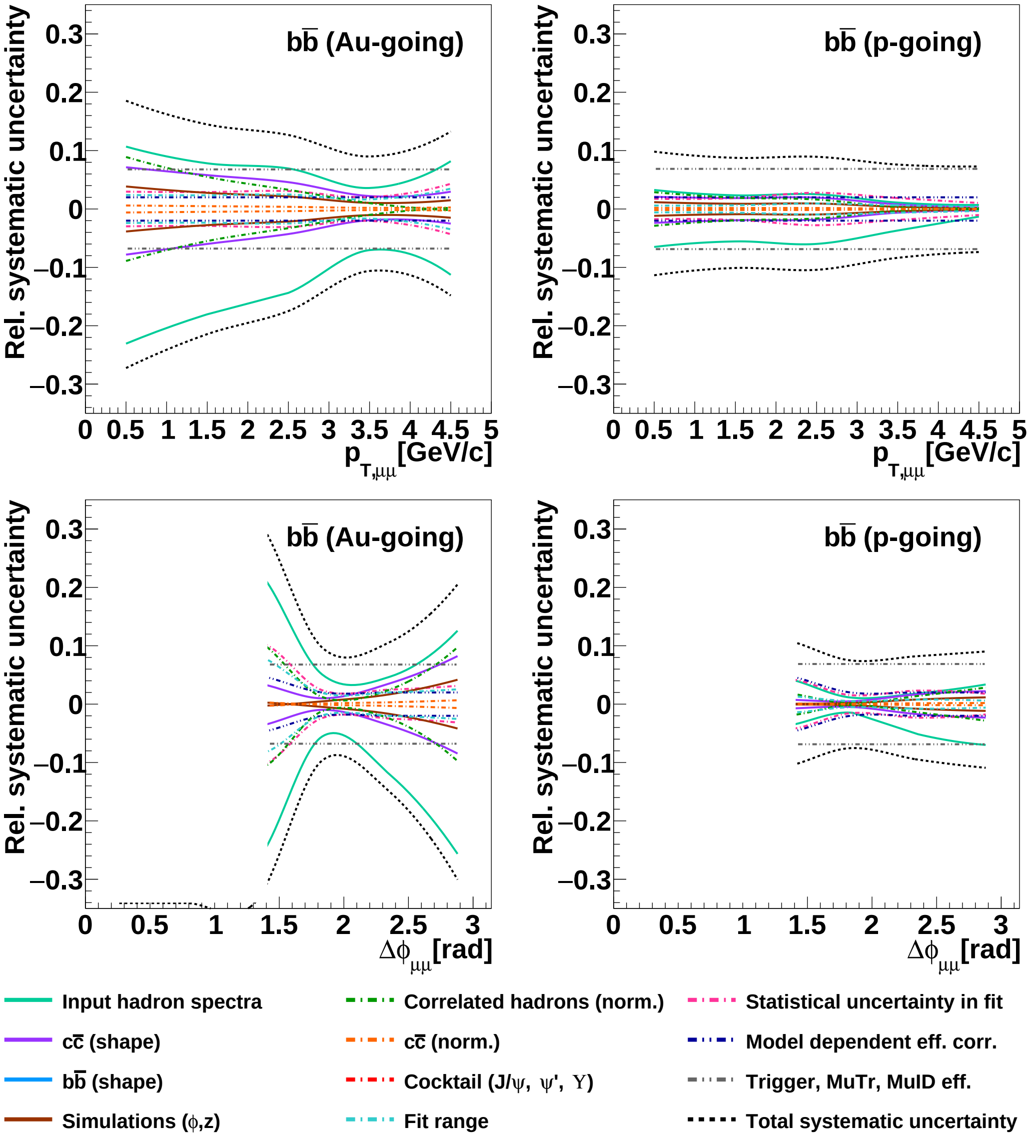

Figure 79: Relative systematic uncertainties for $b\bar{b}$ measurements as a function of $\Delta\phi_{\mu\mu}$ or $p_{T,\mu\mu}$. The shaded regions are excluded from the respective measurements.

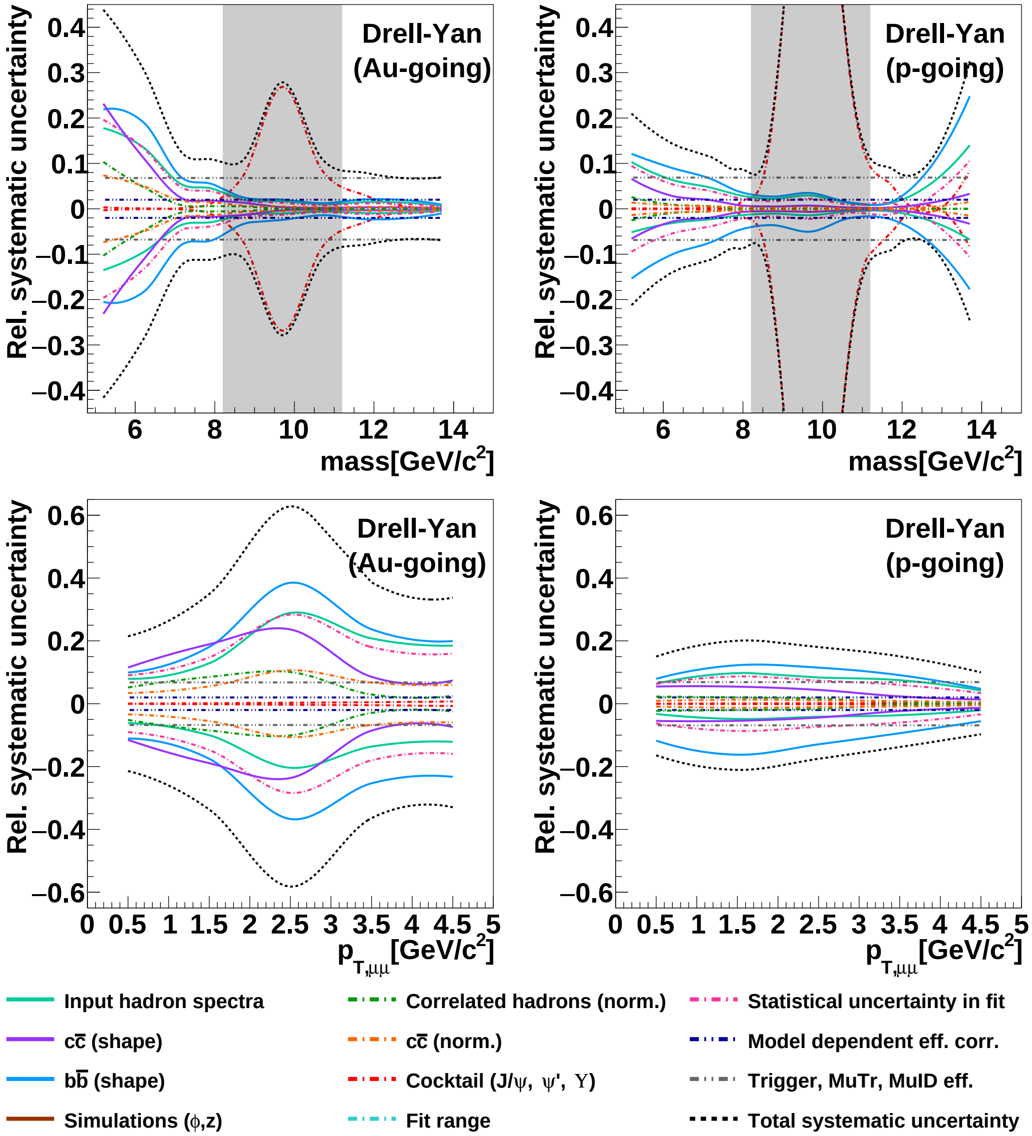

Figure 80: Relative systematic uncertainties for Drell-Yan measurements as a function of mass or $p_{T,\mu\mu}$. The shaded regions are excluded from the respective measurements.

- Shift all R_{p+Au} data points up or down by one sigma of the assigned systematic uncertainty and fit. See Fig. 81.
- Vary the slope of the R_{p+Au} data points such that data points at the boundaries (i.e. $p_T = 1.6$ GeV/c and $p_T = 9.0$ GeV/c) move up and down, or down and up, by one sigma of the systematic uncertainties. See Fig. 82.
- Vary the extrapolated R_{p+Au} in the p_T region 0.6 GeV/c to 1.5 GeV/c, where there are no measurements. See Fig. 83. The lower limit for the R_{p+Au} at $p_T = 0.6$ GeV/c is 0.3 for both arms, which is somewhat unphysical and very conservative. We do not consider unphysical cases where the R_{p+Au} rise as we go lower in p_T.

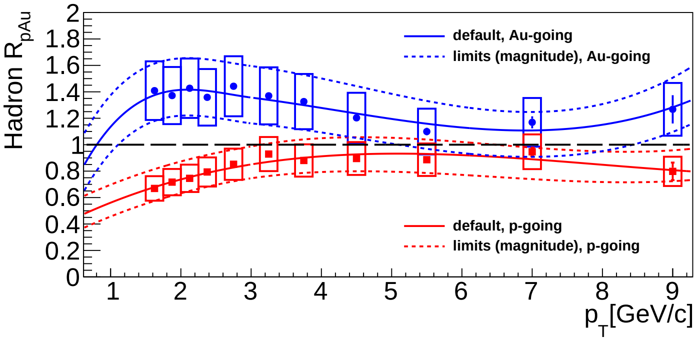

Figure 81: R_{p+Au} of inclusive hadrons as a function of p_T for the Au-going ($-2.2 < \eta < 1.2$) and p-going directions. Uncertainty bands corresponding to an overall shift in the data points are shown.

The full analysis procedure is repeated for the three cases. Assuming that half of the systematic uncertainties on the data points give an overall shift and half give a slope change, we assign the systematic uncertainty on our measure yields as the quadrature sum of these two sources of uncertainties divided by $\sqrt{2}$. We then add the quadrature the uncertainty associated to low p_T extrapolation.

4.6.1.2 Input Charm Spectra The charm contribution is normalized using the normalization factor obtained in p+p collisions scaled by N_{coll}, and in addition, scaled with the measured R_{d+Au} as a function of the muon p_T.

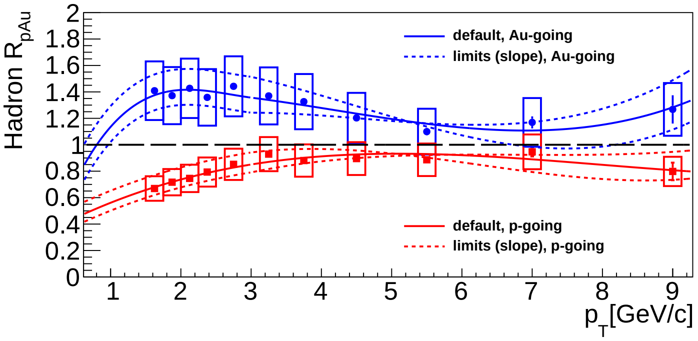

Figure 82: R_{p+Au} of inclusive hadrons as a function of p_T for the Au-going $(-2.2 < \eta < 1.2)$ and p-going directions. Uncertainty bands corresponding to variations in the slope of the data points are shown.

Besides a systematic uncertainty of 16% in the normalization (see Sec. 4.6.2.4), there are also systematic uncertainties in the shape of the mass and p_T distributions.

These uncertainties affect the $b\bar{b}$ yield via muon hadron pairs from $c\bar{c}$, and affect the Drell-Yan yield via open heavy flavor pairs from $c\bar{c}$. To estimate these uncertainties, we first shift all R_{d+Au} data points by one sigma up or down by one sigma of systematic uncertainty. The analysis is repeated with this varied set of R_{d+Au}. We then vary the slope of the R_{d+Au} data points such that the data points at the two boundaries move up and down, or vice versa, by one sigma of systematic uncertainty. These variations, as well as the central fit, are shown in Fig. 84. The final assigned systematic uncertainty is the quadrature sum of these two extreme cases divide by $\sqrt{2}$. Since $c\bar{c}$ is enhanced for the Au-going side but suppressed for the p-going side, this systematic uncertainty is much larger for the Au-going side compared to the p-going side. We do not consider uncertainties in extrapolating to lower p_T as for the hadron case, because the $p_T < 1$ GeV/c muons $c\bar{c}$ contribution is negligible in the kinematic range in which the measurements are extracted.

4.6.1.3 Input bottom spectra The $b\bar{b}$ contribution is an important background for the Drell-Yan measurement, extracted using unlike-sign pairs in the high mass region. The method of estimating the R_{p+Au} of B-hadrons, and propagating the input R_{p+Au} of B-hadrons to an R_{p+Au} of muon pair mass and p_T spectra has been discussed above, and the resultant simulated

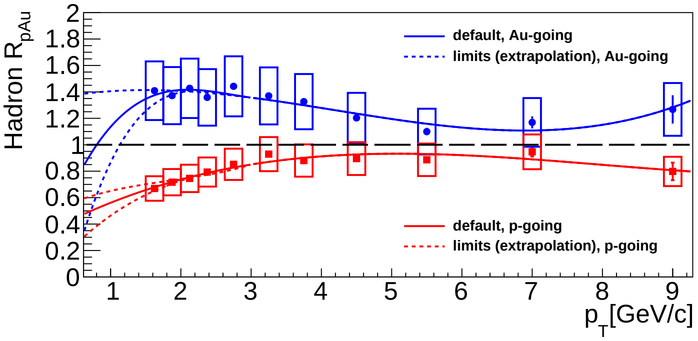

Figure 83: R_{p+Au} of inclusive hadrons as a function of p_T for the Au-going ($-2.2 < \eta < 1.2$) and p-going directions. Uncertainty bands corresponding to variations associated to low p_T extrapolation.

R_{p+Au} for unlike-sign pairs in the Drell-Yan mass region, obtained from this procedure are shown in Fig. 85.

One can see that variations in the peak position lead to larger variations in the higher mass and low p_T, while variations in the peak height and width has a larger effect at high p_T. We take the mean of all the variations as the central values of our estimation, and as a conservative measure, take the extreme variation for each mass or pair p_T bin as the systematic limit. The systematic uncertainties in the $b\bar{b}$ background are then propagated to the Drell-Yan yield.

4.6.1.4 FastMC simulations We assign 5% uncertainty to the $\Delta\phi$ distributions generated using the FastMC, which is estimated by comparing $\Delta\phi$ distributions of mixed pairs between FastMC and real data.

4.6.2 Normalization of simulated distributions

In addition to uncertainties due to the shape of distributions, uncertainties on the normalization of one component can affect the extracted yield of other components. The sources of such uncertainties are detailed as follows.

4.6.2.1 Fit Range The lower bound of the fit range is varied from 1.0 GeV/c^2 to 2.0 GeV/c^2. The variation on κ_h is 1.7% for the Au-going side and 1.0% for the p-going side. These propagates to uncertainties of $\sim$ 2%

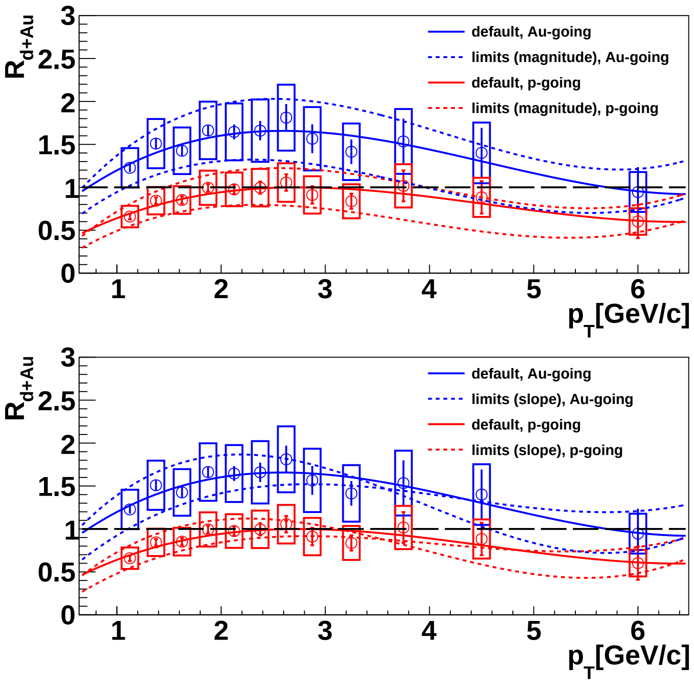

Figure 84: R_{d+Au} of single heavy flavor muons as a function of p_T [20]. The solid lines are central fits to the data, while the doted lines are for estimation of systematic uncertainties.

and $\sim 1\%$ for the $b\bar{b}$ yields for the Au-going and p-going sides respectively, and give rise to negligible uncertainties for the Drell-Yan cross sections.

4.6.2.2 Statistical uncertainty in fit result The statistical uncertainty on κ_h from fitting is 2% and 3% for the Au-going and p-going sides respectively, which translates to 3% and 2% uncertainties in the $b\bar{b}$ yields. Since the contribution from combinatorial pairs are negligible to the Drell-Yan cross sections, the statistical uncertainty on κ_h has a negligible effect. However, the statistical uncertainty on $\kappa_{b\bar{b}}$ (16% and 14% for the Au-going and p-going sides respectively) does have a significant impact on the extracted Drell-Yan cross section. These uncertainties are mass and $p_{T,\mu\mu}$ dependent, typically $\sim 15\%$ and $\sim 6\%$ respectively for the Au-going and p-going sides respectively.

4.6.2.3 Normalization of resonances Since we explicitly avoided the mass regions in which the resonances dominate, despite the large uncertainties on the normalizations of the resonances ($\sim 30\%$), the systematic uncertainties on the extracted Drell-Yan cross sections are negligible in the mass regions considered ($< 2\%$).

4.6.2.4 Normalization of $c\bar{c}$ We assign a systematic uncertainty of 16% in the absolute normalization of $c\bar{c}$, which comes from the p+p measurement. The main contributions to this uncertainty are the global normalization in p+p collisions and uncertainties in the hadronic pair background.

4.6.2.5 Normalization of correlated hadrons The uncertainty on κ_h in p+p collisions is 12%, which predominantly comes from the global normalization in p+p collisions. However, recall that we use hadron simulations with the MuTr and MuID set-up in p+p collisions instead of p+Au collisions for the fastMC. To diagnose the difference, we have verified, using $b\bar{b}$ simulations, that the ratio between the generated mass spectra using the MuTr and MuID simulation set up for p+Au and p+p, is a constant over all masses considered in this analysis, which indicates that the mass resolution is largely unaffected by the enhanced occupancy in p+Au collisions. For pairs from hadron simulations, this statement should hold true, since the muon candidates from hadrons mostly arise from decay muons at low p_T and punch-through hadrons at high p_T, both of which have similar characteristics to those of prompt muons. We assign an additional uncertainty of 5% to take into account of effects from enhanced occupancy in p+Au collisions, leading to a total of 14% uncertainty on the normalization of the hadronic background.

4.6.3 Acceptance and Efficiency

4.6.3.1 Model dependence on efficiency correction The $b\bar{b}$ measurements are corrected to represent the yield of $\mu\mu$ pairs inside the ideal muon arm acceptance. To estimate uncertainties in the efficiency corrections due to the input distributions, we compare the efficiency as a function of $p_{T,\mu\mu}$ and $\Delta\phi_{\mu\mu}$, using the same sets of input B-hadron spectra used to estimate the $b\bar{b}$ model dependence. Variations of $\sim 3\%$ in the efficiency corrections are observed and is assigned as the systematic uncertainty.

For the Drell-Yan measurements, the model dependence of the acceptance and efficiency corrections are estimated by varying the intrinsic k_T of the PYTHIA set up from 0.9 GeV/c to 1.3 GeV/c. No model dependence of the acceptance and efficiency corrections are observed.

4.6.3.2 Trigger and reconstruction efficiency As in the p+p analysis, the possible discrepancy between the software trigger emulator and the hardware trigger is quantified by comparing the real data trigger decision with the offline software trigger. The discrepancy is within 1% for both the Au-going and p-going sides. We assign the same uncertainties 1.0%(1.5%) for the Au- (p-) going sides respectively, identical to the p+p analysis.

In the p+p analysis, the systematic uncertainties assigned to the MuTr and MuID reconstruction efficiency are 4% and 2% respectively. Due to the larger occupancy in p+Au collisions, additional uncertainty may arise due to occupancy effects in the MuTr and MuID. This has been quantified by embedding real data hits into simulations as detailed in Sec. 4.4.1. We assign an uncertainty of 5% to both the Au-going and p-going sides.

4.6.4 Global normalization uncertainties

For both the $b\bar{b}$ and Drell-Yan measurements, the bias factor C_{bias} in Eqs. 33, 34 and 35 incur a normalization uncertainty of 1.6%. For the Drell-Yan measurements only, there is an additional 10% uncertainty on σ_{inel}^{pAu}, added in quadrature to the uncertainty on C_{bias}.

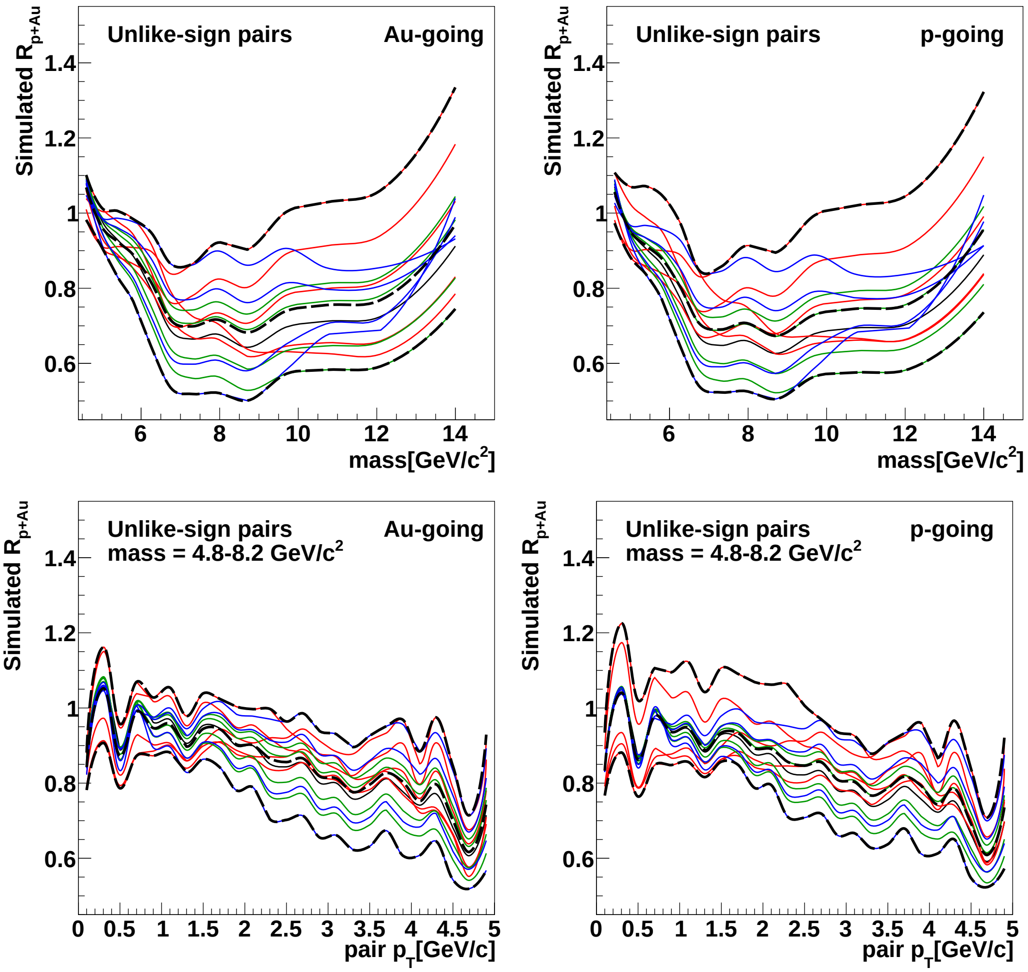

Figure 85: Simulated R_{p+Au} of unlike-sign pairs pair as a function of mass and p_T, obtained from weighting with input R_{p+Au} of B-hadrons shown in Fig. 69. The color coding is the same. Black lines indicate the systematic limits and central values.

4.7 Cross-checks

To ensure the robustness of the results, we carried out the cross-checks detailed as follows:

4.7.1 Varying the mass window

For the p+Au Drell-Yan p_T spectra, we chose a mass window of 4.8–8.2 GeV/c^2, consistent with the p+p measurement presented in the previous section. The analysis for p+p and p+Au were repeated with two other mass selections, 5.2–8.2 GeV/c^2 and 5.6–8.2 GeV/c^2. This is motivated by the fact that the relative background contributions from $c\bar{c}$ and correlated hadrons decrease as a function of mass. As shown in Fig. 86 and Tab. 7, the relative contributions from $c\bar{c}$ and correlated hadrons both drop by a factor of two when we increase the lower threshold of mass from 4.8 GeV/c^2 to 5.6 GeV/c^2.

Table 7: Relative contributions of Drell-Yan background components as a function of p_T for three different mass selections.

mass interval [GeV/c^2]	N_{cor}/N_{incl}	$N_{c\bar{c}}/N_{incl}$	$N_{b\bar{b}}/N_{incl}$
Au-going			
4.8-8.2	0.043 ± 0.003	0.16 ± 0.01	0.36 ± 0.02
5.2-8.2	0.033 ± 0.003	0.14 ± 0.01	0.37 ± 0.03
5.6-8.2	0.026 ± 0.003	0.11 ± 0.01	0.35 ± 0.03
p-going			
4.8-8.2	0.015 ± 0.001	0.060 ± 0.003	0.30 ± 0.02
5.2-8.2	0.011 ± 0.001	0.052 ± 0.003	0.29 ± 0.02
5.6-8.2	0.009 ± 0.001	0.036 ± 0.003	0.26 ± 0.02

The Drell-Yan cross sections per nucleon as a function of p_T for all three mass selections are shown in Fig. 87. In all cases, we see the same trend for R_{p+Au}: for the Au-going side R_{p+Au} scatter around unity, whereas for the p-going side, while all data points are consistent with unity, the data points for $p_T > 2$ GeV/c tend to lie above unity.

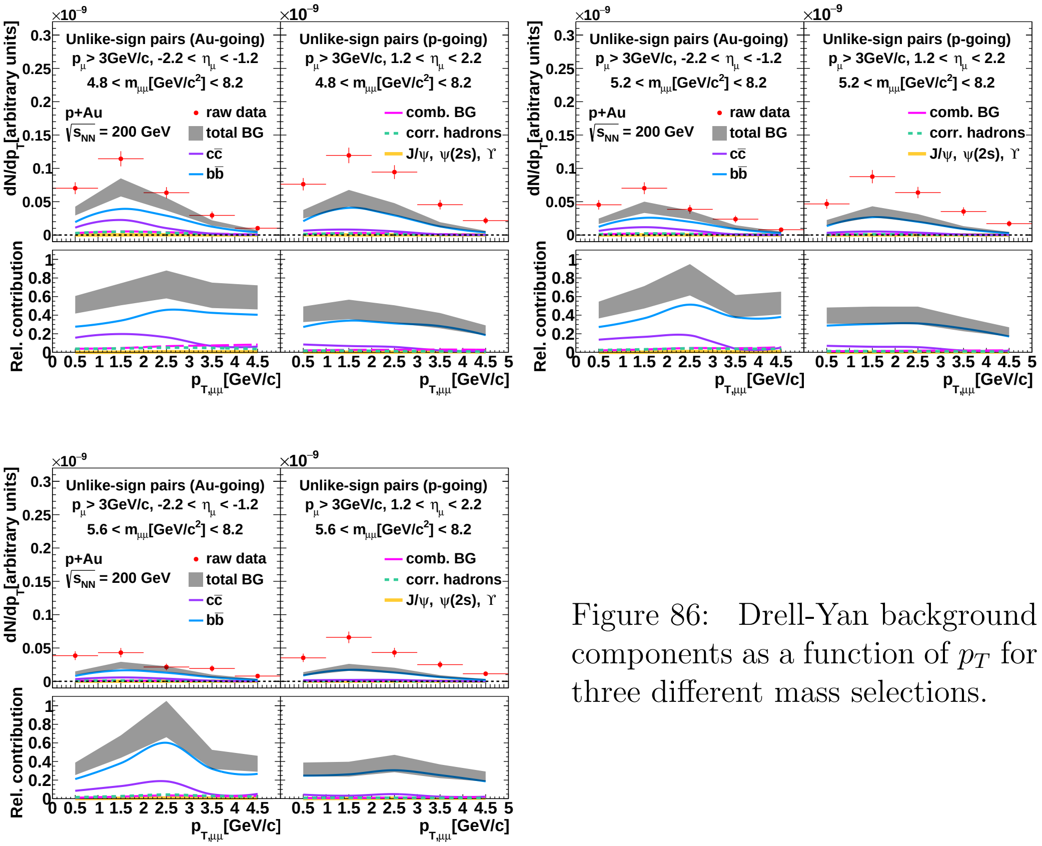

Figure 86: Drell-Yan background components as a function of p_T for three different mass selections.

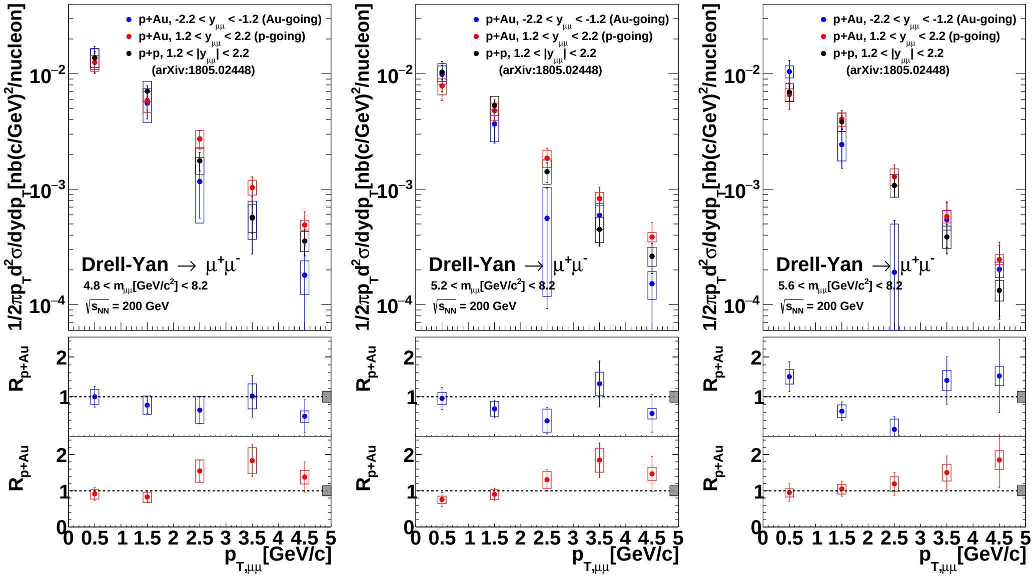

Figure 87: Drell-Yan differential cross sections as a function of p_T for three different mass selections.

4.7.2 Like-sign subtraction

For the p+p and p+Au analysis described above, the Drell-Yan counts are obtained using Eq. 24, i.e.

$$N_{\mathrm{DY}}^{+-} = N_{\mathrm{incl}}^{+-} - N_{b\bar{b}}^{+-} - N_{c\bar{c}}^{+-} - N_{J/\psi,\psi'}^{+-} - N_{\Upsilon}^{+-} - N_{\mathrm{cor}}^{+-} - N_{\mathrm{comb}}^{+-}.$$

An alternative method which is commonly used in dilepton analysis is to apply like-sign subtraction instead, according to the following:

$$N_{\mathrm{DY}}^{+-} = N_{\mathrm{incl}}^{+-} - N_{\mathrm{incl}}^{\pm\pm} - N_{c\bar{c}}^{+-} - N_{J/\psi,\psi'}^{+-} - N_{\Upsilon}^{+-} - (N_{b\bar{b}}^{+-} - N_{b\bar{b}}^{\pm\pm}) \tag{37}$$

The like-sign pairs comprise correlated hadronic pairs, combinatorial pairs and pairs from $b\bar{b}$ decays, i.e. $N_{\mathrm{incl}}^{\pm\pm} = N_{\mathrm{cor}}^{\pm\pm} + N_{\mathrm{comb}}^{\pm\pm} + N_{b\bar{b}}^{\pm\pm}$. Thus, the like-sign subtraction method assumes the following relations:

$$N_{\mathrm{comb}}^{+-} = N_{\mathrm{comb}}^{\pm\pm} \tag{38}$$
$$N_{\mathrm{cor}}^{+-} = N_{\mathrm{cor}}^{\pm\pm} \tag{39}$$

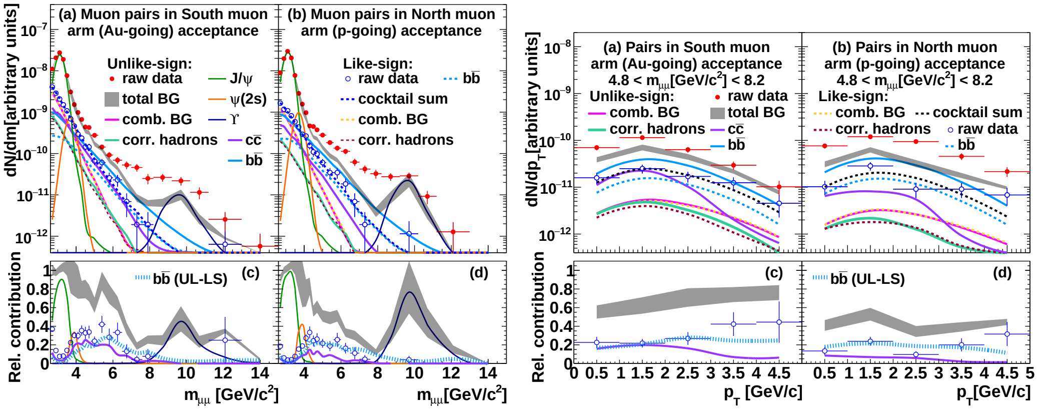

Figure 88: The unlike- and like-sign $\mu\mu$ pair data as a function of mass (a,b) or (c,d) pair p_T are shown. Contributions to unlike- and like-sign from all known sources other than the Drell-Yan process are also shown. Panels (c,d,g,h) give the ratio of different components to the total yield. Gray bands indicate the systematic uncertainty on the sum of all background components according to Eq. 37.

to hold. These relations have been verified, using the event mixing technique for N_{comb} and PYTHIA simulations for N_{cor}^{+-}, to hold well for pairs with in the kinematic regions of interest (see Fig. 88). Although this method introduces additional statistical fluctuations to the data, it decreases the reliance on hadron simulations and avoids the usage of event mixing. Moreover, the model dependence on the $b\bar{b}$ component is lessened, since the like-sign $b\bar{b}$ component is now taken directly from data.

The unlike- and like-sign data and all cocktail components are shown in Fig. 88. The subtracted yield is then corrected for acceptance and efficiency and the extracted Drell-Yan cross sections are again extracted as a function of mass and p_T using the like-sign subtraction method as shown in Figs. 89 and 90. We observe that the cross sections obtained using the like-sign method is consistent with the cross sections using the default method. We conclude that the modelling of the various backgrounds and the systematic uncertainties assigned are appropriate.

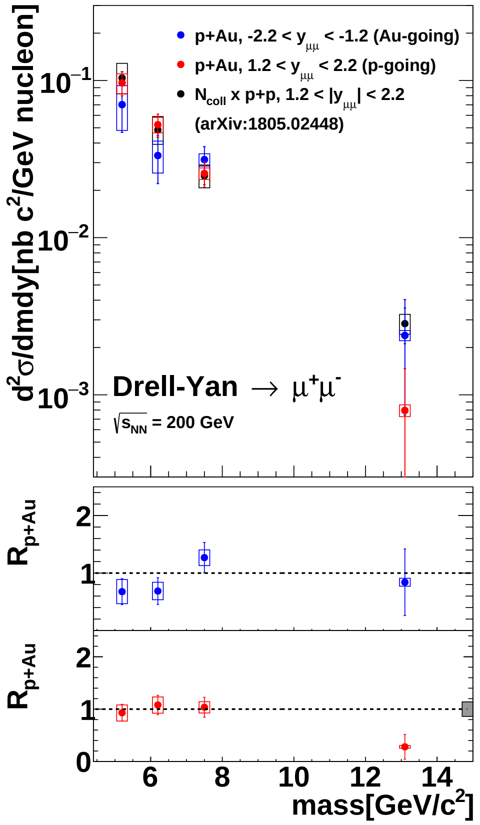

Figure 89: The corrected $\mu\mu$ yield from Drell-Yan in pair rapidity region $1.2 < |y^{\mu\mu}| < 2.2$ as a function or pair mass using the like-sign subtraction method. Results are shown separately for the south and north muon arms.

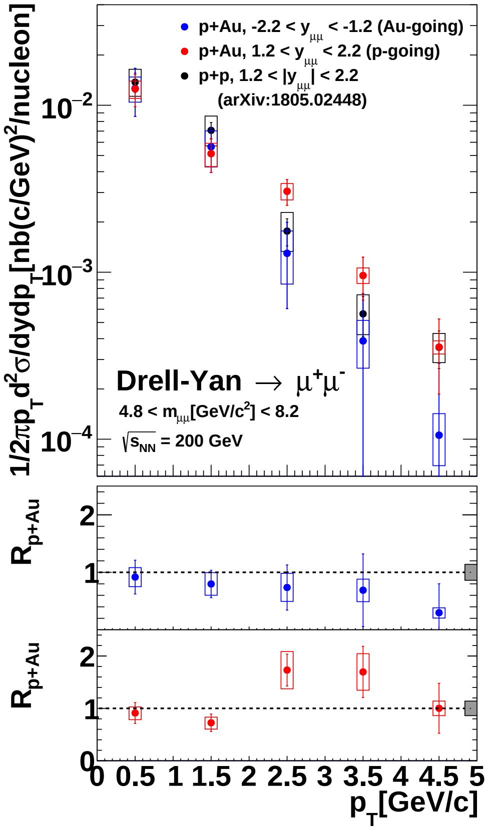

Figure 90: The corrected $\mu\mu$ yield from Drell-Yan in pair rapidity region $1.2 < |y^{\mu\mu}| < 2.2$ and mass region $4.8 < m < 8.2$ GeV/c^2 as a function of pair p_T using the like-sign subtraction method. Results are shown separately for the south and north muon arms.

5 Results

5.1 Open Heavy Flavor

5.1.1 Bottom cross section in p+p collisions

In order to determine the heavy flavor production cross sections, the $\mu\mu$ pair data need to be extrapolated from the small kinematic region covered by the PHENIX detector to the full phase space. The use of model calculations is necessary for this extrapolation. For charm, the significant discrepancies between the differential distributions calculated by different models lead to a large model dependence in the extrapolation [21]. However, the model dependence is much smaller for the case of bottom production. The kinematic distributions of $\mu\mu$ pairs from $b\bar{b}$ are dominated by decay kinematics, and model dependent systematic uncertainties on the extrapolation are much less dominant. We determine the average of the bottom cross sections obtained from PYTHIA and POWHEG using the fitting procedure, and assign systematic uncertainties on model dependence according to the difference between PYTHIA and POWHEG.

The extracted cross sections using PYTHIA and POWHEG are shown in Table. 8. The first two columns display the cross sections obtained by fitting data from the south and north muon arm, which covers $-2.2 < y < -1.2$ and $1.2 < y < 2.2$, respectively. These values are extrapolated to the average rapidity of the south and north muon arms, i.e. $y = -1.7$ and $y = +1.7$, respectively.

Table 8: $\sigma_{b\bar{b}}$ from fit using different models. Only statistical uncertainties are shown.

	south	north	combined
PYTHIA $\sigma_{b\bar{b}}$ [μb]	3.71 ± 0.29	3.42 ± 0.35	3.59 ± 0.22
POWHEG $\sigma_{b\bar{b}}$ [μb]	3.94 ± 0.31	3.94 ± 0.40	3.94 ± 0.25
average $\sigma_{b\bar{b}}$ [μb]	3.82 ± 0.30	3.65 ± 0.38	3.75 ± 0.24

The results are shown in Fig. 91 and compared to other PHENIX bottom-cross-section measurements via various channels ($B \to J/\psi$ [87], dielectrons [21], e-h correlations [88]), which cover different rapidity regions. These

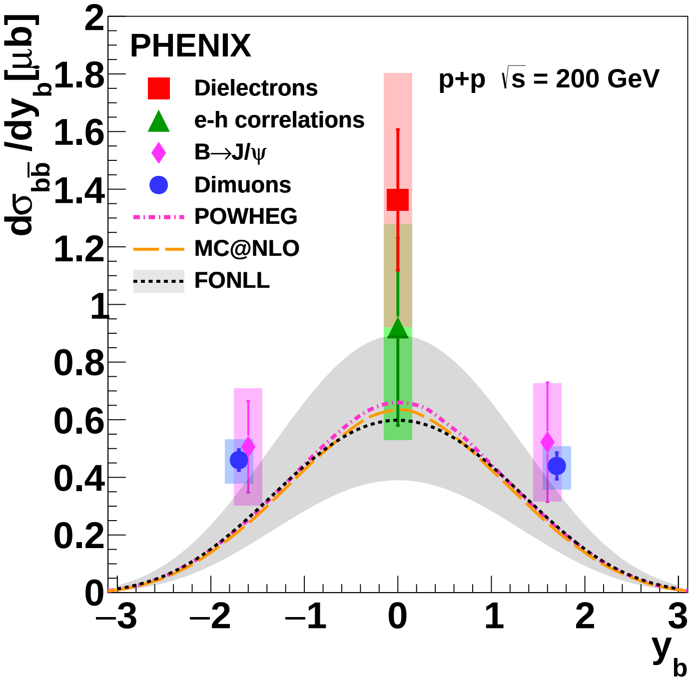

Figure 91: Rapidity density $d\sigma_{b\bar{b}}/dy_b$ in p+p collisions at $\sqrt{s} = 200$ GeV measured in PHENIX via various channels compared to theoretical calculations. Here y_b is the rapidity of a b quark.

measurements are compared to differential cross sections computed using FONLL [66], MC@NLO [69] and POWHEG [68]. In all the theoretical calculations, we adopted the "standard" value of the bottom quark mass, $m_b = 4.75$ GeV/c^2 [70]. This choice of the bottom quark mass is primarily motivated by the mass of $\Upsilon(1S)$. It has been shown in previous studies that the NLO pQCD calculations using this standard value of m_b can reproduce the p+A and π+p bottom cross sections at low energies reasonably well to within large experimental and theoretical uncertainties [139]. The uncertainty in the renormalization and factorization scale, bottom quark mass and PDF choices contribute to the theoretical uncertainties. We observe that the model dependence on the differential bottom cross section as a function of rapidity, which is mainly due to the uncertainties in the PDFs, is small ($< 10\%$). The shaded band correspond to theoretical uncertainties that are estimated

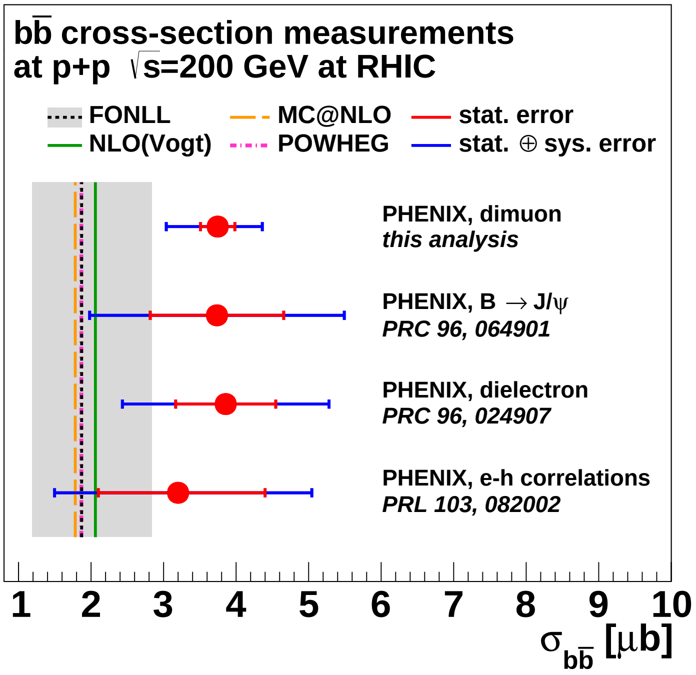

Figure 92: Bottom cross section $\sigma_{b\bar{b}}$ in p+p collisions at $\sqrt{s}$ = 200 GeV measured at RHIC via various channels compared to NLL and NLO calculations. The gray band represents the systematic uncertainty in the FONLL calculation.

using a FONLL calculation, which includes uncertainties on the renormalization and factorization scales, bottom quark mass (varied between 4.5 and 5.0 GeV/c^2), and PDFs. These uncertainties are added in quadrature. We observe that the measurements at $\sqrt{s}$ =200 GeV tend to prefer the upper limit of this uncertainty band.

We combine the measurements using the two muon arms to give a more precise measurement of the total bottom cross section, $\sigma_{b\bar{b}}[\mu b] = 3.75 \pm 0.24(stat)^{+0.35}_{-0.50}(syst) \pm 0.45(global)$, which is the most precise measurement of the bottom cross section at $\sqrt{s}$ = 200 GeV to date. We compare this measurement to other total bottom cross section measurements at RHIC in Fig. 92.

As shown in Figs. 91 and 92, all RHIC bottom cross section measure-

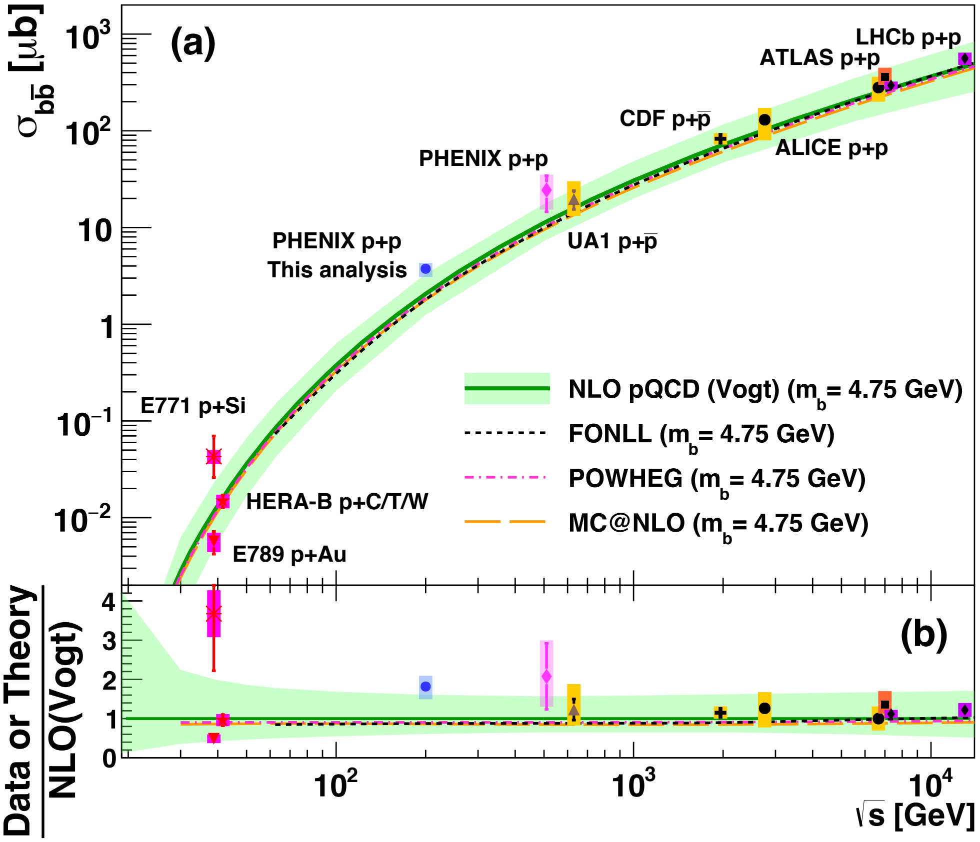

Figure 93: Bottom cross section $\sigma_{b\bar{b}}$ as a function of $\sqrt{s}$. Uncertainties due to rapidity extrapolation are not included in the LHCb measurements. Measured cross sections are compared to NLL and NLO calculations.

ments are consistent with each other. We compare to the total cross sections obtained from various next-to-leading order (NLO) or next-to-leading logarithmic (NLL) calculations, including the NLO calculation from Ref. [70]. In all cases, we use the value $m_b = 4.75$ GeV$/c^2$ for the bottom quark mass. The total bottom cross section is around a factor of two higher than all theoretical calculations with $m_b = 4.75$ GeV$/c^2$.

These measurements can also be compared to the global trend of the $b\bar{b}$ cross section as a function of $\sqrt{s}$ [140, 141, 142, 93, 143, 144, 95, 145, 91, 92], as shown in Fig. 93. The variation of the different theoretical calculations is less than 8% despite spanning 5 orders of magnitude in cross section and

3 orders of magnitude in beam energy. At beam energies larger than 2 TeV, the measured cross sections from the Tevatron and the LHC are in good agreement with the central values of the theoretical calculations, in contrast to measurements at $\sqrt{s} = 200$ GeV at RHIC. The weighted average of the $\sigma_{b\bar{b}}$ measurements at RHIC, obtained from the unconstrained averaging procedure adopted by the PDG [1], is 3.8 ± 0.5 μb, which is $> 3\sigma$ higher than the theoretical central values (see Fig. 92). This may suggest that while the current central or default settings of these theoretical calculations may reasonably describe the measured bottom cross sections at high beam energies, they fail to describe the cross section at $\sqrt{s} = 200$ GeV.

It is found that an input bottom quark mass $m_b = 4.12 \pm 0.11$ GeV/c^2 is required for POWHEG to reproduce the bottom cross section measured at $\sqrt{s} = 200$ GeV. This mass is significantly lower than the pole mass of the bottom quark, 4.78 GeV/c^2 [1], hence it is unlikely that the discrepancy between the measured bottom cross section and the theoretical calculations can be explained solely by the uncertainty in the bottom quark mass.

This measurement suggests that an effect which is more visible at lower beam energies may still be missing in current theoretical calculations. Future measurements at beam energies between ~ 10 GeV and ~ 1000 GeV with higher accuracy should help shed light on this issue.

5.1.2 Azimuthal opening angle and pair p_T distributions for $\mu\mu$ pairs from $c\bar{c}$ and $b\bar{b}$ in p+p collisions

The unlike-(like-)sign $\mu\mu$ pair yield from $c\bar{c}$ ($b\bar{b}$) decays in the mass ranges $1.5 - 2.5(3.5 - 10.0)$ GeV/c^2 are shown in Figs. 94 and 95 as a function of $\Delta\phi$ and pair p_T. The muons are in the nominal acceptance of $p > 3$ GeV/c and $1.2 < |\eta| < 2.2$. The yields for the forward and backward pseudorapidity regions are consistent with each other. Due to the mass selection, the $\Delta\phi$ and p_T distributions are highly correlated with each other.

The spectra for the two pseudorapidity regions are combined and compared to model calculations based on PYTHIA and POWHEG. Pairs generated by the models are filtered with the same kinematic cuts that are applied in the data analysis. The model curves are normalized using the fitting procedure discussed in Sec. 3.7. The comparison is shown in Figs. 96 and 97.

For $c\bar{c}$ the model calculations are normalized in the kinematic region $1.4 < m < 2.5$ GeV/c^2 and $p_T < 2$ GeV/c to the data. Consequently, as seen in Fig. 97, the p_T spectrum is adequately described by both PYTHIA

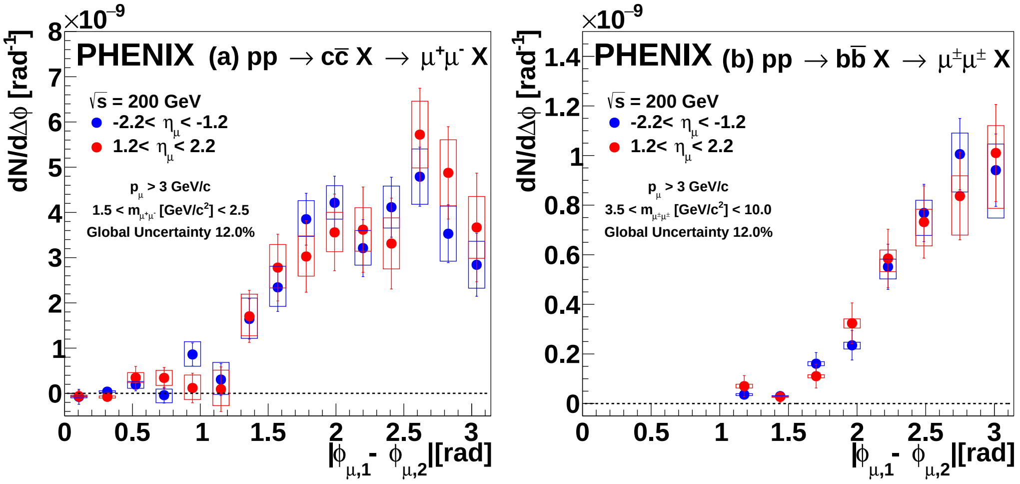

Figure 94: The corrected $\mu\mu$ yield as a function of $\Delta\phi$ from (a) charm and (b) bottom decays. The error bars correspond to statistical uncertainties, and the boxes correspond to the type B systematic uncertainties. The 12.0% type C systematic uncertainty is not shown. Results are given separately for the south and north muon arms.

and POWHEG for $p_T < 2$ GeV/c. However, for $p_T > 2$ GeV/c, the yield predicted by POWHEG is systematically higher than the data, while the yield from PYTHIA is more consistent with the data.

The larger yield predicted by POWHEG also manifests itself in the $\Delta\phi$ projection at $\Delta\phi < 1.5$. For $c\bar{c}$, the azimuthal correlation determined with POWHEG is significantly wider compared to those from PYTHIA. Again, the data favor PYTHIA in the probed kinematic region. This is particularly apparent at $\Delta\phi < \pi/2$.

Because both PYTHIA and POWHEG use the PYTHIA fragmentation scheme and very similar parton distribution functions, the differences between the model calculations must result from the underlying correlation between the c and $\bar{c}$ quarks that originate from the pQCD differential cross section calculation. Our data are more consistent with PYTHIA than with POWHEG. We note that this preference is not limited to data taken in the kinematic region accessible in this analysis; it also holds true for the mid-forward kinematic region probed by the PHENIX electron-muon measurement [22] and mid-mid kinematic region probed by the PHENIX dielectron measurement [21].

For $b\bar{b}$, PYTHIA shows a slightly wider peak in $\Delta\phi$ than POWHEG. How-

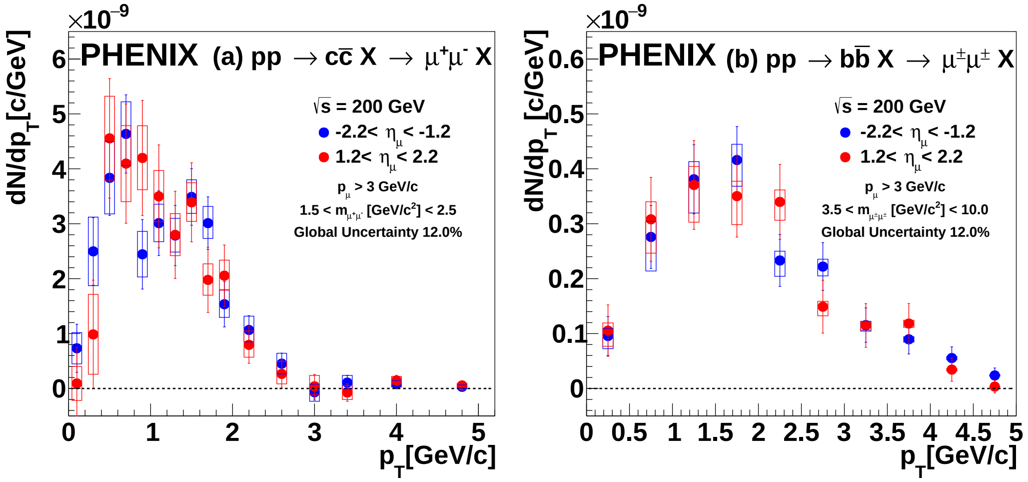

Figure 95: The corrected $\mu\mu$ yield as a function of pair p_T from (a) charm and (b) bottom decays. The error bars correspond to statistical uncertainties, and the boxes correspond to the type B systematic uncertainties. The additional 12.0% type C systematic uncertainty is not shown. Results are presented separately for the south and north muon arms.

ever, within uncertainties the data are well described by both generators in $\Delta\phi$ as well as p_T. The smaller model dependence can be traced back to the larger b quark mass, which is much larger than the muon mass [21]. For the bulk of B meson decays, the momentum of the muon is nearly uncorrelated to the momentum of the B meson. Therefore, the opening angle between two muons from $b\bar{b}$ is randomized. In other words, the distributions of $\mu\mu$ pairs from $b\bar{b}$ are mostly determined by the decay kinematics and are less sensitive to the correlation between the b and $\bar{b}$ quark.

For the PYTHIA calculation we can distinguish heavy flavor production from different processes, specifically pair creation, flavor excitation, and gluon splitting. To separate these we access the ancestry information using the PYTHIA event record. Despite the fact that the measured azimuthal opening angle and pair p_T distributions are constrained due to the limited acceptance and the mass selection, there are clear differences between the shapes generated by the different processes. The leading order pair creation features a strong back-to-back peak, whereas next-to-leading-order processes exhibit much broader distributions. For $b\bar{b}$, PYTHIA predicts negligible con-

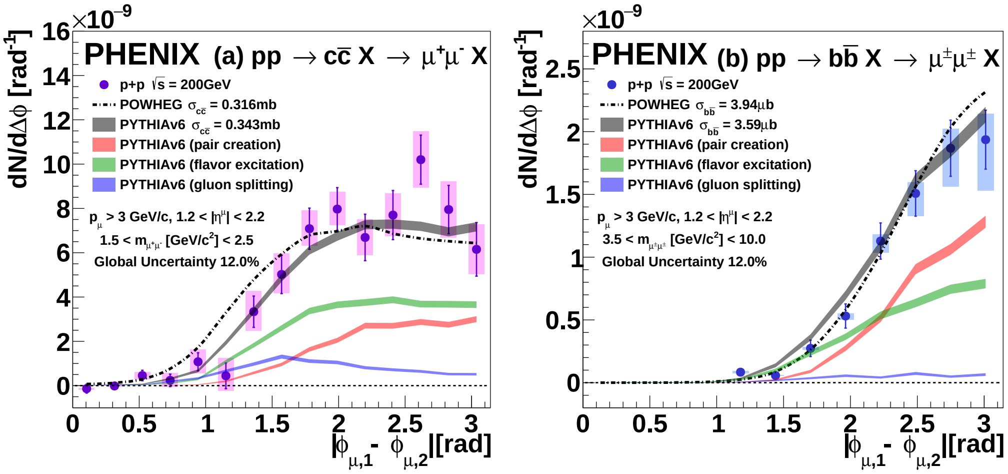

Figure 96: The corrected $\mu\mu$ yield as a function of azimuthal opening angle from (a) charm and (b) bottom decays. The data are compared to the distributions calculated with POWHEG and PYTHIA. The model calculations are normalized to the data (see text for details). For PYTHIA the $\mu\mu$ pair yield is broken down into contributions from pair creation, flavor excitation, and gluon splitting.

tribution from gluon splitting, whereas for $c\bar{c}$, there is significant contribution from gluon splitting, particularly for $\Delta\phi < 1$ and $p_T > 3$ GeV/c. For both $c\bar{c}$ and $b\bar{b}$, the default ratios and shapes of the three different processes from PYTHIA describe the data well.

Although for POWHEG a similar separation is not possible, it seems as if contributions from higher order processes with characteristics similar to gluon splitting are more frequent in POWHEG than in PYTHIA, leading to a broader azimuthal opening angle distribution and a harder p_T spectrum for pairs from $c\bar{c}$. More constraints on the $c\bar{c}$ correlations, which seem to drive the observed model differences, could be obtained from a quantitative and systematic study of heavy flavor correlations for p+p collisions at $\sqrt{s} = 200$ GeV obtained from different kinematic regions. This will be explored in an extended study as discussed in the following section.

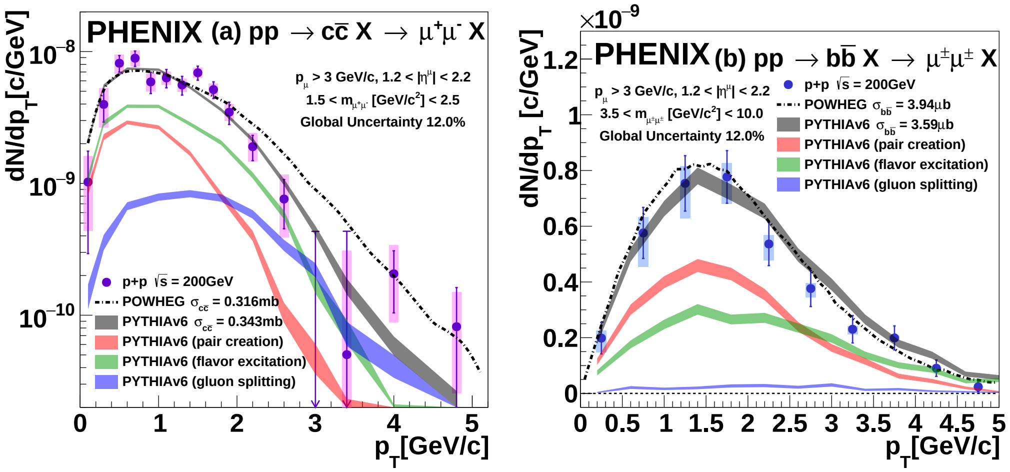

Figure 97: The corrected $\mu\mu$ yield as a function of pair p_T from (a) charm and (b) bottom decays. Presentation of the comparison to POWHEG and PYTHIA is the same as Fig. 96. The upper limits on panel (a) indicate 95% confidence level (For a data point with value d and statistical uncertainty σ, the upper limit u is is determined by the following relation: $\int_0^u f / \int_0^\infty f = 0.95$, where f is a Gaussian distribution with mean d and width σ.)

5.1.3 Extended study: Azimuthal correlations of $\mu\mu$, $e\mu$, and ee pairs in p+p collisions at from $\sqrt{s} = 200$ GeV and implications for $c\bar{c}$ and $b\bar{b}$ production mechanisms

5.1.3.1 Introduction The $\mu\mu$ data presented in this dissertation, together with the previous ee and $e\mu$ measurements cover a wide kinematic range. Here, we present an analysis of $c\bar{c}$ and $b\bar{b}$ correlations in p+p collisions at $\sqrt{s} = 200$ GeV, where we combine the $\mu\mu$, $e\mu$ and ee measurements to constrain the $c\bar{c}$ and $b\bar{b}$ production mechanisms.

5.1.3.2 Data sets used for this study

5.1.3.2.1 $\mu\mu$ For this study, we use the measured unlike-sign $\mu\mu$ yield from $c\bar{c}$ as a function of the azimuthal opening angle, and the like-sign $\mu\mu$ yield from $c\bar{c}$ as a function of the azimuthal opening angle. Fig. 98 shows the measured $\mu\mu$ yields. The measurements cover the pseudorapidity region $1.2 < |\eta_\mu| < 2.2$.

The measured yields are compared to the calculations from PYTHIA and POWHEG. PYTHIA uses LO matrix elements for the hard scattering process and implements NLO corrections with a parton-shower approach, while POWHEG uses NLO matrix elements for the hard scattering process to generate the hardest radiation, and interfaces to a parton showering program (PYTHIA in this case) to generate subsequent softer radiation [146]. For the PYTHIA calculations, contributions from pair creation (PC), flavor excitation (FE), and gluon splitting (GS) [12] are shown separately. The different processes are classified according to the number of heavy quarks at the hard vertex [12] (2, pair creation; 1, flavor excitation; 0. gluon splitting). Such a classification is applicable to PYTHIA but not to POWHEG; there is no trivial connection between the classes of processes in PYTHIA and POWHEG.

5.1.3.2.2 *ee* The lower panel of Fig. 99 shows the previously measured heavy flavor *ee* yields [21] as a function of the opening angle of the electron pair. The measured yield contains both $c\bar{c}$ and $b\bar{b}$ contributions, though the $c\bar{c}$ component is much more dominant. The measurements cover the pseudorapidity region $|\eta_e| < 0.35$. All imposed kinematic cuts are also shown in Fig. 99. The combinatorial background is estimated using the like-sign method and the correlated background is estimated using simulations with the input distributions constrained from previous measurements.

5.1.3.2.3 $e\mu$ The lower panel of Fig. 99 shows the previously measured heavy flavor $e\mu$ yields [22] as a function of the azimuthal opening angle of the electron and the muon. The measured yield contains both $c\bar{c}$ and $b\bar{b}$ contributions, though the $c\bar{c}$ component is much more dominant. The measurement cover the pseudorapidity region $|\eta_e| < 0.5, 1.4 < |\eta_\mu| < 2.1$. All imposed kinematic cuts are also shown in Fig. 99. The background (combinatorial and correlated) is estimated using the like-sign method.

5.1.3.3 Comparison of theoretical calculations with data Although the correlations of the lepton pairs are measured within limited detector acceptance and have additional kinematic constraints, a strong back-to-back peak is observed for leading order PC for both $c\bar{c}$ and $b\bar{b}$. Distributions from FE and GS are significantly broader than those from PC. To quantify the consistency with data, we calculate a modified χ^2 [147] that takes systematic uncertainties into account. We focus on the $\mu\mu$ measurements first.

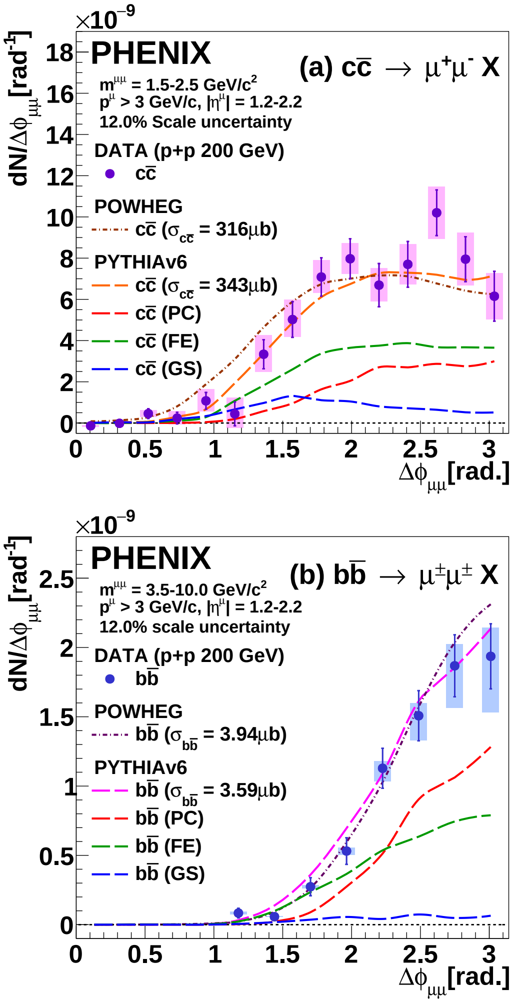

Figure 98: Dimuon azimuthal correlations from $c\bar{c}$ (a) and $b\bar{b}$ (b) compared to PYTHIA and POWHEG.

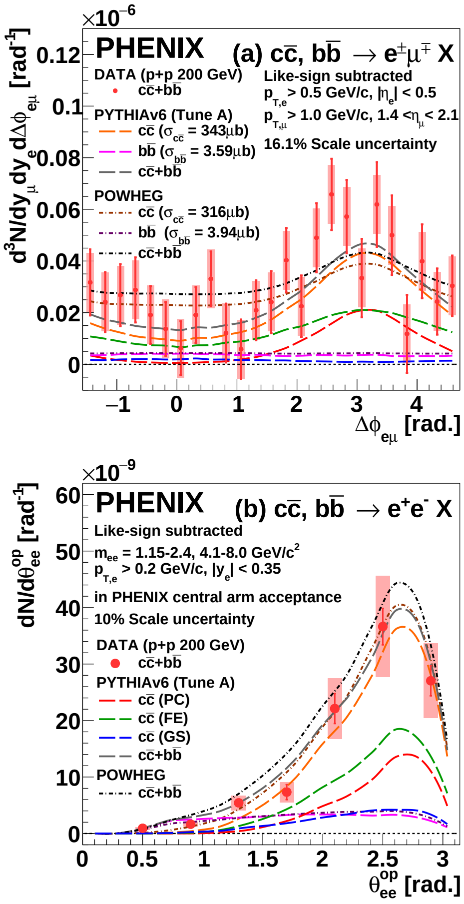

Figure 99: (a) Electron-muon azimuthal correlations from $c\bar{c}$ and $b\bar{b}$ (a) and (b) dielectron opening-angle distributions from $c\bar{c}$ and $b\bar{b}$, compared to PYTHIA and POWHEG. The legends are shared among panels (a) and (b).

For $b\bar{b}$, the χ^2/NDF values for PYTHIA and POWHEG are 9.8/7 and 7.2/7, respectively, which indicates that the the azimuthal correlations for $b\bar{b}$ are well described by both models. For $c\bar{c}$, the χ^2/NDF values of PYTHIA and POWHEG are 20.1/14 and 35.8/14, respectively. This $c\bar{c}$ data are reasonably described by PYTHIA, while the generated distributions from POWHEG seem to be slightly wider than the data.

For the ee and $e\mu$ data sets, recall that the normalizations of the PYTHIA and POWHEG comparisons to both the ee and $e\mu$ data are identical to that of the $\mu\mu$ data. Despite the fact that the phase space areas covered by the three measurements are completely different, in all cases we observe that the data are well described by PYTHIA, while the distribution from POWHEG are wider than in the data. The χ^2/NDF value obtained by comparing PYTHIA to the $c\bar{c}$ dominated ee and $e\mu$ measurements and the $c\bar{c}$ only $\mu\mu$ measurement is 59.6/47. This indicates that PYTHIA can describe both the rapidity dependence and angular correlations of $c\bar{c}$ production well. The corresponding χ^2/NDF value for POWHEG is 94.2/47. The $\mu\mu$ data is consistent with other lepton pair measurements at the same collision energy and the same collision system, and provides improved accuracy which allows the differentiation between different models calculations.

Azimuthal angle distributions of the decay lepton pairs are correlated with those of their parent heavy quark and anti-quarks. Due to the smaller mass of charm quarks, the correlations between charm quarks and their decay leptons are stronger than those between bottom quarks and their decay leptons (see Fig. 100). The differences in the distributions of the charm decay leptons indicate that the description of c-$\bar{c}$ quark correlations between PYTHIA and POWHEG is intrinsically different at the quark level. In addition, we observe that at $\Delta\phi < \pi/2$ which is dominated by NLO processes, POWHEG always predicts more yield than PYTHIA; while the ratio of the yields at $\Delta\phi > \pi/2$ of POWHEG to PYTHIA decreases with rapidity in the measured phase spaces. Because leading order processes are peaked near $\Delta\phi = \pi$, this may imply that the rapidity dependence of the ratio of LO to NLO contributions is different between the two models.

5.1.3.4 Bayesian Analysis

5.1.3.4.1 Introduction To further constrain the production mechanisms of $c\bar{c}$ and $b\bar{b}$, we perform a simultaneous shape analysis of the $\mu\mu$,

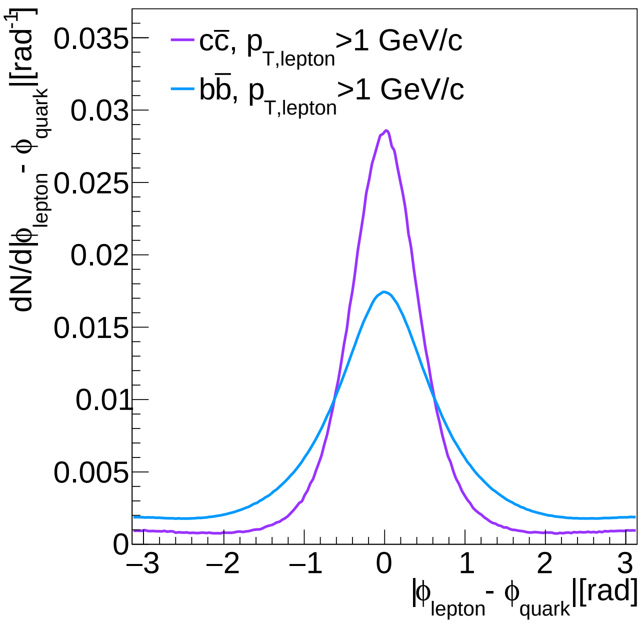

Figure 100: The difference in the azimuthal angle of the heavy quark and its decay lepton from POWHEG simulations, where the decay lepton has a minimum p_T of 1 GeV/c. The minimum p_T of 1 GeV/c is approximately the lower threshold of the experimental data used in this analysis. The $c\bar{c}$ and $b\bar{b}$ distributions are both normalized to unity for shape comparison.

$e\mu$, and ee data shown in Figs. 98 and 99 using Bayesian inference. Because the measurements cover different parts of phase space, extrapolations are unavoidable for this analysis. PYTHIA Tune A gives good agreement with multiple measurements made at the Tevatron [148], as well as jet and underlying event measurements from PHENIX [149] and STAR [150]; we thus focus on Tune A for this study.

The analysis is performed separately for $c\bar{c}$ and $b\bar{b}$. For $b\bar{b}$, we only use the $\mu\mu$ data set, whereas for $c\bar{c}$, the ee, $e\mu$ and $\mu\mu$ data sets are used. For ee and $e\mu$ data, we first subtract the expected $b\bar{b}$ yield from the two data sets and assign additional systematic uncertainties on extrapolation ($\approx 2\%$) and normalization ($\approx 6\%$). The extrapolation uncertainties are estimated by taking the difference between PYTHIA and POWHEG; the uncertainties on the normalization are taken from [151].

For $c\bar{c}$ or $b\bar{b}$, the model prediction of the yield, $\mathbf{T} = \{T_{i,j}\}$ for the i^{th} data set, either $\mu^+\mu^-$, $e\mu$, or ee for $c\bar{c}$ and $\mu^\pm\mu^\pm$ for $b\bar{b}$, in the j^{th} (azimuthal) opening angle bin can be written as:

$$T_{i,j}(\mathbf{F}, \sigma_{\mathrm{HF}}) = \sigma_{\mathrm{HF}} \sum_{\alpha} f_\alpha Y_{\alpha,i,j}, \tag{40}$$

where $\mathbf{F} = (F_{\mathrm{PC}}, F_{\mathrm{FE}}, F_{\mathrm{GS}})$ is the relative contribution to heavy flavor production in 4π phase space from the three considered processes PC, FE, and GS, σ_{HF} is the total heavy flavor cross section in 4π, and $Y_{\alpha,i,j}$ is the yield in the measured phase space of the i^{th} data set (indicated in Figs. 98 and 99) for the j^{th} bin per event generated involving the α process, where α = PC, FE or GS. The quantity that we constrain from the data is the relative contribution $\mathbf{F}$, which is directly related to the shape of the angular distributions. The total heavy flavor cross section σ_{HF} sets the overall normalization and is unimportant for this shape analysis.

The shape analysis of the angular distributions is sensitive to systematic uncertainties. The background subtraction is the dominant source of systematic uncertainty for all lepton-pair combinations. It introduces systematic uncertainties of ≈20% for $\mu\mu$ from $c\bar{c}$ [151], ≈15% for $\mu\mu$ from $b\bar{b}$ [151], ≈30% for $e\mu$ [22], and ≈20% for ee [21], which affects the data points in a correlated manner. We adopt a Bayesian approach to account for these systematic variations.

5.1.3.4.2 Method In the Bayesian approach, systematic uncertainties are naturally accounted for by incorporating nuisance parameters $\mathbf{n} = n_{i,k}$, where $n_{i,k}$ is the nuisance parameter corresponding to the k^{th} source of systematic uncertainty for the i^{th} data set. For a pedagogical review of the Bayesian method, see [152]. These nuisance parameters are incorporated into the *posterior probability density* according to:

$$P(\mathbf{F}, \sigma_{\mathrm{HF}}, \mathbf{n}|\mathbf{D}) = \frac{P(\mathbf{D}|\mathbf{F}, \sigma_{\mathrm{HF}}, \mathbf{n}) \cdot P(\mathbf{F}, \sigma_{\mathrm{HF}}, \mathbf{n})}{P(\mathbf{D})}. \tag{41}$$

The posterior probability density $P(\mathbf{F}, \sigma_{\mathrm{HF}}, \mathbf{n}|\mathbf{D})$ represents the conditional probability that, given a measurement $\mathbf{D}$ is made and assuming the PYTHIA modelling of the angular distributions, the relative contributions of heavy flavor production is given by $\mathbf{F}$, the total heavy flavor cross section is σ_{HF} and the perturbations on the data points arising from the various sources of systematic uncertainties are described by the set of nuisance parameters $\mathbf{n}$.

The *prior information* is encapsulated in the term $P(\mathbf{F}, \sigma_{\mathrm{HF}}, \mathbf{n})$, which represents our prior knowledge on the relative contributions to heavy flavor production $\mathbf{F}$, the total cross section σ_{HF}, and the systematic uncertainties, via the nuisance parameters $\mathbf{n}$. Since our prior knowledge on these three quantities are independent of each other, this term can be factorized as $P(\mathbf{F}) \cdot P(\sigma_{\mathrm{HF}}) \cdot P(\mathbf{n})$. Because the quantities that we ultimately want to infer from the data are the relative contributions of heavy flavor production, $\mathbf{F}$, we do not wish to bias our results with any prior knowledge on $\mathbf{F}$; we thus assume a noninformative prior for $\mathbf{F}$. More specifically, we assume a uniform distribution in the *physical region*, in which the values F_i, where $i =$ PC, FE, GS, lie between zero and one and sum to one, i.e.

$$\begin{aligned} 0 < F_{PC} &< 1, \\ 0 < F_{FE} &< 1, \\ 0 < F_{GS} &< 1, \\ F_{PC} + F_{FE} + F_{GS} &= 1. \end{aligned} \tag{42}$$

The probability distributions of the nuisance parameters $P(\mathbf{n})$, which characterizes our knowledge of the systematic uncertainties on the data, are assumed to be either Gaussian or uniformly distributed, depending on the nature of the particular source of the systematic uncertainty. Since we want to extract information about the shape of the distributions rather than the normalization, σ_{HF} is constrained via a one-parameter fit to the data, which will be described in the following.

The *likelihood*, $P(\mathbf{D}|\mathbf{F}, \sigma_{\mathrm{HF}}, \mathbf{n})$ represents the probability that, with a certain mix of production processes $\mathbf{F}$, a certain total heavy cross section σ_{HF}, and a certain set of systematic perturbations quantified by the nuisance parameters $\mathbf{n}$, we arrive at a measurement $\mathbf{D}$. Assuming all statistical uncertainties $\sigma_{i,j}^{stat}$ are Gaussian, and denoting systematic uncertainties as $\sigma_{i,j,k}^{sys}$, this probability is proportional to $e^{-\frac{\chi^2}{2}}$, where χ^2 is defined according to Eq. 43:

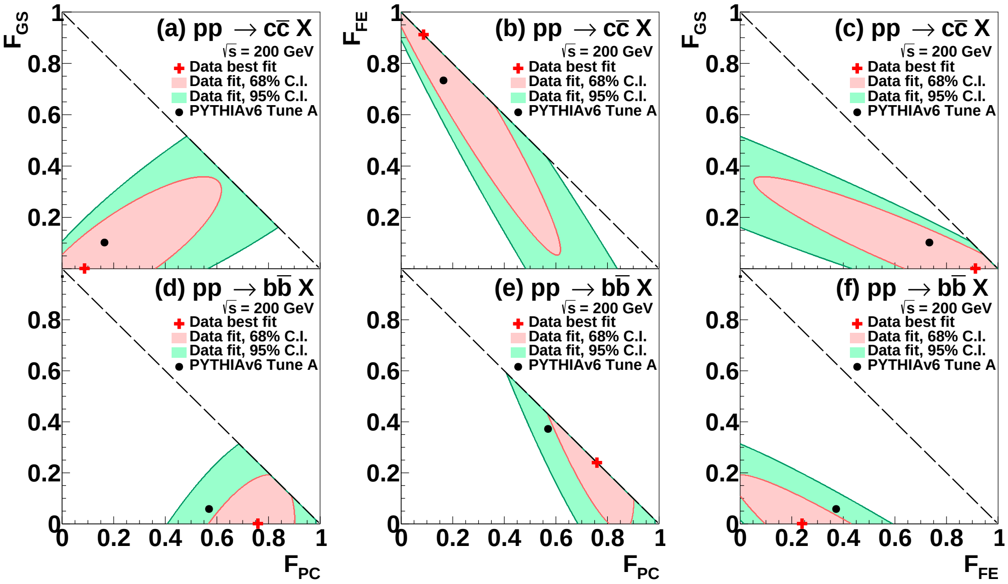

Figure 101: Credible intervals for (a,b,c) $c\bar{c}$ and (d,e,f) $b\bar{b}$ production mechanisms extracted from data and PYTHIA Tune A.

$$\chi^2 = \sum_i \sum_j \sum_k \left[\frac{D_{i,j} + n_{i,k}\sigma^{sys}_{i,j,k} - T_{i,j}(\mathbf{F}, \sigma_{\mathrm{HF}})}{\sigma^{stat}_{i,j}} \right]^2 . \tag{43}$$

Finally, $P(\mathbf{D})$ is often referred to as *model evidence*, and represents the probability to obtain a measurement $\mathbf{D}$ assuming the PYTHIA modelling of the angular correlations. For the purposes of this analysis, this term serves as an overall normalization factor such that $P(\mathbf{F}|\mathbf{D})$ can be interpreted as a probability density. The explicit evaluation of this term is avoided by enforcing the condition that the integral of $P(\mathbf{F}|\mathbf{D})$ over $\mathbf{F}$ is unity.

Ultimately, we want to infer information on the relative contributions to heavy flavor production, $\mathbf{F}$, using the data $\mathbf{D}$. This can be quantified using the conditional probability distribution $P(\mathbf{F}|\mathbf{D})$. To compute this quantity from Eq. 41, we adopt a Monte Carlo approach. Sets of random numbers $\mathbf{n}^*$ are generated according to $P(\mathbf{n})$. For a set of $\mathbf{n}^*$, χ^2 as defined in Eq. 43 is minimized with respect to σ_{HF} as a function of $\mathbf{F}$, i.e. we allow the normalization of the generated azimuthal distributions to be constrained by the data, thus fixing the total heavy flavor cross section σ_{HF}. The posterior probability density $P(\mathbf{F}, \sigma_{\mathrm{HF}}, \mathbf{n^*}|\mathbf{D})$ is then summed over different sets of $\mathbf{n^*}$, and normalized to unity in order to obtain $P(\mathbf{F}|\mathbf{D})$. We construct 68% and 95% credible intervals from $P(\mathbf{F}|\mathbf{D})$; boundaries of the intervals are contours of the posterior probability density $P(\mathbf{F}|\mathbf{D})$.

5.1.3.5 Results and discussion The final results are presented in Fig. 101 in different projections of $\mathbf{F}$. For $c\bar{c}$ and $b\bar{b}$, the PYTHIA Tune A implementation lies within the 68% and 95% credible intervals obtained from our analysis, respectively. For the case of $c\bar{c}$, a positive correlation is observed between F_{PC} and F_{GS}, both of which are individually anti-correlated with F_{FE}. This is explained by the observation that the data sets can be reasonably well described by the following two cases: $\mathbf{F} = (0\%, 100\%, 0\%)$ and $\mathbf{F} = (62\%, 0\%, 38\%)$. From the posterior probability distributions, it is observed that the hierarchy $F_{\mathrm{FE}} > F_{\mathrm{PC}} > F_{\mathrm{GS}}$ is favored, consistent with the expectation from PYTHIA.

In contrast to $c\bar{c}$, PC is clearly the dominant ($76\%^{+14}_{-19}\%$) production process for $b\bar{b}$. Compared to $c\bar{c}$, the ordering of contributions from of PC and FE is reversed $F_{\mathrm{PC}} > F_{\mathrm{FE}} > F_{\mathrm{GS}}$, again consistent with the expectation from PYTHIA. The reversal in the hierarchy for $b\bar{b}$ arises from the larger b quark mass, which sets more demanding kinematic requirements for NLO processes.

The upper limits corresponding to the 95% credible intervals for F_{GS} for $c\bar{c}$ and $b\bar{b}$ are 52% and 31% respectively. These limits take into consideration extreme cases in which only PC and GS contribute to the yield but FE does not. Priors with extra physical considerations may be incorporated to impose more stringent constraints in $\mathbf{F}$, however this is beyond the scope of our study.

In summary, this study indicates that the measured angular correlations of $\mu\mu$, $e\mu$, and ee pairs from $c\bar{c}$ and $b\bar{b}$ measured in p+p collisions at $\sqrt{s} = 200$ GeV at forward-forward, mid-forward, and mid-midrapidity respectively can be consistently described by distributions obtained from PYTHIA Tune A. In contrast, angular correlations generated using POWHEG are broader than those from the data.

Based on PYTHIA Tune A, the shape analysis using the combined data on heavy flavor angular correlations at $\sqrt{s} = 200$ GeV constrains the relative contributions of the leading order pair creation, and next-to-leading order flavor excitation and gluon splitting processes, separately for $c\bar{c}$ and $b\bar{b}$. The data indicate that the dominant production mechanism of $b\bar{b}$ production is pair creation, and supports the scenario in which flavor excitation dominates $c\bar{c}$ production. Similar measurements in p+p collisions at different energies will provide insight on the energy dependence of heavy quark production mechanisms.

At RHIC energies, heavy quarks can be utilized to study initial gluon dynamics due to the small fraction of gluon splitting contribution. Besides p+p collisions, heavy quarks are commonly used to study nuclear matter effects in p+A and A+A collisions with the assumption that heavy quarks are mostly produced in the early stages of collisions. Similar measurements in p+A may shed light on process dependent cold nuclear matter effects. A solid understanding of the contributions of heavy flavor processes in p+p and p+A collisions will be critical to precisely interpret results in A+A collisions, which suffer complications due to the contribution from gluon splitting process, particularly at LHC energies [153, 154].

5.1.4 Azimuthal opening angle and pair p_T distributions for $\mu\mu$ pairs from $b\bar{b}$ in p+Au collisions

The like-sign $\mu\mu$ pair yield from $b\bar{b}$ decays in the mass range 3.5–10.0 GeV/c^2 is shown in Figs. 102 and 103 as a function of $\Delta\phi$ and pair p_T. The muons are in the nominal acceptance of $p > 3$ GeV/c and $1.2 < |\eta| < 2.2$. The Au-going side is shown in blue while the p-going side is shown in red. The yield in p+Au is compared to the binary scaled yield in p+p collisions, shown in black. For the pair p_T data, the p+p data is rebinned in a consistent manner with the p+Au collisions to allow for a direct comparison.

To quantify nuclear effects in p+Au collisions, we calculate the nuclear modification R_{p+Au} defined by:

$$R_{p+Au}(X_{\mu\mu}) = \frac{d^3N_{p+Au}/dX_{\mu\mu}d\eta_{\mu,1}d\eta_{\mu,2}}{\langle N_{coll}\rangle \times d^3N_{p+p}/dX_{\mu\mu}d\eta_{\mu,1}d\eta_{\mu,2}}, \tag{44}$$

where X is $\Delta\phi$ or p_T. In the calculation of the uncertainties in R_{p+Au}, the relative statistical uncertainty is the quadrature sum of the relative statistical uncertainties in N_{p+Au} and N_{p+p}. For systematic uncertainties, correlated uncertainties, i.e. uncertainties common to p+Au and p+p collisions are treated separately from uncorrelated uncertainties. Denoting the value of one sigma of the i^{th} source of correlated systematic uncertainty as $\Delta_{p+p,i}$ and $\Delta_{p+Au,i}$ for p+p and p+Au respectively, the corresponding sigmalized

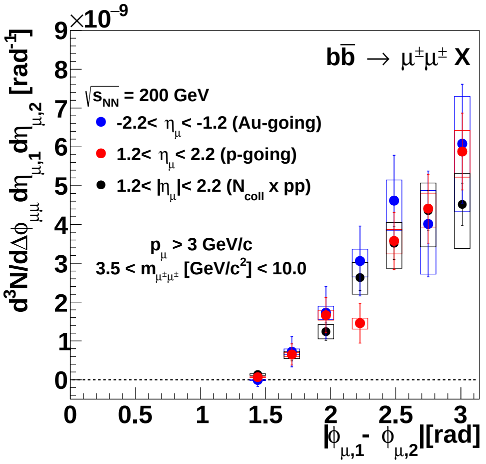

Figure 102: The corrected $\mu\mu$ yield as a function of $\Delta\phi$ from bottom decays in p+Au collisions. The binary scaled yield in p+p collisions are also shown.

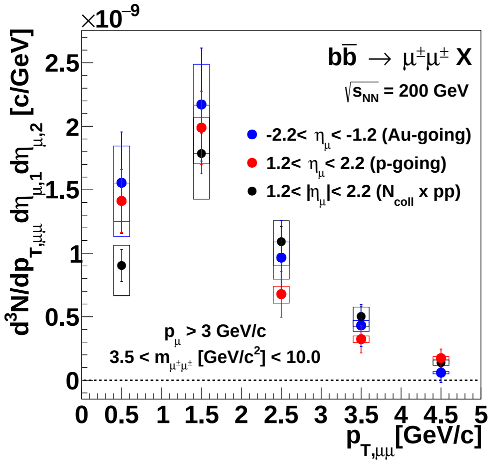

Figure 103: The corrected $\mu\mu$ yield as a function of pair p_T from bottom decays in p+Au collisions. The binary scaled yield in p+p collisions are also shown.

systematic uncertainty for R_{p+Au}, $\Delta R_{p+Au,i}$ is estimated using the following relation:

$$\Delta R_{p+Au,i} = \frac{N_{p+Au} + \Delta N_{p+Au,i}}{\langle N_{coll} \rangle \times (N_{p+p} + \Delta N_{p+p,i})} - \frac{N_{p+Au}}{\langle N_{coll} \rangle \times N_{p+p}}. \tag{45}$$

For the j^{th} source of uncorrelated systematic uncertainty, the corresponding sigmalized systematic uncertainty for R_{p+Au}, $\Delta R_{p+Au,i}$ is estimated using the following relation:

$$\Delta R_{p+Au,j} = \sqrt{\left(\frac{\Delta N_{p+Au,j}}{N_{p+Au}}\right)^2 + \left(\frac{\Delta N_{p+p,j}}{N_{p+p}}\right)^2} \tag{46}$$

The total systematic uncertainty for R_{p+Au} is the quadrature sum of uncorrelated and correlated systematic uncertainties.

The R_{p+Au} is shown as a function of $\Delta\phi$ and pair p_T in Fig. 104 and 105 respectively. No nuclear modification of the azimuthal correlations is observed within the experimental uncertainties. In contrast, the pair p_T spectra from

p+Au collisions seem to be slightly softer in both the p-going and Au-going direction compared to p+p collisions.

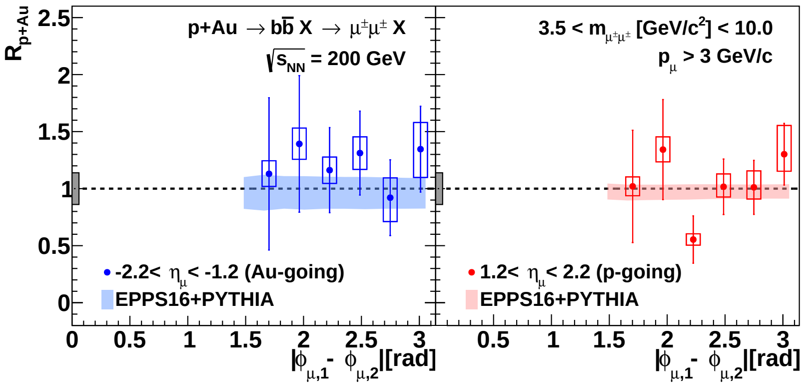

Figure 104: R_{p+Au} for $\mu\mu$ from $b\bar{b}$ as a function of $\Delta\phi$. The results is compared to expected modifications estimated using EPPS16 and PYTHIA.

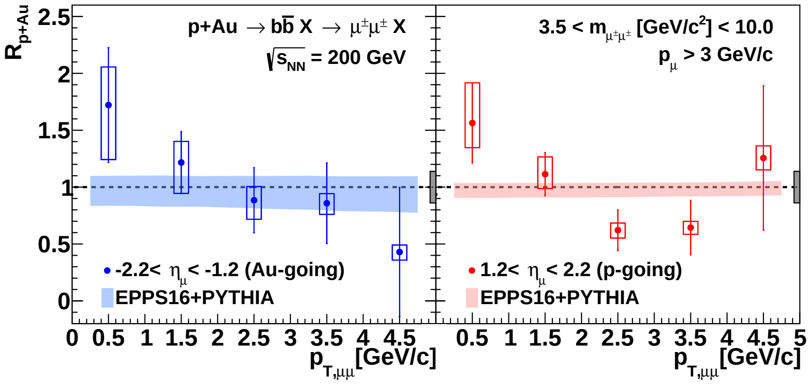

Figure 105: R_{p+Au} for $\mu\mu$ from $b\bar{b}$ as a function of pair p_T. The results is compared to expected modifications estimated using EPPS16 and PYTHIA.

We also compare the measured R_{p+Au} to estimated nuclear modifications arising from nuclear PDFs, calculated using a combination of EPPS16 [25] and PYTHIA. For each $b\bar{b}$ event generated by PYTHIA, a weighting factor is obtained from EPPS16 according to the x_1, x_2 and Q^2 of the event, and is applied to all muon pairs in the event. While the data is consistent with the predictions from EPPS16, the R_{p+Au} estimated using EPPS16 does not show any decreasing trend with increasing pair p_T. This could suggest that there are additional cold nuclear matter effects in addition to the expected modification from nPDFs, such as multiple scattering of partons traversing nuclei. As momentum broadening has been observed from inclusive heavy flavor (dominated by $c\bar{c}$) leptons at forward [20], mid [19] and backward [20] rapidities at RHIC, it is plausible that this effect is also non-negligible for $b\bar{b}$. Measurements in future experiments, such as sPHENIX where precision measurements of $b\bar{b}$ are possible may help shed light on this issue.

5.2 Drell-Yan

5.2.1 Drell-Yan differential cross sections in p+p collisions

The fully corrected $\mu\mu$ pair cross section from the Drell-Yan process in the pair rapidity region $1.2 < |y^{\mu\mu}| < 2.2$, as a function of mass, and a function of p_T for pairs in the mass region $4.8 < m$ [GeV/c^2]< 8.2 are shown in Figs. 106 and 107, respectively. The measured differential Drell-Yan cross section at forward and backward rapidities are consistent with each other.

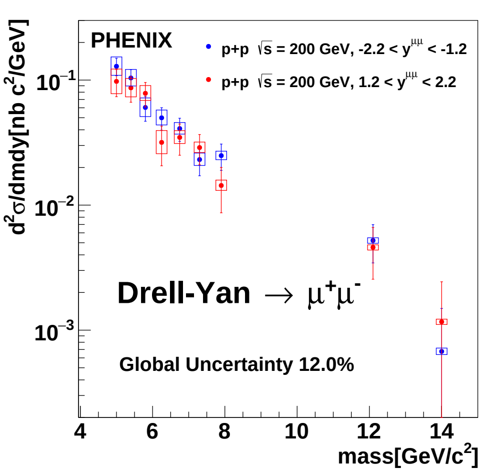

Figure 106: The corrected $\mu\mu$ yield from Drell-Yan in pair rapidity region $1.2 < |y^{\mu\mu}| < 2.2$ as a function or pair mass. Results are shown separately for the south and north muon arms.

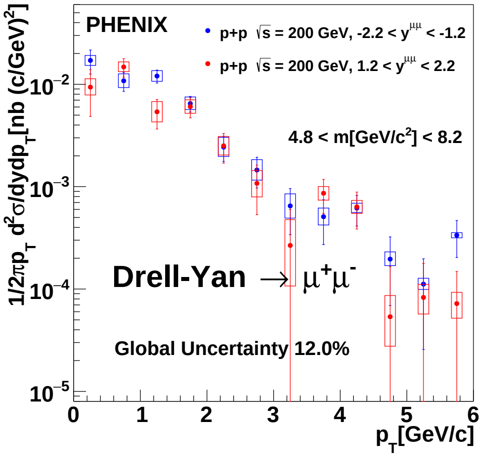

Figure 107: The corrected $\mu\mu$ yield from Drell-Yan in pair rapidity region $1.2 < |y^{\mu\mu}| < 2.2$ and mass region $4.8 < m < 8.2$ GeV/c^2 as a function of pair p_T. Results are shown separately for the south and north muon arms.

We combine the measurements from the two rapidity regions. The mass spectrum is then compared with NLO calculations from Vitev [155] and Qiu J. et al [156] in Fig. 108. Both calculations adopt the factorization approach where higher orders are evaluated order-by-order in perturbation theory. Within experimental uncertainties, the data are well reproduced by NLO calculations. The p_T spectrum of Drell-Yan muon pairs in the mass region 4.8–8.2 GeV/c^2 is shown in Fig. 109 and compared to PYTHIA, where the intrinsic k_T is tuned to 1.1 GeV/c from the procedure described in 3.10.1.4, and normalized from the fitting procedure as documented in the above text. The normalization obtained from the fitting procedure corresponds to a k-factor of 1.23. To date this is the first Drell-Yan measurement at RHIC energies. As Drell-Yan is a common background to various physics processes involving dileptons, the presented data may give a constraint for the background estimation of such measurements. The Drell-Yan cross section as a function of invariant mass and p_T can also provide constraints on the unpolarized transverse-momentum-dependent parton distribution functions (TMD PDFs), which is of critical importance to understanding the internal structure of the proton. This measurement gives input to a previously unexplored phase space and serves as a solid baseline for future measurements.

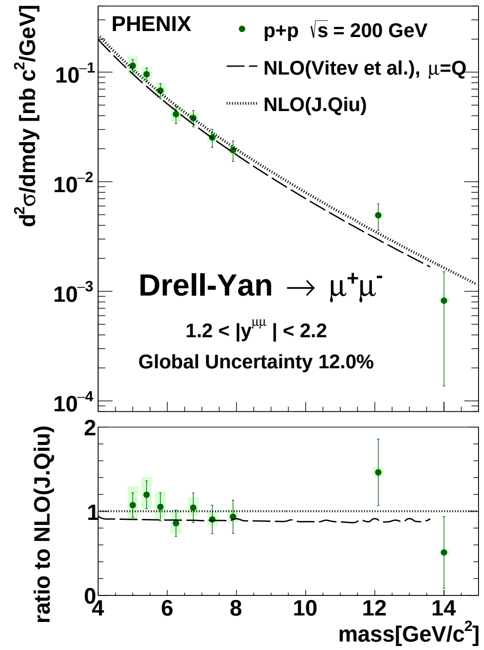

Figure 108: Panel (a) shows the corrected $\mu\mu$ yield from Drell-Yan in pair rapidity region $1.2 < |y^{\mu\mu}| < 2.2$. Data are compared to NLO calculations. Panel (b) gives the ratio of the data to one of the NLO calculations.

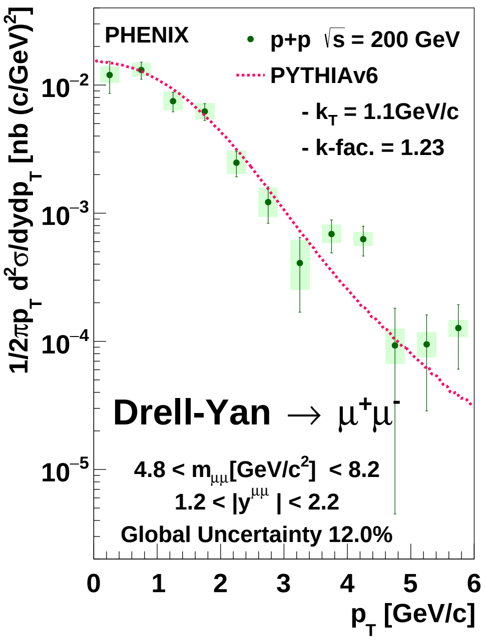

Figure 109: The corrected $\mu\mu$ yield from Drell-Yan in pair rapidity region $1.2 < |y^{\mu\mu}| < 2.2$ and mass region $4.8 < m < 8.2$ GeV/c^2 as a function of pair p_T. Data are compared PYTHIA calculations under settings used for this analysis.

5.2.2 Drell-Yan differential cross sections in p+Au collisions

The $\mu\mu$ pair cross section per nucleon from the Drell-Yan process in p+Au and p+p collisions the pair rapidity region $1.2 < |y^{\mu\mu}| < 2.2$ as a function of mass, and a function of p_T for pairs in the mass region $4.8 < m[\mathrm{GeV}/c^2] < 8.2$ are shown in Figs. 110 and 111 respectively. The data points for p+p are rebinned to the same binning as p+Au.

The nuclear modification factor R_{p+Au} is determined from the p+Au and p+p data and shown in the bottom panels of Figs. 110 and 111. We see that all data points are consistent with unity, indicating that there is no modification observed within the experimental uncertainties.

As in the $b\bar{b}$ case, we use PYTHIA to generate Drell-Yan pairs and according to the x_1, x_2 and Q^2 of each event, and apply a weighting factor determined by EPPS16. The expected modifications are calculated as a function of mass, and as a function of p_T and compared to data. We see that the expectations from EPPS16 are consistent with the data. For the p-going side which corresponds to a Bjorken x range of ~ 0.01, there are, prior to this measurement, no data to constrain the nPDFs, leading to an estimated uncertainty of $\sim 20\%$ from EPPS16. As the uncertainties of the data points are of a similar magnitude to the uncertainty from EPPS16, these data can help constrain the nPDFs.

There is a hint of enhancement ($\sim 2.5\sigma$ significance) for the p-going side for pairs with $p_T > 2$ GeV/c. If confirmed, this may suggest a hint of initial state effects such as initial state scattering of partons traversing through the nuclei, that are present for the p-going side but absent for the Au-going side.

The Fermilab Experiment 772 (E772) and 866 (E866) have measured Drell-Yan dimuon production by 800 GeV/c protons on Be, C, Fe and W targets, and the ratios of the Drell-Yan cross sections from a heavy nuclus (Fe, W) to a light nuclus (Be,C) are presented as a function of mass, x_2, x_F, x_1 and p_T in [42, 43]. The measurements show that while the ratios of the measured cross section per nucleon as a function of mass, x_2, x_F and x_1 are consistent with expectations from shadowing (see Fig. 112), the ratio as a function of p_T is larger than unity in the at high p_T $(1.5 - 3.0)$ GeV/c and smaller than unity at low p_T $(0.0 - 1.0)$ GeV/c (see Fig. 113), a characteristic of initial state parton scattering in nuclei [157].

The Drell-Yan events obtained by E866 extend over the ranges $0.01 < x_2 < 0.12$ and $0.21 < x_1 < 0.95$ with $\langle x_2 \rangle = 0.038$ and $\langle x_2 \rangle = 0.46$, while the results presented in this dissertation cover the ranges $0.004 < x_i < 0.018$

with $\langle x_i \rangle = 0.01$ and $0.1 < x_i < 0.6$ with $\langle x_j \rangle = 0.3$, where $i(j)$ stands for the proton (Au-ion) for the Au- (p-) going side. The x coverage for the p-going side is thus similar to those in E866, hence it may be expected that non-negligible p_T dependent initial state effects are present in the kinematic region probed on the p-going side.

(Anti-)shadowing and other initial state effects are present in both Drell-Yan process and heavy flavor production. More precise measurements of the Drell-Yan cross sections in small systems can help disentangle initial state modifications of nuclear matter from final state modifications, and thus also further our understanding of heavy flavor production in small systems. Understanding the initial and final state modifications of heavy flavor in small systems is a necessary step if heavy flavor is to be used as a probe to study the Quark-Gluon plasma quantitatively in heavy ion collisions.

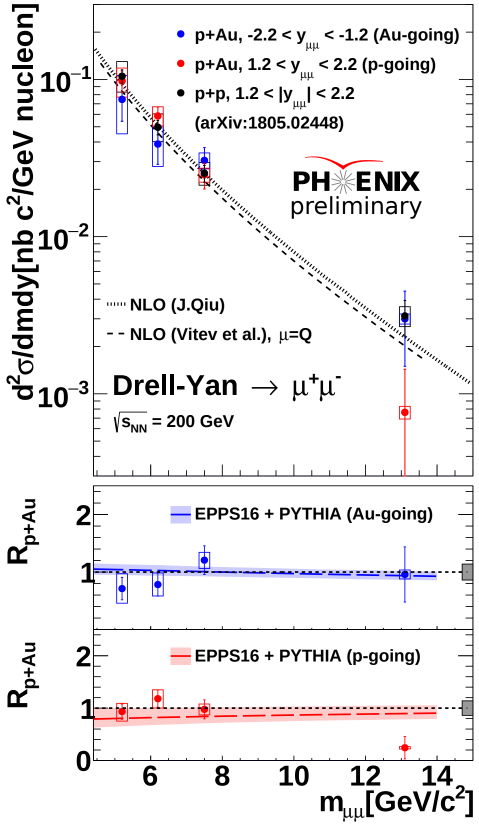

Figure 110: The Drell-Yan→ $\mu\mu$ cross section per nucleon in pair rapidity region $1.2 < |y^{\mu\mu}| < 2.2$ and mass region $4.8 < m < 8.2$ GeV/c^2 as a function of pair p_T for p+Au and p+p collisions. The lower panels shows the nuclear modification, compared to calculations from EPPS16.

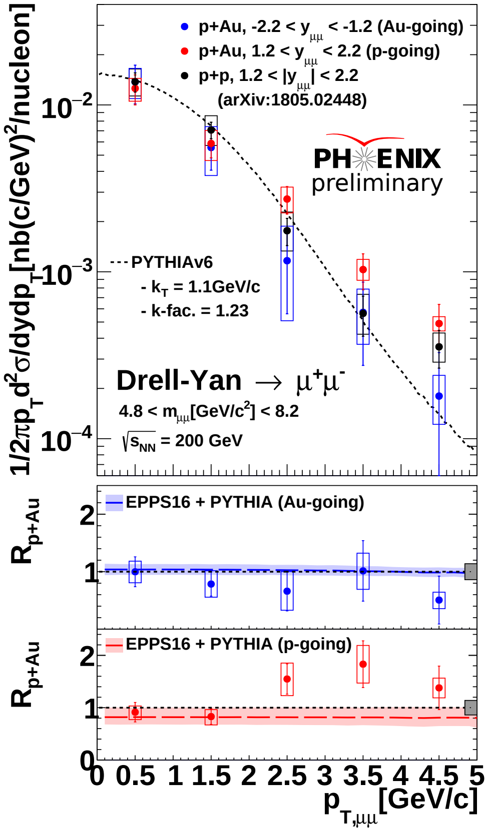

Figure 111: The Drell-Yan→ $\mu\mu$ cross section per nucleon from in pair rapidity region $1.2 < |y^{\mu\mu}| < 2.2$ and mass region $4.8 < m < 8.2$ GeV/c^2 as a function of pair p_T for p+Au and p+p collisions. The lower panels shows the nuclear modification, compared to calculations from EPPS16.

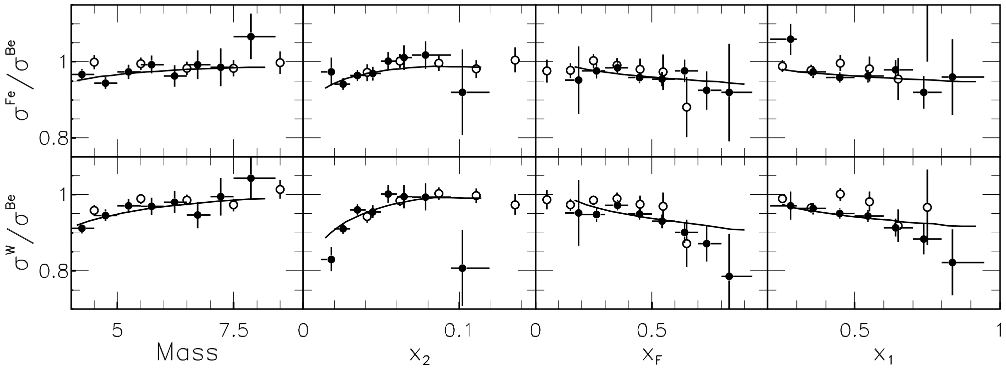

Figure 112: Ratios of the measured Drell-Yan dimuon cross section per nucleon as a function of dimuon mass, x_2, x_F and x_1 [42, 43]. The upper (lower) panels show ratios of Fe/Be (W/Be) from E866 as solid circles and Fe/C (W/C) from E772 as open circles. The errors are statistical only. The solid curves are shadowing predictions from leading-order calculations using EKS98 [44] and MRST [45, 46].

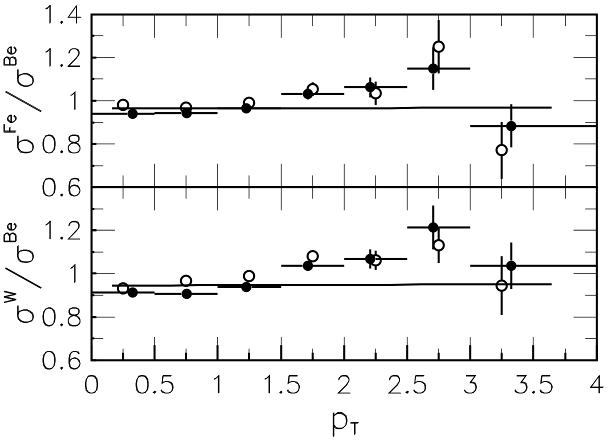

Figure 113: Ratios of the measured Drell-Yan dimuon cross section per nucleon as a function of dimuon p_T [42, 43]. The upper (lower) panels show ratios of Fe/Be (W/Be) from E866 as solid circles and Fe/C (W/C) from E722 as open circles. The errors are statistical only. The solid curves are shadowing predictions from leading-order calculations using EKS98 [44] and MRST [45].

6 Summary

Muon pair measurements from open heavy flavor ($c\bar{c}$ and $b\bar{b}$) decays and the Drell-Yan mechanism in p+p and p+Au collisions at $\sqrt{s_{NN}} = 200$ GeV have been presented.

In p+p collisions, the $\mu\mu$ pair yields from $c\bar{c}$ and $b\bar{b}$ are measured as a function of the azimuthal opening angle $\Delta\phi_{\mu\mu}$ and pair transverse momentum $p_{T,\mu\mu}$ and compared to calculations from different theoretical models, PYTHIA and POWHEG. Within experimental uncertainties, the azimuthal opening angle and pair p_T distributions from $b\bar{b}$ are well described by these models. For $c\bar{c}$, the data favors the description of PYTHIA. The POWHEG calculations predict a systematically higher yield than PYTHIA at smaller opening angles and is disfavored by data in the probed kinematic region. Furthermore, based on the generated distributions of pair creation, flavor excitation and gluon splitting using PYTHIA Tune A, a Bayesian analysis is applied to all available heavy flavor lepton pair data at 200 GeV. The results support the scenario that the dominant source of $b\bar{b}$ production is leading order pair creation.

We find that the high mass like-sign pairs are dominated by decays from open bottom, which provides a strong constraint on the bottom cross section. The measured total bottom cross section 3.75 ± 0.24 (stat) $^{+0.35}_{-0.50}$ (sys) ± 0.45 (global) μb is the most precise measurement at 200 GeV to date. The measurement is consistent with RHIC measurements at the same energy, and is around a factor of two higher than the central value of NLO calculations with an input bottom quark mass of $m_b = 4.75$ GeV/c^2.

The Drell-Yan cross section as a function of mass in 4.8–15.0 GeV/c^2 is presented and compared to NLO calculations. Within uncertainties we find good agreement between NLO calculations and data. The p_T-dependence of the Drell-Yan cross section in the mass region 4.8–8.2 GeV/c^2 is also presented, along with the calculation using the PYTHIA tune that best describes the data.

In p+Au collisions, the $\mu\mu$ pair yields from $b\bar{b}$ are measured as a function of $\Delta\phi_{\mu\mu}$ and $p_{T,\mu\mu}$ and compared to the corresponding p+p yields scaled with the number of binary collisions. Within experimental uncertainties, the nuclear modification factor is consistent with unity, indicating that no nuclear modification is observed.

For p+Au collisions, the Drell-Yan cross section was studied as a function of mass in 4.8–15.0 GeV/c^2, and as a function of p_T for pairs with mass 4.8–8.2 GeV/c^2. Within experimental uncertainties, the p+Au Drell-Yan cross section per nucleon is consistent with Drell-Yan measurements in $p+p$ collisions. The extracted R_{p+Au} is consistent with expectations from the nuclear parton distribution functions obtained from EPPS16. The data at forward rapidity, which corresponds to low Bjorken x values, can provide constraints to the nuclear parton distribution functions, which currently suffer from large uncertainties due to the lack of constraints from experimental data. There is a hint of enhancement compared to $p+p$ collisions for pairs from the Drell-Yan process at $p_T > 2$ GeV/c at forward rapidity, corresponding to the p-going direction. Further measurements with higher precision may help shed light on the initial state effects of nuclear matter.

The results on $p+p$ collisions have been submitted for publication in Physical Review D [151] [158], and a manuscript presenting the results in $p+Au$ is under preparation.

7 Outlook

The PHENIX experiment finished its last data taking run on 26^{th} Jun, 2016. The results presented in this dissertation may very well be the last lepton pair measurements performed using data collected by the PHENIX measurements. However, there are many ongoing experiments, as well as future experiments, in which one may take advantage of some of the techniques presented here to extract interesting physics; not only to further our understanding of heavy flavor production and cold nuclear matter effects; but may also help us explore other important aspects of nuclear physics.

7.1 Energy dependence on heavy flavor correlations

The relative contributions of heavy flavor production vary significantly with energy. At $\sqrt{s} = 200$ GeV, $b\bar{b}$ is primarily produced through pair creation, as confirmed by the results presented in this dissertation. As we go up in beam energy, the flavor excitation component is expected to overtake pair creation at around 1 TeV, and at LHC energies, the gluon splitting contribution becomes more important as well. For $c\bar{c}$, flavor excitation dominates over gluon splitting and pair creation even at $\sqrt{s} = 200$ GeV, and with the gluon splitting contribution becoming increasingly important as the beam energy increases. Systematic measurements of the heavy flavor pair correlations as a function of beam energy can thus probe the energy dependence

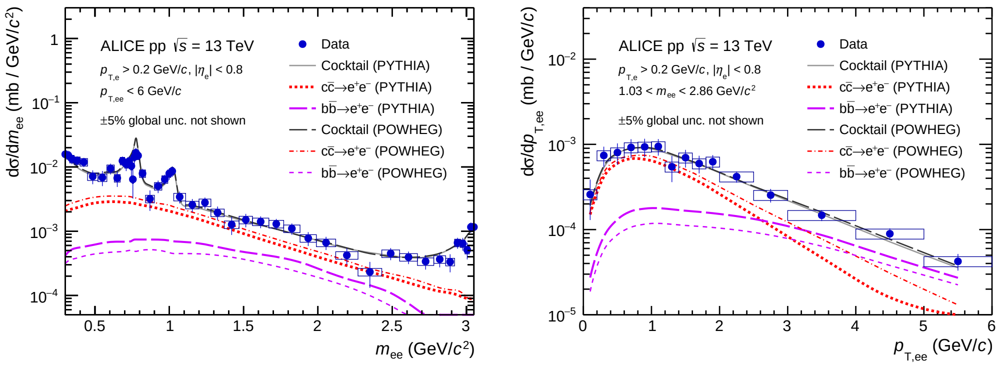

Figure 114: Projection of heavy flavor dielectron fit (grey line) in p+p collisions at $\sqrt{s}$ = 13 TeV onto dielectron mass (left) and $p_{T,ee}$ using PYTHIA and POWHEG [47]. The lines show charm (red) and bottom (magenta) contributions after fitting.

of different heavy flavor production mechanisms and provide constraints to theoretical models.

In particular, at $\sqrt{s}$ = 200 GeV, we have found that there is significant model dependence on $c\bar{c}$ azimuthal correlations. As shown in Fig. 114, the $c\bar{c}$ model dependence is significant even at LHC energies [47]. Currently, theoretical calculations of heavy flavor are often sensitive to input parameters, such as intrinsic transverse momentum, heavy flavor quark masses, etc., which leads to large uncertainties in theoretical calculations. On the other hand, ratios between cross sections at different energies can help limit the systematic uncertainties on theoretical calculations, and can provide stronger discriminating power between model parameters. Thus, heavy flavor correlation measurements at higher energies, utilizing for example p+p data at $\sqrt{s}$ = 510 GeV at RHIC (e.g. STAR) in 2017, or $\sqrt{s}$ = 7 TeV and 13 TeV at the LHC (e.g. ALICE), could be invaluable to improve the precision of theoretical calculations of heavy flavor production.

7.2 Low x Drell-Yan cross sections

Nuclear parton distribution functions encode the modification of the parton distribution functions in nuclei compared to those of the proton; they remain poorly understood. Data from charged lepton-nucleon deep in elastic scatter-

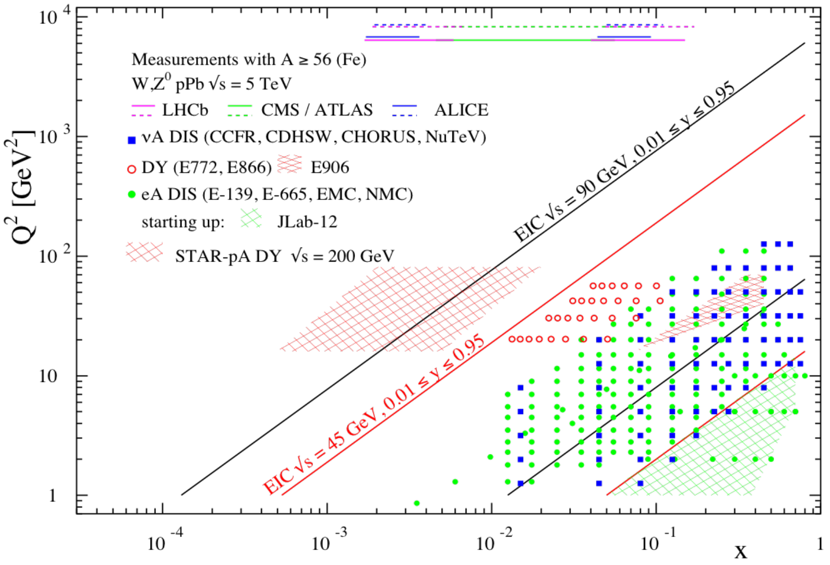

Figure 115: The kinematic coverage in x-Q^2 of past, present and future experiments constraining nPDFs to the exact parton kinematics event-by-event and no fragmentation in the final state [48].

ing, and Drell-Yan dilepton production or pion production in proton/deuteron-nucleus collisions can be used to constrain nPDFs. The most up to date nPDF package, EPPS16 also includes dijet, W and Z production in proton-lead collisions to further constrain nPDFs. However, as shown in Fig. 30, the current uncertainties in nPDFs, especially in the low x regime are still very significant. This is mainly due to the fact that there are no data to constrain the nPDFs in low x. Drell-Yan measurements at foward rapidity in p/d+A collisions serve as a theoretically clean probe to assess the low x component of sea-quark distributions. After the pair is produced through the Drell-Yan mechanism in the hard scattering process, there are no further final state effects, in contrast with pion production or dijet production. The main background to Drell-Yan in high energy collisions is typically $b\bar{b}$, which, as presented in this dissertation, can possibly be measured and constrained to high accuracy by utilizing like-sign pairs.

Although precision Drell-Yan measurements at forward rapidity may not be easily accessible at RHIC currently, there are ongoing plans from the

STAR collaboration and sPHENIX collaboration [48] such that these measurements may be possible in the near future. As shown in Fig. 115, the x-Q^2 coverage after the forward upgrade of STAR (and also forward upgrade of sPHENIX which shares a similar kinematic coverage), extends to beyond the kinematic reach of the future EIC, which are expected give invaluable measurements to further the study of cold QCD.

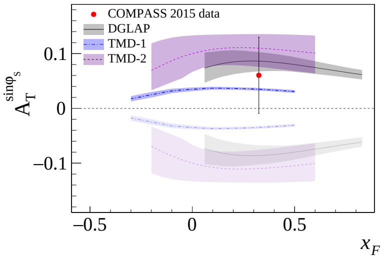

Figure 116: The measured mean Sivers asymmetry and the theoretical predictions for different Q^2 evolution schemes [49]. The dark-shaded (light-shaded) predictions are evaluated with (without) the sign-change hypothesis

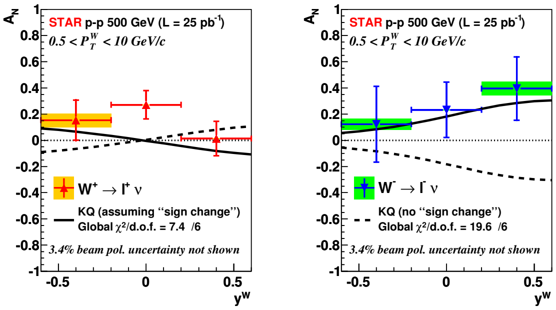

Figure 117: Transverse single-spin asymmetry amplitude for W^+ and W^- versus y^w compared with model calculations, assuming (solid line) or excluding (dashed line) a sign change in the Sivers function [50].

7.3 Drell-Yan transverse single spin asymmetry

Drell-Yan measurements in p+A collisions are very useful to study nuclear parton distribution functions. Measurements differential in mass and p_T can give access to transverse momentum dependent parton distribution functions (TMDs), which is a main physics motivation to the construction of the future EIC.

One particular TMD, known as the Sivers function [159], encodes the correlation between the intrinsic transverse momentum of a parton and the spin of the parent proton, and can be assessed through the transverse single-spin asymmetry in Drell-Yan or W/Z production. In particular, it is predicted that the Sivers function has an opposite sign in semi-inclusive deep inelastic scattering compared to p+p collisions. This is known as the *Sivers sign change* and is a fundamental test of QCD factorization.

There are multiple collaborations striving to confirm this prediction. For example, the COMPASS collaboration recently published a first measurement of transverse-spin-dependent asymmetries in the pion-induced Drell-Yan process [49], as shown in Fig. 116. The STAR collaboration also published first results on transverse single-spin asymmetry in W/Z boson production [50], as shown in Fig. 117. The measurements both favor the case where there is a sign change in the Sivers function, opposed to the case where there is no sign change. More precise measurements in the future utilizing polarized beams can not only confirm the Sivers sign change, but also provide more constraints to the Sivers function to further our understand in proton structure.

A DETAILED DESCRIPTION OF SIMULATION FRAMEWORKS

Details of the two simulation chains used in this analysis, namely the default PHENIX simulation framework and the fastMC, are discussed in the following. The flowchart shown in Fig. 118 summarizes a comparison between the data reconstruction framework and the two simulation chains.

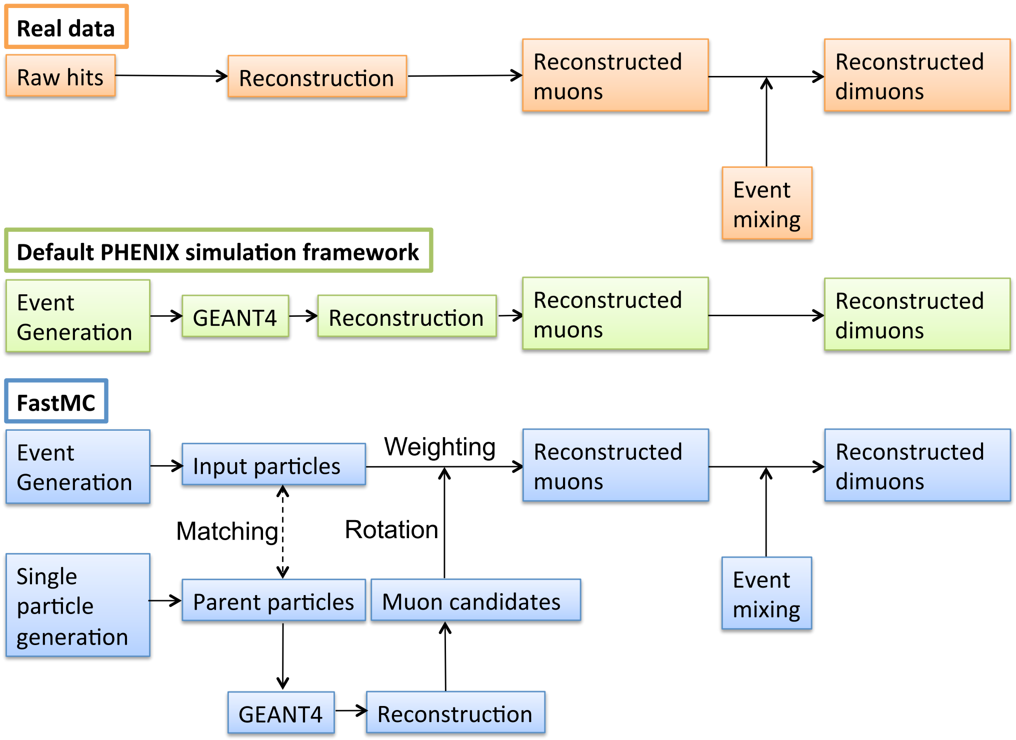

Figure 118: Flow chart of the analysis chain of the dimuon reconstruction for real data, default PHENIX simulation framework, and FastMC framework.

A.1 Default PHENIX simulation framework

The default PHENIX simulation is based on a detailed GEANT4 [123] implementation of the muon arms. This framework takes into account the detector's geometrical acceptance and all inefficiencies from dead channels.

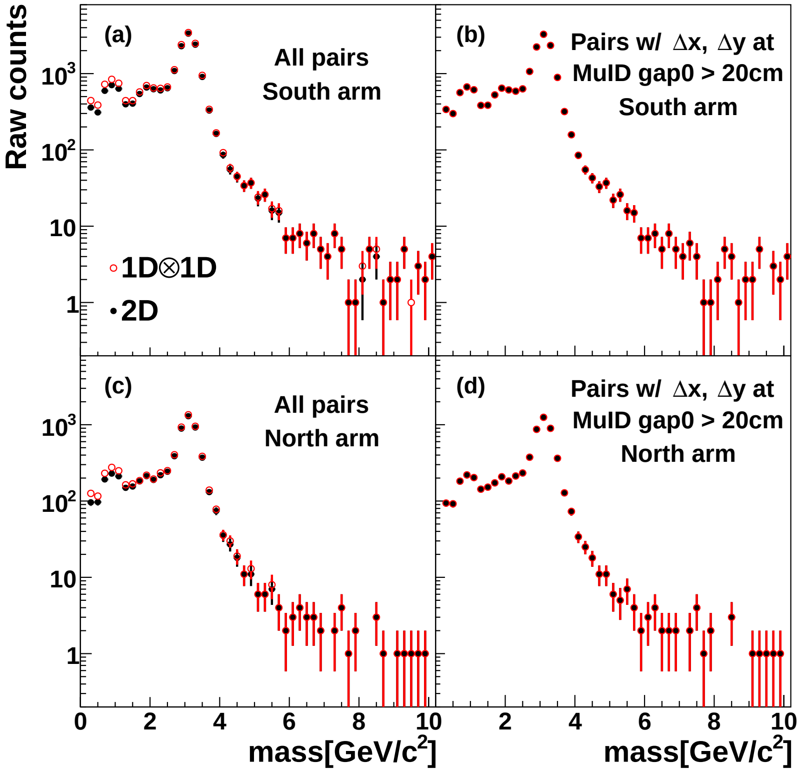

Figure 119: The mass spectra of MuIDLL1-1D triggered data for the (a,b) south arm and (c,d) the north arm are shown separately. Open circles are pairs in which both associated tracks satisfy the MuIDLL1-1D condition, while closed circles are pairs in which the associated tracks satisfy the MuIDLL1-2D condition. Panels (a,c) show all pairs, while the panels (b,d) show only pairs with a spatial separation exceeding 20 cm at MuID gap 0.

To account for variations of detector performance during the data taking period, the data are split into run groups with similar performance. For each group a map of dead channels is created for the MuTr. The simulation randomly selects these maps according to the sampled luminosity for each run group.

Muon pairs from physical sources are simulated with a z-vertex distribution taken from MB p+p data. Once the pairs are processed through the detector simulation, they are reconstructed using the same procedure and

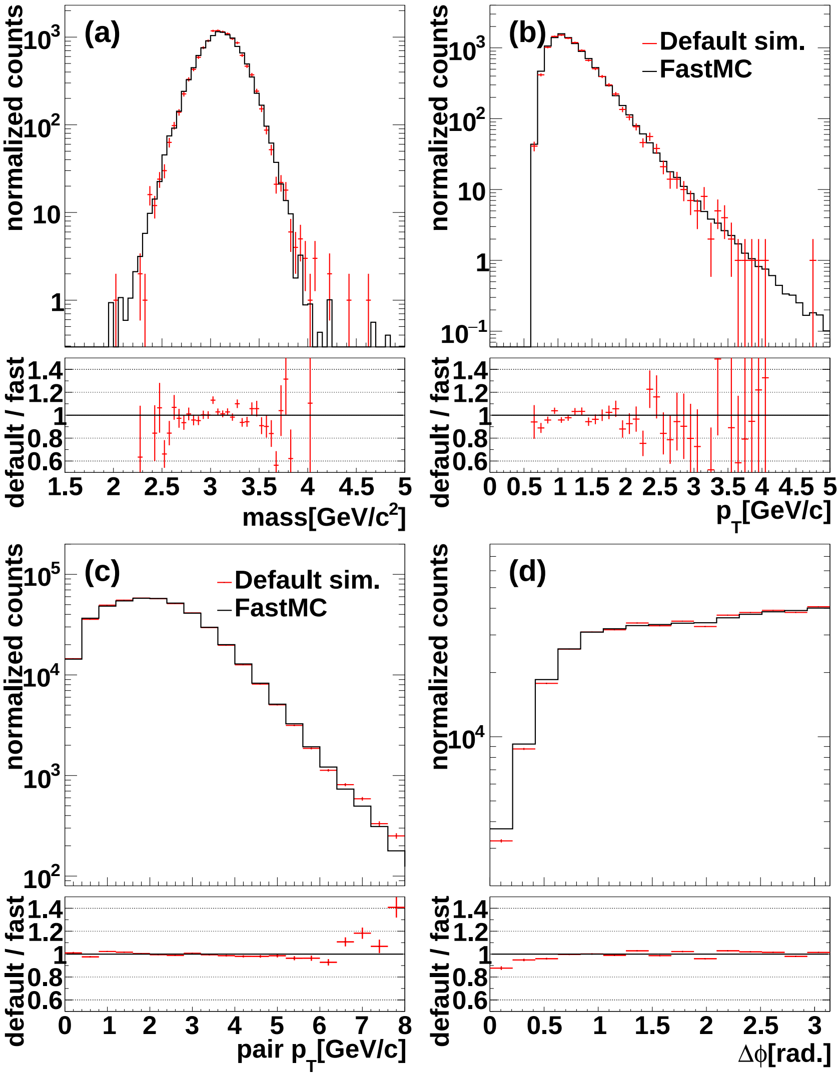

Figure 120: Comparison of distributions from FastMC and default PHENIX simulation framework. (a) mass spectrum of J/ψ muon pairs; (b) single p_T spectrum of muons from $\pi^{\pm}$ and $K^{\pm}$ with realistic input p_T spectra; (c) pair p_T spectrum of muon pairs from $b\bar{b}$; (d) $\Delta\phi$ of muon pairs from $b\bar{b}$.

filtered with the same cuts as used for real data. Thus, all detector effects including acceptance, dead areas, track reconstruction, and analysis cuts are taken properly into account.

Because the analyzed data are triggered with the MuIDLL1-2D trigger, the effects of the trigger also need to be accounted for. To achieve this, we apply an offline software trigger to all simulated tracks, which is an exact replication of the online hardware MuIDLL1-1D trigger. We require that both tracks of a pair fulfill the MUIDLL1-1D trigger condition. Here we make use of the fact that after enforcing a spatial separation of 20 cm between two MuID tracks, the MuIDLL1-2D pair trigger is reduced to a logical AND of the MuIDLL1-1D single track triggers. The separation cut necessary to achieve this factorization was determined from experimental data. In Fig. 119(a,c) a ∼20–30% difference between the mass distribution from data triggered with the MuIDLL1-2D and the data requiring each track fulfills the MuIDLL1-1D is visible at low masses. Once the separation cut is applied the difference disappears, as seen in panels (b) and (d).

A.2 FastMC

In spite of the large hadron rejection power ($\sim 1/1000$) of the muon arms, a significant fraction of the reconstructed muons are from decays of light-flavor mesons ($\pi^{\pm}$, $K^{\pm}$, and K^0). Using the default Monte-Carlo to simulate these pairs is unpractical, because for every 1,000,000 generated pairs of particles in the detector acceptance, only one muon pair would be reconstructed from the simulation. In the FastMC approach we separate the generation of particles that result in reconstructed $\mu\mu$ pairs from the simulation of the detailed detector response to an individual particle. The FastMC proceeds in four steps: (i) generation of a repository of possible detector responses to an individual particle using the default simulation framework, (ii) creation of events with multiple muons from the sources discussed in Sec. 3.4, here the repository created in step (i) is used to determine the detector response, (iii) weighting each reconstructed muon with the appropriate probability for being reconstructed and not rejected by the analysis cuts, and (iv) finally forming muon pairs and calculating their mass, p_T and azimuthal opening angle.

A.2.1 Detector response to individual particles

For each particle species ($\pi^{\pm}$, $K^{\pm}$, K^0, and $\mu^{\pm}$) $\sim 10^9$ particles were simulated. All particles are propagated through the full GEANT4 simulation and reconstruction chain. Light hadrons ($\pi^{\pm}$, $K^{\pm}$, and K^{0}) may give rise to a reconstructed muon either via (i) decaying to a muon in flight (decay muons), or (ii) penetrating all absorber layers (punch-through hadrons). The contribution from protons is negligible ($< 1\%$) compared to kaons and pions and hence neglected in this study.

These *parent particles* are generated with a flat distribution in momentum p and polar angle θ, and a uniform distribution in ϕ. Simulations are performed in three z-vertex regions, $(-22.5, -17.5$ cm$)$, $(-2.5, 2.5$ cm$)$, and $(17.5, 22.5$ cm$)$, to account for variances in detector response along z_{vtx}. Improvements by expanding to full collision z_{vtx} coverage in simulations is expected to be minimal(see Sec. 3.10.1.8). All reconstructed variables are stored along with the generated vertex and parent momentum information. These *muon candidates* are grouped into pools according to parent particle species and parent p and θ, where p and θ ranges from 2 to 32 GeV/c and 0 to 0.8 radians respectively, which covers the kinematic region relevant for this analysis. One single pool covers the kinematic region $\Delta p \times \Delta\theta = 0.1 \times 0.02$ [GeV/c rad]. The minimum number of muon candidates in one pool is ~ 10. These pools are used as repository for the possible detector response to parent particles in the subsequent steps of the FastMC.

A.2.2 Events with reconstructed muons

To create an event with reconstructed muons, we first generate events of particles as discussed in Sec. 3.4.2. For each event the list of particles is filtered so that only $\pi^{\pm}$, $K^{\pm}$, K^{0}, and $\mu^{\pm}$ in the vicinity of the muon arm acceptance are kept, and the momentum information of these particles is stored. We will refer to these particles as *input particles*.

A given input particle is matched to a pool of muon candidates in the repository for that particle species, and the input particle's p and θ. We randomly choose one muon candidate from the pool and use the reconstructed variables from that muon candidate for the input particle. The repository pools were generated from parent particles with a uniform ϕ distribution. While the input particles are matched to the muon candidate in parent p and θ, they are not matched in ϕ. We therefore rotate all reconstructed variables in the azimuthal plane from the ϕ of the parent of the muon candidate to the ϕ of input particle.

At this point we have created a *reconstructed muon* with all the characteristics that could have resulted from propagating the input particle through the default simulation framework. In particular, because the matching of input particles to muon candidates is completely random, the relative contributions and momentum distribution of decay muons and punch-through hadrons are properly accounted for. This procedure is repeated for all input particles in an event.

A.2.3 Weighting each reconstructed muon with its probability

So far each input particle leads to a reconstructed muon. This does not take into account the hadron rejection of the muon arms and the reconstruction efficiencies. Rejection and efficiency are encapsulated in weighting factors that are applied to each reconstructed muon. We factorize the weight into two components $\text{weight}_{\text{reco}}$ and weight_{ϕ}, which are discussed in the following. The final weight is calculated as:

$$\text{weight} = \text{weight}_{\text{reco}} \times \text{weight}_{\phi}. \tag{47}$$

Weighting in p and θ

The survival probability of a decay muon is highly dependent on the momentum of the muon, as well as the amount of material it traverses in the absorber, which in turn is dependent on the input particle's momentum p and the polar angle θ. We associate a weighting factor $\text{weight}_{\text{reco}}(p, \theta, z)$ to each muon candidate. This factor is the probability that an input particle with momentum p and polar angle θ, produced at vertex z, results in the reconstructed muon candidate, averaged over ϕ. The weight is computed by dividing the number of reconstructed muons in each pool by the number of parent particles generated to create the corresponding pool.

Weighting in ϕ

In addition to $\text{weight}_{\text{reco}}(p, \theta, z)$, we also need to weight in ϕ direction, weight_{ϕ}, to account for the ϕ dependent relative survival probability and reconstruction efficiency. These mainly depend on the geometry of the MuTr, thus the weighting factors are determined by a combination of variables (ϕ^{MuTr}, p_T^{MuTr}, p_z^{MuTr}), which are the azimuthal position, transverse momentum, and longitudinal momentum evaluated at MuTr Station 1. To determine weight_{ϕ}, we generate single muons with a realistic momentum distribution and propagate these muons through the default simulation framework. Because the overall survival probability is factored into $\mathrm{weight}_{\mathrm{reco}}$, weight_{ϕ} is normalized by requiring the average value of weight_{ϕ} to be one, i.e.

$$\begin{aligned}&\mathrm{weight}_{\phi}(\phi^{\mathrm{MuTr}}, \mathrm{p}_{\mathrm{T}}^{\mathrm{MuTr}}, \mathrm{p}_{\mathrm{z}}^{\mathrm{MuTr}}) \\ &= \frac{N_{\mathrm{reco}}(\phi^{\mathrm{MuTr}}, p_T^{\mathrm{MuTr}}, p_z^{\mathrm{MuTr}}) \int_{-\pi}^{+\pi} d\phi^{\mathrm{MuTr}}}{\int_{-\pi}^{+\pi} d\phi^{\mathrm{MuTr}} N_{\mathrm{reco}}(\phi^{\mathrm{MuTr}}, p_T^{\mathrm{MuTr}}, p_z^{\mathrm{MuTr}})}.\end{aligned} \tag{48}$$

A.2.4 Constructing muon pairs

In each event all reconstructed muons are combined to pairs. The pair variables are constructed from the reconstructed muon information following the exact same procedure as in real data. The weighting factor for a muon pair is the product of the weighting factors of the two reconstructed muons:

$$\mathrm{weight}_{12} = \mathrm{weight}_1 \times \mathrm{weight}_2. \tag{49}$$

This assumes that the pair reconstruction efficiency is a product of single track reconstruction efficiencies, which is true for tracks that are spatially separated in the MuTr and MuID. The latter is assured by the pair cuts we apply.

To estimate the accuracy of the FastMC, which is used to simulate muon-hadron and hadron-hadron pairs, we propagate $\mu\mu$ pairs and single hadrons through the default simulation framework and FastMC and compared the resulting distributions. We find that the mass resolution, $\Delta\phi$, single and pair p_T distributions are well reproduced by the FastMC (see Fig. 120). Small discrepancies are observed in the azimuthal opening angle distribution $\Delta\phi$ between the two muons for small $\Delta\phi$. This is likely due to the ϕ weighting procedure. The related systematic uncertainties will be discussed in Sec. 3.10.

B SIMULATION PARAMETERS

Table 9: Parameters used in PYTHIA Tune A simulation.

Parameter	Setting	Description
MSEL	1	Turn on all QCD processes
PARP(67)	4.0	Set hard scattering scale μ^2
PARP(82)	2.0	Turn off p_T for multiparticle interactions
PARP(84)	0.4	Radius of core Gaussian matter
PARP(85)	0.9	Probability that two gluons are produced with colors connected to the nearest neighbors
PARP(86)	0.95	Probability that two gluons are produced with PARP(85) conditions or closed loop
PARP(89)	1800	Reference energy scale of the turn-off p_T
PARP(90)	0.25	Energy dependence of the turn-off p_T
PARP(91)	1.5	Primordial k_T Gaussian width
CKIN(3)	1.5	Lower cutoff on $\hat{p}_\perp$
MSTP(51)	7	CTEQ 5L, leading order PDF

Table 10: Parameters used in PYTHIA Drell-Yan simulations.

Parameter	Setting	Description
MSEL	0	Select subprocesses manually
MSTP(43)	3	Select Drell-Yan process Complete Z^0/γ^* structure
MSUB(1)	1	Turn on $q + \bar{q} \rightarrow Z^0/\gamma^* \rightarrow \mu^+\mu^-$
MSTP(91)	1	Gaussian primordial k_T
PARP(91)	1.1	Gaussian width of k_T in GeV/c
MSTP(33)	1	Inclusion of k-factors in hard cross sections
MSTP(32)	4	Use $Q^2 = \hat{s}^2$
CKIN(1)	0.5	Lower cutoff on $\hat{m} = \sqrt{\hat{s}}$
CKIN(2)	-1	Upper cutoff on $\hat{m} = \sqrt{\hat{s}}$
CKIN(3)	0.0	Lower cutoff on $\hat{p}_\perp$
CKIN(4)	-1	Upper cutoff on $\hat{p}_\perp$
MSTP(51)	7	CTEQ 5L, leading order PDF

C DATA TABLES

Table 11: The differential yield $dN/d\phi$ of unlike-sign muon pairs from charm with mass 1.5–2.5 GeV/c^2 in the ideal muon arm acceptance, as a function of the pair azimuthal opening angle.

$\lvert\phi_{\mu,1} - \phi_{\mu,2}\rvert$ [rad]	$dN/d\phi$ $10^{-9}\times$[rad^{-1}]	stat. error $10^{-9}\times$[rad^{-1}]	sys. error (B) $10^{-9}\times$[rad^{-1}]	sys. error (C) $10^{-9}\times$[rad^{-1}]
$0 - \frac{\pi}{15}$	-0.136	0.199	$^{+3.3\times10^{-2}}_{-4.3\times10^{-2}}$	1.6×10^{-2}
$\frac{\pi}{15} - \frac{2\pi}{15}$	-1.43 $\times10^{-2}$	0.130	$^{+4.87\times10^{-2}}_{-3.22\times10^{-2}}$	1.7 $\times10^{-3}$
$\frac{2\pi}{15} - \frac{3\pi}{15}$	0.456	0.237	$^{+0.165}_{-0.174}$	5.5×10^{-2}
$\frac{3\pi}{15} - \frac{4\pi}{15}$	0.238	0.280	$^{+0.334}_{-0.298}$	2.9×10^{-2}
$\frac{4\pi}{15} - \frac{5\pi}{15}$	1.08	0.41	$^{+0.57}_{-0.51}$	0.13
$\frac{5\pi}{15} - \frac{6\pi}{15}$	0.443	0.579	$^{+0.792}_{-0.685}$	5.3×10^{-2}
$\frac{6\pi}{15} - \frac{7\pi}{15}$	3.34	0.71	$^{+0.94}_{-0.85}$	0.40
$\frac{7\pi}{15} - \frac{8\pi}{15}$	5.02	0.87	$^{+0.95}_{-0.85}$	0.60
$\frac{8\pi}{15} - \frac{9\pi}{15}$	7.09	0.93	$^{+0.83}_{-0.77}$	0.85
$\frac{9\pi}{15} - \frac{10\pi}{15}$	7.97	0.97	$^{+0.77}_{-0.73}$	0.96
$\frac{10\pi}{15} - \frac{11\pi}{15}$	6.69	1.05	$^{+0.82}_{-0.80}$	0.80
$\frac{11\pi}{15} - \frac{12\pi}{15}$	7.70	1.11	$^{+0.98}_{-0.96}$	0.92
$\frac{12\pi}{15} - \frac{13\pi}{15}$	10.2	1.1	$^{+1.3}_{-1.3}$	1.2
$\frac{13\pi}{15} - \frac{14\pi}{15}$	7.95	1.09	$^{+1.28}_{-1.27}$	0.95
$\frac{14\pi}{15} - \pi$	6.15	1.21	$^{+1.13}_{-1.12}$	0.74

Table 12: The differential yield $dN/d\phi$ of like-sign muon pairs from bottom with mass 3.5–10.0 GeV/c^2 in the ideal muon arm acceptance, as a function of the pair azimuthal opening angle.

$\lvert\phi_{\mu,1} - \phi_{\mu,2}\rvert$ [rad]	$dN/d\phi$ $10^{-9}\times$[rad^{-1}]	stat. error $10^{-9}\times$[rad^{-1}]	sys. error (B) $10^{-9}\times$[rad^{-1}]	sys. error (C) $10^{-9}\times$[rad^{-1}]
$\frac{4\pi}{12}$–$\frac{5\pi}{12}$	8.36×10^{-2}	3.47×10^{-2}	$^{+9.2\times10^{-3}}_{-9.2\times10^{-3}}$	1.0×10^{-2}
$\frac{5\pi}{12}$–$\frac{6\pi}{12}$	5.74×10^{-2}	2.72×10^{-2}	$^{+3.5\times10^{-3}}_{-3.6\times10^{-3}}$	6.9×10^{-3}
$\frac{6\pi}{12}$–$\frac{7\pi}{12}$	0.274	6.6×10^{-2}	$^{+1.1\times10^{-2}}_{-1.2\times10^{-2}}$	3.3×10^{-2}
$\frac{7\pi}{12}$–$\frac{8\pi}{12}$	0.531	9.6×10^{-2}	$^{+2.3\times10^{-2}}_{-2.8\times10^{-2}}$	6.4×10^{-2}
$\frac{8\pi}{12}$–$\frac{9\pi}{12}$	1.13	0.14	$^{+5\times10^{-2}}_{-9\times10^{-2}}$	0.14
$\frac{9\pi}{12}$–$\frac{10\pi}{12}$	1.51	0.18	$^{+9\times10^{-2}}_{-0.18}$	0.18
$\frac{10\pi}{12}$–$\frac{11\pi}{12}$	1.87	0.22	$^{+0.16}_{-0.30}$	0.22
$\frac{11\pi}{12}$–π	1.94	0.24	$^{+0.21}_{-0.41}$	0.23

Table 13: The differential yield dN/dp_T of unlike-sign muon pairs from bottom with mass 1.5–2.5 GeV/c^2 in the ideal muon arm acceptance, as a function of the pair transverse momentum.

p_T [GeV/c]	dN/dp_T $10^{-9}\times$[c/GeV]	stat. error $10^{-9}\times$[c/GeV]	sys. error (B) $10^{-9}\times$[c/GeV]	sys. error (C) $10^{-9}\times$[c/GeV]
0–0.2	1.02	0.73	$^{+0.59}_{-0.59}$	0.12
0.2–0.4	3.97	1.05	$^{+1.32}_{-1.31}$	0.48
0.4–0.6	8.16	1.17	$^{+1.37}_{-1.36}$	0.98
0.6–0.8	8.91	1.19	$^{+1.22}_{-1.21}$	1.07
0.9-1.0	5.89	1.08	$^{+0.92}_{-0.91}$	0.71
1.0–1.2	6.31	1.00	$^{+0.75}_{-0.73}$	0.76
1.2–1.4	5.58	0.90	$^{+0.66}_{-0.64}$	0.67
1.4–1.6	6.91	0.84	$^{+0.62}_{-0.60}$	0.83
1.6–1.8	5.15	0.75	$^{+0.58}_{-0.53}$	0.62
1.8–2.0	3.46	0.67	$^{+0.53}_{-0.49}$	0.42
2.0–2.4	1.90	0.41	$^{+0.50}_{-0.43}$	0.23
2.4–2.8	0.761	0.309	$^{+0.408}_{-0.370}$	9.1×10^{-2}
2.8–3.2	-5.97×10^{-2}	0.239	$^{+0.353}_{-0.298}$	7.2×10^{-3}
3.2–3.6	5.02×10^{-2}	0.203	$^{+0.259}_{-0.242}$	6.0×10^{-3}
3.6–4.4	0.206	0.102	$^{+0.135}_{-0.118}$	2.5×10^{-2}
4.4–5.2	8.18×10^{-2}	8.03×10^{-2}	$^{+6.77\times10^{-2}}_{-5.64\times10^{-2}}$	9.8×10^{-3}

Table 14: The differential yield dN/dp_T of like-sign muon pairs from bottom with mass 3.5–10.0 GeV/c^2 in the ideal muon arm acceptance, as a function of the pair transverse momentum.

p_T [GeV/c]	dN/dp_T $10^{-9}\times$[c/GeV]	stat. error $10^{-9}\times$[c/GeV]	sys. error (B) $10^{-9}\times$[c/GeV]	sys. error (C) $10^{-9}\times$[c/GeV]
0–0.5	0.199	5.7×10^{-2}	$^{+2.7\times10^{-2}}_{-5.0\times10^{-2}}$	2.4×10^{-2}
0.5–1.0	0.576	9.2×10^{-2}	$^{+5.6\times10^{-2}}_{-0.122}$	6.9×10^{-2}
1.0–1.5	0.754	9.9×10^{-2}	$^{+6.1\times10^{-2}}_{-0.126}$	9.0×10^{-2}
1.5–2.0	0.777	9.5×10^{-2}	$^{+5.0\times10^{-2}}_{-9.6\times10^{-2}}$	9.3×10^{-2}
2.0–2.5	0.536	7.8×10^{-2}	$^{+3.3\times10^{-2}}_{-5.8\times10^{-2}}$	6.4×10^{-2}
2.5–3.0	0.376	6.5×10^{-2}	$^{+2.0\times10^{-2}}_{-3.1\times10^{-2}}$	4.5×10^{-2}
3.0–3.5	0.230	4.9×10^{-2}	$^{+1.1\times10^{-2}}_{-1.8\times10^{-2}}$	2.8×10^{-2}
3.5–4.0	0.199	4.3×10^{-2}	$^{+8\times10^{-3}}_{-1.0\times10^{-2}}$	2.4×10^{-2}
4.0–4.5	9.05×10^{-2}	2.93×10^{-2}	$^{+3.8\times10^{-3}}_{-4.9\times10^{-3}}$	1.09×10^{-2}
4.5–5.0	2.37×10^{-2}	1.75×10^{-2}	$^{+1.4\times10^{-3}}_{-1.4\times10^{-3}}$	2.9×10^{-3}

Table 15: The differential Drell-Yan cross section $\frac{d^2\sigma}{dmdy}$ as a function of the muon pair mass, where the muon pair rapidity $|y_{\mu\mu}|$ is between 1.2 and 2.2.

$m_{\mu\mu}$ [GeV/c^2]	$\frac{d^2\sigma}{dmdy}$ [pb c^2/GeV]	stat. error [pb c^2/GeV]	sys. error (B) [pb c^2/GeV]	sys. error (C) [pb c^2/GeV]
5	114	16	$^{+24}_{-19}$	14
5.4	95.6	13.3	$^{+16.8}_{-13.4}$	11.5
5.8	67.8	10.7	$^{+11.6}_{-9.1}$	8.1
6.25	41.3	7.5	$^{+7.6}_{-5.9}$	5.0
6.75	38.1	6.5	$^{+4.6}_{-3.6}$	4.6
7.3	25.3	4.8	$^{+2.9}_{-2.3}$	3.0
7.9	19.4	4.1	$^{+1.7}_{-1.4}$	2.3
12.1	4.94	1.33	$^{+0.19}_{-0.19}$	0.59
14	0.823	0.686	$^{+3.9\times10^{-2}}_{-3.4\times10^{-2}}$	9.9×10^{-2}

Table 16: The differential Drell-Yan cross section $\frac{1}{2\pi p_T}\frac{d^2\sigma}{dy dp_T}$ as a function of the muon pair transverse momentum, where the muon pair mass $m_{\mu\mu}$ is between 4.8 and 8.2 GeV/c^2 and the muon pair rapidity $|y_{\mu\mu}|$ is between 1.2 and 2.2.

p_T [GeV/c]	$\frac{1}{2\pi p_T}\frac{d^2\sigma}{dy dp_T}$ [pb (c/GeV)^2]	stat. error [pb (c/GeV)^2]	sys. error (B) [pb (c/GeV)^2]	sys. error (C) [pb (c/GeV)^2]
0.25	12.0	3.4	$^{+1.9}_{-1.6}$	1.4
0.75	13.1	2.0	$^{+1.8}_{-1.4}$	1.6
1.25	7.48	1.30	$^{+1.42}_{-1.14}$	0.90
1.75	6.22	0.93	$^{+1.00}_{-0.81}$	0.75
2.25	2.48	0.55	$^{+0.59}_{-0.46}$	0.30
2.75	1.22	0.39	$^{+0.37}_{-0.29}$	0.15
3.25	0.408	0.239	$^{+0.206}_{-0.157}$	4.9×10^{-2}
3.75	0.688	0.198	$^{+0.123}_{-0.103}$	8.3×10^{-2}
4.25	0.627	0.164	$^{+8.4\times10^{-2}}_{-7.1\times10^{-2}}$	7.5×10^{-2}
4.75	9.29×10^{-2}	8.84×10^{-2}	$^{+3.30\times10^{-2}}_{-2.59\times10^{-2}}$	1.12×10^{-2}
5.25	9.47×10^{-2}	6.61×10^{-2}	$^{+2.28\times10^{-2}}_{-1.98\times10^{-2}}$	1.14×10^{-2}
5.75	0.127	6.6×10^{-2}	$^{+1.9\times10^{-2}}_{-1.9\times10^{-2}}$	1.5×10^{-2}

Table 17: The differential yield $d^3N/d\phi_{\mu\mu}d\eta_{\mu,1}d\eta_{\mu,2}$ of like-sign muon pairs from bottom with mass 3.5–10.0 GeV/c^2 in the ideal muon arm acceptance in p+Au and p+p collisions at $\sqrt{s_{NN}}$ = 200 GeV, as a function of the pair azimuthal opening angle.

$\lvert\phi_{\mu,1}-\phi_{\mu,2}\rvert$ [rad]	$\frac{d^3N}{d\phi_{\mu\mu}d\eta_{\mu,1}d\eta_{\mu,2}}$ $10^{-9}\times$[rad^{-1}]	stat. error $10^{-9}\times$[rad^{-1}]	sys. error (B) $10^{-9}\times$[rad^{-1}]	sys. error (C) $10^{-9}\times$[rad^{-1}]
p+p				
$\frac{5\pi}{12}$–$\frac{6\pi}{12}$	0.134	6.3×10^{-2}	$^{+2.0\times10^{-2}}_{-2.1\times10^{-2}}$	1.9×10^{-2}
$\frac{6\pi}{12}$–$\frac{7\pi}{12}$	0.639	0.153	$^{+9.3\times10^{-2}}_{-9.4\times10^{-2}}$	8.9×10^{-2}
$\frac{7\pi}{12}$–$\frac{8\pi}{12}$	1.24	0.22	$^{+0.18}_{-0.19}$	0.17
$\frac{8\pi}{12}$–$\frac{9\pi}{12}$	2.63	0.34	$^{+0.39}_{-0.43}$	0.37
$\frac{9\pi}{12}$–$\frac{10\pi}{12}$	3.52	0.42	$^{+0.54}_{-0.65}$	0.49
$\frac{10\pi}{12}$–$\frac{11\pi}{12}$	4.36	0.52	$^{+0.71}_{-0.93}$	0.61
$\frac{11\pi}{12}$–π	4.52	0.55	$^{+0.79}_{-1.14}$	0.63
p+Au (Au-going)				
$\frac{5\pi}{12}$–$\frac{6\pi}{12}$	-4.84×10^{-3}	0.165	$^{+1.7\times10^{-2}}_{-1.8\times10^{-2}}$	8×10^{-5}
$\frac{6\pi}{12}$–$\frac{7\pi}{12}$	0.722	0.390	$^{+7.1\times10^{-2}}_{-6.7\times10^{-2}}$	1.2×10^{-2}
$\frac{7\pi}{12}$–$\frac{8\pi}{12}$	1.73	0.67	$^{+0.17}_{-0.18}$	3×10^{-2}
$\frac{8\pi}{12}$–$\frac{9\pi}{12}$	3.06	0.90	$^{+0.30}_{-0.41}$	5×10^{-2}
$\frac{9\pi}{12}$–$\frac{10\pi}{12}$	4.61	1.17	$^{+0.53}_{-0.76}$	7×10^{-2}
$\frac{10\pi}{12}$–$\frac{11\pi}{12}$	4.01	1.37	$^{+0.86}_{-1.29}$	6×10^{-2}
$\frac{11\pi}{12}$–π	6.08	1.53	$^{+1.21}_{-1.75}$	0.10
p+Au (p-going)				
$\frac{5\pi}{12}$–$\frac{6\pi}{12}$	6.74×10^{-2}	0.111	$^{+8.3\times10^{-3}}_{-8.2\times10^{-3}}$	1.1×10^{-3}
$\frac{6\pi}{12}$–$\frac{7\pi}{12}$	0.651	0.273	$^{+4.9\times10^{-2}}_{-5.0\times10^{-2}}$	1.0×10^{-2}
$\frac{7\pi}{12}$–$\frac{8\pi}{12}$	1.66	0.45	$^{+0.12}_{-0.13}$	3×10^{-2}
$\frac{8\pi}{12}$–$\frac{9\pi}{12}$	1.46	0.51	$^{+0.13}_{-0.15}$	2×10^{-2}
$\frac{9\pi}{12}$–$\frac{10\pi}{12}$	3.58	0.74	$^{+0.29}_{-0.33}$	6×10^{-2}
$\frac{10\pi}{12}$–$\frac{11\pi}{12}$	4.41	0.89	$^{+0.39}_{-0.47}$	7×10^{-2}
$\frac{11\pi}{12}$–π	5.88	0.99	$^{+0.53}_{-0.65}$	9×10^{-2}

Table 18: The differential yield $d^3N/dp_{T,\mu\mu}d\eta_{\mu,1}d\eta_{\mu,2}$ of like-sign muon pairs from bottom with mass 3.5–10.0 GeV/c^2 in the ideal muon arm acceptance in p+Au and p+p collisions at $\sqrt{s_{NN}} = 200$ GeV, as a function of the pair transverse momentum.

$p_{T,\mu\mu}$ [GeV/c]	$\frac{d^3N}{dp_{T,\mu\mu}d\eta_{\mu,1}d\eta_{\mu,2}}$ $10^{-9}\times$[GeV/c]	stat. error $10^{-9}\times$[GeV/c]	sys. error (B) $10^{-9}\times$[GeV/c]	sys. error (C) $10^{-9}\times$[GeV/c]
		p+p		
0–1	0.903	0.126	$^{+0.160}_{-0.237}$	0.126
1–2	1.78	0.16	$^{+0.28}_{-0.36}$	0.25
2–3	1.09	0.12	$^{+0.17}_{-0.19}$	0.15
3–4	0.502	7.6×10^{-2}	$^{+7.4\times10^{-2}}_{-7.7\times10^{-2}}$	7.0×10^{-2}
4–5	0.138	4.0×10^{-2}	$^{+2.0\times10^{-2}}_{-2.1\times10^{-2}}$	1.9×10^{-2}
		p+Au (Au-going)		
0–1	1.56	0.40	$^{+0.29}_{-0.42}$	2×10^{-2}
1–2	2.17	0.44	$^{+0.31}_{-0.466}$	3×10^{-2}
2–3	0.966	0.293	$^{+0.122}_{-0.169}$	1.5×10^{-2}
3–4	0.431	0.166	$^{+3.9\times10^{-2}}_{-4.6\times10^{-2}}$	7×10^{-3}
4–5	5.93×10^{-2}	7.66×10^{-2}	$^{+7.9\times10^{-3}}_{-8.8\times10^{-3}}$	9×10^{-4}
		p+Au (p-going)		
0–1	1.41	0.25	$^{+0.14}_{-0.16}$	2×10^{-2}
1–2	1.99	0.29	$^{+0.17}_{-0.20}$	3×10^{-2}
2–3	0.678	0.181	$^{+6.1\times10^{-2}}_{-7.1\times10^{-2}}$	1.1×10^{-2}
3–4	0.324	0.109	$^{+2.5\times10^{-2}}_{-2.7\times10^{-2}}$	5×10^{-3}
4–5	0.174	7.1×10^{-2}	$^{+1.3\times10^{-2}}_{-1.3\times10^{-2}}$	3×10^{-3}

Table 19: The nuclear modification factor R_{p+Au} of like-sign muon pairs from bottom with mass 3.5–10.0 GeV/c^2 in the ideal muon arm acceptance in p+Au at $\sqrt{s_{NN}}$ = 200 GeV, as a function of the azimuthal opening angle.

	$\Delta\phi_{\mu\mu}$ [rad]	R_{p+Au}	stat. error	sys. error (B)	sys. error (C)
Au-going	$\frac{6\pi}{12}$–$\frac{7\pi}{12}$	1.13	0.67	$^{+0.11}_{-0.11}$	0.14
	$\frac{7\pi}{12}$–$\frac{8\pi}{12}$	1.39	0.60	$^{+0.14}_{-0.13}$	0.14
	$\frac{8\pi}{12}$–$\frac{9\pi}{12}$	1.16	0.37	$^{+0.11}_{-0.12}$	0.14
	$\frac{9\pi}{12}$–$\frac{10\pi}{12}$	1.31	0.37	$^{+0.14}_{-0.14}$	0.14
	$\frac{10\pi}{12}$–$\frac{11\pi}{12}$	0.921	0.332	$^{+0.174}_{-0.210}$	0.14
	$\frac{11\pi}{12}$–π	1.35	0.38	$^{+0.23}_{-0.25}$	0.14
p-going	$\frac{6\pi}{12}$–$\frac{7\pi}{12}$	1.02	0.49	$^{+0.08}_{-0.08}$	0.14
	$\frac{7\pi}{12}$–$\frac{8\pi}{12}$	1.34	0.44	$^{+0.11}_{-0.11}$	0.14
	$\frac{8\pi}{12}$–$\frac{9\pi}{12}$	0.554	0.208	$^{+0.050}_{-0.049}$	0.14
	$\frac{9\pi}{12}$–$\frac{10\pi}{12}$	1.02	0.24	$^{+0.11}_{-0.09}$	0.14
	$\frac{10\pi}{12}$–$\frac{11\pi}{12}$	1.01	0.24	$^{+0.14}_{-0.10}$	0.14
	$\frac{11\pi}{12}$–π	1.30	0.27	$^{+0.25}_{-0.15}$	0.14

Table 20: The nuclear modification factor R_{p+Au} of like-sign muon pairs from bottom with mass 3.5–10.0 GeV/c^2 in the ideal muon arm acceptance in p+Au collisions at $\sqrt{s_{NN}}$ = 200 GeV, as a function of the pair transverse momentum.

	$p_{T,\mu\mu}$ [GeV/c]	R_{p+Au}	stat. error	sys. error (B)	sys. error (C)
Au-going	0–1	1.72	0.50	$^{+0.33}_{-0.48}$	0.14
	1–2	1.22	0.27	$^{+0.19}_{-0.27}$	0.14
	2–3	0.885	0.286	$^{+0.120}_{-0.167}$	0.14
	3–4	0.858	0.355	$^{+0.084}_{-0.098}$	0.14
	4–5	0.429	0.568	$^{+0.062}_{-0.071}$	0.14
p-going	0–1	1.56	0.35	$^{+0.35}_{-0.22}$	0.14
	1–2	1.11	0.19	$^{+0.15}_{-0.13}$	0.14
	2–3	0.621	0.179	$^{+0.063}_{-0.069}$	0.14
	3–4	0.644	0.239	$^{+0.055}_{-0.059}$	0.14
	4–5	1.26	0.63	$^{+0.11}_{-0.10}$	0.14

Table 21: The differential Drell-Yan cross section per nucleon $\frac{d^2\sigma}{dmdy}$ as a function of the muon pair mass, where the muon pair rapidity $|y_{\mu\mu}|$ is between 1.2 and 2.2.

$m_{\mu\mu}$ [GeV/c^2]	$\frac{d^2\sigma}{dmdy}$ [nb c^2/GeV]	stat. error [nb c^2/GeV]	sys. error (B) [nb c^2/GeV]	sys. error (C) [nb c^2/GeV]
		p+p		
5.2	0.104	0.010	$^{+0.024}_{-0.020}$	0.012
6.2	4.84×10^{-2}	5.1×10^{-3}	$^{+9.9\times10^{-3}}_{-8.5\times10^{-3}}$	5.8×10^{-3}
7.5	2.47×10^{-2}	3.0×10^{-3}	$^{+3.9\times10^{-3}}_{-3.6\times10^{-3}}$	3.0×10^{-3}
13.1	2.84×10^{-3}	7.3×10^{-4}	$^{+3.6\times10^{-4}}_{-3.6\times10^{-4}}$	3.4×10^{-4}
		p+Au (Au-going)		
5.2	7.37×10^{-2}	2.02×10^{-2}	$^{+3.23\times10^{-2}}_{-3.07\times10^{-2}}$	7.1×10^{-3}
6.2	3.79×10^{-2}	9.7×10^{-3}	$^{+1.17\times10^{-2}}_{-1.09\times10^{-2}}$	3.6×10^{-3}
7.5	2.98×10^{-2}	6.2×10^{-3}	$^{+3.5\times10^{-3}}_{-3.5\times10^{-3}}$	2.9×10^{-3}
13.1	2.72×10^{-3}	1.36×10^{-3}	$^{+2.0\times10^{-4}}_{-2.0\times10^{-4}}$	2.6×10^{-4}
		p+Au (p-going)		
5.2	9.65×10^{-2}	1.50×10^{-2}	$^{+2.03\times10^{-2}}_{-2.05\times10^{-2}}$	9.2×10^{-3}
6.2	5.71×10^{-2}	8.0×10^{-3}	$^{+8.3\times10^{-3}}_{-8.0\times10^{-3}}$	5.5×10^{-3}
7.5	2.41×10^{-2}	4.5×10^{-3}	$^{+2.5\times10^{-3}}_{-2.5\times10^{-3}}$	2.3×10^{-3}
13.1	6.91×10^{-4}	6.09×10^{-4}	$^{+6.3\times10^{-5}}_{-6.5\times10^{-5}}$	6.6×10^{-5}

Table 22: The nuclear modification factor for pairs from the Drell-Yan process as a function of the muon pair mass, where the muon pair rapidity $|y_{\mu\mu}|$ is between 1.2 and 2.2.

	$m_{\mu\mu}$ [GeV/c^2]	R_{p+Au}	stat. error	sys. error (B)	sys. error (C)
Au-going	5.2	0.711	0.195	$^{+0.274}_{-0.269}$	0.14
	6.2	0.781	0.201	$^{+0.209}_{-0.205}$	0.14
	7.5	1.21	0.25	$^{+0.14}_{-0.15}$	0.14
	13.1	0.958	0.480	$^{+0.078}_{-0.078}$	0.14
p-going	5.2	0.931	0.145	$^{+0.160}_{-0.183}$	0.14
	6.2	1.18	0.16	$^{+0.17}_{-0.18}$	0.14
	7.5	0.976	0.182	$^{+0.102}_{-0.106}$	0.14
	13.1	0.244	0.214	$^{+0.023}_{-0.024}$	0.14

Table 23: The differential Drell-Yan cross section per nucleon $\frac{1}{2\pi p_T}\frac{d^2\sigma}{dydp_T}$ as a function of the muon pair transverse momentum, where the muon pair mass is between 4.8 and 8.2 GeV/c^2 and the muon pair rapidity $|y_{\mu\mu}|$ is between 1.2 and 2.2.

p_T [GeV/c]	$\frac{1}{2\pi p_T}\frac{d^2\sigma}{dydp_T}$ [nb (c/GeV)^2]	stat. error [nb (c/GeV)^2]	sys. error (B) [nb (c/GeV)^2]	sys. error (C) [nb (c/GeV)^2]
		p+p		
0.5	1.37×10^{-2}	1.8×10^{-3}	$^{+2.7\times10^{-3}}_{-2.4\times10^{-3}}$	1.9×10^{-3}
1.5	7.08×10^{-3}	8.0×10^{-4}	$^{+1.54\times10^{-3}}_{-1.36\times10^{-3}}$	9.8×10^{-4}
2.5	1.76×10^{-3}	3.3×10^{-4}	$^{+5.2\times10^{-4}}_{-4.3\times10^{-4}}$	2.4×10^{-4}
3.5	5.63×10^{-4}	1.52×10^{-4}	$^{+1.70\times10^{-4}}_{-1.41\times10^{-4}}$	7.8×10^{-5}
4.5	3.55×10^{-4}	9.0×10^{-5}	$^{+7.5\times10^{-5}}_{-6.8\times10^{-5}}$	4.9×10^{-5}
		p+Au (Au-going)		
0.5	1.37×10^{-2}	3.6×10^{-3}	$^{+2.9\times10^{-3}}_{-2.9\times10^{-3}}$	1.3×10^{-3}
1.5	5.56×10^{-3}	1.49×10^{-3}	$^{+1.94\times10^{-3}}_{-1.87\times10^{-3}}$	5.3×10^{-4}
2.5	1.17×10^{-3}	6.1×10^{-4}	$^{+7.3\times10^{-4}}_{-6.8\times10^{-4}}$	1.1×10^{-4}
3.5	5.71×10^{-4}	2.97×10^{-4}	$^{+2.21\times10^{-4}}_{-2.08\times10^{-4}}$	5.5×10^{-5}
4.5	1.80×10^{-4}	1.48×10^{-4}	$^{+6.1\times10^{-5}}_{-5.9\times10^{-5}}$	1.7×10^{-5}
		p+Au (p-going)		
0.5	1.26×10^{-2}	2.6×10^{-3}	$^{+1.9\times10^{-3}}_{-2.1\times10^{-3}}$	1.2×10^{-3}
1.5	5.87×10^{-3}	1.05×10^{-3}	$^{+1.18\times10^{-3}}_{-1.24\times10^{-3}}$	5.6×10^{-4}
2.5	2.73×10^{-3}	5.1×10^{-4}	$^{+4.9\times10^{-4}}_{-4.8\times10^{-4}}$	2.6×10^{-4}
3.5	1.03×10^{-3}	2.5×10^{-4}	$^{+1.6\times10^{-4}}_{-1.4\times10^{-4}}$	1.0×10^{-4}
4.5	4.90×10^{-4}	1.5×10^{-4}	$^{+4.9\times10^{-5}}_{-4.8\times10^{-5}}$	4.7×10^{-5}

Table 24: The nuclear modification factor for pairs from the Drell-Yan process as a function of the muon pair pair transverse momentum, where the muon pair mass is between 4.8 and 8.2 GeV/c^2 and the muon pair rapidity $|y_{\mu\mu}|$ is between 1.2 and 2.2.

	$p_{T,\mu\mu}$ [GeV/c]	R_{p+Au}	stat. error	sys. error (B)	sys. error (C)
Au-going	0.5	0.999	0.260	$^{+0.195}_{-0.201}$	0.14
	1.5	0.785	0.211	$^{+0.245}_{-0.243}$	0.14
	2.5	0.661	0.343	$^{+0.354}_{-0.346}$	0.14
	3.5	1.01	0.53	$^{+0.32}_{-0.33}$	0.14
	4.5	0.507	0.417	$^{+0.140}_{-0.153}$	0.14
p-going	0.5	0.914	0.186	$^{+0.121}_{-0.144}$	0.14
	1.5	0.830	0.149	$^{+0.134}_{-0.161}$	0.14
	2.5	1.55	0.29	$^{+0.31}_{-0.32}$	0.14
	3.5	1.83	0.45	$^{+0.36}_{-0.36}$	0.14
	4.5	1.38	0.42	$^{+0.19}_{-0.19}$	0.14

D References

References

[1] C. Patrignani et al. Rev. of Particle Phys. *Chin. Phys. C*, 40(10):100001, 2016.

[2] Michael Schmelling. Status of the Strong Coupling Constant.

[3] Alexei Bazavov. Lattice QCD at Non-Zero Temperature. In *Proceedings, 32nd International Symposium on Lattice Field Theory (Lattice 2014): Brookhaven, NY, USA, June 23-28, 2014*, 2015.

[4] Frithjof Karsch. Lattice results on QCD thermodynamics. *Nucl. Phys.*, A698:199–208, 2002.

[5] S. S. Adler et al. Identified charged particle spectra and yields in Au+Au collisions at S(NN)**1/2 = 200-GeV. *Phys. Rev.*, C69:034909, 2004.

[6] A. Adare et al. Scaling properties of azimuthal anisotropy in Au+Au and Cu+Cu collisions at s(NN) = 200-GeV. *Phys. Rev. Lett.*, 98:162301, 2007.

[7] J. Adams et al. Multi-strange baryon elliptic flow in Au + Au collisions at $\sqrt{s_{NN}} = 200$ GeV. *Phys. Rev. Lett.*, 95:122301, 2005.

[8] John Adams et al. Particle type dependence of azimuthal anisotropy and nuclear modification of particle production in Au + Au collisions at $\sqrt{s_{NN}} = 200$ GeV. *Phys. Rev. Lett.*, 92:052302, 2004.

[9] K. Adcox et al. Suppression of hadrons with large transverse momentum in central Au+Au collisions at $\sqrt{s_{NN}} = 130$-GeV. *Phys. Rev. Lett.*, 88:022301, 2002.

[10] J. Adams et al. Evidence from d + Au measurements for final state suppression of high $\sqrt{p_T}$ hadrons in Au+Au collisions at RHIC. *Phys. Rev. Lett.*, 91:072304, 2003.

[11] A. Adare et al. Energy Loss and Flow of Heavy Quarks in Au+Au Collisions at $\sqrt{s_{NN}} = 200$ GeV. *Phys. Rev. Lett.*, 98:172301, 2007.

[12] E. Norrbin and T. Sjostrand. Production and hadronization of heavy quarks. *Eur. Phys. J. C*, 17:137, 2000.

[13] P. Ilten, N. L. Rodd, J. Thaler, and Mike Williams. Disentangling Heavy Flavor at Colliders. *Phys. Rev. D*, 96(5):054019, 2017.

[14] A. Adare et al. Heavy Quark Production in $p + p$ and Energy Loss and Flow of Heavy Quarks in Au+Au Collisions at $\sqrt{s_{NN}} = 200$ GeV. *Phys. Rev. C*, 84:044905, 2011.

[15] S . Acharya et al. Measurement of D-meson production at mid-rapidity in pp collisions at $\sqrt{s} = 7$ TeV. *Eur. Phys. J. C*, 77(8):550, 2017.

[16] Donald F. Geesaman, K. Saito, and Anthony William Thomas. The nuclear EMC effect. *Ann. Rev. Nucl. Part. Sci.*, 45:337–390, 1995.

[17] Ringaile Placakyte. Parton Distribution Functions. In *Proceedings, 31st International Conference on Physics in collisions (PIC 2011): Vancouver, Canada, August 28-September 1, 2011*, 2011.

[18] A. Adare et al. Spectra and ratios of identified particles in Au+Au and d+Au collisions at $\sqrt{s_{NN}} = 200$ GeV. *Phys. Rev.*, C88(2):024906, 2013.

[19] A. Adare et al. Cold-nuclear-matter effects on heavy-quark production in d+Au collisions at $\sqrt{s_{NN}} = 200$ GeV. *Phys. Rev. Lett.*, 109(24):242301, 2012.

[20] A. Adare et al. Cold-Nuclear-Matter Effects on Heavy-Quark Production at Forward and Backward Rapidity in d+Au Collisions at $\sqrt{s_{NN}} = 200$ GeV. *Phys. Rev. Lett.*, 112(25):252301, 2014.

[21] A. Adare et al. Measurements of e^+e^- pairs from open heavy flavor in p+p and d+A collisions at $\sqrt{s_{NN}} = 200$ GeV. *Phys. Rev. C*, 96(2):024907, 2017.

[22] A. Adare et al. Heavy-flavor electron-muon correlations in p+p and d+Au collisions at $\sqrt{s_{_{NN}}} = 200$ GeV. *Phys. Rev. C*, 89(3):034915, 2014.

[23] A. Adare et al. Dielectron production in Au+Au collisions at $\sqrt{s_{NN}}$=200 GeV. *Phys. Rev. C*, 93(1):014904, 2016.

[24] Shreyasi Acharya et al. Measurement of dielectron production in central Pb-Pb collisions at $\sqrt{s_{\mathrm{NN}}} = 2.76$ TeV. 2018.

[25] Kari J. Eskola, Petja Paakkinen, Hannu Paukkunen, and Carlos A. Salgado. EPPS16: Nuclear parton distributions with LHC data. *Eur. Phys. J.*, C77(3):163, 2017.

[26] K. Kovarik et al. nCTEQ15 - Global analysis of nuclear parton distributions with uncertainties in the CTEQ framework. *Phys. Rev.*, D93(8):085037, 2016.

[27] U.S. Department of Energy. User Facilities: Relativistic Heavy Ion Collider (RHIC). *Online.*

[28] Brookhaven National Lab. Run Overview of the Relativistic Heavy Ion Collider. *Online.*

[29] M. Allen et al. NIM A499 549-559.

[30] K. Dehmelt. Overview of the PHENIX Detector. *PHENIX School.*

[31] H. Akikawa et al. NIM A499 537-548.

[32] Phenix on-line systems. *Nuclear Instruments and Methods in Physics Research Section A: Accelerators, Spectrometers, Detectors and Associated Equipment*, 499(2):560 – 592, 2003. The Relativistic Heavy Ion Collider Project: RHIC and its Detectors.

[33] A. Adare et al. Inclusive cross-section and double helicity asymmetry for π^0 production in p+p collisions at $\sqrt{s}$= 200 GeV: Implications for the polarized gluon distribution in the proton. *Phys. Rev. D*, 76:051106, 2007.

[34] S. S. Adler et al. Mid-rapidity neutral pion production in proton proton collisions at $\sqrt{s}$=200 GeV. *Phys. Rev. Lett.*, 91:241803, 2003.

[35] A. Adare et al. Identified charged hadron production in $p+p$ collisions at $\sqrt{s} = 200$ and 62.4 GeV. *Phys. Rev. C*, 83:064903, 2011.

[36] A. Adare et al. Measurement of neutral mesons in p+p collisions at $\sqrt{s}$=200 GeV and scaling properties of hadron production. *Phys. Rev. D*, 83:052004, 2011.

[37] S. S. Adler et al. High transverse momentum η meson production in p+p, d+Au and Au+Au collisions at $\sqrt{s_{NN}}$= 200 GeV. *Phys. Rev. C*, 75:024909, 2007.

[38] A. Adare et al. Cross section and double helicity asymmetry for η mesons and their comparison to neutral pion production in p+p collisions at $\sqrt{s} = 200$ GeV. *Phys. Rev. D*, 83:032001, 2011.

[39] I. Arsene et al. Production of mesons and baryons at high rapidity and high p_T in proton-proton collisions at $\sqrt{s}$= 200 GeV. *Phys. Rev. Lett.*, 98:252001, 2007.

[40] A. Adare et al. Low-mass vector-meson production at forward rapidity in p+p collisions at $\sqrt{s} = 200$ GeV. *Phys. Rev. D*, 90(5):052002, 2014.

[41] A. Adare et al. Ground and excited charmonium state production in $p + p$ collisions at $\sqrt{s} = 200$ GeV. *Phys. Rev. D*, 85:092004, 2012.

[42] M. A. Vasilev et al. Parton energy loss limits and shadowing in Drell-Yan dimuon production. *Phys. Rev. Lett.*, 83:2304–2307, 1999.

[43] D. M. Alde et al. Nuclear dependence of dimuon production at 800-GeV. FNAL-772 experiment. *Phys. Rev. Lett.*, 64:2479–2482, 1990.

[44] K. J. Eskola, V. J. Kolhinen, and C. A. Salgado. The Scale dependent nuclear effects in parton distributions for practical applications. *Eur. Phys. J.*, C9:61–68, 1999.

[45] Alan D. Martin, R. G. Roberts, W. James Stirling, and R. S. Thorne. Parton distributions: A New global analysis. *Eur. Phys. J.*, C4:463–496, 1998.

[46] Eduardo Basso, Victor P. Goncalves, Michal Krelina, Jan Nemchik, and Roman Pasechnik. Nuclear effects in Drell-Yan pair production in high-energy pA collisions. *Phys. Rev.*, D93(9):094027, 2016.

[47] Shreyasi Acharya et al. Dielectron and heavy-quark production in inelastic and high-multiplicity proton?proton collisions at $\sqrt{s_{NN}}$ = 13TeV. *Phys. Lett.*, B788:505–518, 2019.

[48] Elke-Caroline Aschenauer et al. The RHIC Cold QCD Plan for 2017 to 2023: A Portal to the EIC. 2016.

[49] M. Aghasyan et al. First measurement of transverse-spin-dependent azimuthal asymmetries in the Drell-Yan process. *Phys. Rev. Lett.*, 119(11):112002, 2017.

[50] L. Adamczyk et al. Measurement of the transverse single-spin asymmetry in $p^{\uparrow} + p \rightarrow W^{\pm}/Z^{0}$ at RHIC. *Phys. Rev. Lett.*, 116(13):132301, 2016.

[51] S. T. C. Siklos G. W. Gibbons, S. W. Hawking. The Very Early Universe. 1985.

[52] H. Georgi and S. L. Glashow. Unity of All Elementary Particle Forces. *Phys. Rev. Lett.*, 32:438–441, 1974.

[53] Edward Shuryak. Strongly coupled quark-gluon plasma in heavy ion collisions. *Rev. Mod. Phys.*, 89:035001, 2017.

[54] David J. Gross and Frank Wilczek. Ultraviolet Behavior of Nonabelian Gauge Theories. *Phys. Rev. Lett.*, 30:1343–1346, 1973. [,271(1973)].

[55] H. David Politzer. Reliable Perturbative Results for Strong Interactions. *Phys. Rev. Lett.*, 30:1346–1349, 1973. [,274(1973)].

[56] David J. Gross and Frank Wilczek. Ultraviolet Behavior of Nonabelian Gauge Theories. *Phys. Rev. Lett.*, 30:1343–1346, 1973. [,271(1973)].

[57] Larry D. McLerran and Benjamin Svetitsky. A Monte Carlo Study of SU(2) Yang-Mills Theory at Finite Temperature. *Phys. Lett.*, 98B:195, 1981. [283(1980)].

[58] I. Arsene et al. Quark gluon plasma and color glass condensate at RHIC? The Perspective from the BRAHMS experiment. *Nucl. Phys.*, A757:1–27, 2005.

[59] B. B. Back et al. The PHOBOS perspective on discoveries at RHIC. *Nucl. Phys.*, A757:28–101, 2005.

[60] John Adams et al. Experimental and theoretical challenges in the search for the quark gluon plasma: The STAR Collaboration's critical assessment of the evidence from RHIC collisions. *Nucl. Phys.*, A757:102–183, 2005.

[61] K. Adcox et al. Formation of dense partonic matter in relativistic nucleus-nucleus collisions at RHIC: Experimental evaluation by the PHENIX collaboration. *Nucl. Phys.*, A757:184–283, 2005.

[62] K. Aamodt et al. The ALICE experiment at the CERN LHC. *JINST*, 3:S08002, 2008.

[63] G. Aad et al. The ATLAS Experiment at the CERN Large Hadron Collider. *JINST*, 3:S08003, 2008.

[64] S. Chatrchyan et al. The CMS Experiment at the CERN LHC. *JINST*, 3:S08004, 2008.

[65] A. Augusto Alves, Jr. et al. The LHCb Detector at the LHC. *JINST*, 3:S08005, 2008.

[66] M. Cacciari, M. Greco, and P. Nason. The p_T spectrum in heavy flavor hadroproduction. J. High Energy Phys. **05 (1998)** 007.

[67] T. Sjostrand, S. Mrenna, and P. Z. Skands. PYTHIA 6.4 Phys. and Manual. J. High Energy Phys. **05 (2006)** 026 .

[68] S. Frixione, P. Nason, and G. Ridolfi. A Positive-weight next-to-leading-order Monte Carlo for heavy flavour hadroproduction. J. High Energy Phys. **09 (2007)** 126.

[69] S. Frixione, P. Nason, and B. R. Webber. Matching NLO QCD and parton showers in heavy flavor production. J. High Energy Phys. **08 (2003)** 007.

[70] R. Vogt. The Total charm cross-section. *Eur. Phys. J. ST*, 155:213, 2008.

[71] Ekkard Schnedermann, Josef Sollfrank, and Ulrich W. Heinz. Thermal phenomenology of hadrons from 200-A/GeV S+S collisions. *Phys. Rev.*, C48:2462–2475, 1993.

[72] Michael L. Miller, Klaus Reygers, Stephen J. Sanders, and Peter Steinberg. Glauber modeling in high energy nuclear collisions. *Ann. Rev. Nucl. Part. Sci.*, 57:205–243, 2007.

[73] Steffen A. Bassa et al. Hot and Dense QCD Matter Unraveling the Mysteries of the Strongly Interacting Quark-Gluon-Plasma.

[74] Ivan Vitev and Miklos Gyulassy. High p_T tomography of d + Au and Au+Au at SPS, RHIC, and LHC. *Phys. Rev. Lett.*, 89:252301, 2002.

[75] Hendrik van Hees, Vincenzo Greco, and Ralf Rapp. Heavy-quark probes of the quark-gluon plasma at RHIC. *Phys. Rev.*, C73:034913, 2006.

[76] Guy D. Moore and Derek Teaney. How much do heavy quarks thermalize in a heavy ion collision? *Phys. Rev.*, C71:064904, 2005.

[77] Jorge Casalderrey-Solana and Derek Teaney. Heavy quark diffusion in strongly coupled N=4 Yang-Mills. *Phys. Rev.*, D74:085012, 2006.

[78] John C. Collins, Davison E. Soper, and George F. Sterman. Factorization of Hard Processes in QCD. *Adv. Ser. Direct. High Energy Phys.*, 5:1–91, 1989.

[79] Matteo Cacciari, Stefano Frixione, Nicolas Houdeau, Michelangelo L. Mangano, Paolo Nason, and Giovanni Ridolfi. Theoretical predictions for charm and bottom production at the LHC. *JHEP*, 10:137, 2012.

[80] R. Vogt. Heavy Flavor Azimuthal Correlations in Cold Nuclear Matter. *Phys. Rev.*, C98(3):034907, 2018.

[81] C. Aidala et al. Cross section and transverse single-spin asymmetry of muons from open heavy-flavor decays in polarized p+p collisions at $\sqrt{s} = 200$ GeV. *Phys. Rev. D*, 95(11):112001, 2017.

[82] Guannan Xie. Measurement of D^0 Meson Production and Azimuthal Anisotropy in Au+Au Collisions at $\sqrt{s_{NN}} = 200$ GeV. *Nucl. Part. Phys. Proc.*, 289:209, 2017.

[83] D. Acosta et al. Measurement of prompt charm meson production cross sections in $p\bar{p}$ collisions at $\sqrt{s} = 1.96$ TeV. *Phys. Rev. Lett.*, 91:241804, 2003.

[84] Roel Aaij et al. Measurements of prompt charm production cross-sections in pp collisions at $\sqrt{s} = 13$ TeV. J. High Energy Phys. **03 (2016)** 159; [Erratum: J. High Energy Phys. **05 (2017)** 074].

[85] G. Aad et al. Measurement of $D^{*\pm}$, $D^{\pm}$ and $D_s^{\pm}$ meson production cross sections in pp collisions at $\sqrt{s} = 7$ TeV with the ATLAS detector. *Nucl. Phys. B*, 907:717, 2016.

[86] A. M Sirunyan et al. Nuclear modification factor of D0 mesons in PbPb collisions at $\sqrt{s_{NN}} = 5.02$ TeV. arXiv:1708.04962.

[87] C. Aidala et al. B-meson production at forward and backward rapidity in $p + p$ and Cu+Au collisions at $\sqrt{s_{_{NN}}} = 200$ GeV. *Phys. Rev. C*, 96(6):064901, 2017.

[88] A. Adare et al. Measurement of Bottom versus Charm as a Function of Transverse Momentum with Electron-Hadron Correlations in $p + p$ Collisions at $\sqrt{s} = 200$ GeV. *Phys. Rev. Lett.*, 103:082002, 2009.

[89] M. M. Aggarwal et al. Measurement of the Bottom contribution to non-photonic electron production in $p + p$ collisions at $\sqrt{s}$=200 GeV. *Phys. Rev. Lett.*, 105:202301, 2010.

[90] B. Abbott et al. The $b\bar{b}$ production cross section and angular correlations in $p\bar{p}$ collisions at $\sqrt{s} = 1.8$ TeV. *Phys. Lett.*, B487:264–272, 2000.

[91] Betty Bezverkhny Abelev et al. Beauty production in pp collisions at $\sqrt{s} = 2.76$ TeV measured via semi-electronic decays. *Phys. Lett.*, B738:97–108, 2014.

[92] Georges Aad et al. Measurement of the b-hadron production cross section using decays to $D^{*}\mu^{-}X$ final states in pp collisions at sqrt(s) = 7 TeV with the ATLAS detector. *Nucl. Phys.*, B864:341–381, 2012.

[93] D. Acosta et al. Measurement of the J/ψ meson and $b-$hadron production cross sections in $p\bar{p}$ collisions at $\sqrt{s} = 1960$ GeV. *Phys. Rev. D*, 71:032001, 2005.

[94] Serguei Chatrchyan et al. Measurement of the B^0 production cross section in pp Collisions at $\sqrt{s} = 7$ TeV. *Phys. Rev. Lett.*, 106:252001, 2011.

[95] R. Aaij et al. Measurement of the b-quark production cross-section in 7 and 13 TeV pp collisions. *Phys. Rev. Lett.*, 118(5):052002, 2017. [Erratum: Phys. Rev. Lett. **119**, 169901 (2017)].

[96] J. W. Cronin, Henry J. Frisch, M. J. Shochet, J. P. Boymond, R. Mermod, P. A. Piroue, and Richard L. Sumner. Production of hadrons with large transverse momentum at 200, 300, and 400 GeV. *Phys. Rev.*, D11:3105–3123, 1975.

[97] J. J. Aubert et al. The ratio of the nucleon structure functions F_2^N for iron and deuterium. *Phys. Lett.*, 123B:275–278, 1983.

[98] J. Seely et al. New measurements of the EMC effect in very light nuclei. *Phys. Rev. Lett.*, 103:202301, 2009.

[99] A. Bodek and J. L. Ritchie. Fermi Motion Effects in Deep Inelastic Lepton Scattering from Nuclear Targets. *Phys. Rev.*, D23:1070, 1981.

[100] Stephen Scott Adler et al. J/psi production and nuclear effects for d+Au and p+p collisions at $\sqrt{s_{NN}} = 200$ GeV. *Phys. Rev. Lett.*, 96:012304, 2006.

[101] K J. Eskola A, H Paukkunen A, and C A. Salgado C. Eps09 a new generation of nlo and lo nuclear parton distribution functions. *Journal of High Energy Physics*, 2009, 03 2009.

[102] C. Aidala et al. Creating small circular, elliptical, and triangular droplets of quark-gluon plasma. 2018.

[103] Vardan Khachatryan et al. Evidence for collectivity in pp collisions at the LHC. *Phys. Lett.*, B765:193–220, 2017.

[104] S. D. Drell and T.-M. Yan. Massive Lepton Pair Production in Hadron-Hadron Collisions at High-Energies. *Phys. Rev. Lett.*, 25:316, 1970. [Erratum: Phys. Rev. Lett.25,902(1970)].

[105] J. H. Christenson, G. S. Hicks, L. M. Lederman, P. J. Limon, B. G. Pope, and E. Zavattini. Observation of massive muon pairs in hadron collisions. *Phys. Rev. Lett.*, 25:1523, 1970.

[106] S. L. Glashow. Partial Symmetries of Weak Interactions. *Nucl. Phys. A*, 22:579, 1961.

[107] D. Acosta et al. Measurements of $b\bar{b}$ azimuthal production correlations in $p\bar{p}$ collisions at $\sqrt{s} = 1.8$ TeV. *Phys. Rev. D*, 71:092001, 2005.

[108] V. Khachatryan et al. Measurement of $B\bar{B}$ Angular Correlations based on Secondary Vertex Reconstruction at $\sqrt{s} = 7$ TeV. J. High Energy Phys. **03 (2011)** 136.

[109] R Aaij et al. Observation of double charm production involving open charm in pp collisions at $\sqrt{s}$=7 TeV. J. High Energy Phys. **06 (2012)** 141; [Addendum: J. High Energy Phys. **03 (2014)** 108].

[110] Roel Aaij et al. Study of $b\bar{b}$ correlations in high energy proton-proton collisions. *JHEP*, 11:030, 2017.

[111] A. Adare et al. Detailed measurement of the e^+e^- pair continuum in $p + p$ and Au+Au collisions at $\sqrt{s_{NN}} = 200$ GeV and implications for direct photon production. *Phys. Rev. C*, 81:034911, 2010.

[112] L. Adamczyk et al. Dielectron Mass Spectra from Au+Au Collisions at $\sqrt{s_{\rm NN}}$=200 GeV. *Phys. Rev. Lett.*, 113(2):022301, 2014. [Addendum: Phys. Rev. Lett. **113**, 049903 (2014)].

[113] PHENIX. Overview of the PHENIX Detector. *Online*.

[114] K. Adcox et al. NIM A499 489-507.

[115] M. Aizawa et al. NIM A499 508-520.

[116] L. Aphecetche et al. NIM A499 521-536.

[117] John Koster. The phenix muon piston calorimeter. 10 2006.

[118] S. Campbell et al. A Proposal for the Muon Piston Calorimeter Extension (MPC-EX) to the PHENIX Experiment at RHIC. 2013.

[119] E. Levin. Saturation at low x. 2001.

[120] S.M. Aronson et al. PHENIX magnet system. *Nucl. Instrum. Meth.*, A499:469–479, 2003.

[121] C Y. Chi, Brian Cole, H Cunitz, J L. Nagle, W Sippach, and Lingyushan Zhang. The phenix data acquisition system. 04 1997.

[122] James Nagle. Run-15 p+Au @ 200 GeV Centrality Categorization. *PHENIX Analysis Notes an*, 1265.

[123] S. Agostinelli et al. GEANT4 Collaboration: A Simulation toolkit. *Nucl. Instrum. Methods Phys. Res., Sec. A*, 506:250, 2003.

[124] G. J. Gounaris and J. J. Sakurai. Finite width corrections to the vector meson dominance prediction for $\rho \to e^+e^-$. *Phys. Rev. Lett.*, 21:244, 1968.

[125] A. Adare et al. Measurement of the relative yields of $\psi(2S)$ to $\psi(1S)$ mesons produced at forward and backward rapidity in p+p, p+Al, p+Au, and ^{3}He+Au collisions at $\sqrt{s_{_{NN}}}$ = 200 GeV. *Phys. Rev. C*, 95(3):034904, 2017.

[126] A. Adare et al. $\Upsilon(1S+2S+3S)$ production in d+Au and p+p collisions at $\sqrt{s_{NN}}$ = 200 GeV and cold-nuclear matter effects. *Phys. Rev. C*, 87(4):044909, 2013.

[127] T. Sjostrand, S. Mrenna, and P. Z. Skands. A Brief Introduction to PYTHIA 8.1. *Comput. Phys. Commun.*, 178:852, 2008.

[128] A. Adare et al. Cross section for $b\bar{b}$ production via dielectrons in d+Au collisions at $\sqrt{s_{_{NN}}}$ = 200 GeV. *Phys. Rev. C*, 91(1):014907, 2015.

[129] R Arnaldi et al. Evidence for the production of thermal-like muon pairs with masses above 1-GeV/c^2 in 158-A-GeV Indium-Indium Collisions. *Eur. Phys. J. C*, 59:607, 2009.

[130] S. S. Adler et al. Jet structure from dihadron correlations in d+Au collisions at $\sqrt{s_{NN}}$=200 GeV. *Phys. Rev. C*, 73:054903, 2006.

[131] S. S. Adler et al. Dense-Medium Modifications to Jet-Induced Hadron Pair Distributions in Au+Au Collisions at $\sqrt{s_{NN}}$ = 200 GeV. *Phys. Rev. Lett.*, 97:052301, 2006.

[132] S. S. Adler et al. Centrality dependence of pi0 and eta production at large transverse momentum in $\sqrt{s_{NN}}$ = 200 GeV d+Au collisions. *Phys. Rev. Lett.*, 98:172302, 2007.

[133] Alan D. Martin, R. G. Roberts, W. J. Stirling, and R. S. Thorne. MRST2001: Partons and α_s from precise deep inelastic scattering and Tevatron jet data. *Eur. Phys. J.*, C23:73–87, 2002.

[134] M. Glck, E. Reya, and A. Vogt. Dynamical parton distributions revisited. *Eur. Phys. J.*, C5:461–470, 1998.

[135] Sanghoon Lim. Charged Hadrons with FVTX in Run15pp200 and RpA. *PHENIX Analysis Notes an*, 1341.

[136] Murad Sarsour Xiaochun He. Phi meson production in small systems at forward rapidity at 200 GeV. *PHENIX Analysis Notes an*, 1289.

[137] Sanghoon Lim Krista Smith Matthew Durham, Anthony Frawley. J/psi as a function of pT in small systems. *PHENIX Analysis Notes an*, 1391.

[138] Deepali Sharma Axel Drees.

[139] R. Vogt. Heavy quark production in heavy ion colliders. *Acta Phys. Hung. A*, 18:11, 2003.

[140] T. Alexopoulos et al. A Measurement of the b anti-b cross-section in 800-GeV/c proton silicon interactions. *Phys. Rev. Lett.*, 82:41, 1999.

[141] D. M. Jansen et al. Measurement of the bottom quark production cross-section in 800-GeV/c proton-gold collisions. *Phys. Rev. Lett.*, 74:3118, 1995.

[142] I. Abt et al. Improved measurement of the b-anti-b production cross section in 920-GeV fixed-target proton-nucleus collisions. *Phys. Rev. D*, 73:052005, 2006.

[143] B. Abelev et al. Measurement of electrons from beauty hadron decays in pp collisions at $\sqrt{s} = 7$ TeV. *Phys. Lett. B*, 721:13, 2013. [Erratum: Phys. Lett.B **763**, 507 (2016)].

[144] C. Albajar et al. Beauty production at the CERN p anti-p collider. *Phys. Lett. B*, 256:121, 1991. [Erratum: Phys. Lett. B **262**, 497 (1991)].

[145] C. Aidala et al. Measurements of $B \to J/\psi$ at forward rapidity in p+p collisions at $\sqrt{s}$=510 GeV. *Phys. Rev. D*, 95(9):092002, 2017.

[146] Paolo Nason and Bryan Webber. Next-to-Leading-Order Event Generators. *Ann. Rev. Nucl. Part. Sci.*, 62:187–213, 2012.

[147] A. Adare et al. Quantitative Constraints on the Opacity of Hot Partonic Matter from Semi-Inclusive Single High Transverse Momentum Pion Suppression in Au+Au collisions at $\sqrt{s_{NN}} = 200$ GeV. *Phys. Rev. C*, 77:064907, 2008.

[148] R. Field. Physics at the Tevatron. *Acta Phys. Polon. B*, 39:2611, 2008.

[149] A. Adare et al. Event Structure and Double Helicity Asymmetry in Jet Production from Polarized $p + p$ Collisions at $\sqrt{s} = 200$ GeV. *Phys. Rev. D*, 84:012006, 2011.

[150] L. Adamczyk et al. Longitudinal and transverse spin asymmetries for inclusive jet production at mid-rapidity in polarized $p + p$ collisions at $\sqrt{s} = 200$ GeV. *Phys. Rev. D*, 86:032006, 2012.

[151] Adare. A et al. Measurements of $\mu\mu$ pairs from open heavy flavor and Drell-Yan in p+p collisions at $\sqrt{s} = 200$ GeV. arXiv:1805.02448.

[152] J. O. Berger, B. Liseo, and R. L. Wolpert. Integrated likelihood methods for eliminating nuisance parameters. *Statist. Sci.*, 14(1):1, 02 1999.

[153] J. Huang, Z.-B. Kang, and Ivan Vitev. Inclusive b-jet production in heavy ion collisions at the LHC. *Phys. Lett. B*, 726:251, 2013.

[154] J. Huang, Z.-B. Kang, I. Vitev, and H. Xing. Photon-tagged and B-meson-tagged b-jet production at the LHC. *Phys. Lett. B*, 750:287, 2015.

[155] R. B. Neufeld, I. Vitev, and B.-W. Zhang. A possible determination of the quark radiation length in cold nuclear matter. *Phys. Lett. B*, 704:590, 2011.

[156] G. Fai, J. Qiu, and X.-F. Zhang. Probing small-x gluons by low-mass Drell-Yan pairs at colliders. *Phys. Rev. C*, 71:014901, 2005.

[157] Geoffrey T. Bodwin, Stanley J. Brodsky, and G. Peter Lepage. Initial State Interactions and the Drell-Yan Process. *Phys. Rev. Lett.*, 47:1799, 1981.

[158] C. Aidala et al. *arXiv:*, page 1805.04075.

[159] Dennis W. Sivers. Single Spin Production Asymmetries from the Hard Scattering of Point-Like Constituents. *Phys. Rev.*, D41:83, 1990.